DOE/NV/11508–35
UC-703

RECEIVED
AUG 13 1998
OSTI

EVALUATION OF GROUNDWATER FLOW AND TRANSPORT AT THE SHOAL UNDERGROUND NUCLEAR TEST: AN INTERIM REPORT

prepared by

Greg Pohll, Jenny Chapman, Ahmed Hassan, Charalambos Papelis,
Roko Andricevic, and Craig Shirley

submitted to

Nevada Operations Office
U.S. Department of Energy

JULY 1998

DISTRIBUTION OF THIS DOCUMENT IS UNLIMITED

MASTER

Publication No. 45162

This report was prepared as an account of work sponsored by the United States Government. Neither the United States nor the United States Department of Energy, nor any of their employees, makes any warranty, express or implied, or assumes any legal liability or responsibility for the accuracy, completeness or usefulness of any information, apparatus, product or process disclosed, or represents that its use would not infringe privately owned rights. Reference herein to any specific commercial product, process, or service by trade name, mark, manufacturer, or otherwise, does not necessarily constitute or imply its endorsement, recommendation, or favoring by the United States Government or any agency thereof. The views and opinions of authors expressed herein do not necessarily state or reflect those of the United States Government or any agency thereof.

This report has been reproduced directly from the best available copy.

Available to DOE and DOE contractors from the Office of Scientific and Technical Information, P.O. Box 62, Oak Ridge, TN 37831; prices available from (423) 576–8401.

Available to the public from the National Technical Information Service, U.S. Department of Commerce, 5285 Port Royal Rd., Springfield, VA 22161.

DISCLAIMER

Portions of this document may be illegible in electronic image products. Images are produced from the best available original document.

This page intentionally left blank

DOE/NV/11508–35
UC-703

EVALUATION OF GROUNDWATER FLOW AND TRANSPORT AT THE SHOAL UNDERGROUND NUCLEAR TEST: AN INTERIM REPORT

prepared by

Greg Pohll, Jenny Chapman, Ahmed Hassan, Charalambos Papelis,
Roko Andricevic, and Craig Shirley
Water Resources Center
Desert Research Institute
University and Community College System of Nevada

Publication No. 45162

submitted to

Nevada Operations Office
U.S. Department of Energy
Las Vegas, Nevada

July 1998

The work upon which this report is based was supported by the U.S. Department of Energy under Contract #DE–AC08–95NV11508.

EXECUTIVE SUMMARY

Numerical modeling is used to characterize groundwater flow and contaminant transport at the Shoal site in north-central Nevada. Project Shoal consisted of a 12-kiloton yield, underground nuclear detonation in 1963 (DOE, 1993). Site characterization activities in the early 1960s provide data on geological and hydrological conditions at the test location in the granite of the Sand Springs Range, and in adjacent alluvium-filled valleys to the east and west. Four new wells were drilled in 1996 and were subject to hydraulic testing and groundwater sampling to further refine the understanding of the flow system. It is important to note that this report is interim in nature. All of the currently available data were used to construct a preliminary groundwater flow and transport model of the Shoal site. There are uncertainties in the data that characterize the subsurface and these uncertainties lead to uncertainties in solute transport behavior.

Hydraulic data indicate that Shoal is located in a regional recharge area, consistent with the location of the site at the top of a mountain range. A groundwater flow divide is located west of the cavity so that flow is toward the southeast, presumably to Fairview Valley. Bulk hydraulic conductivity values for the fractured granite aquifer range from 1.48×10^{-6} to 8.6×10^{-5} cm/sec. Discrete hydraulic conductivity measurements, performed using stressed flowmeter testing at 10 m intervals, range from 4.42×10^{-7} to 7.7×10^{-4} cm/sec. This range in hydraulic conductivity is small and reflects the inability of the field campaign to successfully measure conductivities in the very low range. Isotopic data indicate recharge after the last pluvial conditions, but isolation from the atmosphere of from 6000 to 12,500 years. Chemical variability supports the assumption of heterogeneity in the flow field. Chemical and isotopic differences between water at the site and water in the downgradient valley suggest that water underlying Shoal is either not a major contributor to the valley (as sampled at well HS-1), or that travel times are very long.

The numerical flow model is oriented northwest to southeast, with an upgradient no-flow boundary at the approximate location of the groundwater flow divide, no-flow boundaries on the lateral sides (parallel to the direction of flow), and a specified head boundary downgradient of the intersection of the eastern land withdrawal boundary and the model domain. Recharge is allowed through the upper modeled surface, at a rate of 1.45 cm/yr, as determined by analysis of the thermal profile through the unsaturated zone. The fractured rock aquifer is modeled using an equivalent porous medium approach. Field data are used to characterize the fracture system into classes: large, medium, and no/small fracture zones. Hydraulic conductivities are assigned based on discrete interval measurements and are 1.61×10^{-5} cm/sec for the large fracture class, 7.78×10^{-6} cm/sec for the medium fracture class, and 4.0×10^{-7} cm/sec for the no/small fracture class. The no-fracture class is poorly represented in the field data and was used for calibration. Fracture orientation and persistence are based on downhole logs and surface mapping. Two fracture sets are indicated: one striking N25E and dipping 44°SE, and one striking N8W and dipping 31°E. A correlation scale of 700 m along the strike and dip is used to simulate all fracture classes.

The flow model was calibrated to the hydraulic head measurements in wells HC-1, -2, and -4. A reasonable fit was not obtained to well HC-3, located in the downgradient portion of the model

domain. The true water table elevation in this location is uncertain due to drilling and well completion problems, with resultant water level fluctuation in HC-3. A large component of downward flow occurs in the model, driven by the modeled recharge and boundary conditions. The value of effective porosity is uncertain and is assigned to be 6×10^{-3} based on investigations in fractured granite aquifers. This leads to mean horizontal groundwater velocities across the site of 5 m/yr, though the non-linear gradient causes lower velocities in the upgradient reach and increasing velocities along the flowpath. This rate is inconsistent with the general groundwater ages and flow conditions inferred from the isotopic data, which suggest residence times on the order of thousands of years for groundwater in the model domain, suggesting velocities at least one order of magnitude less than simulated.

Contaminants from the Shoal test are assumed to all be located within the cavity. Prompt injection of tritium away from the cavity was found to increase the arrival of mass at the control plane but not to significantly impact calculated concentrations due to increased spreading. Radionuclides were apportioned between surface deposits and volume deposits in nuclear melt glass, based on their volatility and previous observations. Surface-deposited radionuclides are released hydraulically after equilibration of the cavity with the surrounding groundwater system, and as a function of groundwater flow through the higher-porosity cavity into the low-porosity surrounding aquifer. Release from the nuclear melt glass is patterned after dissolution of volcanic glass and assuming a specific surface area of 0.05 m^2/g, as measured on fragments of nuclear glass from the Nevada Test Site. Half of the starting glass mass is dissolved within approximately 800 years, a relatively rapid rate driven by the highly uncertain specific surface area parameter.

Equilibrium sorption experiments were conducted using granite from the Shoal site for several cations and anions. These were used to calculate a surface-based sorption constant using the specific surface area of the laboratory material. The dimensionless retardation factor for the fracture system used the surface-based sorption constant and an estimate of fracture aperture derived from field transmissivity data. The resulting retardation coefficients are 1.72 for cesium and 83.7 for lead. These values were assigned to other radionuclides based on assumption of probable chemical form and behavior. Anion sorption, based on experiments using chromate and selenite, was not significant enough to include in the transport calculations. Dissolution of strontium occurred from the granite samples used in the experiments, so that no sorption was evident.

Transport of radionuclides from the cavity to the control plane at the site land withdrawal boundary was calculated using particle tracking methods. Processes modeled included the release functions, retardation, radioactive decay, and ingrowth of daughter products. Matrix diffusion and prompt injection were considered in a sensitivity analysis, but colloidal transport was not included. Unit mass values were used to avoid classified data security issues and the results can be scaled.

Unclassified estimates of tritium, ^{90}Sr, and ^{137}Cs mass are used to present breakthrough curves, contaminant concentrations and standard deviations crossing the control plane. Peak mean concentrations are 13,000, 35,000, and 12,000 pCi/L for tritium, ^{90}Sr, and ^{137}Cs, respectively. One standard deviation is 2000, 4000 and 1800 pCi/L for tritium, ^{90}Sr, and ^{137}Cs, respectively. The time

of maximum mass flux occurs 146, 154, and 247 years after the nuclear test, for tritium, ^{90}Sr, and ^{137}Cs, respectively, driven by the transport conditions and radioactive decay. The plumes show relatively little transverse dispersion crossing the control plane as a result of the simulated fracture orientation and the size of the source being equivalent to the scale of heterogeneity modeled. Behavior of the other radionuclides is affected by the slow chemical release and retardation behavior, such that the peak mass breakthrough is smaller and has a longer tail.

The transport calculations are sensitive to many flow and transport parameters. Chief among these are the heterogeneity of the flow field (*i.e.*, fractures and hydraulic conductivity), the specified head boundary condition, recharge, and effective porosity. For reactive solutes, retardation and the glass dissolution rate are also critical. The concentrations calculated are subject to these uncertainties, as well as to the understanding that they represent concentrations averaged over the volume of water contained in one 41.9 m^3 model grid cell. Sample collection, particularly under pumping conditions for groundwater supply, will introduce groundwater mixing that could significantly alter *in situ* contaminant concentrations. The model will be used to assess future data collection activities via a data decision analysis (DDA). The DDA will identify which data are critical in the reduction of model uncertainties.

ACKNOWLEDGEMENTS

The work reported here is the product of a team effort that required the commitment and contributions of a large number of people and organizations. We gratefully acknowledge the contributions made by the many people involved with the Shoal Project and specifically note the following: the support and guidance of the Department of Energy, Nevada Operation Office, specifically Peter Sanders, Robert Bangerter, and Monica Sanchez; the insightful reviews and discussions of the Modeling Subcommittee of the Underground Test Area Technical Working Group, comprised of Andrew Tompson, Andrew Wolfsberg, Mike Sully, Karl Pohlmann, Dave Morgen, and Sirous Djafari; David Smith, of Lawrence Livermore National Laboratory for his assistance in source term issues; Jeff Wurtz and Rick Deshler, IT Corporation, for their supervision of the HC well drilling and geophysical logging; Brad Lyles, Todd Mihevc and Sam Earman, DRI, for invaluable field data collection; Ron Hershey, Roger Jacobson, Britt Jacobson, and Marjory Jones, DRI, for providing internal reviews; and Debi Noack and Heather Nelson, DRI, for their outstanding electronic publishing support.

CONTENTS

EXECUTIVE SUMMARY ii

ACKNOWLEDGEMENTS v

LIST OF FIGURES ix

LIST OF TABLES xii

LIST OF ACRONYMS xiii

1.0 Introduction 1
- 1.1 Purpose 1

2.0 Hydrogeologic Setting 1
- 2.1 General Description of Study Area 1
- 2.2 Previous Work 4
- 2.3 Geology 4
- 2.4 Hydrogeology 5
  - 2.4.1 Local Physical Flow System 7
    - 2.4.1.1 Direction of Groundwater Flow 7
    - 2.4.1.2 Hydraulic Properties 10
    - 2.4.1.3 Groundwater Velocity 12
    - 2.4.1.4 Impact of the Nuclear Test on the Groundwater System 12
    - 2.4.1.5 Estimates of Radionuclide Transport 13
  - 2.4.2 Hydrochemical Environment 13
    - 2.4.2.1 Chemical and Isotopic Characteristics of Site Groundwater 14
    - 2.4.2.2 Comparison of Site Groundwater to Other Water in the Sand Springs Range 19
    - 2.4.2.3 Regional Flow Implications of the Groundwater Chemistry 19

3.0 Conceptual Model 22
- 3.1 Conceptual Flow Model 22
- 3.2 Conceptual Transport Model 23

4.0 Methodology 25
- 4.1 Representation of Geologic Heterogeneity 25
  - 4.1.1 Simulating Fracture Class Fields 27
- 4.2 Numerical Flow Code Description 28
  - 4.2.1 Calibration of the Groundwater Flow Model 29
- 4.3 Numerical Transport Model Description 30
  - 4.3.1 Output Control 31
  - 4.3.2 Radioactive Decay 31

5.0 Flow Model 32
- 5.1 Characterization of Fracture Classes 32
  - 5.1.1 Fracture Orientation 33
  - 5.1.2 Fracture Class Spatial Persistence 37
- 5.2 Hydraulic Conductivity Representation 45
- 5.3 Model Grid 46

5.4 Boundary Conditions 48
5.4.1 Surface Recharge 48
5.4.2 Constant Head Boundary 50
5.5 Groundwater Flow Model Results 51
5.5.1 Hydraulic Conductivity Fields 51
5.5.2 Calibration 51
5.5.3 Water Table Elevation 53
5.5.4 Flux Fields 53
5.5.5 Velocities 56

6.0 Transport Model 57
6.1 Source Term 57
6.1.1 Radionuclide Source Term 57
6.1.2 Non-radionuclide Hazardous Materials 62
6.2 Release Functions 63
6.2.1 Volume/Surface Mode Designation 64
6.2.2 Cavity Infill Analysis 66
6.2.3 Nuclear Melt Glass Dissolution 68
6.2.3.1 Dissolution Rate Equation 70
6.2.3.2 Dissolution Rate Constant 70
6.2.3.3 Specific Surface Area 70
6.2.3.4 Dissolution Rate for Shoal Nuclear Melt Glass 73
6.3 Retardation 73
6.3.1 Laboratory Results 75
6.3.1.1 Limitations 78
6.3.2 Assignment of Distribution Coefficient 78
6.3.3 Calculation of Retardation 80

7.0 Results 82
7.1 Breakthrough Curves 85
7.2 Specific Examples 87
7.3 Sensitivity and Uncertainty Analysis 91
7.3.1 Geochemical Release Function 91
7.3.2 Boundary Conditions 92
7.3.3 Matrix Diffusion 94
7.3.4 Prompt Injection 95
7.3.5 Porosity 97
7.3.6 Retardation 98
7.3.7 Heterogeneity 98
7.3.8 Recharge 100

8.0 Discussion 101
8.1 Summation of Tritium, Strontium and Cesium 101
8.2 Impact of Sensitivity Analysis 101
8.3 Contamination Boundaries 103
8.4 Interpretation of Contaminant Concentration Predictions 104

9.0 Conclusions 106
10.0 Recommendations for Future Work 109
11.0 Bibliography 111
Appendices
1: Shoal Water Levels 1–1
2: Vertical Conductance 2–1
3: Fracture Code Plots 3–1
4: Letter Report – Shoal Field Operations 4–1
5: Stressed Flowmeter Testing Shoal Wells HC-1 and HC-2 5–1
6: Stressed Flowmeter Testing Shoal Wells HC-1 and HC-4 6–1
7: Equilibrium Studies of Lead, Cesium, Strontium, Chromate, and Selenite Sorption on Granite from the Project Shoal Test Site, Fallon, Nevada 7–1
8: Radionuclides of Interest in Transport from Underground Nuclear Tests and their Decay Chains 8–1

LIST OF FIGURES

2.1. Study location. 2

2.2. Shoal site looking northeast. 3

2.3. Study location with local monitoring wells and regional groundwater flow directions. 6

2.4. Hydrographs of the bedrock holes prior to the Shoal test. 8

2.5. Generalized groundwater flow system and well locations at the Shoal site. 9

2.6. Piper diagram showing the relative ionic composition of groundwater samples from the HC wells at the Shoal site, as well as that of other samples from wells and springs in the area. 14

2.7. Comparison of ion concentrations of groundwater quality parameters for the HC wells. 16

2.8. Stable isotopic composition of water from wells and springs in the immediate Shoal area. 17

2.9. Stable isotopic composition of groundwater in the Shoal area, compared to other water in the region. 21

3.1. Vertical cross section near the Shoal site showing idealized groundwater flow directions. 22

3.2. A diagrammatic representation of the transport model source and processes considered. 24

5.1. Videolog showing no/small fractures from HC-3. 34

5.2. Videolog showing medium-sized fractures from HC-3. 34

5.3. Videolog showing large fractures from HC-3. 35

5.4. Schematic of borehole and acoustic televiewer log showing how interpretation of fracture is performed. 35

5.5. Schematic showing how fractures are transformed into an equal area net. 36

5.6. Observed orientation frequencies of intermediate and large fractures from borehole acoustic televiewer logs. 37

5.7. ECH-D fracture analysis, adapted from University of Nevada (1964). 38

5.8. Surface geologic structure map near ground zero. 40

5.9. Directional (N30E) indicator semi-variogram for the indicator transformed surface geologic structure map. 41

5.10. Vertical indicator semi-variogram for the integer fracture codes 1→(2,3). 42

5.11. Vertical indicator semi-variogram for the integer fracture codes (1,2)→3. 42

5.12. One realization of the integer fracture codes for simulation A, simulation B and the superimposed set. 44

5.13. Site diagram of the Shoal site showing the areal extents of the model domain and boundary conditions for the groundwater flow model. 47

5.14. Measured versus simulated vertical temperatures for PM-1. 50

5.15 Frequency of absolute error for each calibration trial. 52

5.16. Simulated (single realization) and measured water levels. 54

5.17. Relative magnitude and direction of simulated (one realization) fluid fluxes for a vertical slice in the model domain. 54

5.18. Frequency of the x-direction fluxes from one flow realization. 55

5.19. Frequency of the y-direction fluxes from one flow realization. 55

5.20. Frequency of the z-direction fluxes from one flow realization. 56

6.1. The initial water table shape following detonation. 68

6.2. Relationship of specific surface area of Rainier nuclear melt glass to particle size. . . . 71

6.3. Dissolution of Shoal nuclear melt glass, assuming an analog to volcanic glass dissolution, using the parameters described in the text. 74

7.1. Site diagram of the Shoal site showing the areal extents of the model domain and the location of the downgradient control plane. 83

7.2. Cross section of control plane showing its vertical position. 84

7.3. Normalized mean mass flux (*i.e.*, assumes unit initial mass with no decay) for the seven transport cases. 86

7.4. Simulated mean tritium concentration, standard deviation and mass flux at the downgradient control plane. 88

7.5. Simulated mean ^{90}Sr concentration, standard deviation and mass flux at the downgradient control plane. 89

7.6. Simulated mean ^{137}Cs concentration, standard deviation and mass flux at the downgradient control plane. 90

7.7. Simulated mean ^{90}Sr mass flux for the two values of the geochemical slow release coefficient. 93

7.8. Simulated mean ^{99g}Tc normalized mass flux for the two values of the geochemical slow release coefficient. 93

7.9. Mean mass flux of tritium across the downgradient control plane for the base case (specified head = 1210) and a simulated lower boundary condition of 1100 m above MSL. 94

7.10. Simulated mean mass flux of tritium at the downgradient control plane with and without the inclusion of prompt injection. 97

7.11. Simulated mean mass flux of tritium for the three values of effective porosity. 98

7.12. Mean mass flux of tritium for three conceptual models of heterogeneity at the downgradient control plane. 99

7.13 Normalized mean mass flux of tritium (unit initial mass and no decay) at the downgradient control plane for two values of surface recharge. 100

8.1. Map of the Shoal site with the simulated boundary (50th percentile) for tritium at 20,000 pCi/L.. 105

8.2. Cross section of the Shoal site with the simulated boundary (50th percentile) for tritium at 20,000 pCi/L. 106

LIST OF TABLES

2.1. Investigations and associated scope for Shoal-related projects. 4

2.2. Well summary for wells near the Shoal site. 7

2.3. Chemical analyses of water samples collected from the HC wells at the Shoal Site, along with analyses of groundwater from other wells in the area of the Sand Springs Range. 15

2.4. Groundwater-age calculations based on carbon isotopic data. 18

5.1. Strike and dip orientations for each fracture class as determined from the acoustic televiewer analysis.. 36

5.2. Geostatistical parameters for each fracture class. 41

5.3. SIS parameters used for each fracture class. 43

5.4. Prior probabilities of each fracture class for original and upscaled data. 46

5.5. Summary of hydraulic analysis from thermal flowmeter tests. 51

5.6. Simulated values of hydraulic conductivity for each fracture class. 53

6.1. List of radionuclides important for investigations of transport from underground nuclear tests, as presented by Smith et al. (1995). 59

6.2. Daughter products generated by radionuclides in Table 6.1.. 61

6.3. Release functions assigned to Shoal source term nuclides, based on literature references described in the text. 64

6.4. Comparison between chemical composition of natural volcanic glass and nuclear melt glass. 69

6.5. Linear and Freundlich isotherm parameters. 77

6.6. Assignment of sorption behavior to radionuclide source elements. 79

6.7. Retardation coefficients assigned to radionuclide daughter products that are contrary to their expected transport behavior. 80

6.8. Estimated fracture apertures. 81

6.9. Results from hydraulic tests for the Shoal site. 82

7.1. Values of general parameters used in transport simulations. 85

7.2. Case-specific transport parameters. 85

LIST OF ACRONYMS

BHTV	borehole televiewer
CADD	Corrective Action Decision Document
CAIP	Corrective Action Investigation Plan(s)
CFR	*Code of Federal Regulations*
DOD	U.S. Department of Defense
DOE	U.S. Department of Energy
DOE/NV	U.S. Department of Energy, Nevada Operations Office
DRI	Desert Research Institute
FFACO	*Federal Facility Agreement and Consent Order*
GIS	geographical information system
MPC	maximum permissible concentration
MSL	mean sea level
MWL	meteoric water line
NA	not analyzed
NTS	Nevada Test Site
PSA	Project Shoal Area
PTRW	Particle Tracking Random Walk
SGS	sequential Gaussian simulation
SIS	sequential indicator simulation
SMOW	standard mean ocean water

This page intentionally left blank

1.0 Introduction

Since 1962, all United States nuclear tests have been conducted underground. A consequence of this testing has been the deposition of large amounts of radioactive materials in the subsurface, sometimes in direct contact with groundwater. The majority of this testing occurred on the Nevada Test Site, but a limited number of experiments were conducted in other locations. One of these is the subject of this report, the Project Shoal Area (PSA), located about 50 km southeast of Fallon, Nevada. The Shoal test consisted of a 12-kiloton-yield nuclear detonation (DOE, 1993), which occurred on October 26, 1963. Project Shoal was part of studies to enhance seismic detection of underground nuclear tests, in particular, in active earthquake areas.

Characterization of groundwater contamination at the Project Shoal Area is being conducted by the U.S. Department of Energy (DOE) under the Federal Facility Agreement and Consent Order (FFACO) with the State of Nevada Department of Environmental Protection and the U.S. Department of Defense (DOD). This order prescribes a Corrective Action Strategy (Appendix VI), which, as applied to underground nuclear tests, involves preparing a Corrective Action Investigation Plan (CAIP), Corrective Action Decision Document (CADD), Corrective Action Plan, and Closure Report.

The CAIP for the Project Shoal Area was approved in September 1996 and prescribed the work described herein. The scope of the CAIP is flow and transport modeling to establish contaminant boundaries that are protective of human health and the environment. This interim report describes the current status of the flow and transport modeling for the PSA. This model will be used in conjunction with a data decision analysis (DDA) to identify parameters that yield the most modeling uncertainty. After the completion of the DDA, critical input parameters will be identified and additional field characterization may be performed. Once additional data are collected, a second groundwater model will be constructed. The second phase of the modeling effort will support the development of the CADD for the site.

1.1 Purpose

The purpose of this work is to characterize groundwater flow and contaminant transport at the PSA through numerical modeling which utilizes site-specific hydrologic data. This requires a scope including development of a conceptual model of the groundwater flow environment at Shoal based on geologic, hydrologic, and chemical information, development of a numerical flow model, development of a conceptual model of contaminant release and transport properties from the nuclear test cavity, development of the numerical model of transport, and performance of associated sensitivity and uncertainty analyses. The focus of contaminant transport is on tritium, as specified in Section 5.2 of the FFACO, Appendix VI, though the full radionuclide source term is also considered.

2.0 Hydrogeologic Setting

2.1 General Description of Study Area

The PSA consists of a 10.4 km^2 (4 mi^2) area in the Sand Springs Range, located near Fallon, Nevada, in Churchill County (Figure 2.1). Ground zero of the underground nuclear test is located

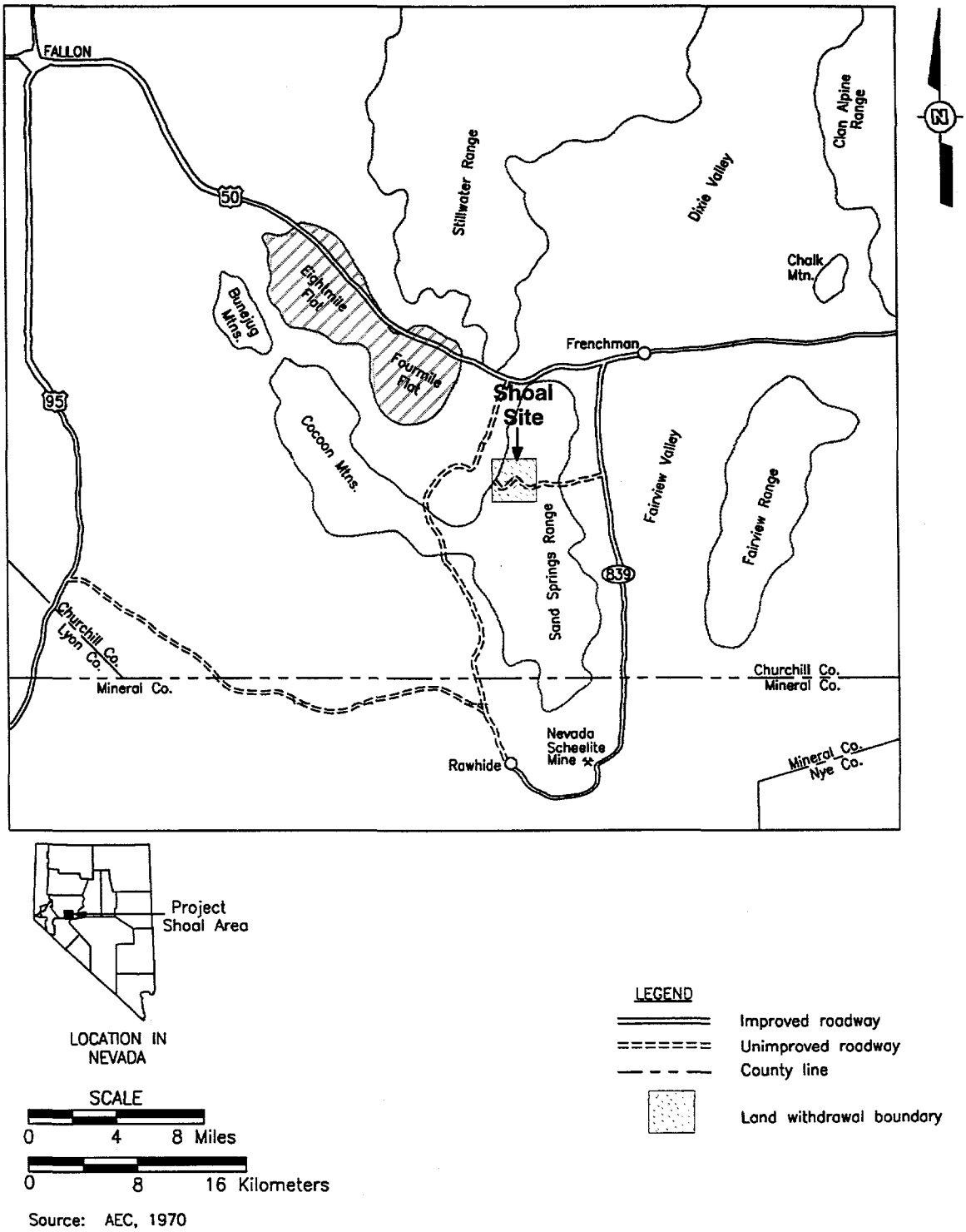

Figure 2.1. Study location.

at North 493828 (m), East 169939 (m) (Nevada Grid Coordinates), with a land elevation of 1594 m (MSL) (5230 ft). The nuclear device was emplaced 367 m below the land surface, at the end of a 305-m-long drift mined east from a vertical shaft. Figure 2.2 shows the area near ground zero looking northeast.

The Sand Springs Range is a north-south-trending range with a total relief between the range and valleys of about 500 m. A major intermittent drainage course in Ground Zero Canyon leads east to Fairview Valley. No permanent water bodies or streams exist. Sparse, low vegetation covers the area. The ground slopes steeply west to Fourmile Flat and east to Fairview Valley. Ground zero is at the crest of the range on a minor intramountain plateau named Gote Flat, which is about 800 m wide. At a depth of 367 m below the land surface, the Shoal working point is nearly at grade with the adjacent valley floors.

The Shoal site is in a sub-humid to semi-arid region of Nevada's Great Basin. Annual rainfall varies from about 13 cm in the valleys to about 30 cm in the high mountain ranges (Hardman, 1949). Most precipitation in the mountain ranges occurs as snow. The annual precipitation estimate for the Shoal site varies between 20 cm (Gardner and Nork, 1970) and 30 cm (Hardman, 1949). Using the relationship between precipitation and recharge described by Maxey and Eakin (1949), an estimated 3 to 7 percent (0.6 to 2.1 cm/yr) of the annual precipitation will infiltrate and become groundwater recharge. Daily temperature fluctuations in excess of 50°F (28°C) can occur. Maximum temperatures exceed 100°F (38°C) in July and August and minimum temperatures of 0°F (-18°C) occur in December and January.

Figure 2.2. Shoal site looking northeast.

2.2 Previous Work

Numerous investigations have been performed to characterize the subsurface hydrogeology and radionuclide transport from the Shoal underground nuclear test. Table 2.1 shows the primary investigations and associated scope. The University of Nevada (1965) reports on the original site characterization performed in support of Project Shoal.

Table 2.1. Investigations and Associated Scope for Shoal-Related Projects.

Investigation	Scope
Cohen and Everett, 1963	regional groundwater hydrology and recharge in the Dixie-Fairview Valley area
University of Nevada, 1965	aerial photography, topographic maps, geological mapping, mineralogical studies, age determinations, drilling operations and associated geophysical analysis, gravity survey, aeromagnetic survey, refraction survey, physical tests of borehole cores, general surface and subsurface hydrology, groundwater chemistry
Hazelton-Nuclear Science, 1965	radionuclide transport, source term analysis, cavity infill time
Gardner and Nork, 1970	detonation type and products, climatology, geology, hydrology, cavity infill time, radionuclide transport, radioactivity distribution
Glancy and Katzer, 1975	regional groundwater hydrology
DOE, 1984	off-site environmental monitoring program
Chapman *et al.*, 1994a, DRI #45130	regional isotopic and hydrochemical analysis
Chapman *et al.*, 1995, DRI #45132	scoping calculations of tritium transport
DOE, 1998	drilling operations (fall 1996), geology, geophysics, radiologic monitoring

2.3 Geology

The Shoal test occurred in typical Basin and Range terrain, consisting of fault-block mountains and valleys. The Sand Springs Range trends north-south with boundaries defined by nearly vertical northeast- and northwest-trending faults. The range is comprised of metamorphosed Paleozoic and Mesozoic marine sediments surrounding a central granitic intrusive body of Cretaceous age. East of the range, the Fairview Valley contains Tertiary and Quaternary alluvial and aeolian sediments as much as 1765 m thick. Fourmile Flat is a pediment west of the Sand Springs Range consisting of alluvial fans, pediment sand and gravels, and aeolian and playa deposits. The Fourmile Flat sediment is underlain by a relatively shallow west-sloping crystalline basement. The unconsolidated deposits thicken westward to about 395 m. Active tectonic history appears in many of the geologic

features. The region's seismic activity, as evidenced by the 1954 Dixie Valley earthquake (Zones, 1957) was a desirable factor in siting the Shoal test. Intermittent faulting is present both in the high- and moderate-angle, northeast- and northwest-trending faults within the center of the Sand Springs Range.

2.4 Hydrogeology

The Shoal test was conducted within the granitic uplift of the Sand Springs Range. The highland area around ground zero is a regional groundwater recharge area, with regional discharge occurring both in the Fourmile and Eightmile flats area to the west of the range, and in the Humboldt Salt Marsh in Dixie Valley to the northeast of the range. Beneath the Sand Springs Range, groundwater occurs within fractured, predominantly fresh, granite. Groundwater occurs about 300 m below ground surface in the general vicinity of the test. Decreasing hydraulic potentials with depth were noted during site characterization studies (University of Nevada, 1965), supporting the interpretation of the range as a recharge area. A few high altitude springs discharging from perched zones in the granite can be found to the south in the range. In the adjacent valleys, groundwater occurs in alluvial material eroded from the highland areas and hydraulic testing indicates much higher transmissivity than found in the granite (University of Nevada, 1965).

Granitic bedrock is relatively near the surface beneath a veneer of alluvium to the west of the Sand Springs Range and hydrologic data are available from one well, H-3, completed in bedrock in that area (Figure 2.3 and Table 2.2). The water level in H-3 is about 99 m (325 ft) below land surface. Farther to the west, and in Fairview Valley to the east, bedrock occurs at greater depths and is not penetrated by wells. Discharge of water originating in the Sand Springs Range occurs at springs and by evapotranspiration along the edge of the salt pan in Fourmile Flat. Groundwater potentials beneath Fourmile Flat generally increase with depth, which is common in discharge zones. Data from well H-2, completed in the alluvium between the range and the salt pan, suggest that a counterflow of dense, saline water may be moving back toward the range from the playa, driven by buoyancy forces, with fresh water moving from the Sand Springs Range confined to a thin lens at the top of the saturated zone in Fourmile Flat (Chapman *et al.*, 1994a).

The alluvium is much thicker in Fairview Valley, as compared to Fourmile Flat. Though three alluvial aquifers, separated by clay horizons, were identified in site characterization studies, it was concluded that the units act as a single hydraulic system (University of Nevada, 1965). The flow in Fairview Valley is primarily lateral with no vertical gradients. No discharge to the surface occurs in Fairview Valley. Groundwater in Fairview Valley moves northward to the regional discharge area in Dixie Valley. One monitoring well, HS-1, exists in Fairview Valley. This alluvial well was used as the supply well during drilling both in the 1960s and during the recent 1996 drilling. It also serves as a cattle ranching supply well during parts of the year. Another well, H-4, is located near HS-1 but is no longer accessible. Water level depths are 91 m (300 ft) in this area.

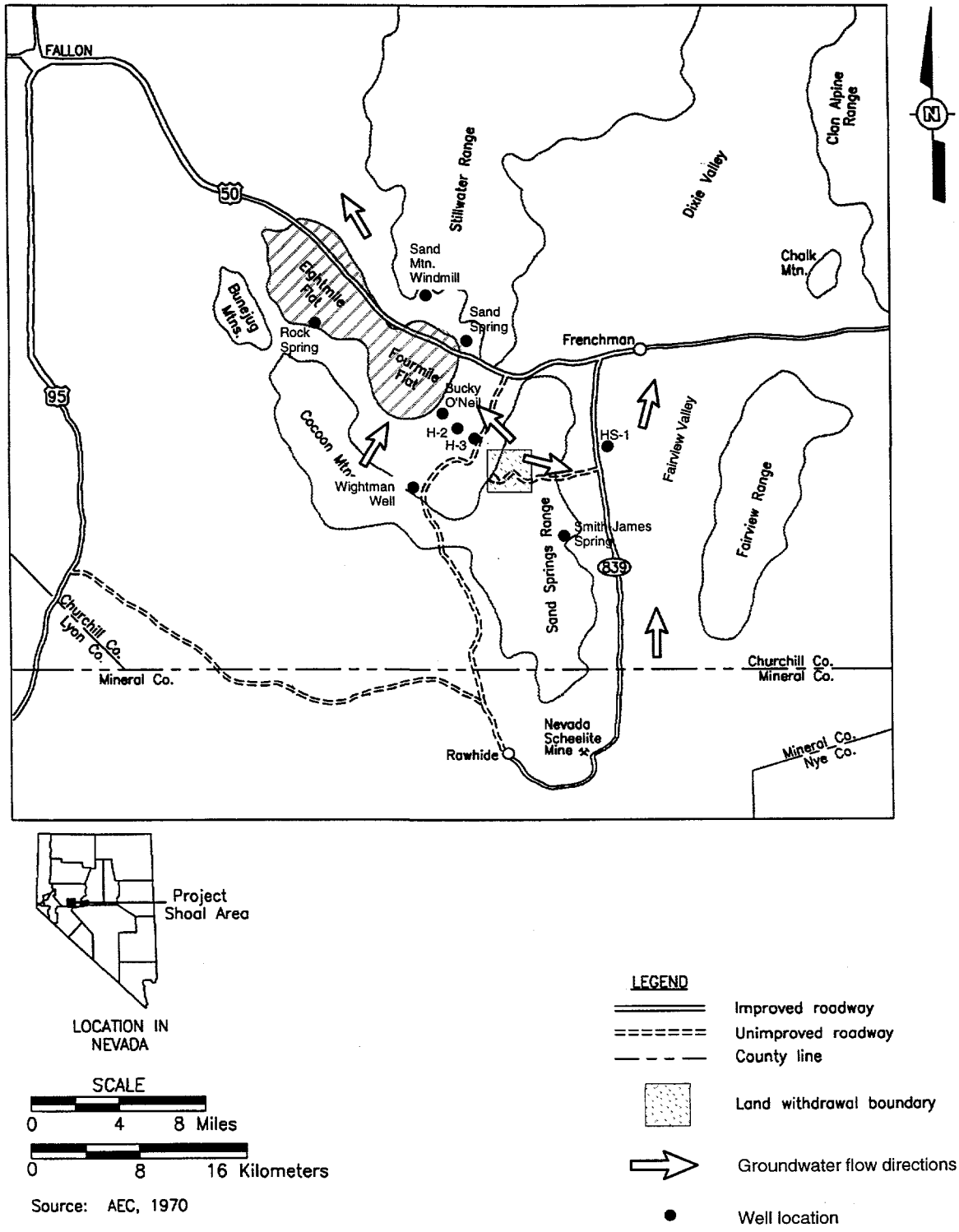

Figure 2.3. Study location with local monitoring wells and regional groundwater flow directions.

Table 2.2. Well Summary for Wells Near the Shoal Site. Details of well drilling and completion can be found in University of Nevada (1965) and DOE (1997).

Well	North (ft)	East (ft)	Total Depth (m)	Grd. Sur. Elv. (m MSL)	Water Table Elv. (m MSL)
HS-1	1622141.28	576875.65	213.06	1293.19	1201.71
H-2	1631585.00	543132.00	237.74	1224.38	1190.59
H-3	1627331.86	548884.86	146.30	1289.97	1189.91
H-4	1622285.67	576914.39	284.99	1292.94	1201.74
PM-1	1618717.83	556030.63	408.13	1633.13	1299.46
PM-2	1621842.43	558120.94	394.72	1620.79	1356.34
PM-3	1619192.76	559336.33	334.37	1563.65	1237.23
PM-8	1619967.78	557532.73	283.46	1596.48	1344.11
USBM-1	1619992.41	557949.92	452.90	1588.62	1312.16
ECH-A	1619292.70	558740.30	579.12	1572.43	n/a
ECH-D	1619975.70	556545.50	614.17	1593.78	1299.97
PS-1	1620168.00	557539.00	n/a	n/a	n/a
Shaft	1620150.00	556549.00	310.29	1610.99	<1300.58
GZ	1620137.00	557494.00	366.98	1593.98	n/a
HC-1	1621927.00	557360.40	405.38	1617.81	1293.90
HC-2	1620208.30	555447.80	369.42	1629.50	1292.70
HC-3	1618822.90	560114.70	364.21	1548.34	1192.70
HC-4	1619560.70	557188.00	377.95	1603.04	1285.50

2.4.1 Local Physical Flow System

2.4.1.1 Direction of Groundwater Flow

University of Nevada (1965) conducted an extensive investigation to characterize the geology and hydrogeology of the Project Shoal Area. They concluded that a groundwater divide may exist northwest of the test cavity and that the main component of lateral movement of groundwater from the cavity is southeast toward Fairview Valley. They also note that there is a large component of downward groundwater motion. The water levels observed during their study are highly uncertain due to the introduction of drilling and testing waters. Figure 2.4 shows the hydrographs of the bedrock wells near ground zero before the nuclear test. The water levels in the wells fluctuate hundreds of feet due to the addition of drilling fluids and slug tests. Figure 2.5 shows the location of these features for the local flow system.

A prime objective of the recent drilling effort was to determine with greater confidence the direction of groundwater flow from the nuclear test. Seven wells (PM-1, PM-2, PM-3, PM-8, USBM-1, ECH-A, ECH-D) were installed during the 1960s site characterization work and provided some information regarding hydraulic properties, but all were plugged shortly after the Shoal test

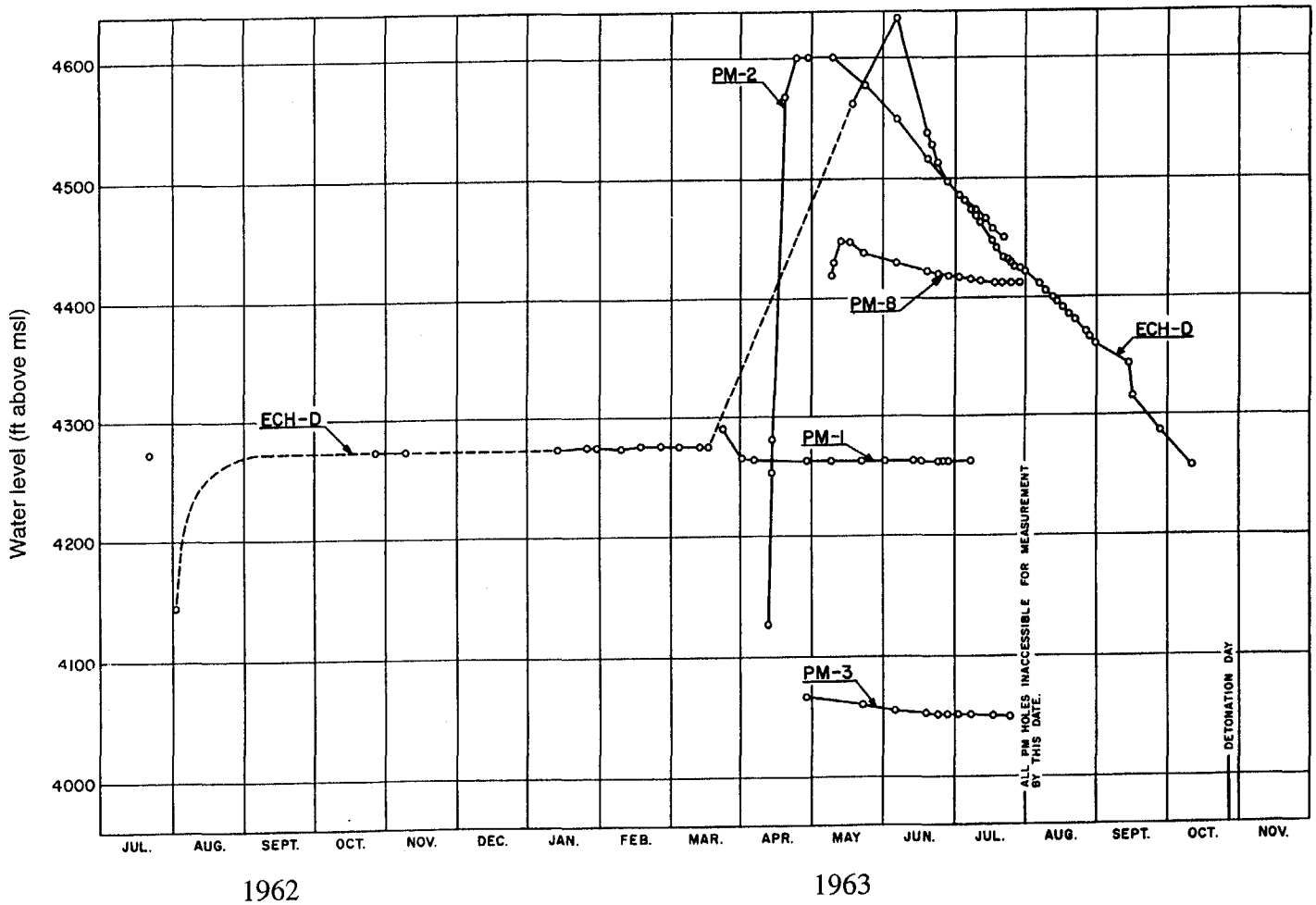

Figure 2.4. Hydrographs of the bedrock holes prior to the Shoal test (adapted from University of Nevada, 1965).

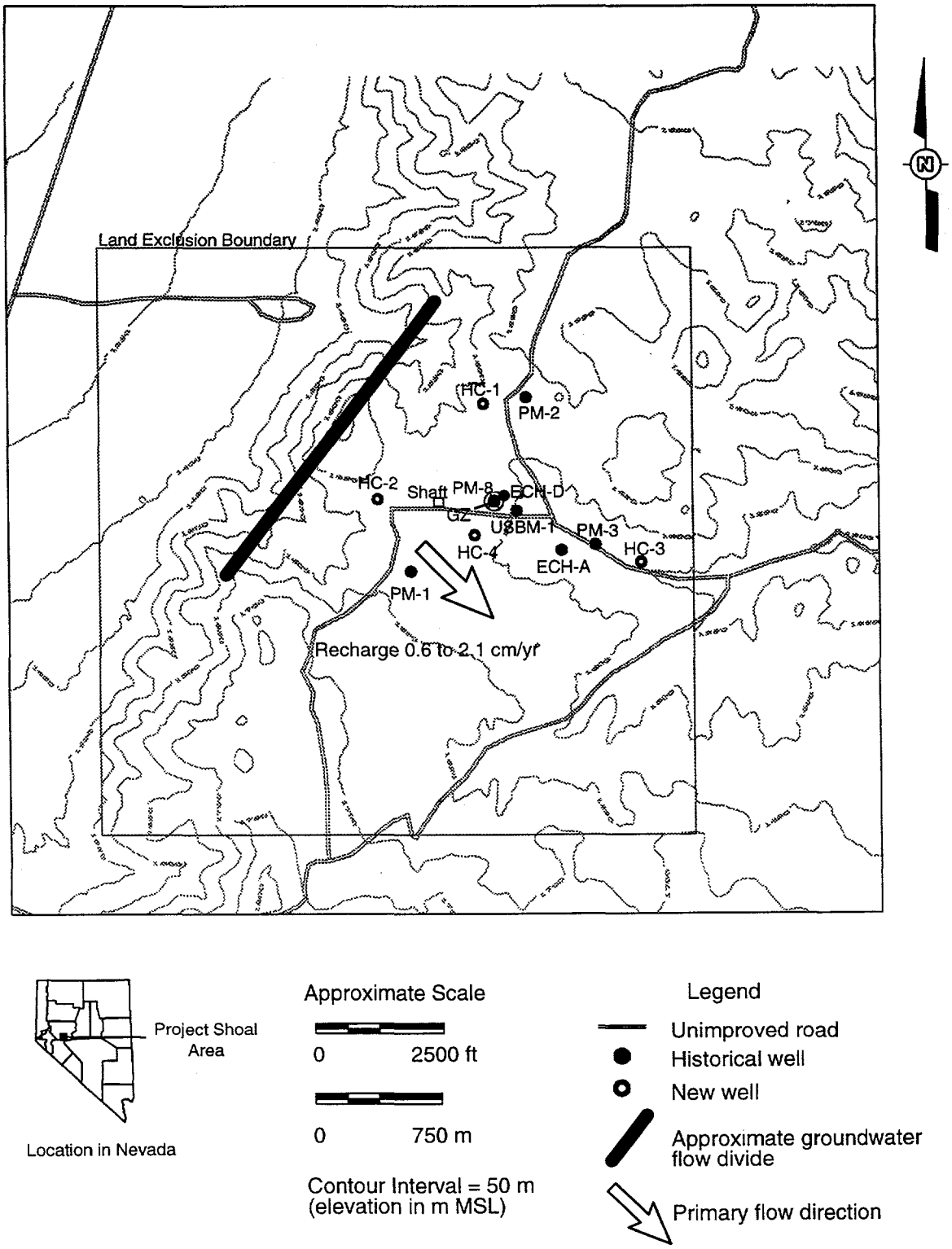

Figure 2.5. Generalized groundwater flow system and well locations at the Shoal site.

was completed. The original shaft was accessible until 1996, and a final videolog prior to filling showed no water saturation to a depth of 310 m (1018 ft). Four new wells were installed in the fall of 1996 to characterize the subsurface hydraulic properties near ground zero. See Appendix 1 for temporal plots of water level elevations in the new wells.

The water levels determined from the new hydrologic characterization (HC) wells confirm the earlier conclusion of generally eastward directed groundwater flow from the test location. The wells were drilled with a minimal introduction of fluids and were completed within the first 100 m of the saturated zone. The groundwater flow divide lies to the west of an equipotential line described by the hydraulic head measurements at HC-1 and HC-2. From HC-1 and HC-2, there is a reduction in head of approximately eight m at HC-4 (near the cavity location).

The hydraulic head measured at HC-3 varied dramatically during drilling and completion. It originally appeared to stabilize at an elevation of 1217.1 m, but subsequently dropped to 1192.7 m. This final value is approximately 10 m below the hydraulic head measured in the presumed downgradient valley well, HS-1. It is also below the water levels elsewhere downgradient in Fairview Valley and below that recorded for a stock well in Dixie Valley north of U.S. Highway 50 (University of Nevada, 1965). The Humboldt Salt Marsh, the probable regional discharge area for groundwater flow from Shoal, lies at an elevation of 1025 m (Bateman and Hess, 1978), while Fourmile Flat lies between 1186 and 1201 m. Well HC-3 suffered many drilling difficulties, as the borehole apparently followed a major fault, and could not be completed similar to the other wells (it has a 5-cm-diameter piezometer installed rather than the open borehole completion of the other HC wells). This completion has prevented hydraulic testing to investigate the anomalously low water level.

2.4.1.2 Hydraulic Properties

Four measurements of transmissivity in the granite aquifer were made within 1.6 km of the Shoal test, in wells PM-1, PM-3, USBM-1, and H-3, by the University of Nevada (1965). They express no confidence in the interpretation of the test results because of the many differences between conditions in the granite and the idealized conditions under which the testing theory was developed. The University of Nevada (1965) concluded that the granite near the site has a transmissivity less than 3×10^{-5} m^2/s (original units were 200 gpd/ft). In addition, they state that the aquifer beneath the range has a lower transmissivity than that measured at well H-3, west of the range.

Other workers have since provided interpretations of the hydraulic test results reported in University of Nevada (1965). Gardner and Nork (1970) report that the apparent hydraulic conductivity of the Sand Springs granite ranges from 10^{-6} to 10^{-5} cm/sec. Using ranges of contributing thickness derived from well logs, Chapman *et al.* (1995) calculated a range in hydraulic conductivity for PM-1, PM-3 and USBM-1 of 4.7×10^{-6} to 1.1×10^{-4} cm/sec. Using the full saturated thickness of H-3 (46 m), they similarly calculated a hydraulic conductivity of 6.1×10^{-5} cm/sec, based on the aquifer test performed there.

Hazelton-Nuclear Science (1965) used an analysis of groundwater inflow into the shaft-drift complex to estimate the hydraulic properties of the granite. Using the Dupuit Equation, they obtained a hydraulic conductivity of 10^{-5} cm/sec.

Aquifer tests were performed in wells HC-1, -2, and -4 and are reported in detail in Appendix 4 (Earman and Pohll, 1997). The hydraulic conductivity resulting from these fully penetrating tests ranges from 1.48×10^{-6} at HC-2 to 4.7×10^{-5} cm/sec at HC-1. A numerical analysis of the HC-1 test resulted in a hydraulic conductivity value of 8.60×10^{-5} cm/sec.

In addition to borehole hydraulic testing, a program of discrete hydraulic conductivity measurements was undertaken for the HC wells, with the aim of understanding the hydrogeologic heterogeneity of the fracture system at Shoal. Two methods were employed, stressed flowmeter testing and straddle packer testing. Stressed flowmeter testing determines the vertical distribution of hydraulic conductivity by either pumping or injecting fluid at a constant rate and measuring the vertical flow distribution. Straddle packer testing essentially performs a hydraulic test over a discrete interval by isolating a section of borehole between two inflated packers and measuring the aquifer response to an applied pressure pulse. The flowmeter testing is simpler to implement in the field, but has a limited lower resolution (cannot quantify very low hydraulic conductivities). Unfortunately, difficulties in the field implementation of the straddle packer testing (primarily resulting from the expansion from a 12.7-cm casing to a nominal 20.32-cm borehole) prohibited successful measurements.

Stressed flowmeter testing was successfully carried out in wells HC-1 and HC-4. Measurements were made at 10-m intervals and are reported in detail in Appendices 5 and 6. Hydraulic conductivities ranged from 4.4×10^{-7} to 7.7×10^{-4} cm/sec. Measurements were attempted in well HC-2, but the very low hydraulic conductivity of the well prevented equilibrium flow conditions from being achieved under either pumping or injection conditions. The inconclusive nature of the HC-2 thermal flowmeter analysis points out the limitations of this hydraulic test. When the hydraulic conductivities are very low, equilibrium conditions cannot be met without severe drawdowns, which then impair the testing procedure. Secondly, areas of low conductivity do not produce much water relative to other portions of the borehole. The procedure relies on relative changes in discharge to calculate a conductivity value (see Appendix 5 for details). This limitation in resolution impacts the parameterization of the hydraulic conductivity, especially in zones of little to no fracturing, and therefore impacts the ability to describe the subsurface heterogeneity.

It is sometimes found that hydraulic conductivity decreases with depth in deep groundwater systems. There are two sources of information that dispute this hypothesis at the Shoal site. First, University of Nevada (1965) drilled a deep well (ECH-D) to a total depth of 614 m bgs. There was no indication of decreased fracture density or fracture aperture with depth in ECH-D. Secondly, the hydraulic testing the recent HC wells did not show any correlation of hydraulic conductivity (discrete tests) with depth.

2.4.1.3 Groundwater Velocity

Based on their observations during well drilling and testing, and during mining operations, the University of Nevada (1965) concluded that the rate of groundwater movement in the vicinity of the detonation site is low. They note that this is shown by the recovery tests, steep potentiometric gradients, and rapid increases in ion concentration downgradient. The rate of movement of groundwater in the granite was believed to be a fraction of that computed for the valley fill. The estimate of groundwater velocity in the alluvium was 10 m/yr (University of Nevada, 1965).

Using the data developed by the University of Nevada (1965), several estimates of groundwater velocity are available. Hazelton-Nuclear Science gave a range of fluid velocity at Shoal between 3 and 7 m/yr. Gardner and Nork (1970) estimate that the groundwater velocity ranges from 0.3 to 30 m/yr. Chapman *et al.* (1995) used a velocity of 3 m/yr for flow eastward from Shoal.

2.4.1.4 Impact of the Nuclear Test on the Groundwater System

The Shoal nuclear test created a cavity, which then collapsed and formed a rubble chimney. This chimney did not propagate to the land surface. The cavity radius is reported to be 26 m (Hazelton-Nuclear Science, 1965). The top of the chimney is located 108.5 m above the shot location, at an elevation of 1342.5 m above sea level. The top of the chimney contains a void 11 m high. The cavity is initially unsaturated as a result of the thermal and compressional forces of the nuclear explosion. Hazelton-Nuclear Science (1965) estimated that at least 10 years would be required for the cavity to re-saturate. Gardner and Nork (1970) estimated an infill time of 12 years.

Fracture intensity caused by an underground nuclear test varies with distance from the working point. General relationships are described by Borg *et al.* (1976) and are as follows. Immediately adjacent to the cavity, and in the chimney, a zone of highly crushed rock is found, extending to a distance of about 1.3 cavity radii at the level of the shot. A pervasively fractured zone then extends between 2.5 to 4 cavity radii. Beyond this is a region of widely spaced fractures with less frequent interconnection. Generally, at distances between 3.5 and 5.2 cavity radii, the compressive strength of the shock wave is too small to fracture the rock (the limit of shear failure). For many tests, the limit of shear failure coincides with the height of the chimney. Though tensile fracturing may take place beyond the shear failure limit, the fractures are typically widely spaced and are considered to contribute little to an increase in overall permeability. Experience specifically in granite at a French nuclear testing site resulted in smaller predicted distances (a fracture zone radius of 26 times the third root of the device yield in kilotons; Derlich, 1970).

Using the specific characteristics of the Sand Springs granite and the Shoal test, the predicted radial cracking distance was 159 m (Beers, 1964). Post shot drilling encountered unbroken granite at a depth of 408 m, implying a fracture radius of 41 m below the shot location (Gardner and Nork, 1970). This distance is believed to encompass the zone of intense fracturing and is reasonably close to the fracturing predicted based on the French experience noted above (60 m for Shoal). Shock-induced fractures between the depths of 198 and 350 m in hole USBM-1 indicated that the lateral extent of subsurface fractures was a minimum of 135.6 m from the detonation point

(Atkinson, 1964). Surface fractures extended out to 458 m south, 794 m north, 366 m east, and 610 m west, but these were due to the effects of spalling, which was only predicted to occur to a depth of 122 m below land surface.

2.4.1.5 Estimates of Radionuclide Transport

Concentrations of tritium, ^{90}Sr, and ^{137}Cs are predicted to be many orders of magnitude higher than permissible concentrations in the cavity groundwater (Hazelton-Nuclear Science, 1965). However, given an estimated low groundwater velocity, Hazelton-Nuclear Science (1965) considered it very unlikely that greater-than-acceptable concentrations of tritium would extend more than 1000 m from the explosion zone. They predicted even more limited aqueous transport of ^{90}Sr and ^{137}Cs due to chemical interaction with the granite. Overall, given the distance of 5000 m to the nearest groundwater use point, the relatively slow groundwater movement, radioactive decay, retardation of ^{90}Sr and ^{137}Cs, and dilution due to dispersion, Hazelton-Nuclear Science (1970) conclude that there is a negligible radiocontamination hazard to regional groundwater supplies from the Shoal test.

Gardner and Nork (1970) reiterate the analysis presented in Hazelton-Nuclear Science (1965) and consider postshot monitoring data. They conclude that no radionuclides above the one Concentration Guide level will enter the alluvial formations in valleys adjacent to the Sand Springs Range. Their Concentration Guide levels were 1×10^6 pCi/L tritium, 100 pCi/L ^{90}Sr, and 7000 pCi/L ^{137}Cs.

Chapman *et al.* (1995) investigated the transport times for tritium and the associated health risks at assumed downgradient control planes. Their work utilized analytical methods to calculate the downgradient breakthrough of tritium. The uncertainty in the spatial variability was accounted for directly in the analysis, but there were other parameters that were not well known and were handled through a sensitivity analysis. The analysis yielded a large range in predicted tritium concentrations at the downgradient control plane. For their base case parameters (variance in lnK of 0.3 and no uncertainty in mean velocity), the peak concentration of 280 pCi/L passes the boundary 206 years after the nuclear test. As one incorporates more uncertainty in lnK and the fluid velocity, the simulated peak concentration increases and the travel time decreases. They note that many uncertainties existed in the assignment of flow and transport parameters.

2.4.2 Hydrochemical Environment

Hydrochemical investigations during the corrective action process at Shoal relied on the collection of groundwater samples from the new wells. Sample collection occurred after purging the wells of remnant drilling fluid, and at the completion of borehole aquifer testing. Samples could only be collected from three wells, HC-1, HC-2, and HC-4, because difficulties in the completion of HC-3 precluded adequate development and purging. The details of sampling are provided in Appendix 4 (Earman and Pohll, 1997). The chemical and isotopic analytical results are presented below, and placed in the context of existing regional information.

Groundwater samples from the Shoal site were also collected during original site characterization work in the early 1960s (University of Nevada, 1965). Unfortunately, many of the

analyses suffer from large charge-balance errors. In addition, large amounts of drilling fluid (originating from well HS-1 in Fairview Valley) were used and lost during well drilling and testing. For these reasons, samples from the new Shoal wells are used here to characterize the site hydrochemistry.

2.4.2.1 Chemical and Isotopic Characteristics of Site Groundwater

The groundwater from the site wells is part of the mixed-cation and mixed-anion chemical facies (Figure 2.6 and Table 2.3). Water quality is good, with total dissolved solids contents ranging from about 330 to 480 mg/L. The pH is near neutral, around a value of 8. Equilibrium solubility calculations (using WATEQF; Plummer *et al.*, 1976) indicate saturation with respect to calcite, aragonite, barite, chalcedony, quartz and talc. This reflects a history of silicate hydrolysis and dissolution of carbonate minerals. The carbonate probably originates primarily from carbonate dust during the recharge process. The granite is primarily comprised of quartz and feldspar, which are undergoing dissolution and alteration.

Within the same broad chemical characteristics, the three groundwater samples exhibit marked variations (Figure 2.7). The water from well HC-1 contains lower dissolved ion concentrations, as evidenced by chloride and sulfate concentrations almost half the value found in water from the other

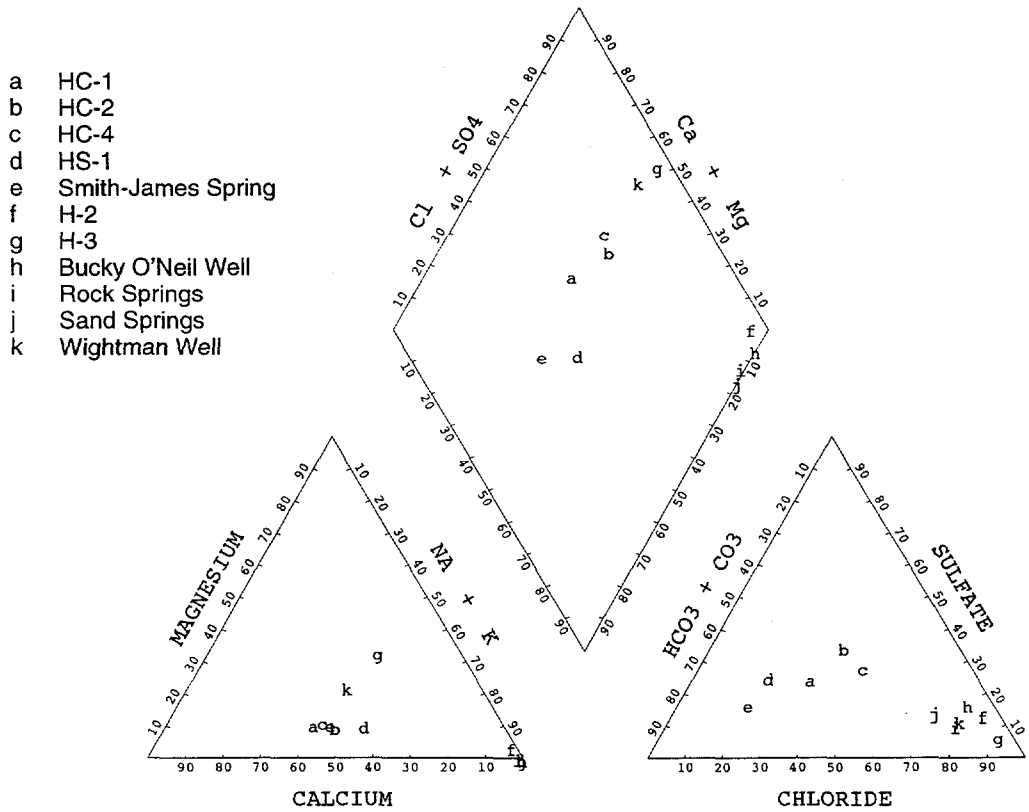

Figure 2.6. Piper diagram showing the relative ionic composition of groundwater samples from the HC wells at the Shoal site, as well as that of other samples from wells and springs in the area.

Table 2.3. Chemical Analyses of Water Samples Collected from the HC Wells at the Shoal Site, along with Analyses of Groundwater from other Wells in the Area of the Sand Springs Range (from Chapman *et al.*, 1994a). All units are mg/L unless noted otherwise.

Well	Depth (m)	Date	T (°C)	pH[1] (S.U.)	EC[1] (μS/cm)	SiO_2 (mg/L)	Ca (mg/L)	Mg (mg/L)	Na (mg/L)	K (mg/L)	Cl (mg/L)	SO_4 (mg/L)	HCO_3 (mg/L)	CO_3 (mg/L)	NO_3 (mg/L)	Br (mg/L)
HC–1	336	2-21-97	13.6	8.00/8.01	423/467	19.8	45.7	6.01	38.7	2.79	47.7	52.2	116		11.1	0.7
HC–2	347	3-19-97	NA	NA/8.03	NA/670	20.8	58.1	7.87	64.8	3.48	80.8	108.0	118		0.44	0.59
HC–4	327	2-24-97	13.7	7.20/8.04	658/727	22.7	66.4	9.87	63.7	3.67	101.0	90.3	113		26.8	1.67
Bucky O'Neil	land surface	12-Jun-91 6-12-91	20	8.81/8.68	14,700/ 14,000	35.3	6.06	1.59	3260	103	3810	1140	660/547	52.5	0.04	18
Wightman Well	NA	26-Aug-92		7.97	1630	47.1	106	40.8	138	11.5	380	80	96.1		9.83	1.6
Rock Spring	land surface	12-Jun-91	18.5	8.22/8.28	4920/ 5230	85.0	11.7	2.01	1070	68.2	1350	246	410/398	7.6	0.09	3.5
Sand Spring	land surface	13-Jun-91	24.5	9.25/9.21	4050/ 4050	33.4	2.52	0.54	876	39.7	885	253	500/363	74.1	<0.04	2.7
Smith-James Spring	land surface	13-Jun-91	22	8.35/8.31	800/749	33.9	72.2	10.4	76.4	3.29	52.0	65.2	290/311	1.38	0.13	0.25
HS–1	NA	30-Mar-92		7.72/8.14	428/438	68.7	31.5	5.37	47.2	7.11	29.3	51.5	110/140		3.99	<0.1
H–3	129	26-Aug-92		7.76	4830	6.5	197	183	457	15.8	1400	148	99.4		0.80	4.1
H–2	pumped 91.4	25-Aug-92		7.8	42,100	33.0	133	219	10,800	63.1	14,900	3320	1340		0.04	48.5

[1]First number is a measurement in the field at the time of sample collection. Second number is a laboratory measurement. If there is only one number, it is a laboratory measurement.

Isotopic Analyses for Groundwater Samples from the Shoal Site.

Well	^{14}C Percent Modern Carbon	δD (‰)	$\delta^{13}C$ (‰)	$\delta^{18}O$ (‰)	Tritium (pCi/L)
HC–1	48.68 ± 0.83	–114	–10.8	–14.5	<5
HC–2	22.13 ± 0.51	–115	–10.4	–14.5	<5
HC–4	5408 ± 51.9	–113	–11.2	–14.2	1130±15
Bucky O'Neil	14.5 ± 0.3	–86	–3.5	–9.1	<10
Wightman Well	27.7 ± 1.6	–121	–7.0	–14.8	<10
Rock Spring		–121		–13.9	<10
Sand Spring		–107		–11.6	<10
Smith-James Spring		–106		–14.1	51 ± 10
HS–1	8.3 ± 0.9	–123	–9.9	–16.3	<10
H–3	44.0 ± 0.8	–111	–3.3	–12.8	<10
H–2	2.4 ± 0.3	–85	–3.3	–7.9	<10

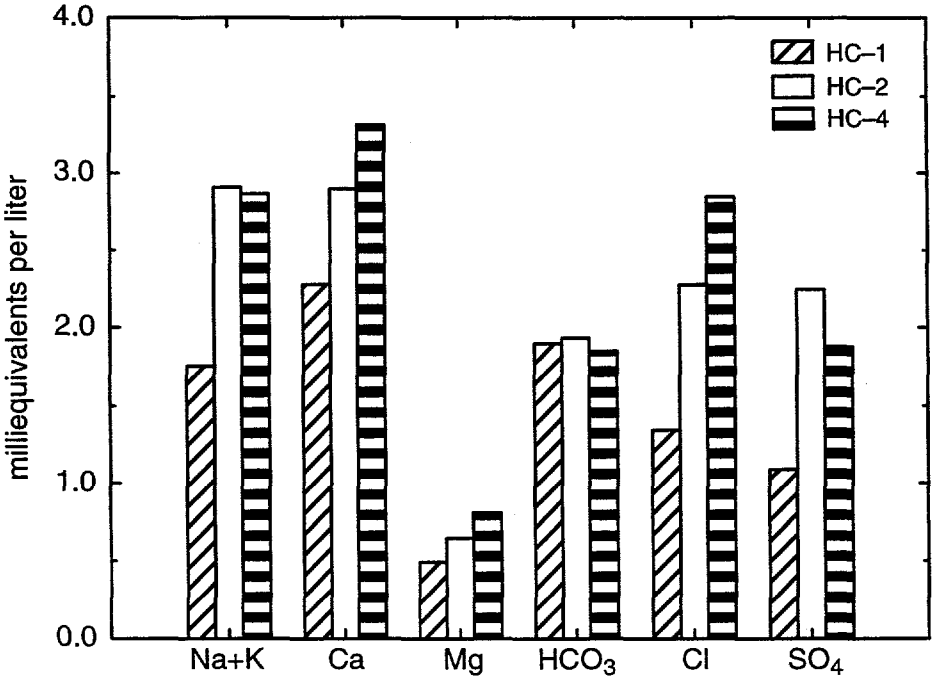

Figure 2.7. Comparison of ion concentrations of groundwater quality parameters for the HC wells.

wells. The one exception is in the bicarbonate concentration, HCO_3, which is very similar and suggests a solubility control, presumably calcite saturation.

The stable hydrogen and oxygen isotopic composition of the groundwater samples is essentially identical within the analytical precision of $\pm 1‰$ for δD and $\pm 0.2‰$ for $\delta^{18}O$. This indicates that, despite the chemical differences, the groundwater samples were all recharged under similar climatic conditions. The relationship between δD and $\delta^{18}O$ (Figure 2.8) is consistent with that of a meteorically derived water. The HC groundwater isotopic compositions plot slightly to the right ($\delta^{18}O$ enriched) of the estimated local meteoric water line (Jacobson *et al.*, 1983), but that phenomenon is frequently encountered in arid regions and has been suggested to occur due to slight evaporation during infiltration (Allison *et al.*, 1984). The HC wells isotopic composition is intermediate between the isotopically light groundwater found at HS-1 and the more heavy-isotope enriched groundwater encountered west of the Sand Springs Range. The isotopic and chemical differences between the HC wells and HS-1 reflect different recharge conditions (in time and/or space) and are discussed in section 2.4.2.3. The stable isotopic enrichment and corresponding salinity increases of wells on the west side of the Range (H-2, H-3, Bucky O'Neil Well, Sand Spring) are interpreted as the result of mixing with residual brines from the dessication of Lake Lahontan (Chapman *et al.*, 1994). The source of the groundwater mixing with the refluxing Lahontan brine was interpreted by Chapman et al. (1994) as being isotopically lighter than that found at H-3, consistent with the composition of the HC wells. Though the previously discussed hydraulic head data demonstrate that the HC wells themselves are on the opposite (eastern) side of a groundwater divide, it is likely that groundwater with a similar character occurs west of the divide and provides recharge into the Fourmile Flat basin.

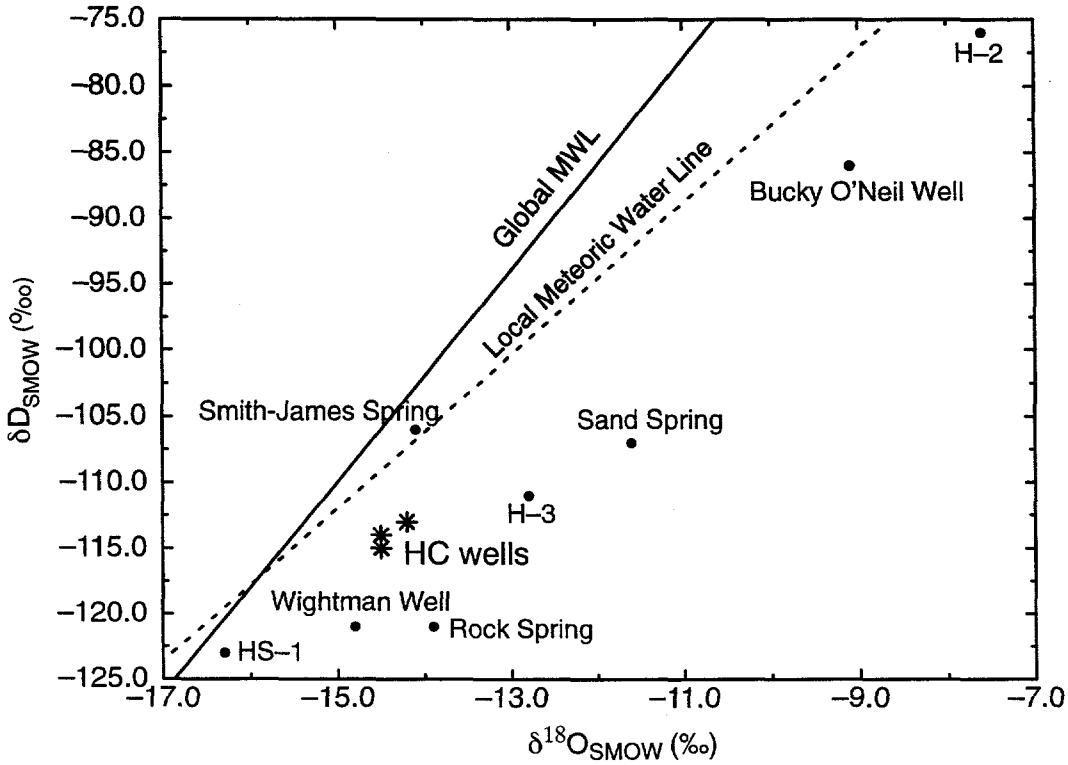

Figure 2.8. Stable isotopic composition of water from wells and springs in the immediate Shoal area. The HC wells are shown by the stars. The Local Meteoric Water Line is from Jacobson et al. (1983).

The stable carbon isotopic compositions are identical within analytical precision (±0.2‰) for HC-1 and HC-4, and for HC-1 and HC-2, though HC-2 is very slightly enriched compared to HC-4. The radiogenic carbon contents vary significantly from well to well. Percent modern carbon contents of 49 and 22, from HC-1 and HC-2, respectively, result in significantly different groundwater ages. Little influence of addition of dead carbon by carbonate mineral dissolution is expected in the granitic aquifer, though some dissolution of carbonate dust is likely during infiltration of precipitation. Soil gas $\delta^{13}C$, produced by the site's C-3 vegetation in this semi-arid setting, is expected to vary from -21 to -16.5‰ (Hershey *et al.*, 1989). Using a value of -20‰ and an equilibrium fractionation of 9‰ between the soil gas carbon and carbon dissolved in the recharging water (consistent with a temperature between the mean annual value of about 10°C and the groundwater temperature of about 13.7°C; Mook, 1980), the starting $\delta^{13}C$ of groundwater recharge is expected to be about -11‰. This value is very close to those measured in the groundwater, indicating that the apparent groundwater ages need not be corrected for a dead carbon influence.

The calculated groundwater ages are given in Table 2.4 and range from approximately 6000 years before present for HC-1 to 12,500 years before present for HC-2. This age represents the time the water has been isolated from the atmosphere and is consistent with the absence of detectable tritium in the samples. Despite the 300 m extent of the unsaturated zone at the Shoal site, the diffusion of CO_2 gas is quite rapid and can be expected to penetrate to great depths below the land

surface (Chapman *et al.*, 1994b). Nevertheless, some portion of the ages given above may represent infiltration time, in addition to residence time below the water table. Despite the 6000-year difference in ^{14}C ages, the stable hydrogen, oxygen, and carbon isotopic compositions indicate that recharge occurred under similar climate and vegetation conditions. This indicates that the water in both wells was recharged under climatic conditions established after the end of the last pluvial period in the region between about 12,000 and 14,000 years before present, based on water level estimates for Lake Lahontan (Benson and Thompson, 1987).

Table 2.4. Groundwater-Age Calculations Based on Carbon Isotopic Data.

Well	$\delta^{13}C$ (‰)	Percent Modern Carbon	± error	Apparent Age (YBP)
HC-1	-10.8	48.68	0.83	5810 to 6090
HC-2	-10.6	22.13	0.51	12,300 to 12,700
HC-4	-11.2	5408.05	51.9	NA
HS-1	-9.9	8.3	0.9	19,700 to 21,500

The shorter residence time indicated for groundwater at HC-1 is consistent with the relative hydrologic properties, as HC-1 not only has a higher bulk hydraulic conductivity, it also intercepted the most conductive fractures measured at the site (see section on hydrologic data). Conversely, HC-2 yielded the lowest measurement of bulk hydraulic conductivity. Presumably, the water pumped from HC-1 was primarily produced from the most transmissive fracture zone and represents groundwater in a more rapid flow regime than that at HC-2.

The difference in age may also relate to the differences in major ion concentrations between the two wells. One possibility is that the longer residence time indicated by the HC-2 age has allowed more opportunity for mineral-water reactions. However, the increased chloride and sulfate concentrations are difficult to justify solely on residence time. Neither ion is a major constituent of the rock-forming minerals in the Sand Springs Range. Their presence at dissolved concentrations in excess of 50 mg/L is probably the result of the position of the range in the immediate downwind direction from Fourmile Flat and the Carson Desert at large. Aeolian deposition of fine material (containing halite and gypsum) deflated from the salt flats occurs as the predominant northwest wind loses velocity and carrying power at ground level as it rises to pass over the range. Windblown silty material mantles several of the major depressions in the crest of the range (University of Nevada, 1965). This material is available to go into solution during recharge. The higher chloride and sulfate concentrations for groundwater at HC-2 relative to HC-1 may represent either spatial or temporal variability in the amount of silt encountered by recharging water. For instance, conditions may have been much dustier closer to the time of major lake level declines at 12,500 years before present than they were millennia after that initial desiccation.

Given the similarity in bulk hydraulic properties and total dissolved solids load between HC-2 and HC-4, HC-4 may also have an older groundwater age than HC-1. However, the ^{14}C and tritium measurements for water from well HC-4 reflect the presence of radionuclides produced by the Shoal

underground nuclear test and cannot be used to estimate a groundwater age. The ^{14}C activity measured was 733.33 disintegrations per minute per gram of carbon. Assuming all of the dissolved carbon can be represented by the HCO_3 concentration, this equates to a concentration of about 7 pCi/L for ^{14}C (for reference, the concentration assumed to cause a 4 mrem/yr dose rate by the EPA in 40CFR141.16 is 2000 pCi/L). The tritium concentration of 1130 pCi/L is also well above any possible naturally derived value. Separate analyses by EPA confirmed the elevated tritium value, and did not detect ^{137}Cs, ^{89}Sr, or ^{90}Sr (Appendix 4).

2.4.2.2 Comparison of Site Groundwater to Other Water in the Sand Springs Range

The closest water sample from the Sand Springs Range to the Shoal site wells was collected from a small spring in a canyon to the south (Chapman *et al.*, 1994a). This spring, locally known as Smith-James Spring, but designated simply as "spring" on the Chukar Canyon 7.5-minute Quadrangle map, has a very low discharge. It is located several kilometers south of Shoal in a cross-gradient direction and discharges from an elevation (approximately 1600 m amsl) above that of the water table at the Shoal site (approximately 1280 to 1311 m amsl).

There are notable differences between the groundwater sampled at Shoal and Smith-James Spring. Smith-James Spring is more saline (a total dissolved solids value of about 600 mg/L), and contains proportionally more bicarbonate with associated cations. The spring's deuterium composition is more enriched as compared to the groundwater, with little associated difference in the $\delta^{18}O$, so that the spring plots directly on the local meteoric water line (Figure 2.8). Though no carbon isotopic data are available, the spring water contained 51 ± 10 pCi/L tritium, indicating that it is the product of modern recharge. Given the hydrologic setting described above, the tritium cannot be related to Shoal, but rather reflects atmospheric tritium.

The chloride and sulfate contents of the spring water fall within the ranges observed for the Shoal samples. Given that these ions are interpreted above as being the result of dust dissolved during recharge, this suggests that the recharge processes are similar, with the dissolution of additional bicarbonate somewhere along the flowpath or during the discharge process. The close fit of the spring stable isotopic composition to the meteoric water line, along with the tritium content, is consistent with recharge that more closely matches local precipitation, and perhaps is also more variable in time (due to less mixing).

2.4.2.3 Regional Flow Implications of the Groundwater Chemistry

Regional groundwater analyses are available from the early 1960s (University of Nevada, 1965), but many of them suffer from serious charge-balance errors. Considering only those with errors less than 15 percent, a different chemical signature is evident for groundwater in the basin west of the Sand Springs Range (Fourmile Flat) and groundwater in the eastern basin (Fairview Valley). This difference was confirmed with more recent sampling, which identified not only chemical but also stable isotopic distinctions between the two valleys (Chapman *et al.*, 1994a). Groundwater in Fourmile Flat is characterized by higher salinity, a dominance of sodium and chloride ions, and generally heavy-isotope-enriched values. In addition to low salinity and heavy-isotope depletion, the groundwater in the eastern valley has a mixed cation-bicarbonate facies water.

The higher salinity and sodium-chloride dominance in Fourmile Flat is believed to be due primarily to the existence of a brine occupying deep portions of the system (Chapman *et al.*, 1994a). The brine is a remnant of the desiccation of Lake Lahontan and ongoing playa evaporation. Conversely, Fairview Valley was not part of a pluvial lake system, and the small Labou Flat playa does not discharge groundwater, so there is no build-up of salts. The water sampled at well HS-1 (confirmed by historic analyses from now-abandoned well H-4 also in Fairview Valley) is a low salinity, mixed cation-HCO_3 type.

Groundwater in both Fourmile Flat and Fairview Valley is expected to receive some portion of its recharge by flow from the Sand Springs Range. Hydraulic data demonstrate that the HC wells are all located east of the flow divide such that the groundwater sampled from HC-1, -2, and -4 is presumed to be upgradient of well HS-1 (the head in HC-3 is discussed in a previous section). However, chemical and isotopic differences are so great between the HC wells and HS-1, that groundwater at HS-1 cannot be derived solely from the groundwater sampled at the Shoal site. For example, the concentration of chloride, which is not part of any major rock-forming minerals along the flowpath, decreases from values of 47.7 to 101 mg/L at the Shoal site, to 29.3 mg/L at HS-1.

The stable isotopic composition of groundwater from well HS-1 is also markedly depleted in the heavy isotopes, as compared to groundwater sampled beneath the range (Figure 2.8). The stable isotopic composition of the HS-1 groundwater is similar to that of artesian wells sampled in Dixie Valley (Figure 2.9), which are presumed to be recharged in the Stillwater Range, at higher altitudes and under cooler temperatures than the Sand Springs Range (Chapman *et al.*, 1994a). The radiogenic carbon content is very low (8.3 percent modern carbon with a $\delta^{13}C$ value of -9.9‰), indicating a groundwater age in excess of 19,000 years.

There are three possible explanations for the chemical and isotopic differences between the Shoal wells and HS-1 (Chapman *et al.*, 1994a): groundwater in Fairview Valley could be predominantly recharged in the Fairview Peak-Slate Mountain range to the east rather than the Sand Springs Range, recharge to groundwater in the valley may be primarily from infiltration of runoff from the Sand Springs Range rather than groundwater flow, and/or groundwater in the valley was recharged during glacial conditions. Though lower salinity is reasonable for recharge in the Fairview Peak area because it is farther downwind of the major dust source (and is borne out by the salinity of Slate Spring, which has a similar chemical composition to HS-1), the recharge potential of the eastern range is not significantly larger than that of the Sand Springs Range.

Recharge from runoff seems very likely for the portion of Fairview Valley adjacent to the Sand Springs Range. The range presents a very steep, abrupt mountain front on the western side, offering limited drainage area for runoff to Fourmile Flat. Conversely, there are well-developed networks draining most of the highland area and leading down to Fairview Valley on the east. HS-1 itself is downslope from the large Ground Zero Canyon drainageway and is near an ephemeral channel that carries runoff from several other canyons to the south. Recharge into the alluvium from runoff is likely to have a lower salinity because larger volumes of water are available to dilute dryfall encountered in the streamcourses. Additionally, given the groundwater age at HS-1, infiltration

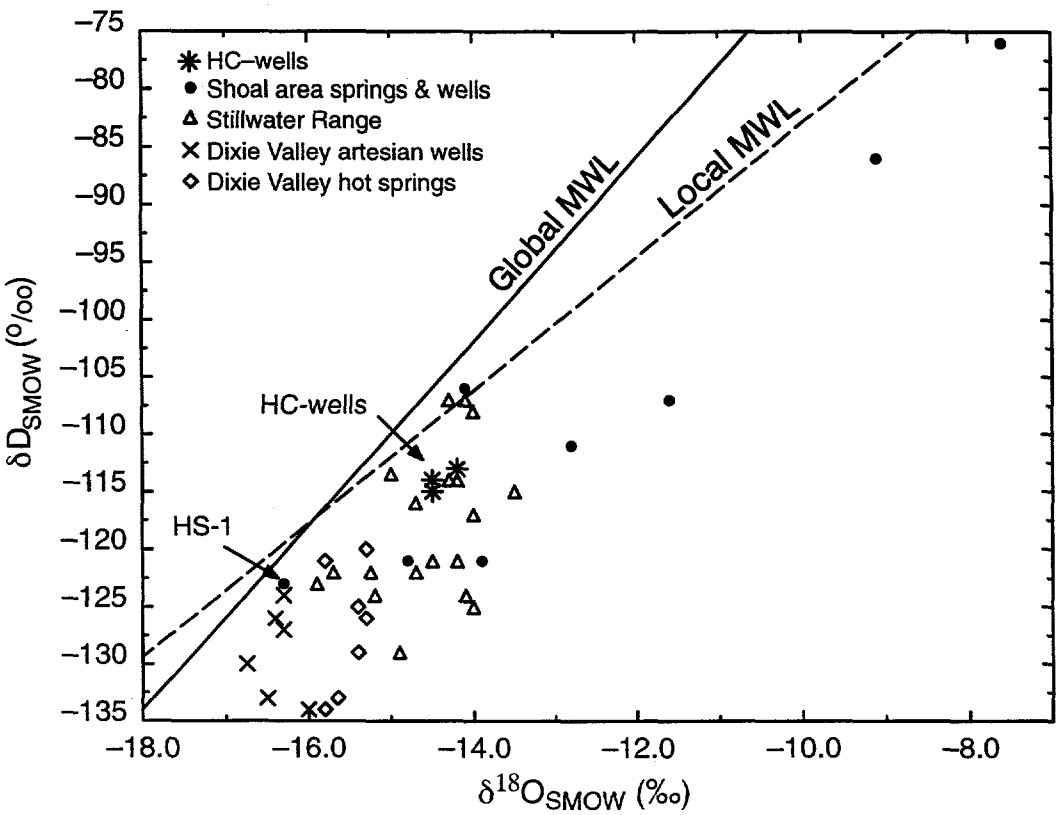

Figure 2.9. Stable isotopic composition of groundwater in the Shoal area, compared to other water in the region (University of Nevada, 1980). Shoal sample identities are singled out in Figure 2.8.

occurred during a period when Lake Lahontan covered the now dry basins to the west, so that dust and dryfall would be greatly reduced.

It is also possible that the time factor alone accounts for the chemical and isotopic discrepancy between the range and the valley. If the travel times are very long between recharge on the range and arrival in the HS-1 area, the groundwater sampled at HS-1 may simply reflect recharge conditions on the Sand Springs Range during the last pluvial period. At the end of the pluvial period (between 12,000 and 14,000 years ago; Benson and Thompson, 1987), the amount of recharge through the range undoubtedly decreased dramatically, resulting in a reduction in the hydraulic gradient forcing flow into the valley. As a result, transit times would increase and groundwater with a chemical and isotopic signature consistent with post-pluvial recharge may not have traversed the distance to HS-1 by the present time.

The chemical and isotopic composition of the groundwater at the Shoal site and in Fairview Valley suggests that groundwater flow from the site area is either not a major contributor to the alluvial aquifers in the valley and/or that travel times are so long that temporal changes in water chemistry and isotopic content brought about by changes in recharge conditions caused by the end of the last pluvial period have not been transmitted to the valley aquifers yet. These interpretations require low flow volumes from range to valley, together with low flow rates.

3.0 Conceptual Model

3.1 Conceptual Flow Model

The first step in the construction of a groundwater flow model is to create a conceptual model that describes the primary features that control the behavior of the flow system. The conceptual model includes the description of hydrogeologic features such as primary flow direction, sources and sinks, groundwater flow divides, fracture location, density and spatial persistence, and boundary conditions.

At the Shoal site, the primary hydrologic features of interest include the fracture network, the location of the groundwater flow divide, magnitude of recharge and a primary flow direction to the southeast. The groundwater flow divide is assumed to be aligned with the topographic divide located in the northwest corner of the land exclusion boundary. The hydraulic head data from the local wells indicate a primary flow direction to the southeast. Recharge estimates for the Shoal site range between 0.60 and 2.14 cm/yr (Maxey and Eakin, 1949; Gardner and Nork, 1970). The recharge conditions are supported based on the water table beneath the range being higher than that in the adjacent valleys, and the observation of decreasing head with depth (vertical gradient) in well ECH-D (University of Nevada, 1965). The local flow system consists of surface recharge that infiltrates through the thin soil layer and enters the relatively deep (~335 m below ground surface) groundwater system. Once fluid reaches the groundwater system it moves downward and laterally southeast toward Fairview Valley. Figure 3.1 shows a vertical cross section from Fairview Valley (east) to Fourmile Flat (west) with idealized groundwater flow directions.

The groundwater flow system in the Sand Springs Range consists of a fractured granitic aquifer. The groundwater flow system is controlled by and restricted to fractures. The larger fractures are oriented primarily northeast-southwest and northwest-southeast and the dip angles are moderate (30-40 degrees) to steeply dipping (near vertical). The smaller fractures do not have a primary orientation. Analysis of the fractures suggests large fracture densities. Although the fractured system produces a highly heterogeneous groundwater flow system, it is assumed that it behaves like an equivalent continuous porous medium. Many researchers have used equivalent

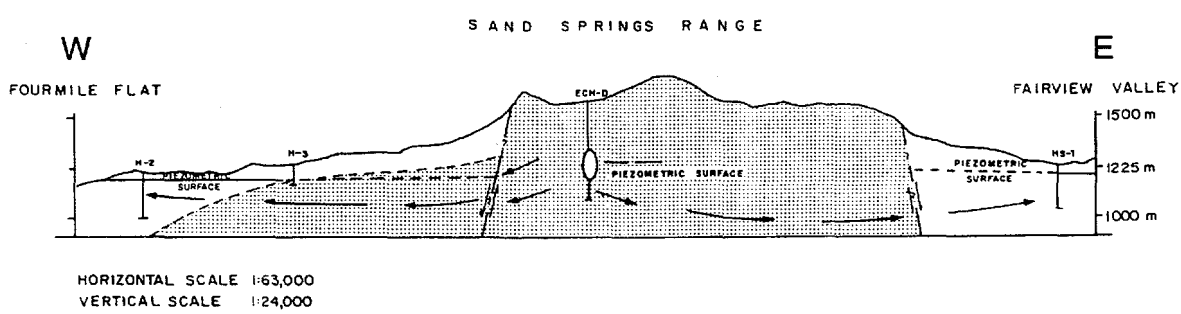

Figure 3.1. Vertical cross section near the Shoal site showing idealized groundwater flow directions. From University of Nevada (1965).

porous medium techniques to characterize fractured aquifer systems (Long *et al.*, 1982; Tsang *et al.*, 1996; Novakowski, 1990; Rehfeldt *et al.*, 1992; Hsieh and Neuman, 1985; Schwartz and Smith, 1988). Long *et al.* (1982) report that an equivalent porous medium will exist for fractured rock when the fractures are relatively dense.

The thermal flowmeter tests yielded a range in hydraulic conductivities from 4.42×10^{-7} to 7.69×10^{-4} cm/sec. This is a range of only three orders of magnitude, which is smaller than found by Tsang *et al.* (1996), who measured a seven order-of-magnitude range in hydraulic conductivity in a granitic aquifer. The limited range found at the Shoal site is primarily due to the testing procedures. The thermal flowmeter was used to determine the *in situ* hydraulic conductivity for each fracture class. The resolution of the flowmeter limits the accuracy of the conductivity estimate for the small fracture classes. To address this uncertainty, the hydraulic conductivity for the smallest fracture class was used only as a starting point for the calibration procedure.

A continuum model of a fractured medium is performed within a Monte Carlo framework such that equiprobable simulations of the fracture network geometry are generated. The method differs slightly from that of Tsang *et al.* (1996) as hydraulic conductivity within each class is constant rather than being spatially variable. This was done for two reasons. First, the field data do not support the inclusion of a parametric description of the hydraulic conductivity within each class. A maximum of five and a minimum of three K values were collected for each class, which are not enough data to describe a statistical distribution of K. Second, the inclusion of complex Neumann-type (recharge) boundary conditions required an adjustment (calibration) of K such that the simulated and measured values were in agreement.

3.2 Conceptual Transport Model

The migration of contaminants from the Shoal underground nuclear test involves a complex system of physical and chemical processes. Some of these processes are poorly understood and are the subject of ongoing research conducted by the U.S. Department of Energy. For the analysis of Shoal, many assumptions were made based on currently available data. A diagrammatic representation of the transport model source and processes considered is shown in Figure 3.2.

The contaminants considered consist of the radionuclides produced by the Shoal test and the daughters that are created by radioactive decay. The nuclides are assumed to all be located within the cavity. This equates to essentially one grid cell in the model. Distribution upward through the chimney region was neglected because in some simulations, the water table dipped into the cell overlying the cavity and could have resulted in the loss of mass into the unsaturated zone. Movement in the unsaturated zone is not considered. Neglecting the unsaturated zone is consistent with the eventual return of most volatile nuclides back to the water table by downward movement of recharge water, and at any rate, conservatively overpredicts starting nuclide masses. Prompt injection of contaminants out into the formation is considered in the sensitivity analysis.

Radionuclides are distributed according to their volatility among surface deposits and volume deposits in nuclear melt glass. Volatile and surface-deposited nuclides are assumed to migrate once

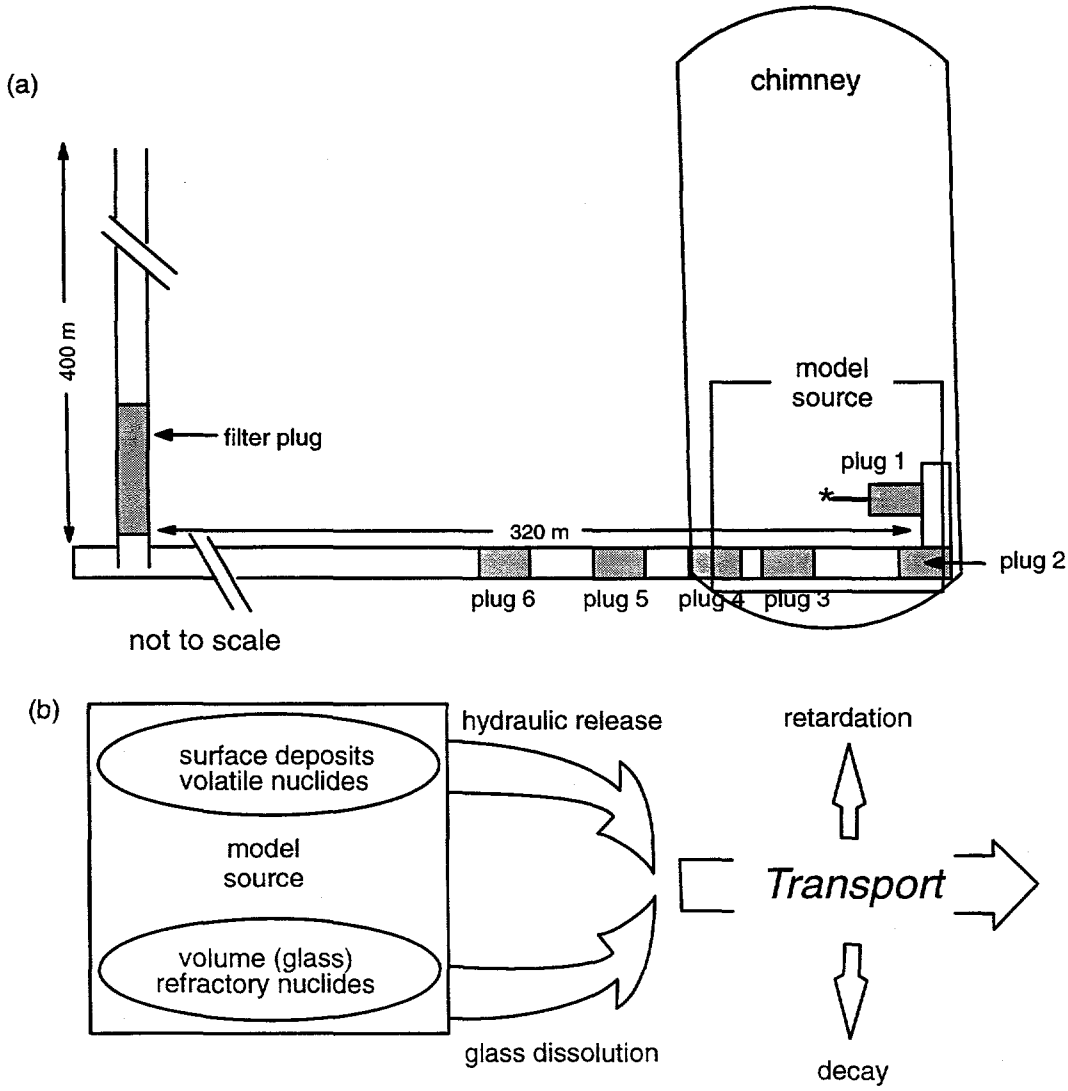

Figure 3.2. A diagrammatic representation of the transport model source and processes considered. Part (a) shows the shaft and drift complex and location of ground zero (asterisk). The cavity radius is 26 m and chimney height 108 m. The source used in the transport model is a cube, 41.9 m on a side, centered on ground zero. Part (b) is a flow chart of the apportioning of source nuclides and transport processes considered.

hydraulic equilibrium conditions are reached (see below). Nuclides within the glass are released according to glass dissolution rates calculated based on volcanic glass dissolution behavior and radionuclide melt glass characteristics.

It is assumed that no migration of radionuclides occurs until the cavity has infilled with groundwater, following the dewatering caused by the thermal and compressional forces of the nuclear test. This assumption neglects any molecular diffusion that occurs during the infill period, presuming that the flow of low-contaminant-concentration groundwater toward the hydraulic sink is much larger than the movement of contaminants away from the sink driven by concentration

gradients. Early-time cavity conditions and near-field properties affected by the nuclear test were not considered in the analysis, presuming that the scale of transport considered here (over a thousand meters) renders the calculations insensitive to the near-cavity environment.

Once released, some nuclides are subjected to a retardation factor to account for reactions with the granite host rock. Retardation factors were calculated from a surface-based sorption constant that relied on estimates of fracture aperture and distribution coefficients derived from batch experiments. Nuclides were grouped according to assumed general sorptive behavior and assigned the same retardation factor because radionuclide-specific data were not available for many of the contaminants in the Shoal environment. Daughter products were necessarily assigned the same retardation factor as the parent nuclide. The sorption experiments used fresh granite samples and no consideration was given to the possibly much higher sorptive properties of weathered material and fracture fillings. The effect of colloidal particles on transport behavior was not modeled due to the lack of data to support such calculations.

The transport calculations were performed using a particle tracking method. An initial mass was released and its movement tracked through the model domain. The peak passage at the control plane was noted (after accounting for radioactive decay) and that time used to sum the particles and convert mass to concentration. Contour plots of these resultant concentrations at the time of the peak are computed, as well as mass breakthrough curves through time. Transport was performed using units of moles to allow for decay to daughter products. The effect of radioactive decay was calculated in a post-processing mode.

All of the contaminant masses used in the transport modeling were assigned a value of one mole. The results can then be scaled by the classified masses available in Goishi *et al.* (1995). Unclassified estimates of the tritium, ^{90}Sr, and ^{137}Cs production of Shoal are available in Hazelton-Nuclear Science (1965). These unclassified values are used to scale the results for presentation in this report and form the basis for the bulk of the sensitivity and uncertainty analyses.

4.0 Methodology

The numerical methods used to describe the heterogeneity of the hydrogeologic system, perform the flow modeling calculations, and perform particle tracking for transport are described below. The application of these methods to the Shoal modeling is presented in Sections 5.0 (flow) and 6.0. (transport).

4.1 Representation of Geologic Heterogeneity

A fractured rock medium exhibits large heterogeneities in hydraulic conductivity due to the large contrast between the hydraulic conductivity of the fractures and the surrounding rock matrix. Descriptions of fractured systems include discrete fracture models (Long *et al.*, 1985; Shapiro and Anderson, 1985), double-porosity models (Bibby, 1981; Huyakorn *et al.*, 1983) and single-continuum models of fracture flow which assume an equivalent porous medium (Tsang *et al.*, 1996; Schwartz and Smith, 1988). The conceptual model at the Shoal site assumes a single-continuum system. Schwartz and Smith (1988) considered only the fracture permeability,

while Tsang *et al.* (1996) include the hydraulic conductivity of both the fractures and the matrix, while still employing a single-continuum approach.

The 1996 field work was designed to collect high resolution hydraulic conductivity data, resulting in development of a conductivity distribution for each fracture class. Serious problems were encountered in the field activities such that high resolution data could not be obtained. However, thermal flowmeter data were sufficient to assign single values of hydraulic conductivity to each of the two larger fracture classes. The conductivity for the small fractures was the result of a calibration process.

Our approach is to first characterize the fracture system by subdividing the fractures into three classes: 1) small, 2) medium, and 3) large fractures. The classification describes the fracture aperture. The fracture classes are then incorporated into a stochastic framework to describe their spatial persistence. Finally, appropriate values of hydraulic conductivity are assigned.

For a strongly heterogeneous system, uncertainties in the prediction of flow and transport arise from uncertainties in conceptual model assumptions and uncertainties in the spatial distribution of fracture classes. The uncertainties in the spatial distribution of fractures and associated hydraulic conductivities can be addressed through conditional stochastic simulation of the fracture classes. The spatial distribution of fracture classes can be simulated via conditional geostatistical techniques to represent many realizations that are consistent with the data. Each data set is fed into a flow and transport model to obtain a range of possible outcomes. When these simulations are performed in a Monte Carlo environment, the uncertainty in model output is addressed explicitly. The uncertainty in the conceptual model is more difficult to quantify yet can be just as important. The uncertainty in the conceptual model is addressed via a less rigorous sensitivity analysis that investigates ranges of possible outcomes based on different conceptual models.

Description of geologic heterogeneity is performed through conditioned geostatistical simulation of the fractured classes. It is assumed that most of the variability arises from the spatial distribution of the fracture classes and not from the variability of the fracture permeability within each fracture class. Therefore, the variability in the fracture classes is simulated, while the hydraulic conductivity of each fracture class is assumed to be homogeneous. The addition of variability in the hydraulic conductivity will impact the transport results. Additional sensitivity simulations are performed to test the impact of hydraulic conductivity variability within each fracture class on the solute transport.

Our approach has been to combine borehole logging data (geophysical and video) with surface geologic structure mapping to describe the geologic heterogeneity created by the fracture systems in the Sand Springs granite. Borehole data from four new wells, in addition to historic data from plugged boreholes on the site, were used to assign fracture classes to the subsurface. These data were combined with the structural trends identified on geologic maps and geophysical logs and used for stochastic simulations of the three-dimensional subsurface using sequential indicator simulation (SIS) methods to generate maps of hydrogeologic heterogeneity.

4.1.1 Simulating Fracture Class Fields

The SIS algorithm was used to generate equiprobable maps of subsurface fracture heterogeneity. The SIS algorithm was implemented using the FORTRAN program SISIMPDF, which simulates integer-coded categorical variables conditioned on known data (Deutsch and Journel, 1992). SIS algorithms have been used widely in stochastic flow and transport simulations to generate maps of subsurface heterogeneity at unsampled locations (Pohlmann and Andricevic, 1994; Shirley *et al.*, 1996; Tsang *et al.*, 1996). This nonparametric technique allows the user to directly input the distribution as is without specifying a parametric distribution. For this application, it is assumed that the majority of the subsurface heterogeneity is defined by the fracture patterns. Once the fracture class maps are created, then a single hydraulic conductivity value is applied to each simulated fracture class. In this case, there are three fracture classes and three associated values of hydraulic conductivities.

To simulate indicator fields (fracture classes), one must specify the prior probabilities (percent of each fracture class), the spatial variability of each indicator variable, and the domain geometry. The geostatistical analysis of the fracture classes indicated that there were two primary orientations. SISIMPDF can simulate the six categorical variables (three for each orientation) that would be required, but numerically could not handle the large anisotropy that would be produced by the two fracture orientations. SISIMPDF works with a limited search neighborhood (a zone in the model domain). The spatial structure beyond the limited search neighborhood is random. When a large number of nodes are used, the search neighborhood is focused along the primary orientations of the spatial structure (strike and dip), to lessen the computational requirements. If the entire domain was used in the search, only a small number of nodes could be simulated. Therefore, each fracture orientation was simulated separately (simulation A and B) with one specified preferred orientation and then the two fracture simulations were superimposed similar to the approach of Tsang *et al.* (1996).

The superposition was performed by first simulating the two indicator fields (one for each fracture orientation) using SISIMPDF. Next, the indicator value is chosen at random (50/50) from either simulation. To ensure that the resulting field exhibited the required prior probabilities, the single field orientation simulated probabilities had to be adjusted. The proper adjustment is found by a solution of a set of linear equations:

$$P(1|A)P(A) + P(1|B)P(B) = P(I = 1) \tag{4.1a}$$

$$P(2|A)P(A) + P(2|B)P(B) = P(I = 2) \tag{4.1b}$$

$$P(3|A)P(A) + P(3|B)P(B) = P(I = 3) \tag{4.1c}$$

$$P(1|A) + P(2|A) + P(3|A) = 1 \tag{4.1d}$$

$$P(1|B) + P(2|B) + P(3|B) = 1 \tag{4.1e}$$

where $P(1|A)$ is the probability of selecting class #1 knowing that you have selected simulation A (*i.e.*, prior probability of class #1 in simulation A). $P(A) = P(B) = 0.5$ (probability of selecting either

simulation A or simulation B. P(I=1) = original prior probability of class #1, therefore this reduces to a set of five equations and four unknowns [P(1|A), P(2|A), P(1|B), P(3|B)], as P(3|A) = 0 and P (2|B) = 0.

4.2 Numerical Flow Code Description

The three-dimensional model MODFLOW (McDonald and Harbaugh, 1988) was used to simulate the groundwater flow system. It was assumed that the fractured flow system could be represented with an equivalent porous medium. MODFLOW uses finite difference approximations to the partial differential equation that describes three-dimensional, steady-state groundwater flow in a heterogeneous porous medium:

$$\nabla \cdot [\mathbf{K}(\mathbf{x})\nabla\phi(\mathbf{x})] = q(\mathbf{x}) \tag{4.2}$$

where $\mathbf{K}(\mathbf{x})$ is the hydraulic conductivity tensor (m/day), $\phi(\mathbf{x})$ is the hydraulic head (m), $q(\mathbf{x})$ is the volumetric flux per unit volume (1/day), which is used to simulate surface recharge, and $(\mathbf{x})$ is the Cartesian coordinate (m).

Application of MODFLOW requires that the study area (model domain) be discretized into a grid of rectangular blocks. The finite difference equation is solved for hydraulic heads at the center of the block. MODFLOW was chosen because of its ability to simulate surface recharge, unconfined flow conditions and because it is widely accepted by numerous groundwater hydrologists.

Many input parameters are required for the modeling effort. These include boundary conditions, hydraulic conductivity at each node, surface recharge flux and numerical convergence criteria.

Although one can use MODFLOW in quasi-three-dimensional fashion, it was used here with a truly three-dimensional formulation. See Appendix 2 for a more detailed discussion of the vertical conductance term.

One of the selection criteria for the groundwater model was the proper simulation of unconfined aquifer conditions which exist at the Shoal site. The free-water surface slopes downward toward Fairview Valley. This sloping water table produces water levels that are below many of the finite difference blocks in the model domain. MODFLOW can simulate this condition by removing nodal cells from the finite difference computation if the water level drops below the lowermost elevation of any cell. Because the water table elevation is not known *a priori*, MODFLOW must iteratively solve for the water table position, then remove cells as required. MODFLOW also recalculates the flow across each water table face to account for the decrease in cross-sectional area. The BCF2 (McDonald *et al.*, 1991) module in MODFLOW allows these cells to rewet if during one iteration the water level was artificially lowered beneath the cell. The rewetting package can be numerically unstable, so the flow simulations were performed without this option. To ensure that cells were not being removed erroneously, simulations were performed to assess the impact of numerical oscillations on the shape of the water table. Test simulations showed that numerical

oscillations could be removed when the number of inner iterations was at least 20. The pre-conjugate gradient II (PCG2, Hill, 1990) solver handles this nonlinearity by first solving the head field in the "inner" iteration phase, then it updates the conductance matrix to account for changes in the cross-sectional area. This allows the water level to slowly decrease to a stable level without overshoot problems.

The PCG2 solver was used to solve the finite difference equations. The PCG2 solver requires the specification of the maximum number of iterations, maximum number of inner iterations, and a head and flow criterion. The maximum number of outer iterations was set to 1000, but the simulations typically required less than 100. As stated above, the number of inner iterations was set to 20 to properly handle the unconfined nonlinearities. The head and flux criteria were set at 0.001 m and 0.1 m^3/day, respectively, and produced global mass-balance errors less than 0.1 percent and local flow errors less than 7.0×10^{-3} m^3/day.

4.2.1 Calibration of the Groundwater Flow Model

The use of a stochastic groundwater flow model automatically provides estimates of the magnitude of the flow system uncertainty. In this case, fracture classes are generated that provide equiprobable estimates of the flow field. The conceptual model and associated numerical model still need to represent the real system. One way to provide a model that represents reality is to calibrate the model until a reasonable level of agreement is met between observed and simulated system response. For this model, the most uncertain parameters include the hydraulic conductivity, surface recharge and the boundary conditions. The uncertainty in the hydraulic conductivity typically yields the most uncertainty in the simulated transport behavior. The uncertainty in the recharge does influence the simulated regional gradient and therefore the magnitude and direction of the groundwater fluxes, but to a lesser degree than the hydraulic conductivity. The boundary conditions influence the regional flow patterns and to a lesser degree the magnitude of the groundwater fluxes. To ensure that the groundwater model is representing the flow system adequately, a calibration process (ASTM Standard Guide for Calibrating a Groundwater Flow Model Application, 1995) was used to provide a general agreement between the observed and simulated water levels. The recharge flux and boundary conditions were not incorporated into the calibration process, as there were not enough water level data to include the additional parameters.

Three of the new wells (HC-1, HC-2 and HC-4) were used in the calibration process. The water level in HC-3 varied dramatically and was below the water level in Fairview Valley, so it was not used in the calibration process. Because the flow model was performed in a stochastic environment, 100 realizations were performed for each calibration trial. A reasonable level of agreement was assumed when the mean of the absolute error from the 100 realizations was less than 5 m.

The calibration process will provide the best estimate of the flow system behavior, especially near the detonation, where most of the hydraulic information is available. Only a post-audit (inclusion of additional data to calibrate and verify the model) would provide more certain results. A post-audit could include the collection of more hydraulic (water level and conductivity) data in

the region downgradient of HC-3. This information might provide enough detail to clarify the flow system behavior where currently not enough data exist to do so.

4.3 Numerical Transport Model Description

Transport of a nonreactive solute in saturated porous media of constant porosity is described by:

$$\frac{\partial c(\boldsymbol{x},t)}{\partial t} + \nabla \cdot [c(\boldsymbol{x},t)v(\boldsymbol{x})] - \nabla \cdot [\mathbf{D}(\boldsymbol{x})\ \nabla c(\boldsymbol{x},t)] = 0 \tag{4.3}$$

where $c(\boldsymbol{x},t)$ represents concentration (moles/m^3) and $\mathbf{D}(\boldsymbol{x})$ represents the local hydrodynamic dispersion tensor (m^2/day). The components of $\mathbf{D}(\boldsymbol{x})$ are:

$$\mathbf{D}(\boldsymbol{x}) = \alpha_T\ |v(\boldsymbol{x})|\ I + (\alpha_L - \alpha_T)\ \frac{v(\boldsymbol{x}) \cdot v(\boldsymbol{x})}{|v(\boldsymbol{x})|}\ I + D^*\ I \tag{4.4}$$

where α_L and α_T are the longitudinal and transverse local dispersivities (m), respectively, I is the three-dimensional identity matrix, D^* is the effective coefficient of molecular diffusion (m^2/day), and $|v(\boldsymbol{x})|$ is the magnitude of fluid velocity (m/day), which is calculated within the groundwater flow model as

$$v(\boldsymbol{x}) = -\frac{1}{n(\boldsymbol{x})}[\mathbf{K}(\boldsymbol{x})\ \nabla\phi(\boldsymbol{x})] \tag{4.5}$$

where n(**x**) is the effective porosity (m^3/m^3).

Numerical problems such as numerical dispersion and oscillations that are commonly associated with the finite difference and the finite-element solutions of Equation (4.3) can be avoided by utilizing the Particle Tracking Random Walk (PTRW) method. In the PTRW method, the solute mass is replaced by a large number of hypothetical particles that can be located at any point within the domain and that travel at pore-scale velocities. Each particle is assigned part of the total mass such that the sum of the particles' masses becomes equivalent to the total injected solute mass. By increasing the number of particles used in the simulation, the solution to Equation (4.3) becomes more consistent and reliable, and predictions of solute concentrations at specific locations become more accurate. Also, the oscillations in the resulting concentrations are significantly reduced when the number of particles increase. However, the accuracy of the prediction of overall plume behavior does not increase to the same degree.

The velocity fields obtained from the flow model are used as input for the transport simulations; however, since the velocities are known only at the model nodes, an inverse-distance weighting algorithm is used for interpolation of the velocity at the particle location. The dispersion coefficient $\boldsymbol{D}(\boldsymbol{x})$ is considered constant within each cell and is determined from Equation (4.4). Let $x^p(t)$ represent the position of the pth particle at time t *(day)*. During each time step Δt, the particle is transported by advective displacement, $\Delta x^p{}_c$ and a dispersive displacement $\Delta x^p{}_d$, such that

$$x^p(t + \Delta t) = x^p(t) + \Delta x^p_c + \Delta x^p_d \tag{4.6}$$

The deterministic advective displacement is a function of velocity at $x^p(t)$, $v(x^p(t))$, and the gradient of the diagonal dispersion tensor at $x^p(t)$

$$\Delta x_c^p = [v(x^p(t)) + \nabla \cdot \mathbf{D}(x^p(t))] \cdot \Delta t \tag{4.7}$$

The gradient terms in Equation (4.7) are important near hydraulic stagnation points because if these terms are neglected, particles may "build up" in regions of low hydraulic conductivity. In three dimensions, the random dispersive displacement in each time step is

$$\Delta x_d^p = [2\mathbf{D}(x^p(t))\Delta t]^{1/2} \cdot z_n \tag{4.8}$$

where z_n is a realization of a random vector (drawn from a normal distribution with zero mean and unit variance) whose size n equals the number of dimensions in the problem.

The selection of Δt is an important decision in the PTRW simulation process because the computational expense of this method is proportional to the number of time steps. If very short time steps are used, the computational time of the entire simulation may be prohibitive. On the other hand, if excessively large time steps are used, overshoot errors may occur during the solution of Equation (4.4) (Tompson and Gelhar, 1990). To avoid these problems, Δt should be chosen such that the cell Courant number, C_c, which is the ratio between the average convective displacement and the grid spacing, is less than unity:

$$C_c = \frac{\overline{v(x)} \cdot \Delta t}{\Delta x} \tag{4.9}$$

where $\overline{v(x)}$ is the mean pore-water velocity. Use of time steps that results in C_c being greater than one may result in overshoot problems.

The Particle Tracking Program and its integration with MODFLOW was verified with two independent data sets. First, the numerical flow and transport results were compared using a simple Darcy experiment, which simulated a homogeneous hydraulic conductivity. Second, the mean velocity from the Shoal groundwater model was used in a simple analytical solute transport solution to compare mean transport behavior.

4.3.1 Output Control

The results of each solute transport simulation are provided in three figures. The presentation provides both temporal and spatial information for each solute of interest. In the temporal domain, the mass flux versus time is presented for a downgradient control plane. The plots of the mean concentration and one standard deviation are created by first selecting the time at which the maximum mass flux occurs. At this time step, the mean and standard deviation are calculated and shown in a contour plot.

4.3.2 Radioactive Decay

Radioactive decay is incorporated into the transport calculations through the application of the expression for the first-order decay reaction:

$$C = C_0 \exp(-t\,\lambda) \tag{4.10}$$

where C is the decayed concentration (moles/m^3), C_0 is the undecayed concentration (moles/m^3), λ is the decay rate of the radionuclide (days^{-1}), and t is time (days).

For the general case of the decay of a parent isotope (N_1) to a radioactive daughter (N_2), which decays to a second daughter (N_3) through the final daughter (N_n):

$$N_1 \rightarrow N_2 \rightarrow N_3 \cdots N_n \tag{4.11}$$

the solution, giving the number of atoms of any member of the decay series as a function of time, for the condition that the initial mass of the daughters is zero ($N_2^0 = N_3^0 = \cdots N_n^0 = 0$) has the form (Faure, 1977):

$$N_n = C_1 e^{-\lambda_1 t} + C_2 e^{-\lambda_2 t} \cdots + C_n e^{-\lambda_n t} \tag{4.12}$$

where the coefficients (C_n) are defined as:

$$C_1 = \frac{\lambda_1 \lambda_2 \cdots \lambda_{n-1} N_3^0}{(\lambda_2 - \lambda_1)(\lambda_3 - \lambda_1) \cdots (\lambda_n - \lambda_1)}$$
$$C_2 = \frac{\lambda_1 \lambda_2 \cdots \lambda_{n-1} N_1^0}{(\lambda_1 - \lambda_2)(\lambda_3 - \lambda_2) \cdots (\lambda_n - \lambda_2)} \tag{4.13}$$

and λ_n is the decay rate for radionuclide N_n.

The cases where the initial mass of the daughter radionuclides was not zero were handled separately.

5.0 Flow Model

5.1 Characterization of Fracture Classes

Historic fracture data from five wells (ECH-D, PM-1, PM-2, PM-3, USBM-1) were combined into a single database. These data contained a subjective analysis of fracture size based on a combination of geophysical and core data (University of Nevada, 1965). The geophysical techniques included the following logs: caliper, temperature, radiation, gamma, resistivity, microlaterlog, frac-finder, and micro-seismogram. A subset of the fracture zones was also verified with cores. The fracture data were categorized into three classes: 1) no/small, 2) medium and 3) large fractures. A large class refers to an interval which contains two or more fractures, as evidenced by geophysical logs. A medium class is one that shows a single, "narrow" correlation across geophysical logs. The classifications were based primarily on caliper logs, density logs, cores and the frac-finder logs (where available). For a more complete description of the fracture classification procedure, see University of Nevada (1965, pp. 165-183).

The four new wells (HC-1, HC-2, HC-3, and HC-4) were used to classify the fracture system based on video, caliper and acoustic televiewer logs. The video logs were reviewed and a fracture

class was assigned to the borehole at 0.3048 m (1 ft) intervals. In locations where the video resolution was too poor to classify the fracture, the caliper log was used instead. Because the video log is not an oriented tool, the acoustic televiewer logs were used to identify fracture orientation. The same three score system was used to classify the fracture system. A three-class system was used such that both the historic and new data could be used to create a single dataset that could be analyzed with geostatistical methods. Although the classification method is subjective in nature, it became apparent that there were clear distinctions between each fracture class. Figures 5.1 through 5.3 show images of each fracture classification.

The fracture classification data for all wells (HC-1, HC-2, HC-3, HC-4, ECH-D, PM-1, PM-2, PM-3, and USBM-1) were combined into a single database. Appendix 3 shows the fracture classes (1 = no/small fractures, 2 = medium fractures, 3 = large fractures) for the individual wells. The fracture class data from the University of Nevada (1965) study and the more recent fracture data are derived using different techniques, which may lead to data discrepancies. An evaluation of the prior probabilities between the old and new wells did not reveal any major differences.

5.1.1 Fracture Orientation

To properly simulate the fracture distribution at unsampled locations in the model domain, one needs to estimate the orientations (strike and dip) and correlation scale (spatial persistence) of each fracture class. The orientations were determined from acoustic televiewer analysis and the correlation scales were determined from both surface fracture mapping and vertical fracture class data.

Three boreholes, HC-1, HC-2, and HC-4, were logged at the Shoal site by Century Geophysical Corp. using an acoustic borehole televiewer (BHTV). The data from HC-4 were primarily used in the analysis because severe out-of-round conditions in HC-1 and HC-2 prevented detailed analysis. The acoustic televiewer uses a transmitter to paint the surrounding borehole walls with an acoustic signal and a receiver to record the travel time and characteristics of the returning signal. The travel time, amplitude and phase coherence are affected by the character of the surrounding rock. In this investigation, marked attenuation is interpreted as a fracture. When a planar feature, such as a fracture, intersects a cylindrical borehole, a sinusoidal trace results, as shown in Figure 5.4.

The vertical distance between the peak and trough of a fracture trace is proportional to the dip angle. The thickness of a trace at any given angle is proportional to the aperture of the fracture. The locations of the trace extrema are normal to the strike of the fracture. These three measurements were tabulated for the logs run on the three holes and used to estimate the orientation and size distribution of fractures at the site.

Like all geophysical logging tools, the BHTV is subject to errors. In this investigation, a number of those errors may be relevant. The BHTV is strongly affected by borehole eccentricity. While it is possible to correct for minor out-of-round conditions, the tool fails to produce useable results if the borehole becomes too elliptical in cross section. Boreholes HC-1 and HC-2 both displayed severe, helical elliptical shape and thus yielded few useable fracture traces. The remaining borehole, HC-4, was the source for most measurements of fracture orientation.

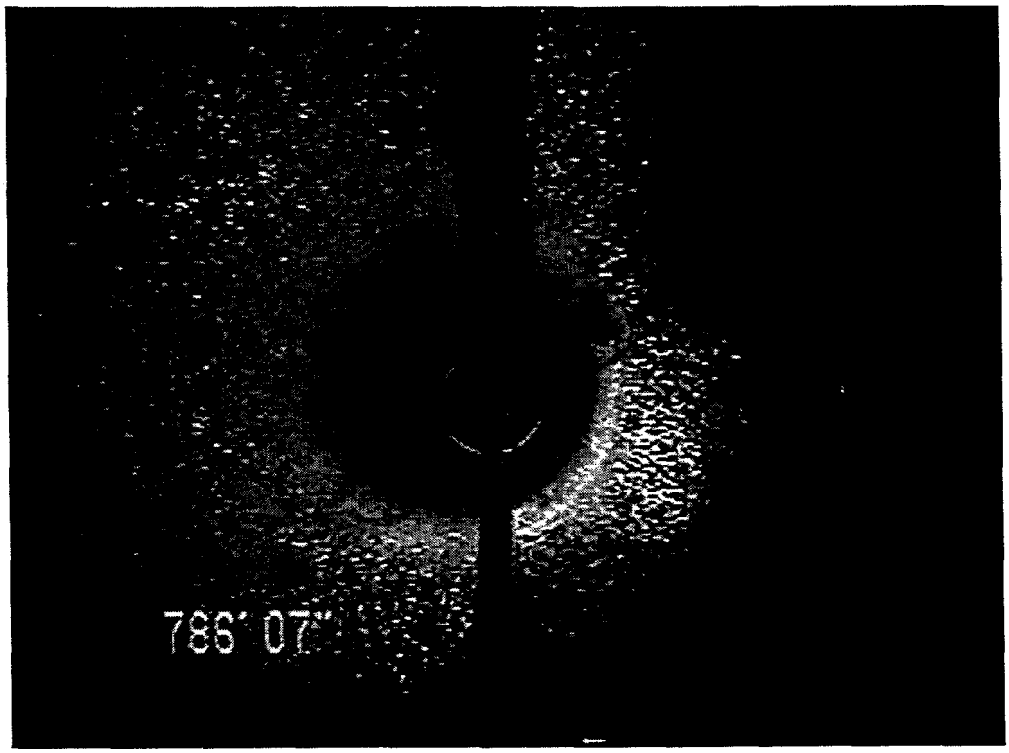

Figure 5.1. Videolog showing no/small fractures from HC-3.

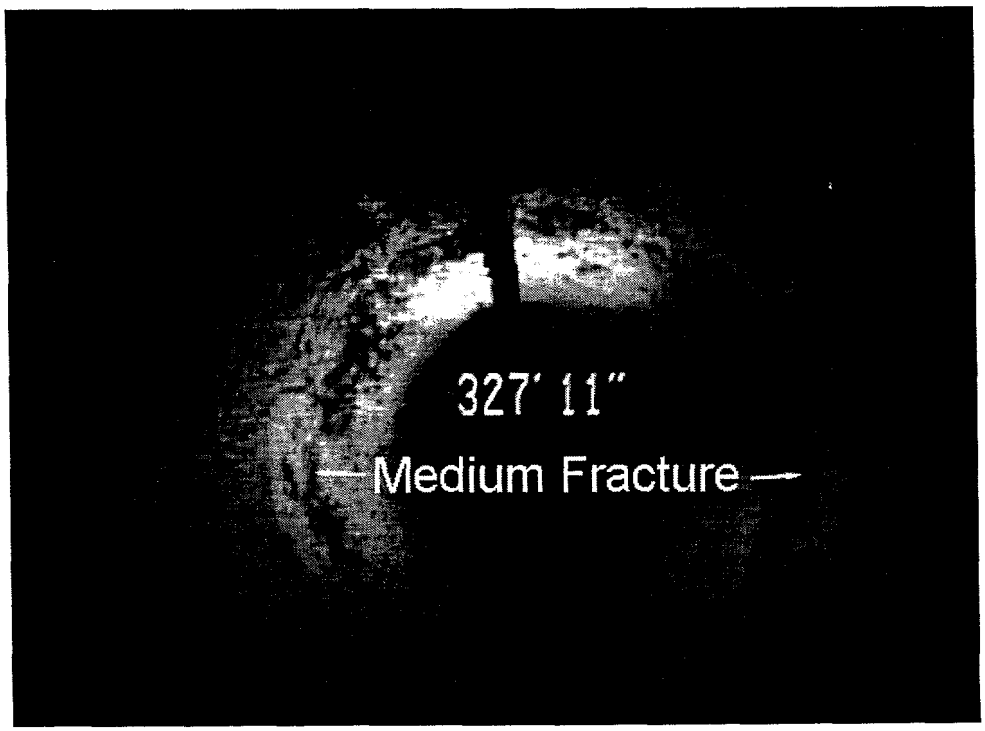

Figure 5.2. Videolog showing medium-sized fractures from HC-3.

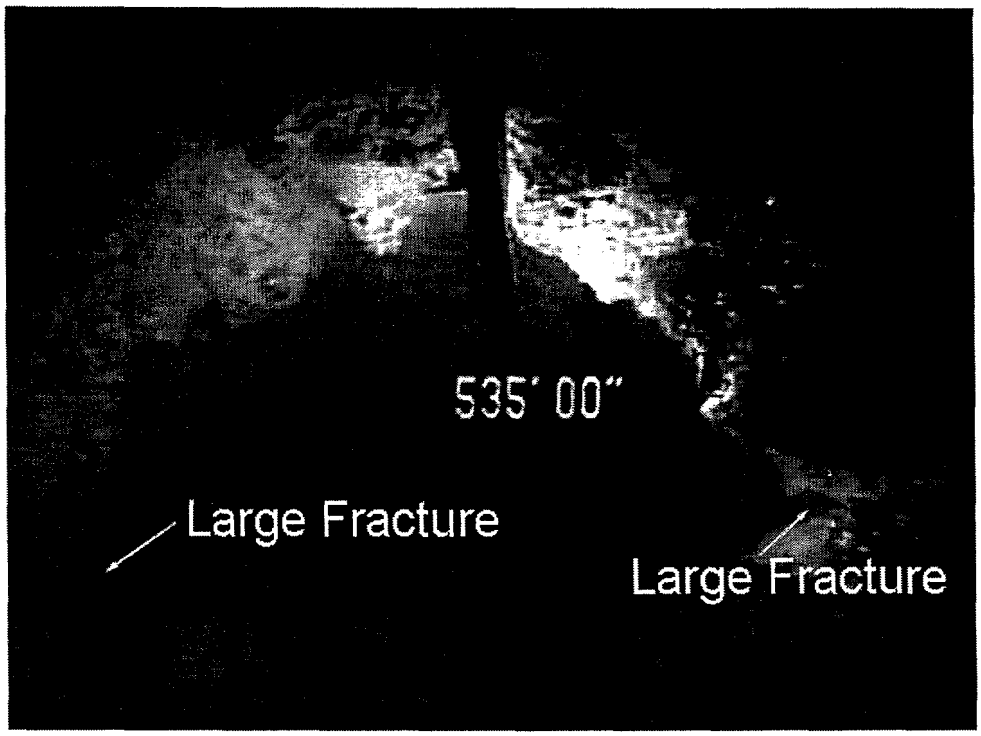

Figure 5.3. Videolog showing large fractures from HC-3.

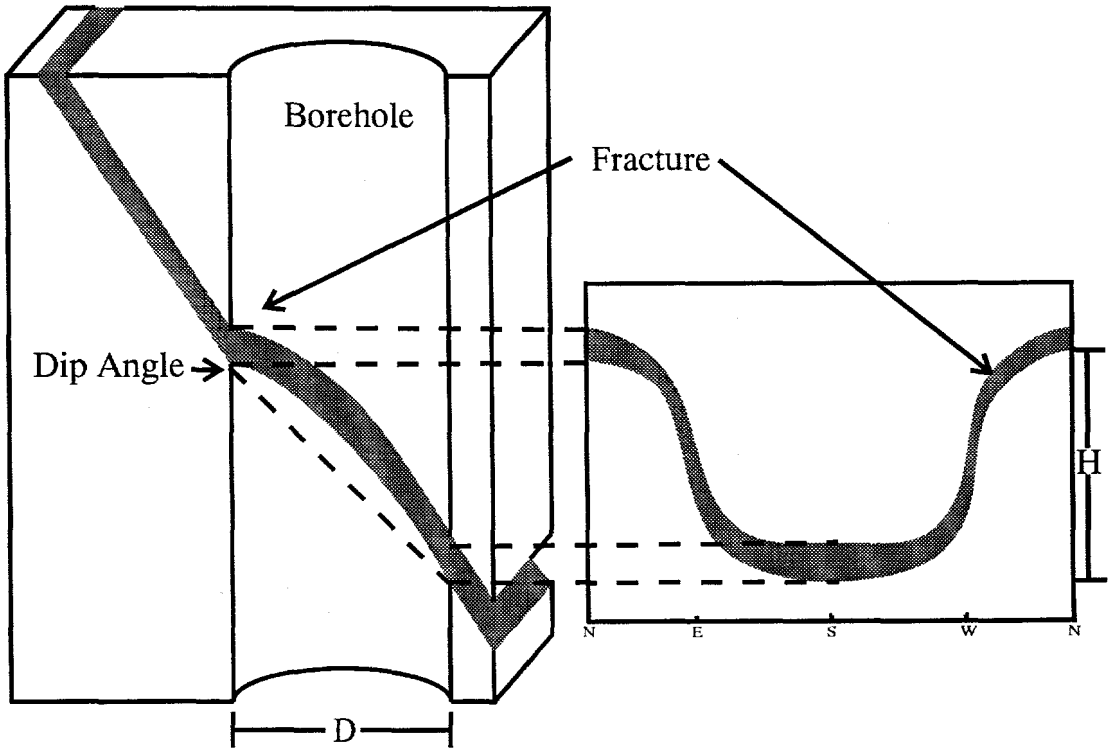

Figure 5.4. Schematic of borehole and acoustic televiewer log showing how interpretation of fracture is performed.

The televiewer is theoretically capable of resolving fractures as small as 1 mm, however, the resolution is a function of how fast the logging proceeds, and how frequently the response is recorded.

The dip and strike of each fracture was measured and the approximate aperture estimated. The data set was split based upon aperture into classes. The aperture sizes used as thresholds were chosen to minimize the spherical variance of the orientation of fractures exceeding that threshold. These data were then plotted using a lower hemisphere projection onto an equal area stereo net as shown in Figure 5.5. Two aperture thresholds were used to assign fractures into three classes. The smallest class did not show any significant preferred orientation, thus no distribution parameter was fit.

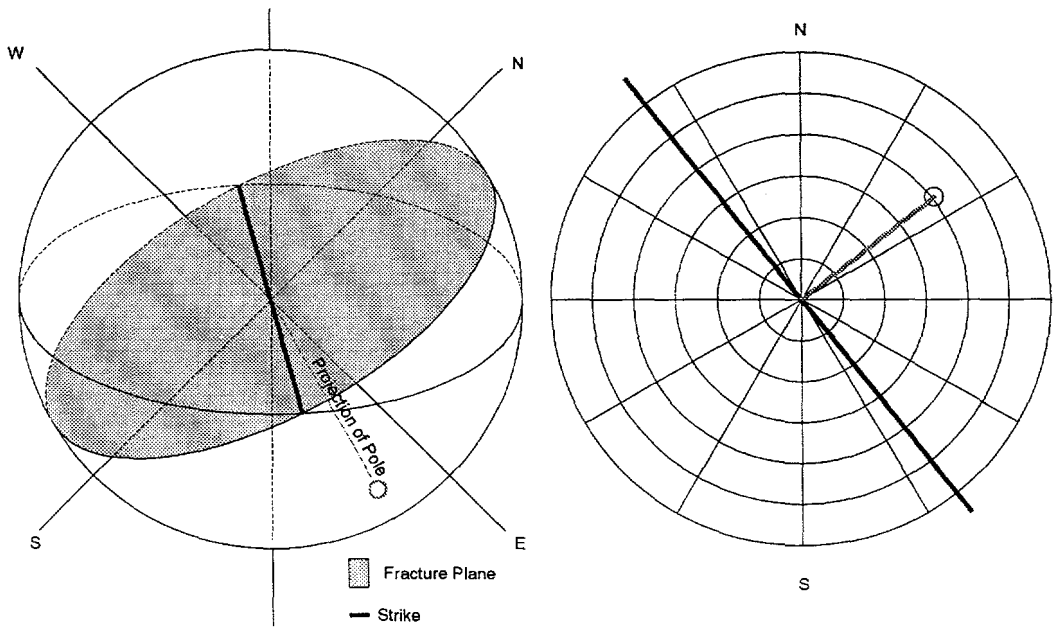

Figure 5.5. Schematic showing how fractures are transformed into an equal area net.

A total of 72 fractures were resolved in HC-4 and HC-1. These fractures were then subdivided into three sets of fractures similar to the classifications described above. Table 5.1 shows the mean and standard deviation for the strike and dip associated with each fracture set.

Table 5.1. Strike and Dip Orientations for Each Fracture Class as Determined from the Acoustic Televiewer Analysis.

Attribute	Class #1	Class #2	Class #3
Mean Strike	random	N25E	N8W
Standard Deviation of Strike	random	41	5
Mean Dip	random	44SE	31E
Standard Deviation of Dip	random	8	1

As shown in the Figure 5.6, the dip and strike is different for the large versus the intermediate fracture classes. The mean and standard deviation of the orientation data from the borehole televiewer logs were calculated following the method of Grossman as cited in Young (1987).

The acoustic televiewer data are in general agreement with the structural analysis of University of Nevada (1965). Their analysis suggested two primary fracture orientations, the first being a system of larger fractures and joints trending N50W and the second, a set of smaller fractures trending N30E. The surface structure mapping indicated steeply dipping fractures, but no high-angle fractures were found in the lower part of ECH-A, which reached an approximate depth of 460 m. The lower portion of the ECH-D core (Figure 5.7) shows both moderate (near 45 degrees) and steeply dipping fractures and faults. The acoustic televiewer analysis of the fracture orientation is assumed to be more representative of the actual fracture patterns at depth. The subsequent statistical analysis of the fracture orientations is possibly more accurate than the subjective core analysis. Therefore, the fracture orientations obtained from the acoustic televiewer were used for simulation purposes.

5.1.2 Fracture Class Spatial Persistence

Surface geologic structure mapping and, to a limited degree, vertical fracture class data were used to measure the spatial persistence of subsurface fracture classes (probability that two fracture classes separated in space are similar). Due to the clustering nature of the borehole fracture class data (less than 1-m vertical spacing with 100s of m horizontal spacing), the borehole data were used only to assess the vertical persistence of the fractures. Structure mapping was used to estimate the

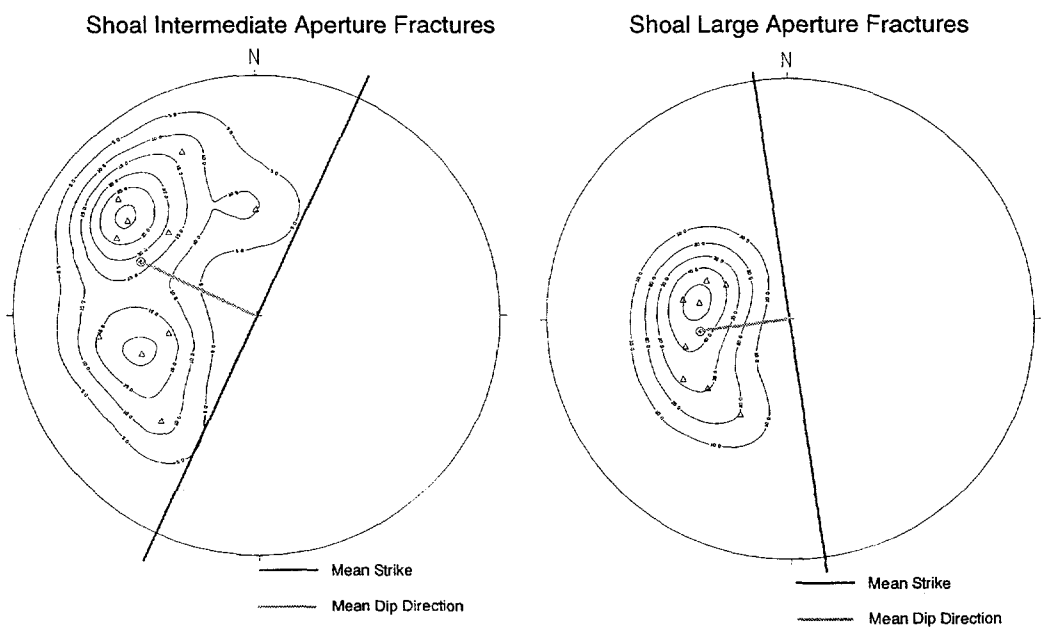

Figure 5.6. Observed orientation frequencies of intermediate and large fractures from borehole acoustic televiewer logs. Contours are relative frequency plotted on an equal area net.

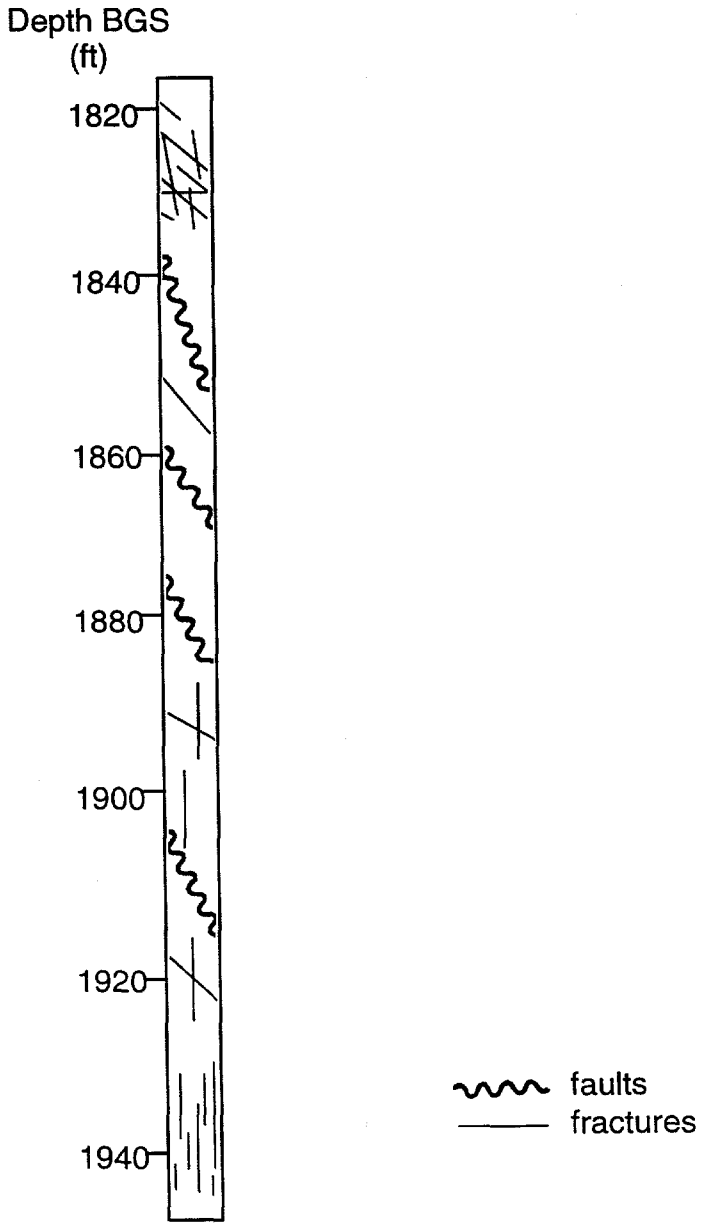

Figure 5.7. ECH-D fracture analysis, adapted from University of Nevada (1965).

persistence along the primary fracture orientation. The surface fractures may not represent subsurface fractures as surface fractures undergo significant weathering.

The fracture map of University of Nevada (1965, Plate 3) was digitized in the region near ground zero. Figure 5.8 shows the digitized version of the surface fracture map. To match the scale of the hydraulic conductivity measurements (approximately 10 m), a 9.1 x 9.1 m (30 ft x 30 ft) grid was placed over the fracture map such that fracture lengths could be calculated within each grid block. A geographical information system (GIS) was used to calculate the fracture lengths within each grid block. The array of fracture lengths (F_L) was then indicator transformed (I(x)) according to:

$$\begin{aligned} I(x) &= 0 \quad F_L < z_{cut} \\ I(x) &= 1 \quad F_L > z_{cut} \end{aligned} \tag{5.1}$$

where z_{cut} is an arbitrary fracture length (set to 1.0 m). An indicator semivariogram was calculated to estimate the correlation length along the primary strike direction. Next, an exponential directional semi-variogram model was fit to the measured indicator semi-variogram assuming an exponential model as:

$$\gamma(h) = c\left[1 - \exp\left(-\frac{h}{\lambda}\right)\right] \tag{5.2}$$

where c (dimensionless) is the sill (indicator variance), h (m) is the lag and λ (m) is the correlation length.

The fracture features shown in Figure 5.8 are curvilinear, which causes artificially reduced correlation lengths because the search window will not follow a non-linear structural feature. Therefore, a second method to estimate the spatial persistence was utilized. The mean length of the surface fractures was calculated in the GIS. Next, SIS methods (see Section 3.0) were used with the indicator semi-variogram models described above to simulate the surface fractures and the mean fracture length was calculated. The correlation scale in the SIS simulation was adjusted until a reasonable level of agreement was met between the simulated and measured fracture length. This method preserves the mean fracture length but does not incorporate the curvilinear nature of the fractures.

Directional indicator semi-variograms were calculated for search windows aligned at 0, 30, 60, 90, 120, and 150 degrees from north. Most of the directional semi-variograms showed pure nugget effect, which indicates no spatial persistence. The semi-variogram aligned N30E showed true spatial correlation since the primary strike orientation is in this direction. The N30E directional indicator semi-variogram is given in Figure 5.9. An exponential semi-variogram (Equation 5.2) was used to simulate the observed spatial correlation structure. A correlation scale of 135 m yielded the best fit between observed and simulated semi-variograms.

A mean fracture length of 636 m was calculated from the surface fracture map. The discrepancy with the calculated 135-m correlation scale given above is believed to be due to the curvilinear nature

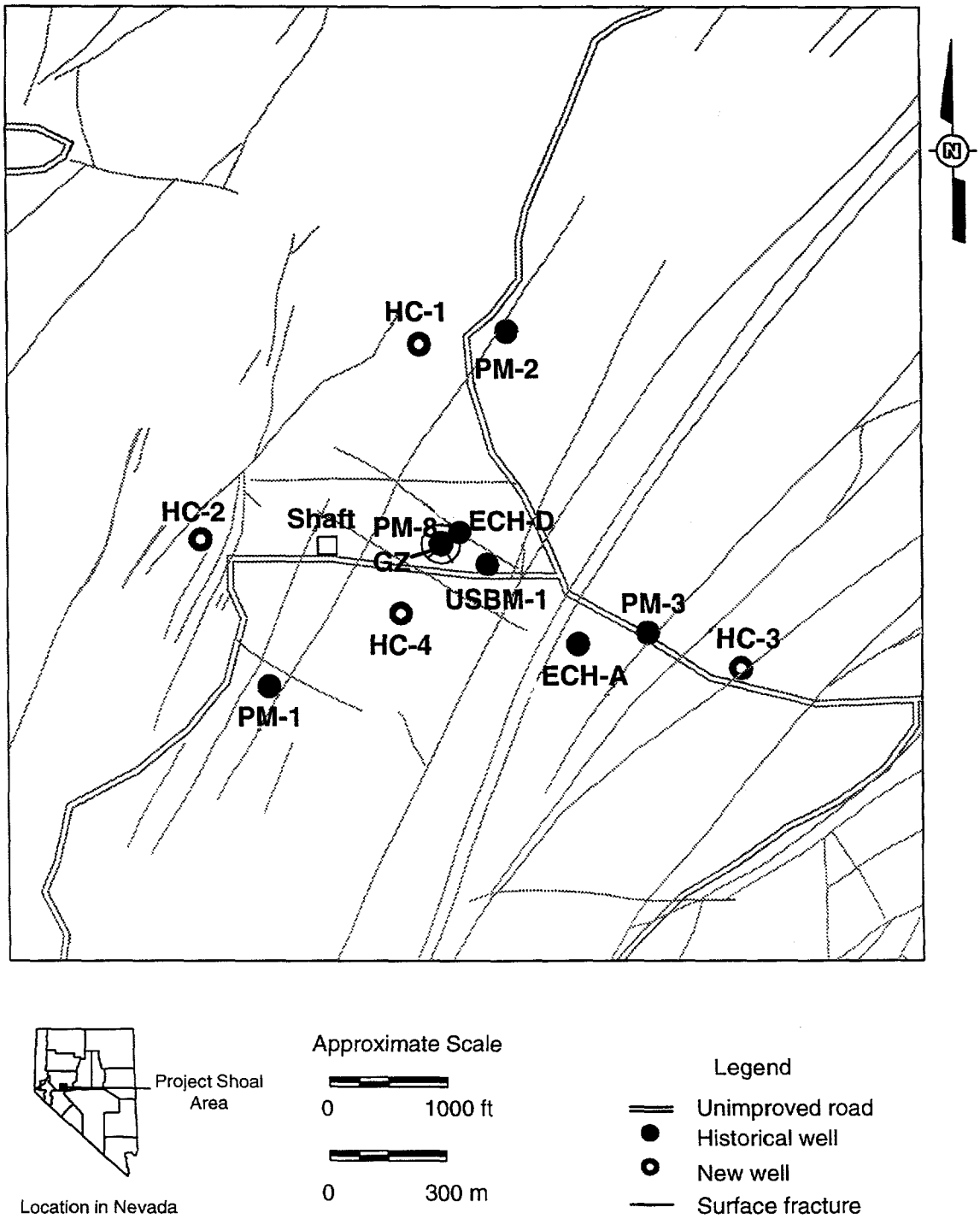

Figure 5.8. Surface geologic structure map near ground zero (adapted from University of Nevada, 1965).

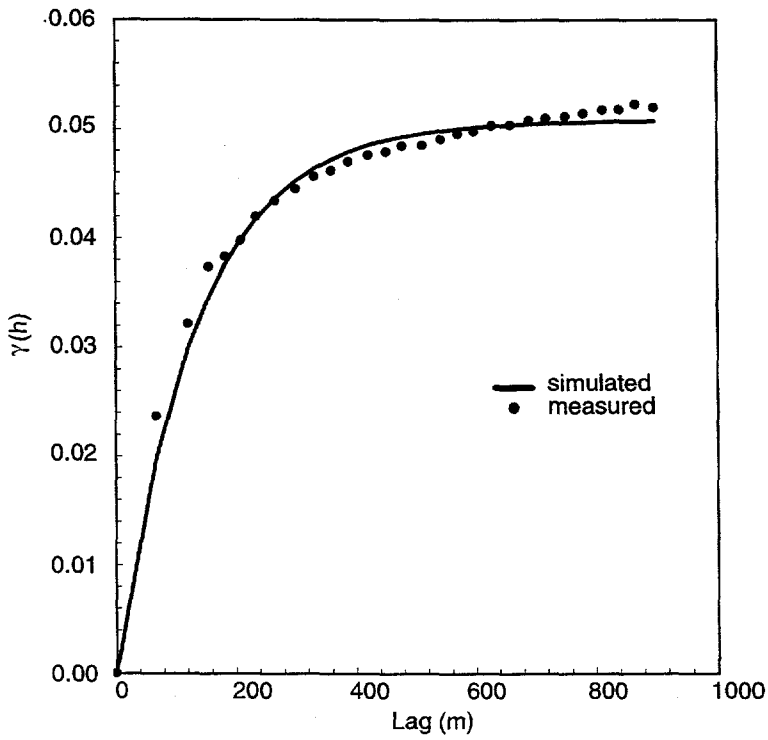

Figure 5.9. Directional (N30E) indicator semi-variogram for the indicator transformed surface geologic structure map.

of the fracture. SIS methods were used to simulate the surface fractures while trying to determine a more appropriate correlation scale such that the simulated and measured mean fracture lengths were in agreement. A correlation scale of 700 m along the strike resulted in a mean fracture length of approximately 630 m. Therefore, a correlation scale of 700 m was used to simulate all fracture classes.

Indicator semi-variograms were calculated for the vertical borehole fracture classes. Directional semi-variograms were calculated in the areal plane, but all showed pure nugget effect, indicating no spatial correlation. The measured and observed vertical indicator semi-variograms are shown in Figures 5.10 and 5.11 for fracture classes #2 and #3, respectively. An exponential semi-variogram was fit to the observed data. Table 5.2 shows the "best-fit" parameters for the exponential semi-variograms. Both classes show a certain degree of nugget effect. Fracture class #2 has a larger indicator variance and smaller correlation scale than class #3.

Table 5.2. Geostatistical Parameters for Each Fracture Class.

Class	Nugget	Sill	Correlation Scale (m)
2	0.05	0.179	13.63
3	0.05	0.168	16.58

For simulation purposes, the correlation scale is required along the dip angle, which is not aligned vertically. Therefore, the vertical semi-variograms cannot be used directly in the

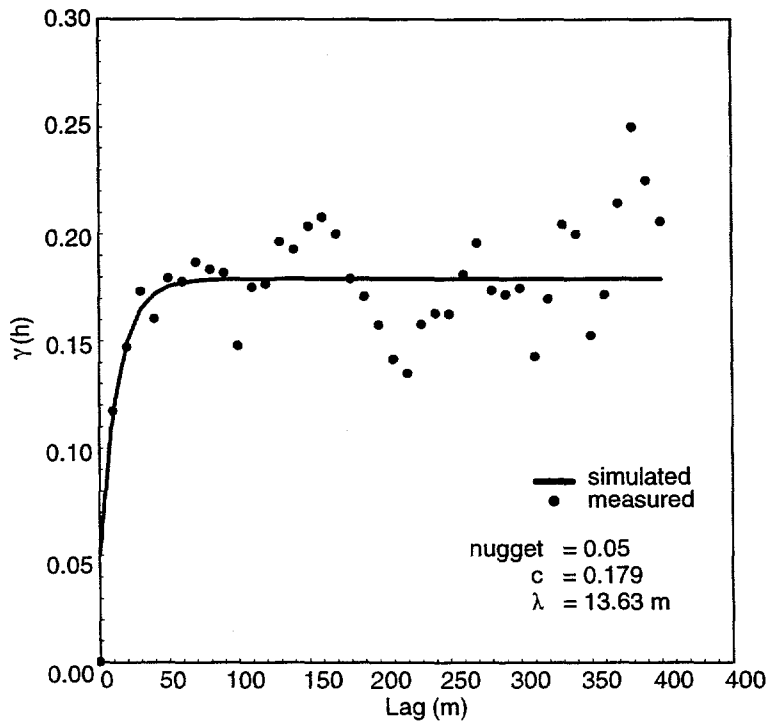

Figure 5.10. Vertical indicator semi-variogram for the integer fracture codes 1→(2,3).

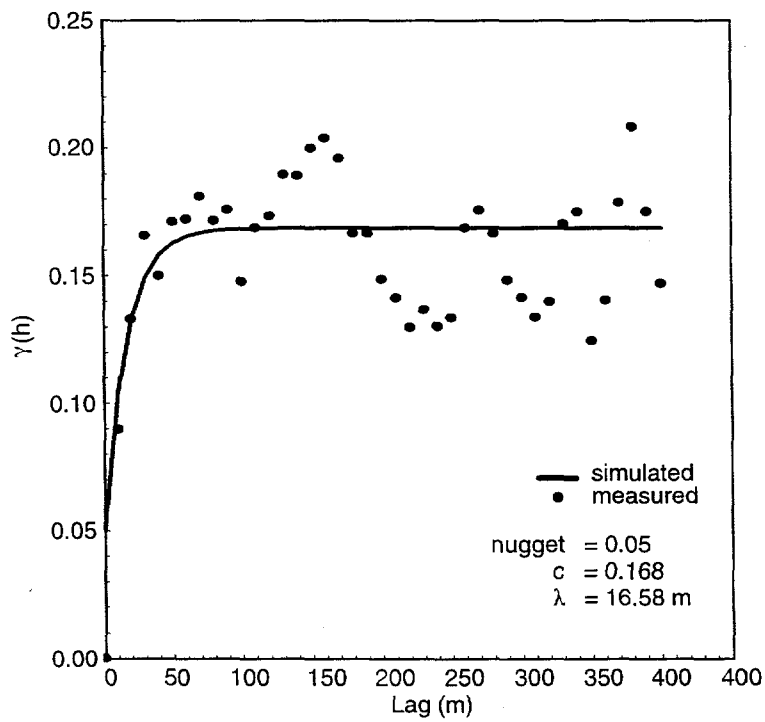

Figure 5.11. Vertical indicator semi-variogram for the integer fracture codes (1,2)→3.

simulations. It was assumed that the dip-correlation scale should be similar to the strike, so a 700 m correlation scale was used. To represent the planar geometry of these fractures, the correlation scale perpendicular to the fracture plane was set to 50 m.

Equations (4.1a) through (4.1e) were solved to determine the proper adjustment of the individual fracture classes. Table 5.3 shows the SIS parameters used to create the singe orientations which were then superimposed. The upscaled ($\Delta x=\Delta y=\Delta z=41.9$-m) fracture class data, which were derived from the borehole logs, were used as conditioning data in the SIS realizations.

Table 5.3. SIS Parameters for Each Fracture Class.

Attribute	Simulation	Class #1	Class #2	Class #3
Adjusted PDF	A	0.69	0.306	0
Nugget	A	0	0	n/a
Indicator Variance	A	0.17	0.17	n/a
λ_1 (m)	A	700	700	n/a
λ_2 (m)	A	700	700	n/a
λ_3 (m)	A	50	50	n/a
Strike (degrees)	A	N25E	N25E	n/a
Dip (degrees)	A	44SE	44SE	n/a
Adjusted PDF	B	0.59	0	0.41
Nugget	B	0	n/a	0
Indicator Variance	B	0.17	n/a	0.17
λ_1 (m)	B	700	n/a	700
λ_2 (m)	B	500	n/a	700
λ_3 (m)	B	50	n/a	50
Strike (degrees)	B	N8W	n/a	N8W
Dip (degrees)	B	31E	n/a	31E

Figure 5.12 shows the results for one realization of the fracture classes using the parameters given in Table 5.3. The figure shows the results for each single orientation SIS simulation (A and B) and the resulting superimposed field for the model domain, which is rotated 45 degrees. The superpositioning preserves the prior probabilities reasonably well. Each realization may not exactly replicate the specified prior probabilities, but the ensemble of many realizations will. For example, the superimposed realization contained 65.9, 12.2 and 21.9 percent of fracture classes 1-3, respectively, while the prior probabilities were 64.2, 15.3, and 20.5. The superimposed fracture field creates nearly continuous groupings of both fracture classes #2 and #3, which is analogous to geologically controlled fracture planes. Once the fracture fields are transformed into conductivity fields, they provide zones of enhanced flow and transport. The fracture-dipping structure will increase the ability of solutes to move downward due to the vertical gradients that are created from the surface recharge flux.

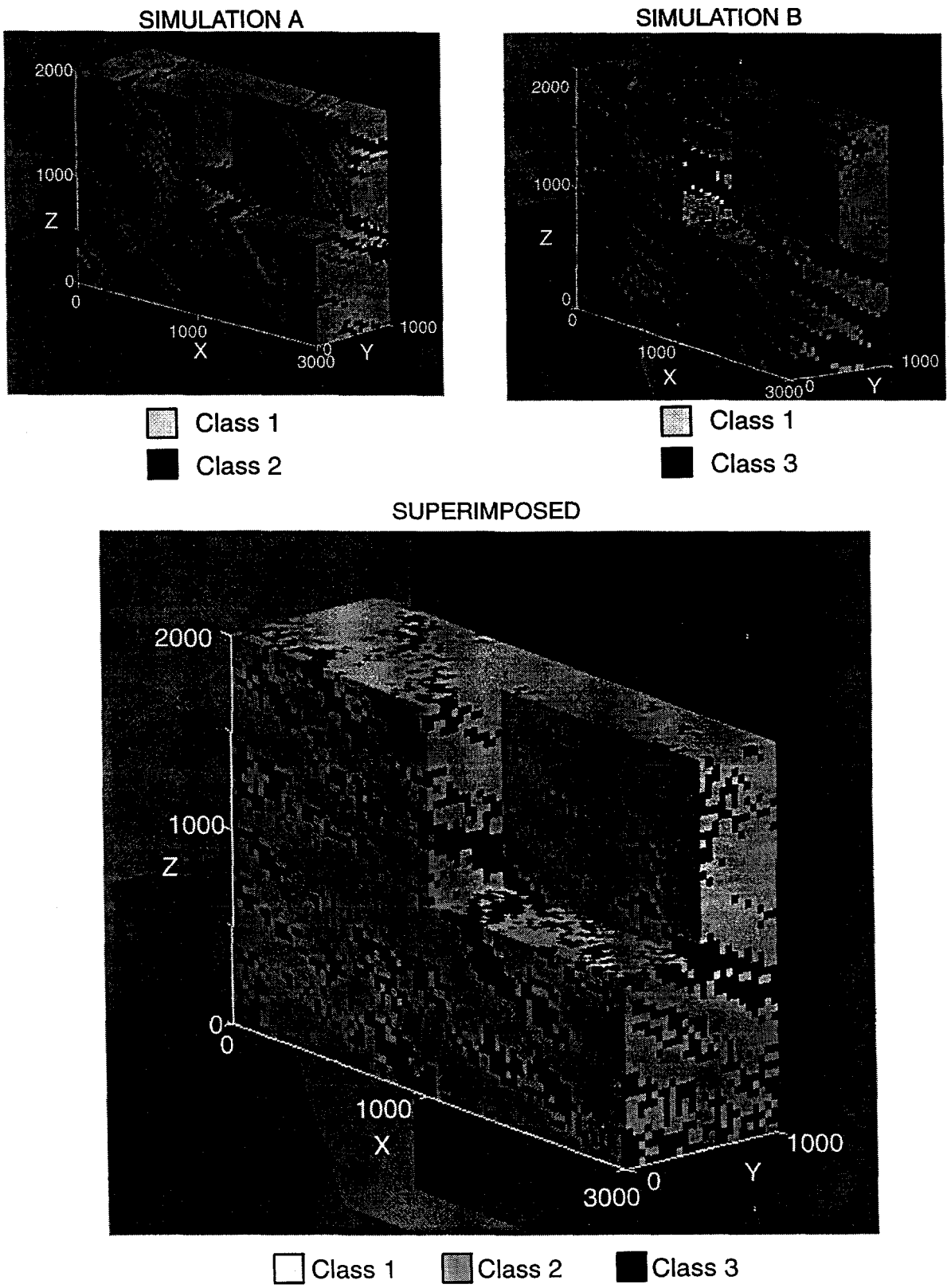

Figure 5.12. One realization of the integer fracture codes for simulation A, simulation B and the superimposed set.

It is also important to recognize that Figure 5.12 represents only one realization of an equiprobable distribution of fracture classes. Each simulation is conditioned on measured data, but differences occur between each realization, especially when few conditioning data are found in the search neighborhood. The ensemble of all simulations represent the prevailing spatial uncertainty, which can be directly linked to the uncertainty in the transport of solutes from the Shoal test.

The simulated fracture fields are not adjusted to account for fracturing induced by the nuclear test, though the video logs that provided the fracture frequency for the HC wells obviously represent the postshot environment. The farthest limit of fracturing observed at Shoal was 135.5 m, and though shot-induced fracturing may have extended even farther along pre-existing zones of weakness, such features are expected to be widely spaced and contribute little to an increase in overall hydraulic conductivity (Borg *et al.*, 1976). In addition, the extreme stress that generated test related fractures was very short lived, and the compressive forces found at depths of hundreds of meters would not allow persistence of large openings once the pressure pulse dissipated. A zone of intense fracturing was determined to exist within 41 m of the shot location (Hazelton-Nuclear Science, 1965; Gardner and Nork, 1970). Though this zone is expected to have a higher hydraulic conductivity than the undisturbed granite, no data are available to postulate separate fracture characteristics. The far-field transport behavior is of interest here and will be controlled primarily by the fracture relationships outside of the zone of impact by the test. The neglected fractured region would occupy half a grid cell around the modeled cavity and would primarily serve to disperse the source. The impact of prompt injection of radionuclides is considered in the Section 7.3 (Sensitivity and Uncertainty Analysis).

5.2 Hydraulic Conductivity Representation

The fracture fields are represented by a three-dimensional array of fracture classes. To convert the fracture classes to a hydraulic conductivity field, a constant hydraulic conductivity was applied to each class. Field measurements of hydraulic conductivity were estimated using thermal flowmeter analysis in discrete sections (approximately 10-m spacing) of the new boreholes (HC-1, HC-2 and HC-4; see Appendices 5 and 6). The fracture analysis provided a fracture class at 0.3048 m (1 ft) intervals in the borehole. Because the fracture data were present at a different scale than the hydraulic data, an integrated measure of the fracture class had to be estimated. The fracture code at 10-m spacings was determined by first calculating the percentage of each fracture class within 10-m-vertical intervals. In a method similar to Tsang *et al.* (1996), it was assumed that if at least one "large" fracture (integer code = 3) was found, then an integer code of "3" was applied to the 10-m section. Likewise, if no "large" fractures were found, but there were at least 10 percent "medium-type" fractures (integer code = 2), then the section was assigned a type "2" code. Otherwise, a type "1" code (no or very small fractures) was assigned to the 10-m interval. This method of upscaling the 0.3048 m (1 ft) fracture data to the scale of the hydraulic measurements (10 m) imposes an adjustment to the prior probabilities. Therefore, the prior probabilities of the upscaled fracture codes were used in the SISIMPDF simulations. Because the groundwater flow model was at yet another scale (41.9 m), the measured fracture classes had to be upscaled (using the same

method) to match the larger grid spacing of the flow model such that the fracture data could be used as conditioning data in the SISIMPDF simulations.

The prior probabilities for the original and upscaled fracture codes are given in Table 5.4. The purpose of the upscaling technique was to create a dataset of integer fracture classes that is on the same scale as the groundwater flow modeling and field hydraulic testing. The goal is to substitute a block of heterogeneous fracture classes with a single fracture class that integrates all of the hydraulic conditions into a single value. The upscaling is subjective, which adds uncertainty to the modeling, but in this case is conservative, as it produces a larger percentage of higher conductivity cells into the groundwater flow simulations.

Table 5.4. Prior Probabilities of Each Fracture Class for Original and Upscaled Data.

	Class #1	Class #2	Class #3
Original Data	0.781	0.1	0.119
Upscaled Data	0.642	0.153	0.205

The hydraulic conductivities derived from the 10-m thermal flow testing were then assigned a fracture class (integrated over the 10-m section) based on its borehole location. The geometric mean of hydraulic conductivity was calculated from the distribution within each fracture class. Because the thermal flowmeter has a finite resolution, it is limited in its ability to estimate very low values of conductivity. Therefore, fracture class "1" (no/small fractures) contains the most uncertainty with respect to the associated geometric mean of hydraulic conductivity. The hydraulic conductivity for fracture class "1" was only used as a starting point for the calibration procedure, which adjusted the value of the hydraulic conductivity (fracture class 1 only) until a reasonable level of agreement was met between the observed and simulated water levels in the new wells (HC-1, HC-2, and HC-4).

5.3 Model Grid

The model domain must be discretized into a grid of regular-spaced blocks. Figure 5.13 shows the areal extent of the groundwater flow model. The uppergradient vertical face of the model was aligned with the groundwater flow divide. This divide was assumed to be aligned with the topographic divide. The coordinates of the northwest corner of the model domain are N494042 (m) E168995 (m) (Nevada State Plane Coordinates, NAD 1927 Datum). The rotation angle of 45 degrees was selected to align the model on the groundwater divide and to be parallel with the direction of mean flow. It should be noted that no head measurements were available in the southeastern portion of the domain, which may impact the correct determination of the mean flow direction.

The extents of the domain were selected to encompass all of the new wells (HC-1, HC-2, HC-3, and HC-4) and laterally beyond the land exclusion boundary such that the solute movement could be calculated at the downgradient intersection of the model domain with the land exclusion

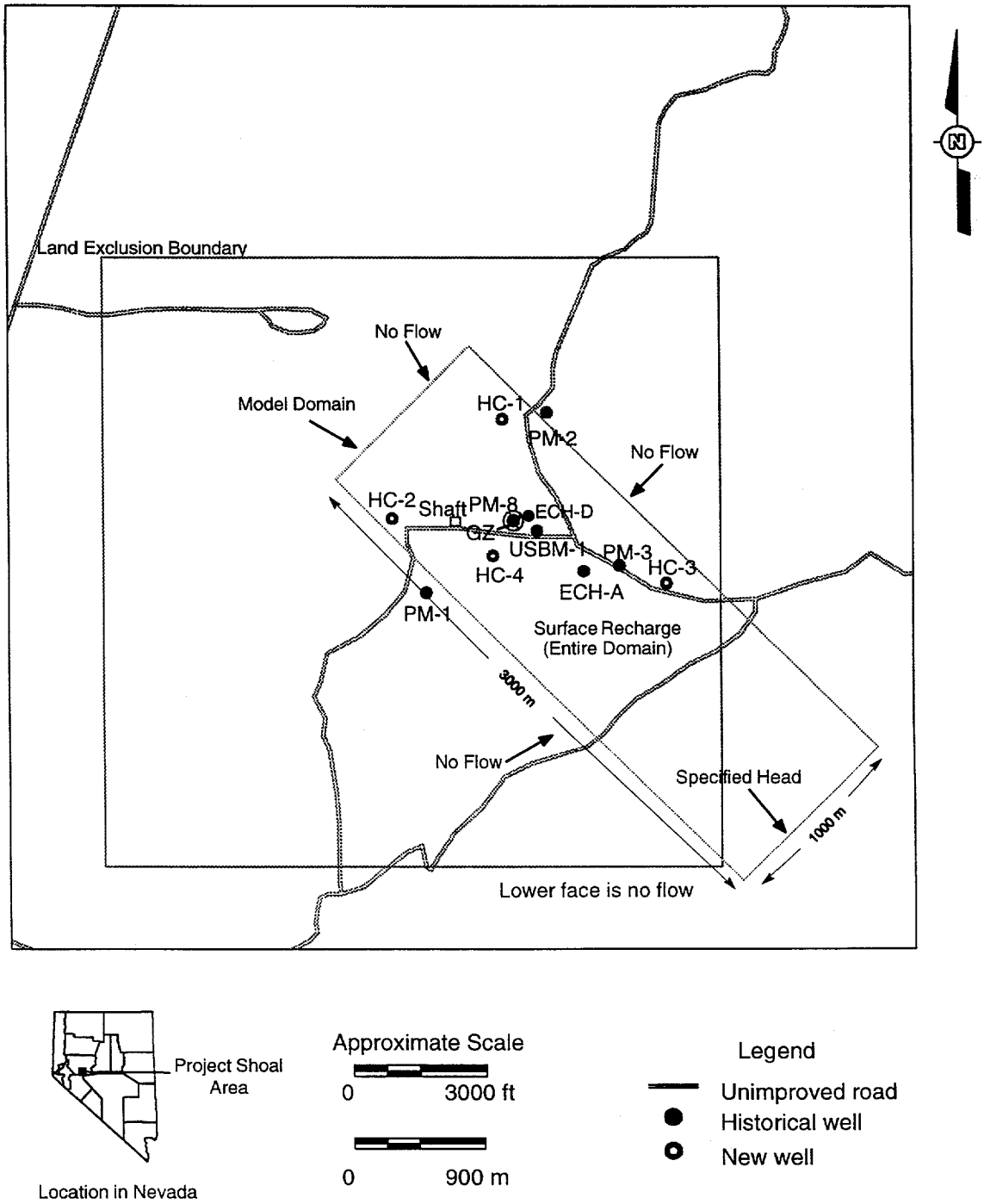

Figure 5.13. Site diagram of the Shoal site showing the areal extents of the model domain and boundary conditions for the groundwater flow model.

boundary. Scoping calculations performed using analytical methods suggested that this domain would encompass the transport distance of interest (Chapman *et al.*, 1995). A 1000-m width was selected so transport simulations would not be impacted by the lateral boundaries. The upper portion of the model begins at an elevation of 1327 m (MSL) and extends 2000 m to -673 m (MSL). The vertical distance was determined by trial-and-error simulation of the transport of conservative particles such that the lower no-flow boundary did not impede vertical movement.

The grid spacing of 41.9 m was selected in all three primary directions ($\Delta x=\Delta y=\Delta z=41.9$m) to properly represent the large correlation scales simulated with SIS. There is a tradeoff between a finer grid resolution to represent the fracture heterogeneity and the inherent computational limits. The geostatistical analysis suggests that the correlation length along the primary fracture directions are nearly 70 percent of the smallest domain length (y direction), so the grid spacing of 41.9 m is valid. Semi-variograms were calculated for the simulated conductivity fields and resulted in minimum correlation scales of approximately $2\Delta z$ in the vertical direction and $4\Delta z$ in the lateral directions (x and y).

5.4 Boundary Conditions

Figure 5.13 shows the boundary conditions used for the groundwater flow model at Shoal. All boundaries are assumed to be no-flow-type boundaries with the exception of the surface recharge boundary and the southeast specified head boundary. The simulation of recharge controls the flow system by creating vertical gradients as is expected in a mountain range. This creates a more realistic model as opposed to an overly constrained model containing only constant head boundaries. Although more realistic, the inclusion of recharge adds additional complexity and uncertainty due to imprecise recharge estimates.

5.4.1 Surface Recharge

The Shoal site is in a sub-humid to semi-arid region of the Great Basin in Nevada. Annual rainfall varies from about 13 cm in the valleys to about 30 cm in the high mountain ranges (Gardner and Nork, 1970). Most precipitation in the mountain ranges occurs as snow (from the Eastgate gauge, 40 km east and 75 m lower than the Shoal site). Due to the rain-shadow effect at the Eastgate site, 20 cm is the estimated annual precipitation at Shoal. The vertical hydraulic gradients reported in well ECH-D by University of Nevada (1965) support the assumption of surface recharge.

Cohen and Everett (1963) utilized the method of Maxey and Eakin (1949) to obtain a preliminary estimate of the average annual groundwater recharge derived from precipitation. The method is based on the assumption that a fixed percentage of a given average annual rate of precipitation ultimately recharges the groundwater reservoir. Maxey and Eakin (1949) report that based on the annual precipitation rate, between three and seven percent of the rainfall will infiltrate and become groundwater recharge. Therefore, with estimates of annual precipitation ranging from 20 - 30 cm/yr, the estimated groundwater recharge ranges between 0.6 and 2.1 cm/yr. These estimates of groundwater recharge are based on averages of both precipitation and net recharge from the entire state of Nevada and are at best gross estimates. To confirm these values, an independent estimate of recharge was determined using a borehole temperature profile.

Vertical fluid movement can affect the flux of heat within the earth. Stallman (1960) presented the basic equations for the simultaneous transfer of heat and water within the subsurface and suggested that temperature measurements can provide a means of measuring fluid velocity. Stallman (1960) presented a method for near-surface temperature fluctuations which assumes the transient flow of both heat and fluid. Bredehoeft and Papadopulos (1965) present the steady-state solution for heat and fluid which is applicable in deeper systems where temporal heat variations become negligible. The differential equation for steady-state, one-dimensional, simultaneous heat and fluid flow through isotropic and homogeneous porous media is given by:

$$\left(\frac{\partial^2 T}{\partial z^2}\right) - \left(\frac{c_0 \varrho_0 v_z}{k}\right)\left(\frac{\partial T}{\partial z}\right) = 0 \tag{5.3}$$

where T is the temperature (°C), z is the vertical Cartesian coordinate (positive downward, cm), c_0 is the specific heat of the fluid (cal/g), ϱ_0 is the density of the fluid (g/cm^3), k is the thermal conductivity of the solid-fluid complex (cal/cm-sec-°C), and v_z (cm/sec) is the vertical component of the fluid velocity (cm/sec). Equation (3.5) is strictly applicable in an isotropic homogeneous, fully saturated porous media, as k is a non-linear function of the water content in the vadose zone. Although not all assumptions required by Equation (5.3) are met at the Shoal site, the steady-state conditions and low-porosity conditions provide an approximation to the simultaneous movement of heat and fluid. Bredehoeft and Papadopulos (1965) provide a solution to Equation (3.5) as:

$$\frac{(T_z - T_0)}{(T_L - T_0)} = \frac{\exp\left(\frac{\beta z}{L}\right) - 1}{\exp(\beta) - 1} \tag{5.4}$$

where T_0 is the temperature at the uppermost elevation (°C), T_L is the temperature at the lowermost elevation (°C), T_z is the temperature at vertical location z (cm), L is the total vertical thickness where thermal data is collected (cm), and $\beta = c_0 \varrho_0 v_z L/k$ is a dimensionless parameter that is positive or negative depending on whether v_z is downward or upward. The vertical fluid velocity v_z is determined by non-linear optimization techniques that search for the value of v_z such that there is a minimum difference between the ensemble observed and simulated temperature profile.

Although temperature measurements were available from multiple well locations (both old and new), it was determined that the PM-1 temperature data were best suited for a more detailed temperature analysis. *In situ* fluid velocities could not be calculated from the other wells because many of the other temperature logs were taken too soon after drilling was completed or the casing was not in continuous contact with the rock. Temperature measurements were made along the entire borehole, but only the section from 134 - 359 m below land surface was used in the analysis. The temperature from the upper portion of the borehole was removed so that transient effects would not influence the analysis. Likewise, the temperature data below the water table were not used, as lateral groundwater flows could not be accounted for in the one-dimensional model.

The parameters required to estimate the vertical fluid velocity include c_0, ϱ_0, k and L. For this study, $c_0 \varrho_0$ = 1.0 cal/cm^3 and L = 22509 cm. University of Nevada (1965) calculated the thermal

conductivity for four intact cores in ECH-D. The thermal conductivity ranged between 3.1 - 4.5 x 10^{-3} cal/cm-sec-°C. The cores were undisturbed and contained minimal fractures. The *in situ* rock may contain more fractures and would therefore possess a lower thermal conductivity. If the thermal conductivity of the *in situ* rock was lower than the lab values, then the true fluid velocities would be lower than predicted. Although the thermal conductivity obtained by University of Nevada (1965) was for the rock matrix, the low porosity of the matrix would not alter the thermal conductivity of the rock-fluid combination, as the fluid volume would be substantially less than the rock matrix.

Figure 5.14 shows the simulated versus measured temperature profiles for PM-1 for $\beta = 0.271$. The four values of thermal conductivity resulted in associated vertical velocities of 1.17 - 1.71 cm/yr, with a mean value of 1.45 cm/yr. The root mean squared error of the measured versus simulated temperatures was 0.08°C. All groundwater model simulations assumed a recharge rate of 1.45 cm/yr applied uniformly to the first saturated cell in the MODFLOW model. Additional simulations were performed to determine the impact of the recharge rate on solute transport behavior.

5.4.2 Constant Head Boundary

The southeastern model boundary is a specified head boundary. The head at this boundary represents the regional hydraulic head downgradient of the detonation. There is no water level information in this portion of the domain so it had to be estimated. The HC-3 well is closest to the boundary, but the water level in this well was temporally unstable and lower than the adjacent water level in Fairview Valley. After the initial drilling, the water level in HC-3 began to rise and then abruptly reversed, declining slowly until the well was completely dry. A small-diameter piezometer was installed into the wellbore to determine the water level below the lowest access point. The water

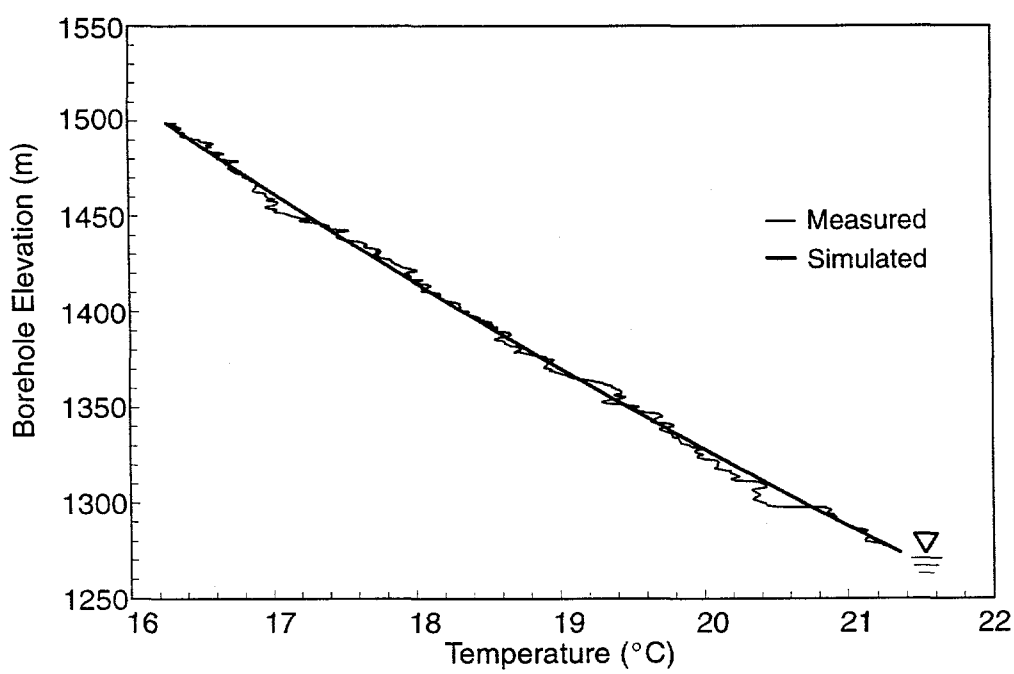

Figure 5.14. Measured versus simulated vertical temperatures for PM-1.

level declined to a point (1192.7 m) which is below the water level in the adjacent Fairview Valley (~1200 m). Because of the large uncertainty in the HC-3 water level, the downgradient specified head boundary was estimated to be 1210 m, which is approximately 10 m above the Fairview Valley water levels. Additional simulations were performed to determine the impact of the lower boundary condition on solute transport behavior.

5.5 Groundwater Flow Model Results

This section provides the results for the groundwater flow model. The results of the transport model are provided in Section 6.0. Included are the results of the calibration process, hydraulic head distribution, the flux fields, and groundwater velocities.

5.5.1 Hydraulic Conductivity Fields

The hydraulic conductivities that were estimated from the thermal flowmeter analysis are shown in Table 5.5.

The trend in hydraulic conductivity is increasing with each fracture class code, which supports the assumption that fracture classification can be used as a surrogate to understand the hydrogeologic system. There is a range of nearly an order of magnitude in the mean of each class, which is much smaller than the many orders of magnitude that were used by Tsang *et al.* (1996).

Table 5.5. Summary of Hydraulic Analysis from Thermal Flowmeter Tests.

Class #1 Summary		Class #2 Summary		Class #3 Summary	
Well	K (cm/sec)	Well	K (cm/sec)	Well	K (cm/sec)
HC-4	4.42E-07	HC-1	1.00E-05	HC-1	3.97E-05
HC-4	3.61E-06	HC-1	1.40E-05	HC-1	7.69E-04
HC-1	3.40E-06	HC-4	3.36E-06	HC-4	1.02E-05
				HC-4	2.27E-06
				HC-4	1.54E-06
K_g =	1.7E-06	K_g =	7.78E-06	K_g =	1.61E-05

Note: Kg = geometric mean

The geometric mean of fracture class #3 (1.61 x 10^{-5} cm/sec) is comparable to the geometric mean of fractured granite (2.35 x 10^{-5} cm/sec), determined from an extensive database of granite conductivities (Raven *et al.*, 1992; Raven *et al.*, 1993). As noted in section 2.4.1.2, there is no evidence to support the hypothesis that hydraulic conductivity decreases with depth at the Shoal site. Therefore, the distribution of hydraulic conductivity was simulated assuming statistical homogeneity.

5.5.2 Calibration

The ASTM Standard Guide for Calibrating a Groundwater Flow Model (ASTM, 1995) was used as a guide in the calibration process. The conductivity of fracture class #1 was adjusted through

a calibration process to obtain a reasonable level of agreement between the observed and simulated hydraulic heads. An absolute error function was used to calculate the residual between measured and simulated head values as:

$$AE = \frac{1}{N}\sum_{i=1}^{N}(\phi_m - \phi_s) \tag{5.5}$$

where AE (m) is the absolute error, N is the number of measured hydraulic head values, H_m (m) is the measured head value (wells HC-1, HC-2 and HC-4), and H_s (m) is the simulated head value.

Figure 5.15 shows the distribution of the absolute error for three sets of Monte Carlo simulations. Each Monte Carlo set contains 100 realizations to determine the most appropriate value of the hydraulic conductivity of the fracture class #1 (K_1). Each realization produces a different absolute error between the measured and observed heads, so the objective in the calibration process was to determine a value of K_1 such that the absolute error distribution was centered over zero. Figure 5.15 shows that $K_1 = 4.0 \times 10^{-7}$ cm/sec produces the best ensemble of absolute errors. Decreasing the K_1 to 2.0×10^{-7} cm/sec produces simulated head values that are consistently greater than measured. Likewise, increasing K_1 to $1.8.0 \times 10^{-6}$ cm/sec yields simulated head values that are lower than measured.

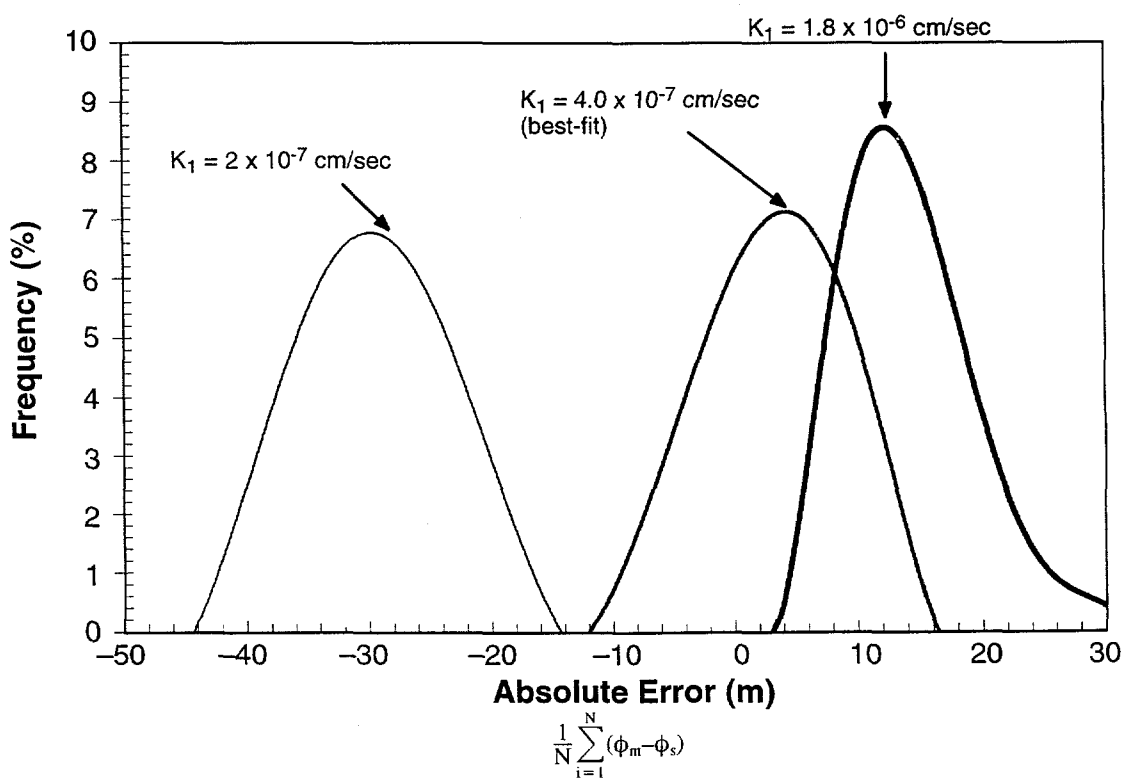

Figure 5.15. Frequency of absolute error for each calibration trial.

The "best-fit" value of K_1 was assumed to be 4.0 x 10^{-7} cm/sec, which is smaller than the geometric mean of the measured conductivities (1.76 x 10^{-6} cm/sec) for fracture class #1. The discrepancy between the measured and calibrated value of K_1 is likely due to the resolution limits of the thermal flow meter. Table 5.6 shows the values of the hydraulic conductivity used in all of the Monte Carlo simulations for each fracture class.

Table 5.6. Simulated Values of Hydraulic Conductivity for Each Fracture Class.

	Class #1	Class #2	Class #3
Hydraulic Conductivity (cm/sec)	4.00E-07	7.78E-06	1.61E-05

5.5.3 Water Table Elevation

The vertical slice of the water table elevation provides an indication of the predicted water table elevation, but it is difficult to clearly identify the exact position of the water table surface. Figure 5.16 shows the measured versus simulated water table elevation obtained by extracting the hydraulic head from the first saturated model grid cell from one realization centered on the y axis. The measured values were projected onto the center line (y = 500 m) for comparison purposes. The simulated water table elevation is relatively flat near the groundwater flow divide, then it dips downward quickly towards Fairview Valley. This single realization slightly underpredicts the water table elevation for HC-1 and HC-2 yet overpredicts for HC-3 and HC-4. Again, the water level in HC-3 is highly uncertain, as it was temporally unstable, and the piezometer may not be measuring the true *in situ* water level.

5.5.4 Flux Fields

The Darcy fluid fluxes, q, can be calculated using the hydraulic head field simulated with MODFLOW as:

$$q(\mathbf{x}) = -\mathbf{K}(\mathbf{x})\nabla\phi(\mathbf{x}) \tag{5.6}$$

where $q(\mathbf{x})$ (m/day) is the Darcy flux field, $\mathbf{K}(\mathbf{x})$ (m/day) is the hydraulic conductivity field tensor, and $\phi(\mathbf{x})$ (m) is the head field obtained from MODFLOW. The relative magnitude and direction of the x and z directional fluid fluxes from one realization are shown in Figure 5.17. The vertical section shows primarily downward flow of lesser magnitude near the groundwater flow divide and larger fluxes in a more horizontal direction downgradient. Figures 5.18 through 5.20 show the distribution of Darcy fluxes from one realization for the x, y and z directions, respectively. Although Figures 5.18 to 5.20 represent only one equiprobable realization, the distributions change very little between realizations, as the prior probabilities of the hydraulic conductivities remain constant. The distribution of x direction fluxes have an arithmetic mean of 8.13 x 10^{-5} m/day with most of the values ranging between 0 and 0.0001 m/day. There exists a positively skewed tail in the x-direction fluxes toward higher fluxes due to the nonlinear head gradient. The distribution of the y-direction fluxes have a much smaller arithmetic mean of -8.72 x 10^{-7} m/day with most of the fluxes centered

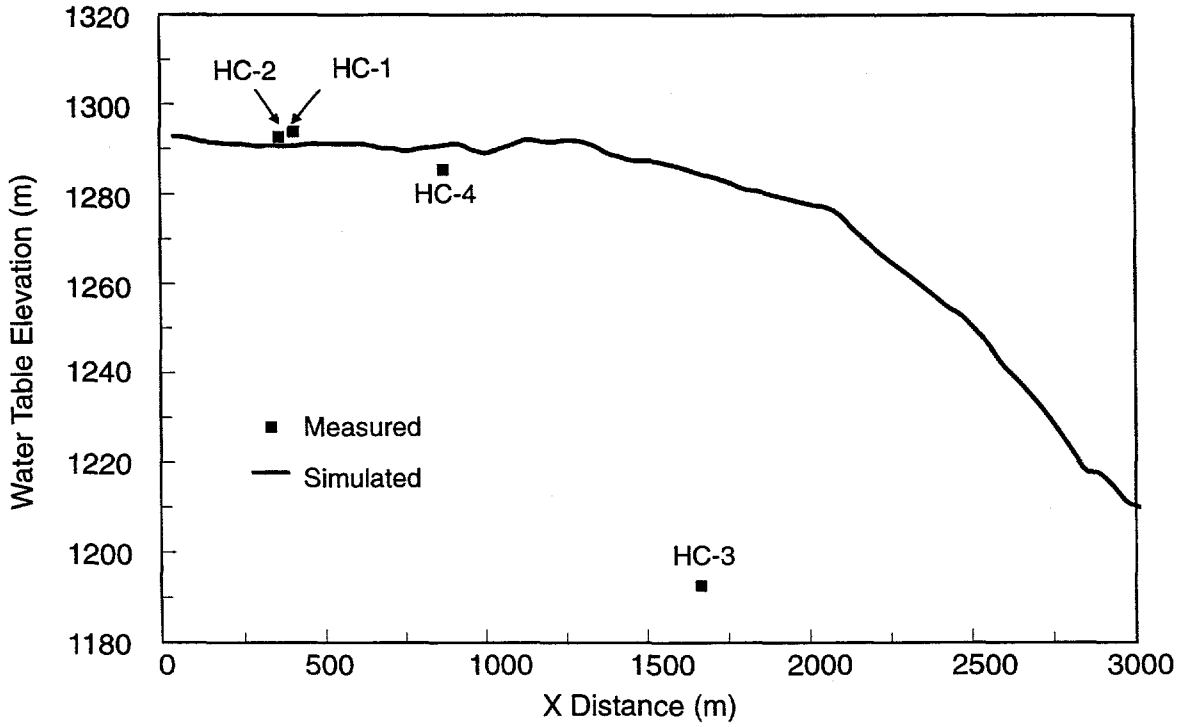

Figure 5.16. Simulated (single realization) and measured water levels.

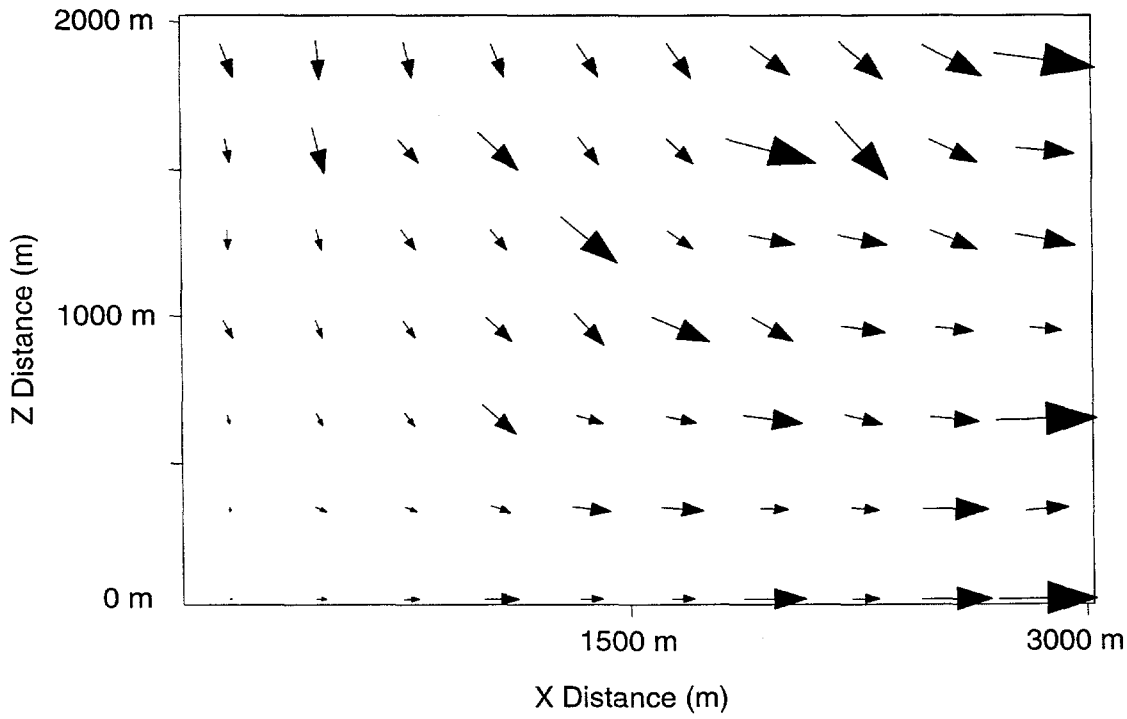

Figure 5.17. Relative magnitude and direction of simulated (one realization) fluid fluxes for a vertical slice in the model domain.

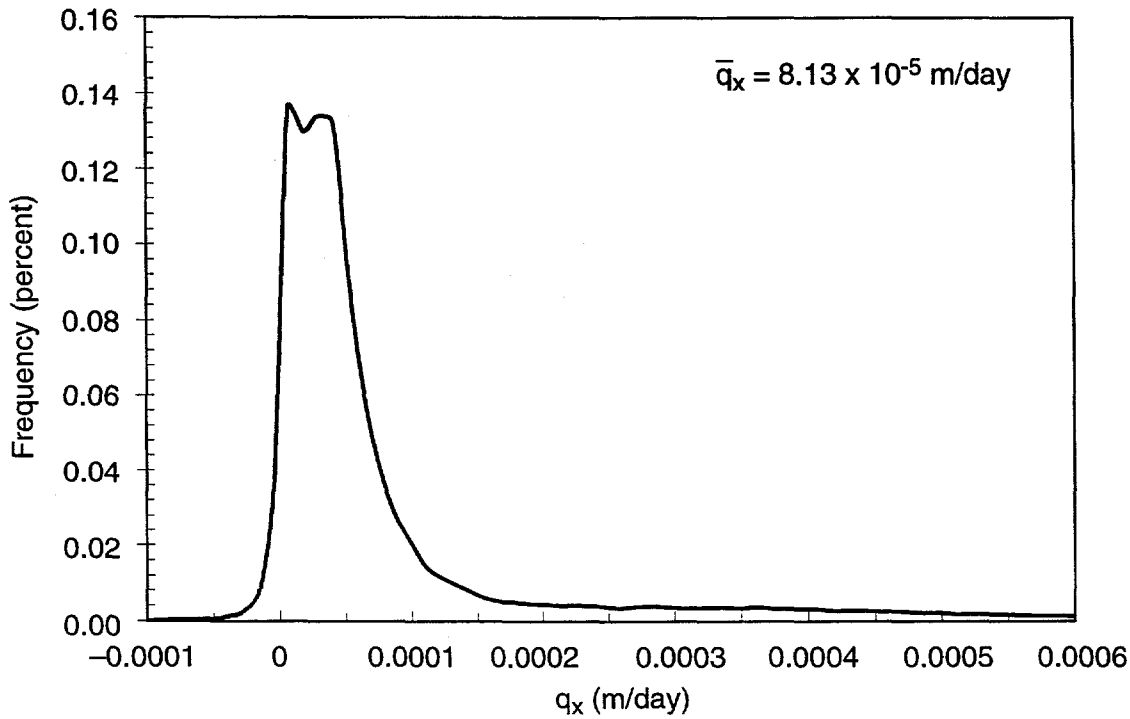

Figure 5.18. Frequency of the x-direction fluxes from one flow realization.

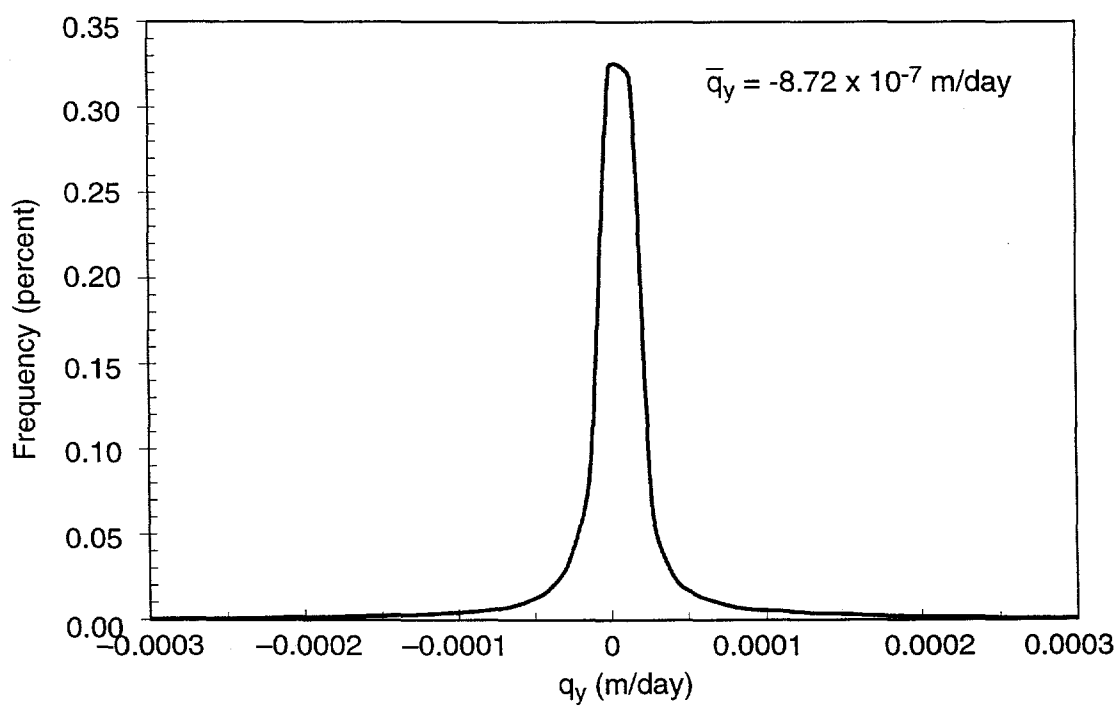

Figure 5.19. Frequency of the y-direction fluxes from one flow realization.

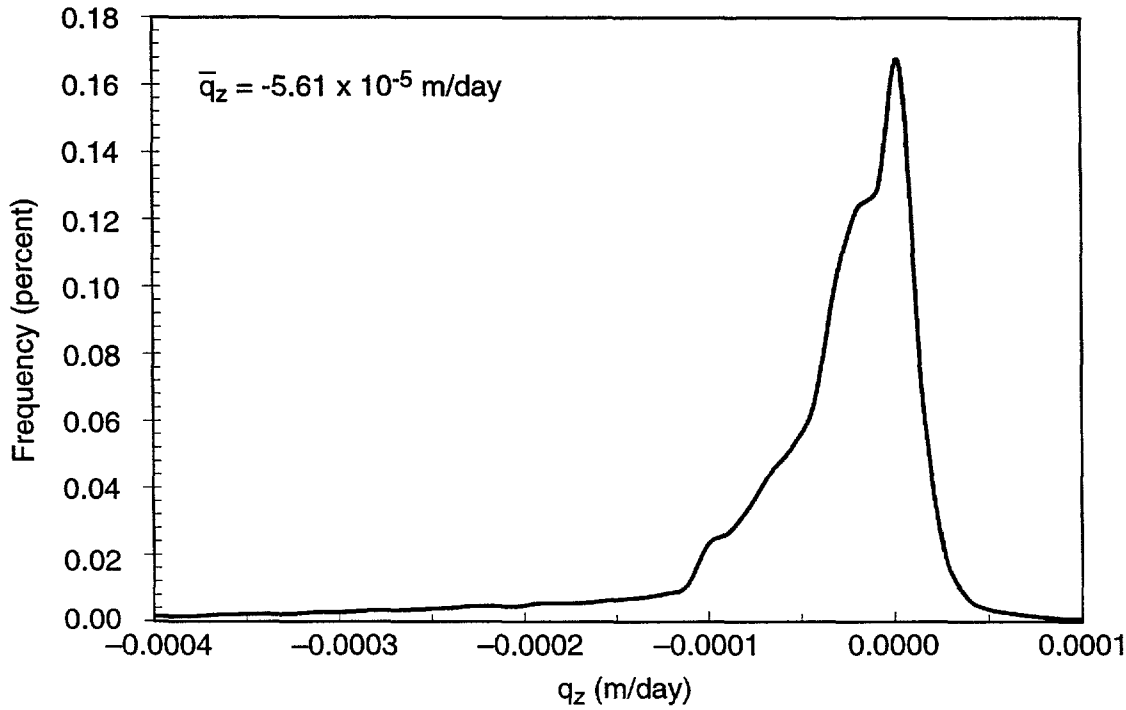

Figure 5.20. Frequency of the z-direction fluxes from one flow realization.

near zero and ranging primarily between -0.0001 and 0.0001 m/day. The vertical direction fluxes are negatively skewed, with a mean of -5.61 x 10^{-5} m/day indicating primarily downward flow.

5.5.5 Velocities

The cell-to-cell fluxes calculated by MODFLOW are converted to velocities as:

$$v(\mathbf{x}) = \frac{q(\mathbf{x})}{n(\mathbf{x})} \tag{5.7}$$

where v(**x**) is the fluid velocity field (m/day), q(**x**) is the fluid flux(m/day), and n(**x**) is the effective porosity. There were no direct measurements of porosity for the Shoal granite, so data from the Aspo Hard Rock Laboratory, in the southeast of Sweden, were used as a surrogate (Werner, 1996). Twenty-two granite rock samples were analyzed for total porosity, using either the water saturation method or the leaching method. Both methods yield an estimate of the total porosity which is a combination of both a transport (*i.e.*, where water or solute transport can take place) and storage component (*i.e.*, the voids which consist of dead-end pores, not contributing to water or solute transport). The effective porosity is defined as the percentage of interconnected pore space, equivalent to the transport porosity, and can be smaller than the total porosity (Domenico and Schwartz, 1990).

A numerical analysis was performed (see Appendix 4 for more details) to estimate the hydraulic conductivity and porosity from the HC-1 aquifer test data. The numerical model was set up to simulate the conditions of the pumping test and then the hydraulic conductivity and porosity were adjusted until there was a minimum error between the observed and simulated water levels.

Although there is a minimum or "best-fit" between the measured and simulated water levels for a conductivity of 0.074 m/day and a porosity of 0.0005, the solution was insensitive to porosity. Any value between 0.0001 and 0.01 yields equiprobable (less than 10 percent change in the objective function) simulated water levels. Since direct measurements of effective porosity were not available, the mean value (0.006) of Werner (1996) was used for all transport simulations. One might expect different values of effective porosity for each fracture class due to various degrees of fracturing. There were no field data to support the inclusion of spatial heterogeneity of porosity. The mean porosity value of 0.006, taken from the extensive analysis of the fractured granitic aquifer at the Aspo site, is assumed to represent the mean behavior at the Shoal site. The source location (cavity) was simulated with a porosity of 0.24 (see Section 6.2.2).

The mean simulated fluid velocity (in the x-direction, parallel to the mean flow direction) is 5 m/yr. This estimate of fluid velocity is within the rather wide range (0.3 to 30 m/yr) determined by others (University of Nevada, 1965; Gardner and Nork, 1970), but appears high when considering the groundwater ages calculated for the HC wells (6000 to 12,500 years), and the chemical and isotopic inconsistencies between the Shoal wells and the well in the downgradient valley (Section 2.4.2).

6.0 Transport Model

The conceptual transport model is described in Section 3.2. Several of the features outlined there require additional discussion to understand how they were implemented in the Shoal calculations. First, the source term is described in more detail. This is followed by a discussion of release functions, including the apportioning of radionuclides among surface and volume (nuclear melt glass) deposits, calculation of a hydraulic release rate, and development of the nuclear melt glass dissolution function. Finally, retardation of transport species is described, involving experimental results and application of equilibrium distribution coefficients along with estimates of fracture aperture to obtain retardation values.

6.1 Source Term

Contaminants resulting from underground nuclear testing can be divided into two broad categories: radionuclides and non-radionuclides. Primary radionuclides can be attributed to three possible origins: 1) residual nuclear material which has not undergone a fission or thermonuclear reaction, 2) direct products of the nuclear reactions (fission products and tritium), and 3) activation products induced by neutron capture in the immediate vicinity of the explosion (Borg *et al.*, 1976). In addition, radionuclide daughter products are produced by decay of many of the primary radionuclides. Non-radionuclide hazardous materials have been identified for some tests at the Nevada Test Site (NTS) (Bryant and Fabryka-Martin, 1991), though the relative simplicity of the Shoal experiment indicates they are not an issue at this site.

6.1.1 Radionuclide Source Term

The Shoal radionuclide source term is included in an inventory prepared by Los Alamos and Lawrence Livermore National Laboratories for nuclear tests conducted at non-NTS locations

(Goishi *et al.*, 1995). The inventory presented in Goishi *et al.* (1995) represents the total radiologic source term, given one constraint: radionuclides were excluded from the inventory if they were produced in such low amounts or decayed so rapidly that if the total amount produced during the test were dissolved into a volume of water equal to the volume of the cavity and allowed to decay for 100 years, the resulting aqueous concentration would be less than one-tenth of the maximum permissible concentration (MPC) (Smith *et al.*, 1995). The MPC used by Goishi *et al.* (1995) is the concentration in drinking water determined by the U.S. Environmental Protection Agency that results in a dose rate of 4 mrem/year to a person drinking two liters of water per day, as listed for many radionuclides in the Federal Register (vol. 56, no. 138, July 18, 1991). These MPC values were proposed but never promulgated by the EPA. For nuclides with no listed MPC, Goishi *et al.* (1995) assumed a conservative value of 10^{-8} μCi/ml. The criterion used by Goishi *et al.* (1995) effectively eliminates radionuclides with half-lives less than about 10 years from their inventory.

Calculations of the radionuclide production from Shoal were also presented by Hazelton-Nuclear Science (1965). Hazelton-Nuclear Science (1965) presents estimates of some of the shorter-lived isotopes that were not included by Goishi *et al.* (1995). Both references present independent calculations for the initial mass of ^{3}H, ^{137}Cs, ^{90}Sr, ^{151}Sm, and ^{113m}Cd. The Hazelton-Nuclear Science estimate for tritium production was 3.0×10^{4} Ci, for ^{90}Sr production was 1.9×10^{3} Ci and for ^{137}Cs production was 2.2×10^{3} Ci.

Given the thorough documentation, access to data, and consistency with calculations performed for other underground nuclear tests, the Goishi *et al.* (1995) data are considered to provide the best definition of the Shoal radionuclide source term. The classified nature of the data presents obvious problems in terms of presenting the results in a public document. The approach taken here is twofold. First, the list of potential radionuclides discussed in the public portion of this document follows that presented in an unclassified publication by Smith *et al.* (1995). This list (Table 6.1) is used to discuss release functions and retardation behavior, and provides the basis for transport calculations using a unit mass value. The radionuclides reported by Smith *et al.* (1995) do not necessarily have a one-to-one correspondence to those presented by Goishi *et al.* (1995), though the classified radionuclide inventory for the NTS (Goishi *et al.* 1994) was used by Smith *et al.* (1995) in compiling their table of important radionuclides. The unit-mass-based transport analyses presented in the body of this report can be converted to true mass in a classified companion document, when the need arises. Second, the unclassified data from Hazelton-Nuclear Science (1965) for ^{3}H, ^{90}Sr, and ^{137}Cs are used to consider transport of these three important nuclides within this document so that the general findings can be publicly related. In addition, these unclassified data are used for much of the sensitivity analysis, again to facilitate understanding of the uncertainties in the calculations.

The decay chains for some of the radionuclides produced by Shoal lead to non-radioactive, but potentially hazardous, elements. For example, ^{63}Ni undergoes beta decay to become stable ^{63}Cu. Given their origin, these daughter products are considered here as part of the radionuclide source. The decay chains considered are given in Appendix 8, and daughter nuclides are included in Table 6.2.

Table 6.1. List of Radionuclides Important for Investigations of Transport from Underground Nuclear Tests, as presented by Smith *et al.* (1995). The MPC listed is the nuclide concentration causing a 4 mrem/yr dose rate per 40 CFR 141.16 (EPA, 1976) and differs from the values given in Smith *et al.* (1995), which were based on proposed regulations.

Nuclide	Half-life (y)	MPC (pCi/L)
^{3}H	12.3	20,000
^{10}Be	1.6×10^{6}	NA*
^{14}C	5730	2000
^{22}Na	2.605	400
^{26}Al	7.3×10^{5}	NA
^{36}Cl	3.01×10^{5}	700
^{39}Ar	269	NA
^{41}Ca	1.03×10^{5}	NA
^{53}Mn	3.7×10^{6}	NA
^{59}Ni	7.6×10^{4}	300
^{60}Co	5.271	100
^{63}Ni	100	50
^{65}Zn	0.66	300
^{79}Se	$\leq 6.5 \times 10^{4}$	NA
^{81}Kr	2.1×10^{5}	NA
^{85}Kr	10.7	NA
^{90}Sr	29.1	8
^{93}Zr	1.5×10^{6}	2000
^{92g}Nb	3.6×10^{7}	NA
^{93m}Nb	16.1	1000
^{94}Nb	2.0×10^{4}	NA
^{93}Mo	~3500	NA
^{98}Tc	4.2×10^{6}	NA
^{99g}Tc	2.13×10^{5}	900
^{106}Ru	1.020	30
^{107}Pd	6.5×10^{6}	NA
^{113m}Cd	14.1	NA
^{121m}Sn	~55	NA
^{125}Sb	2.758	300
^{126}Sn	$\sim 1.0 \times 10^{5}$	NA
^{129}I	1.57×10^{7}	1

Table 6.1. List of Radionuclides Important for Investigations of Transport from Underground Nuclear Tests, as presented by Smith *et al.* (1995) (Continued).

Nuclide	Half-life (y)	MPC (pCi/L)
^{134}Cs	2.065	80
^{135}Cs	2.3×10^{6}	300
^{137}Cs	30.17	200
^{146}Sm	1.03×10^{8}	NA
^{151}Sm	90	1000
^{150}Eu	36	NA
^{152}Eu	13.48	200
^{154}Eu	8.59	60
^{166m}Ho	1.2×10^{3}	90
^{178m}Hf	31	NA
^{186m}Re	2.0×10^{5}	300
^{192m}Ir	24×10^{1}	100
^{193}Pt	60	3000
^{205}Pb	1.5×10^{7}	NA
^{210}Pb	22.3	0.3
^{231}Pa	3.28×10^{4}	NA
^{232}Th	1.40×10^{10}	3
^{232}U	70	90
^{233}U	1.592×10^{5}	90
^{234}U	2.46×10^{5}	90
^{235}U	7.04×10^{8}	90
^{236}U	2.342×10^{7}	90
^{238}U	4.47×10^{9}	100
^{237}Np	2.14×10^{6}	5
^{238}Pu	87.7	8
^{239}Pu	2.410×10^{4}	8
^{240}Pu	6.56×10^{3}	8
^{241}Pu	14.4	300
^{242}Pu	3.75×10^{5}	8
^{241}Am	432.7	10
^{243}Am	7.37×10^{3}	6
^{244}Cm	18.1	10

*NA indicates that 168-hour data are not available in NBS Handbook 69 (U.S. Dept. of Commerce, 1963) for calculating EPA maximum contaminant level per 40 CFR 141.16

Table 6.2. Daughter Products Generated by Radionuclides in Table 6.1. This list does not include daughters produced by parents with a half-life of 10,000 years or greater, nor gaseous daughters.

Nuclide	Half-life (y)	MPC (pCi/L)
^{39}K	stable	
^{63}Cu	stable	
^{85}Rb	stable	
^{90}Y	7.3×10^{-3}	60
^{90}Zr	stable	
^{113}In	stable	
^{121}Sb	stable	
^{134}Ba	stable	
^{137}Ba	stable	
^{151}Eu	stable	
^{150}Sm	stable	
^{152}Gd	1×10^{14}	NA
^{154}Gd	stable	
^{166}Er	stable	
^{228}Th	1.9	10
^{208}Pb	stable	
^{239}Np	5.5×10^{-3}	300

The total radiologic source term for Shoal is not equally available for transport by groundwater. The term "hydrologic source term" (Smith *et al.*, 1995) is used to denote the radioactive material that is dissolved in or available for transport by groundwater, and is considered to be considerably less than the total radiologic source term. The absence of some nuclides of the radiologic source from the hydrologic source term is a result of their release and retardation properties. Both release and retardation are considered in the calculations performed here, so that the total radionuclide source is the source used.

6.1.2 Non-radionuclide Hazardous Materials

The design and implementation of the Shoal experiment was relatively simple, as compared to many tests at the NTS. The objective of the experiment was to detonate a nuclear device in an active seismic area and compare resultant seismic signals with those from earthquakes of the same energy range (U.S. AEC, 1964), and as such, the primary instrumentation involved seismic stations at the land surface. In addition, the device was emplaced in a short drill hole located at the end of a mined shaft-drift complex (Figure 3.2). The result is that no test rack or underground diagnostic instruments (except for a few geophones and cable for them and the firing) were apparently used for Shoal (U.S. AEC, 1964). Stemming of the shaft and drift was accomplished with sand. The emplacement hole was completely filled with sand (Beers, 1964) and the zero room was filled with bagged sand. Five other sand plugs were placed in the drift by filling bulk sand between bulkheads made from plywood, or stacking sand bags (U.S. AEC, 1964). A final filter plug was also installed at the base of the shaft and consisted of 30 m (100 ft) of loose sand poured on top of a bulkhead installed 40 ft up the shaft from the floor of the drift. One photograph also makes note of the presence of bags of vermiculite around some of the geophone terminal boxes (U.S. AEC, 1964, Figure 27).

One ancillary experiment was conducted with the Shoal test and involved evaluating the exposure of minerals and other substances to high-pressure shock waves (Schilling, 1965). Material samples were placed in canisters and emplaced in holes ranging from 9 to 100 m (30 to 329 ft) from the detonation point. A total of nine emplacement locations were used (eight holes and one cannister within one of the sand plugs), which contained a total of 53 canisters. The samples and canisters came from three different organizations: Nevada Bureau of Mines, Pennsylvania State University, and Richfield Oil. Though there were some differences between the canisters used by each group, they were predominantly composed of steel and ranged in length from 6.35 cm to 24.13 cm (2-1/2 in to 9-1/2 in) and up to 7.0 cm (2-3/4 in) in diameter. All of the canisters from the Nevada Bureau of Mines, and three Pennsylvania State University canisters contained rock and mineral samples (*e.g.*, feldspar, granite, biotite, gypsum, quartz, basalt, limestone, sandstone, coal, graphite). Two of those Pennsylvania State canisters also contained samples of carbon disulfide. Another two Pennsylvania State canisters contained rock and mineral samples, along with a variety of chemical compounds (primarily oxides and silicates). The Richfield canisters contained oil sand (19 canisters), extracted oil (8 canisters), n-octane (5 canisters), n-butylbenzene (3 canisters), and octane-2 (2 canisters). The volume of hydrocarbons emplaced in the Richfield canisters was small. They all used the Type A cannister design, and were poured in after the cannister was filled with silica sand. Assuming the sand porosity was 0.4, the volume of hydrocarbon in each cannister was approximately 12 cm^3 (from a total volume of 29 cm^3). The total volume of liquid hydrocarbons emplaced was thus approximately 216 cm^3 (18 liquid hydrocarbon samples), or 0.2 liters. The samples were never recovered for analysis because the planned shaft and drift re-entry did not occur.

Given the very small volumes of potentially hazardous non-radioactive materials that were included in the Shoal test, they are not considered as a contaminant source in this modeling effort.

6.2 Release Functions

Radionuclides produced by an underground nuclear test are present in three basic forms: gases, surface deposits, and volume deposits (Smith *et al.*, 1995), the proportions of which can change with time after the detonation. Immediately after the detonation, essentially all of the radionuclides are part of a superheated, expanding gas (Borg *et al.*, 1976). When the temperature and pressure start to drop, many of the gases condense. The condensation occurs based on the boiling point of the nuclide, with the higher-boiling points (first to condense) referred to as refractory nuclides, and the lower-boiling point species referred to as volatile. A high percentage of the refractory species are trapped in the solidifying melt, much of which collects at the base of the cavity as "puddle glass." These are the volume deposits, whose release is controlled by dissolution of this glass.

Nuclides with somewhat lower boiling points remain volatile longer and are able to migrate upward through cracks in the rubble chimney (*e.g.*, Cl, I). Some portion of these are included within the solidifying puddle glass, but a portion is also deposited as coatings on chimney rubble surfaces. Nuclides included in these surface deposits can be released by relatively rapid processes such as ion exchange, as well as by dissolution, and thus the surface deposits are more susceptible to leaching than the radionuclides that are volume deposited. Ion exchange and dissolution of these surface coatings are dependent upon the mineralogy of the precipitates and their controlling thermodynamics. The specific form that these surface deposits take at Shoal is unknown, and even if it were, it is unlikely that thermodynamic data are available for some of the uncommon forms, much less definition of the transient temperature and pressure conditions under which the reactions will occur. For these reasons, no attempt was made to formulate a geochemical release function for the surface deposited radionuclides. Rather, it was assumed that the surface deposits were immediately dissolved upon contact with groundwater and available for migration through the groundwater system. This assumption results in an overestimation of the availability of the surface-deposited radionuclides for transport, as the dissolution and exchange processes described above may be considerably smaller in magnitude and slower in occurrence than modeled. With no geochemical component to the release, the migration from the cavity of the surface-deposited nuclides is governed by the "hydraulic release." The hydraulic release defines the process of re-equilibration of the hydraulic head within the cavity (recovery to static water level from the depressed condition caused by the test), as well as flushing of contaminants from the cavity by the flow-through of groundwater.

Some of the radionuclides produced remain in gaseous form (*e.g.*, Kr and Xe) and may be incorporated in solidifying phases, dissolved in groundwater, or escape the saturated zone to migrate through the unsaturated section. That portion dissolved in groundwater will migrate as controlled by the hydraulic release described above. Other nuclides are gaseous, but then decay to a non-gaseous nuclide. In these cases, the preceding decay chain behavior is an important control on the distribution and release of daughter nuclides. For example, both ^{137}Cs and ^{90}Sr can be found in surface deposits throughout the chimney, as well as in the puddle glass, because of gaseous precursors. Prompt injection is another release process that may transport gaseous species under early cavity conditions. Gaseous tritium and strontium and cesium precursors may be forced several

cavity radii away from the detonation point through explosion-induced fractures arranged radially away from ground zero (Smith, 1995). It is uncertain whether refractory species are transported by prompt injection.

Several of the processes described above require elaboration to understand how they were implemented in the transport analysis. Following are additional discussions of the apportioning of radionuclides between volume and surface deposits, the hydraulic release function, nuclear melt glass dissolution, and prompt injection.

6.2.1 Volume/Surface Mode Designation

Refractory and volatile behavior designations for the Shoal radionuclides were culled from literature references (Borg *et al.*, 1976; Borg, 1975; Kersting, 1996; Smith, 1995) whenever possible. For those nuclides with no specific literature reference, volatilities of oxides (Bedford and Jackson, 1965; Krikorian, 1981) and melting point temperatures were used to assign a behavior consistent with the volatilities and melting points of known refractory and volatile nuclides.

A small proportion of nuclear melt glass is not incorporated in the bottom puddle, but is distributed through the collapsing chimney as a result of splashes caused by blocks of granite falling into the puddle, or as fine droplets entrained with escaping cavity gases (Smith, 1995). The exact amount distributed in this way at Shoal is not known. Based on broad experience at Lawrence Livermore National Laboratory examining glass samples from underground testing, Borg (1975) estimates that at most, only two to three percent of refractories are lost from good puddle glass. Rabb (1970) found that isotopes other than ^{137}Cs, ^{125}Sb, $^{95}Zr/^{95}Nb$, ^{147}Pm, and ^{185}W were 95 percent or more in the glass with the remainder elsewhere for the Piledriver test. Based on this information, it is assumed here that five percent of the total mass of even the refractory species is lost from the puddle glass. Thus, the designated refractory radionuclides have 5 percent of their mass considered surface deposited, with the remaining 95 percent volume deposited (Table 6.3).

Table 6.3. Release Functions Assigned to Shoal Source Term Nuclides, based on Literature References Described in the Text.

Element	Hydraulic Release	Volume (Glass) Release
H	100%	0%
C	100%	0%
Al	5%	95%
Cl	50%	50%
Ar	100%	0%
K	50%	50%
Ca	5%	95%
Ni	5%	95%
Kr	100%	0%
Sr	40%	60%
Zr	5%	95%

Table 6.3. Release Functions Assigned to Shoal Source Term Nuclides, based on Literature References Described in the Text (Continued).

Element	Hydraulic Release	Volume (Glass) Release
Nb	5%	95%
Tc	5%	95%
Pd	5%	95%
Cd	80%	20%
Sn	80%	20%
I	50%	50%
Cs	80%	20%
Sm	5%	95%
Eu	5%	95%
Ho	5%	95%
Th	5%	95%
U	5%	95%
Np	5%	95%
Pu	5%	95%
Am	5%	95%

Two nuclear experiments have been conducted in granite where the apportioning of ^{90}Sr and ^{137}Cs was investigated (Borg *et al.*, 1976). The Piledriver test, conducted in granodiorite at the NTS, investigated the vertical distribution of the isotopes in nuclear melt glass (an early bulk estimate of the ^{137}Cs distribution estimated 12 percent in the melt, no data on ^{90}Sr were given; Rabb, 1970). At the lowest sampling depth, the amount of ^{137}Cs was about 0.6 times what it would be if it had been homogeneously distributed in the glass (Borg, 1975). This value increased to 0.76 and 1.5 times at higher locations. ^{90}Sr varied from 1.0 times at the middle sampling location to 1.35 at the highest level (no data collected at the lowest level). These findings were part of the basis for understanding the impact of volatile precursors on radionuclide distribution. Based on all of their data, the French experiments in the Hoggar granite resulted in estimates of 0.2 times the ^{137}Cs in their glass samples and 0.4 to 0.8 times the ^{90}Sr (Van Kote and Balard, 1972, as reported by Borg, 1975 and Borg *et al.*, 1976).

The French data are used here as the analog for the Shoal ^{90}Sr and ^{137}Cs distribution. Thus, it is assumed that 20 percent of the ^{137}Cs is contained within the glass puddle and 80 percent is surface deposited through the cavity and chimney, and 60 percent of the ^{90}Sr (the average between the measured French values of 40 and 80 percent) is in the glass puddle and 40 percent is surface deposited. The higher proportion of ^{90}Sr in the glass as compared to ^{137}Cs is consistent with the difference in the half-life of their gaseous precursors. The ^{90}Kr half-life is 33 seconds, whereas the ^{137}Xe half-life is 3.9 minutes, allowing more time for migration of the mass-137 chain to migrate

out of the puddle glass. The intermediate volatility of ^{113m}Cd, ^{121m}Sn, and ^{126}Sn is approximated here by assigning the same volume/surface proportions (20/80) as ^{137}Cs.

The halogens, ^{36}Cl and ^{129}I, can be expected to have volatile behavior in the early time, but there are also natural analogs in the geologic environment whereby halogens are included in volcanic glass. For example, chloride and fluoride are found in trace amounts (less than 1 percent by weight) in a wide variety of volcanic glasses (Hampton and Bailey, 1984). As the steam condenses in the cavity, some of the volatiles will be trapped and incorporated in the glass. It is assumed here that half of the ^{36}Cl and ^{129}I is included in the glass, and half is surface deposited. Similarly, ^{40}K is also assumed to be distributed evenly between the melt and surfaces.

By a similar process, other volatile nuclides are probably entrained in the melt. For example, the French report that more than 50 percent of the available tritium is captured by their glasses (Dupuis, 1970, as reported by Borg, 1975). Borg (1975) reports that only a small (but unquantified) portion of the total tritium produced can be recovered from glasses of tests conducted in saturated alluvium and tuff. At Piledriver, Borg (1975) estimates that 1.53 g of a total 1.8 g produced by activation was contained in the melt, but notes that this was considerably less than the total tritium available. Given these uncertainties and the importance of tritium to the transport calculations, no incorporation in the melt glass is assumed here. The size of the carbon dioxide molecule can limit its inclusion in volcanic glasses, (though carbon monoxide may dissolve; Hampton and Bailey, 1984), and krypton and argon are noncondensable, so these nuclides are also considered subject only to the hydraulic release function.

6.2.2 Cavity Infill Analysis

It is well established that nuclear cavities and chimneys are dewatered and subsequently refilled, though the process through which the dewatering occurs in largely inferred (Borg *et al.*, 1976). Within the cavity itself, the depressed water levels probably result from thermal and compressional forces generated by the nuclear reaction. Dewatering of the chimney area is probably additionally related to bulking caused by the collapse, which creates a region with substantially greater porosity than that of the surrounding rock. This is particularly true at Shoal, where the fractured granite has a very low estimated porosity (see Section 5.5.5). The effect of the rapid porosity increase is to desaturate the material. Following the desaturation immediately after the test, the cavity and chimney will infill with groundwater flowing radially from the surrounding saturated rock.

The postshot drilling data indicate that these processes occurred at Shoal. Geophysical logging of postshot hole PS #1 indicated the presence of a chimney with a height of 108.5 m above the shot point (Hazelton-Nuclear Science, 1965). PS #1 was completed as a hydrologic observation well to monitor chimney infill, though casing constrictions and other apparent obstructions prevented access to the lower portion of the well (below a depth of 377 m). No standing water could be confirmed in the chimney by observations through 1964. On June 28, 1965, a possible water level was detected at a depth of 369 ± 2 m (approximate elevation of 1226 m) (Hazelton-Nuclear Science, 1965). No subsequent measurements have been found, but Hazelton-Nuclear Science (1965)

concluded that infill to 1965 had been very small and calculated that total infill and granite aquifer re-equilibration was not expected for at least 10 years after the detonation.

Calculations of chimney infill time require estimates of the chimney porosity. The bulking porosity of a chimney can be inferred using geometric considerations, if it is assumed that the maximum void space within the chimney is equal to the cavity volume (Borg *et al.*, 1976). Assuming a cylindrical chimney with hemispherical ends, the distributed porosity would be

$$B = \frac{\frac{4}{3}\pi r_c^3}{\frac{4}{3}\pi r_c^3 + h_c \pi r_c^2} \tag{6.1}$$

where h_c is the chimney height, r_c is the cavity radius, and B is the bulking porosity. At Shoal, the chimney height is reported as 108.5 m and the cavity radius is 26 m (Hazelton-Nuclear Science, 1965), leading to a bulking porosity of 24 percent. This value is consistent with the range of 18 to 35 percent reported for B for competent rocks such as granite, basalt, and indurated tuffs (Borg *et al.*, 1976). The porosity of the granite aquifer was estimated to be 0.006 (see Section 5.5.5).

Hazleton-Nuclear Science (1965) estimated the cavity infill time after detonation. Their analysis required the assumption of a homogeneous and isotropic aquifer. They used analytical expressions to calculate the infill after a depression in the water table surrounding the detonation. They estimated the total infill time to be on the order of 10 - 11 years, which included an assumed 80 to 100 days to fill up the drift complex.

The numerical groundwater model (see Section 5.0) was used to develop an independent estimate of infill time based on the newly acquired hydraulic information. Although the groundwater model is stochastic in nature, the model was used deterministically by using one realization of the equiprobable hydraulic conductivity field to predict the infill time. All boundary conditions and model parameters used in this analysis are the same as specified in the previous section. Additional parameters were required to simulate the transient recovery of water into the cavity area. The specific yield of both the cavity and the granitic aquifer were assumed to be 0.24 and 0.006, respectively. The initial water table elevations following the detonation were digitized from the hypothetical postshot potentiometric surface generated in University of Nevada (1965, Figure 17c) (Figure 6.1). The model was used to simulate the recovery of the water table and the recovery time was assumed to be the time at which the water level in the cavity region was 95 percent of the simulated steady-state value.

The water level in the cavity reaches 95 percent of the equilibrium value after 11.5 years. This value is in general agreement with the infill analysis of Hazelton-Nuclear Science (1965). For the purposes of solute transport modeling, it was assumed that no transport occurred until the water levels were within 95 percent of the equilibrium value or 11.5 years after detonation. Chemical diffusion does occur during this initial time frame, but its impact on solute transport is minimal.

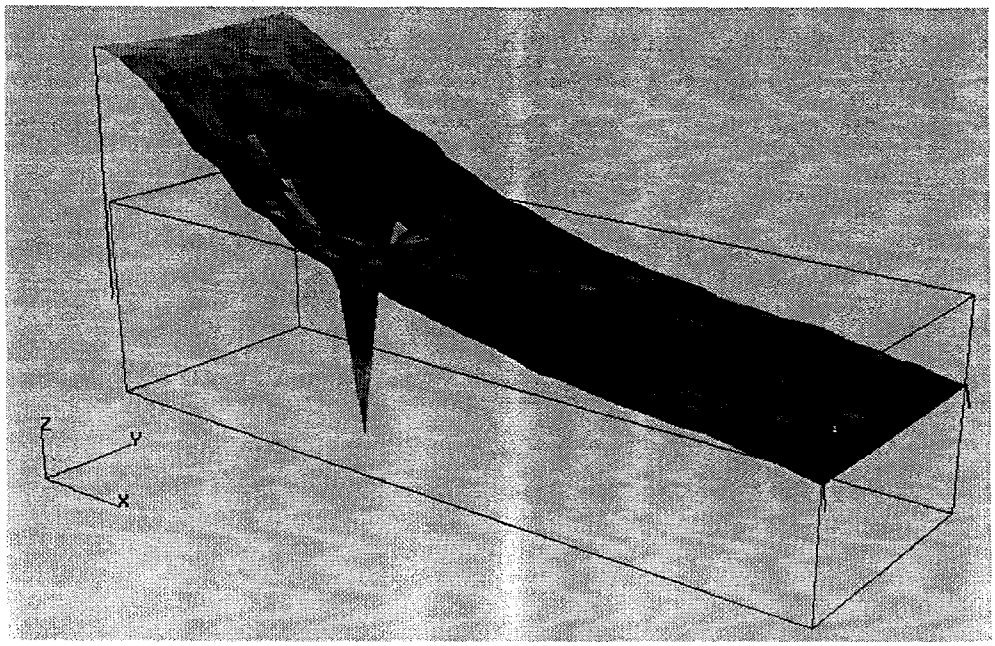

Figure 6.1. The initial water table shape following detonation. These water table elevations were generated from University of Nevada, 1965, Figure 17c. (Note: the water levels are vertically exaggerated.)

6.2.3 Nuclear Melt Glass Dissolution

The rock, fission products, and device components that are vaporized by the tremendous heat and pressure of a nuclear reaction quickly begin to condense and coalesce into nuclear melt glass. This glass (a solid with no crystalline structure) contains much of the radioactivity produced by a nuclear test. Radionuclides must be removed from the melt glass to be transported by groundwater.

Several leaching experiments have been performed with nuclear melt glass. Essington and Sharp (1968) and Wolfsberg (1978) performed static leaching experiments and Ramspott *et al.* (1979) and Failor *et al.* (1983) report on single-pass leaching experiments. All of these studies are summarized by Smith (1993). Essington and Sharp (1968) report on the concentrations of gross alpha and beta activity leached from nuclear glass samples for a variety of size fractions. Wolfsberg (1978) reports the fraction leached per day of about 20 radionuclides (depending on sample grade) from both refractory and volatile samples. Ramspott *et al.* (1979) report the fraction leached per day per surface area of 19 radionuclides. Failor *et al.* (1983) reported leach rates in grams of glass per day per surface area for 13 radionuclides at both slow and fast flow-through rates, for samples with particle sizes less than 150 microns.

There are several significant problems with applying the results from the nuclear melt glass leaching experiments to the problem of predicting release from a true cavity glass. These include disparity in particle sizes between generally finely ground experimental samples and *in situ* glass, continually declining dissolution rates through the experimental life, isotope-specific rates for only some of the radionuclides of concern, and insufficient data reporting to derive general leaching rates

(*e.g.*, on a specific-surface-area basis). Some of the experiments show that leaching rates increase with decreasing particle size, and Essington and Sharp (1968) conclude that glass particles smaller than about 250 microns possess high specific surface area and chemical reactivity that are unlike those of nuclear melt glass *in situ*.

Rather than using nuclear melt glass experimental data, the release of radionuclides from volume-deposited radionuclides at Shoal is calculated based on dissolution rates measured for volcanic glass. Volcanic glass dissolution in contact with natural waters has been studied experimentally and reported in the scientific literature. The bulk composition of volcanic glass and analyzed nuclear melt glass is similar (Table 6.4). Though there is no elemental analysis of melt glass created by the Shoal test, there is no appreciable migration of major elements from a cavity region, so that nuclear melt glass tends to resemble the bulk rock composition (Schwartz *et al.*, 1984). The elemental composition of the Shoal granite is dominated by SiO_2 and Al_2O_3 (Table 6.4). It is assumed that the radionuclide components of the glass will be released as the glass dissolves in bulk, ignoring any intra-glass diffusion that might result in variations in leaching rates from one species to another. This can be considered as etching of the glass, where the structure is broken down, rather than leaching of individual components (Adams, 1984).

Table 6.4. Comparison Between Chemical Composition of Natural Volcanic Glass and Nuclear Melt Glass. Major and trace element composition in terms of oxides, given as weight percents. Parentheses contain standard deviations, when available.

	SiO_2	Al_2O_3	FeO	MgO	CaO	Na_2O	K_2O
Perlite*	74.2	14.1	0.15	0.49	1.0	4.0	4.8
Obsidian*	76.0	13.8	0.40	0.011	0.21	4.4	4.5
Trachytic*	62.8	15.2	1.3	0.38	1.1	8.4	5.1
Nuclear Melt Glass†	73.1 (4.9)	14.2 (2.5)	1.18 (1.59)	0.22 (0.27)	1.06 (0.86)	3.49 (1.68)	6.6 (4.2)
Shoal granite**	68.78 (1.07)	14.96 (0.35)	2.35† (0.25)	0.43***	2.61 (0.23)	4.77***	3.12 (0.36)

*Glassy volcanic rocks, as reported by White (1983)
† Average of six nuclear melt glass samples, as reported by Smith (1995)
**Average of 34 Shoal granite samples obtained at 50 ft intervals in borehole ECH-D (University of Nevada, 1965)
†Fe_2O_3 rather than FeO
***Analysis from Appendix 7

Dissolution of glass under the geochemical conditions found at Shoal is expected based on thermodynamic considerations. The log of the ion activity product to the equilibrium constant (log IAP/K_T) for amorphous silica ranges from -0.68 to -0.62 for groundwaters sampled from the Sand Springs Range at the site, indicating that under equilibrium conditions, silica glass will dissolve in contact with groundwater. Calculating the glass dissolution rate requires selecting an appropriate rate equation, and selecting appropriate values for the rate constant and specific surface area. These factors are discussed below, followed by a discussion of the resulting dissolution rate.

6.2.3.1 Dissolution Rate Equation

Kinetics experiments regarding the dissolution of silicates have fit either a parabolic or linear rate law (White, 1983):

$$\begin{aligned} \textit{parabolic rate equation:}\ & Q = Q_0 + k_p t^{1/2} \\ \textit{linear rate equation:}\ & Q = Q_0 + k_l t \end{aligned} \qquad (6.2)$$

where Q is the mass transfer of a chemical species into aqueous solution per unit surface area of solid (moles/cm^2), Q_0 is the initial surface ion exchange (moles/cm^2), k is either the linear or parabolic rate constant (mole/cm^{2}s or moles/cm^{2}s$^{1/2}$), and t is time (s). White (1983) found that the release of Na and K best fit the parabolic rate equation, while the release of Si and Al was best described by a linear rate. One of the principal reasons for using a volcanic glass dissolution analog is the lack of ion-specific dissolution data for many radionuclides, so the cation-specific rates were not considered. Rather, the dissolution of the glass matrix, composed principally of silica and alumina, is needed, with the assumption that the associated trace components would be released to solution as the glass matrix dissolves around them. As such, the linear rate equation was selected, and results in more rapid release than the parabolic function.

6.2.3.2 Dissolution Rate Constant

The linear rate constant, k_l, used was the rate experimentally derived by White (1983) for an obsidian sample in contact with a water of pH 6.23 (experiment O-2). This value was 0.87 x 10^{-15} moles/cm^{2}s. The associated initial surface exchange value, Q_0, was 0.13 x 10^{-9} moles/cm^2. There was relatively little variation in White's experiments in the k_l values within the generally neutral pH range. Higher rates are observed in experiments with low pH. A compilation of data from water samples collected from nuclear cavities and near cavities (Smith *et al.*, 1997) indicates pH values near neutral to slightly basic, consistent with regional groundwater in the testing areas.

Teng and Grandstaff (1994) report that the loss of Na, Ca, and Mg from glass from the Kilauea volcano, at a pH of 6.5, and k_l of 0.76 x 10^{-15} moles/cm^{2}s was representative of the overall glass dissolution rate. Gislason and Eugster (1987a) found rates varying from 10^{-13} to 10^{-16} moles/cm^{2}sec for Na, K, F, Ca, Mg, Si, and S at pH values greater than 9, for dissolution from a basaltic glass. In their application to a field site in Iceland, Gislason and Eugster (1987b) used the rate for Na of 1.5 x 10^{-15} moles/cm^{2}s. The Hawaii and Iceland samples represent low silicate glasses (49 to 57 percent SiO_2) that are chemically less similar to the nuclear melt glass composition than the volcanic glasses investigated by White (1983). There is a general decrease in glass solubility with increasing SiO_2 content (Glass, 1984).

6.2.3.3 Specific Surface Area

The dissolution rate constant is given on a per unit surface area basis. Experimental work typically measures the specific surface area with a technique such as the Brunauer-Emmet-Teller (BET) method of gas adsorption. Wolfsberg (1978) reported surface areas ranging from 0.63 to 16.5 m^2/g for test debris that had been ground to a powder with particle sizes less than 150 micrometers

(μm). He also used particles between 2 and 5 mm in size for a few experiments, but did not report the surface area of those pieces. Failor *et al.* (1983) also ground their samples and used particle sizes less than 150 μm. They present surface areas measured using BET and calculated from geometric and density considerations. The BET measurements for three different nuclear melt glasses ranged from 0.396 to 0.465 m^2/g, while the geometric surface area ranged from 0.031 to 0.033 m^2/g.

Essington and Sharp (1968) evaluated the relationship between specific surface area and particle size for nuclear glass samples, also using BET. They used glass from the Rainier underground nuclear test and evaluated eight size fractions from zero to 16,000 μm. They found a progressive increase in specific surface area as particle size decreases (Figure 6.2), as well as a positive relationship between surface area of radioactive glass particles and radioactivity in equilibrated water. For particle sizes greater than 1000 μm, the specific surface areas are relatively constant. This constant relationship indicates that the measured surfaces were internal surfaces (Essington and Sharp, 1968), perhaps interconnected micro-fractures and vesicles, rather than external surfaces that depend on particle size and shape. They also found that the specific surface decreased after the samples were equilibrated with groundwater, perhaps due to blocking of internal pores by reaction products.

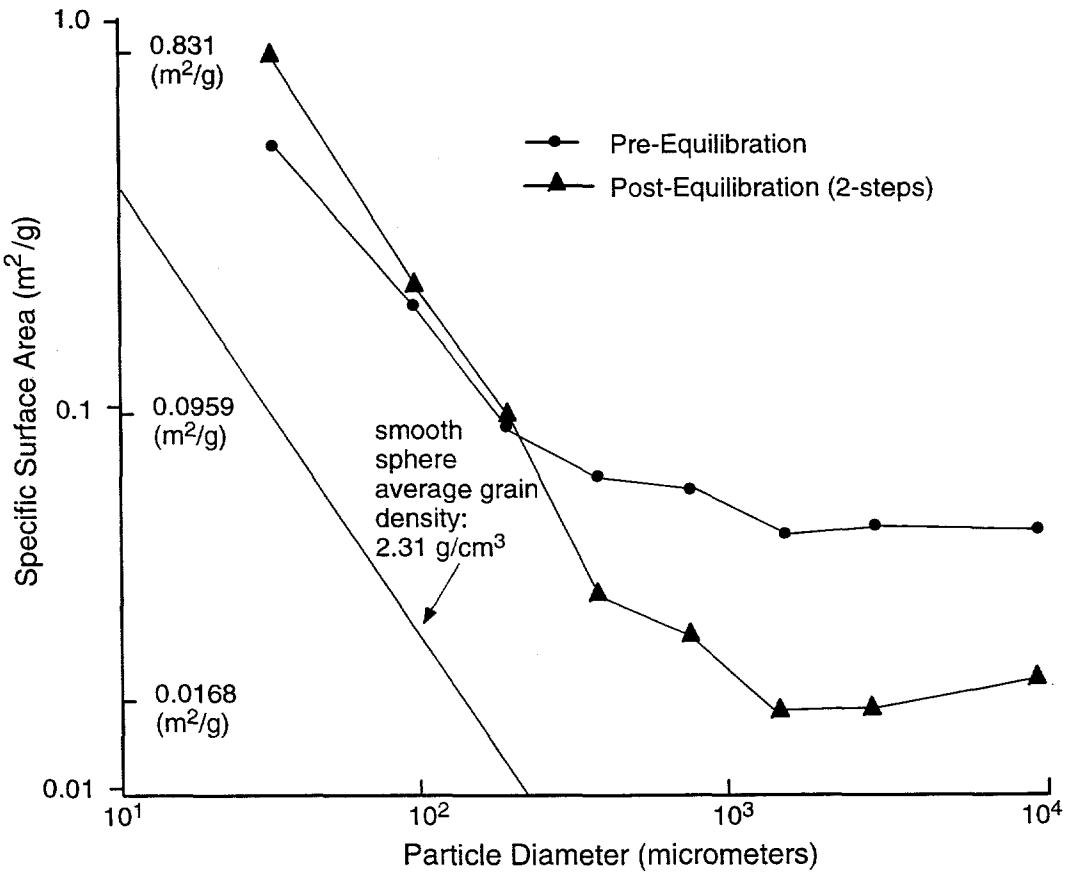

Figure 6.2 Relationship of specific surface area of Rainier nuclear melt glass to particle size (adapted from Essington and Sharpe, 1968).

The specific surface area of Rainier glass *in situ* was estimated by Essington and Sharp (1968) to be equivalent to large particles of glass, on the order of centimeters to meters in dimension. They believed that the constant specific surface area of their larger experimental fractions could be reasonably extended to such larger particle sizes.

Using the estimate of 700 metric tons of rock melted for every kiloton of explosive detonated (Smith, 1993), and the 12.5 kiloton possible yield (Hazelton-Nuclear Science, 1965), the Shoal test produced 8750 metric tons of glass. The French Hoggar granite tests estimated a larger melt production of 1300 metric tons/kiloton (Borg, 1975), but the dissolution calculations are not sensitive to the mass of glass produced because the reaction rates are controlled by surface area, not mass. Postshot drilling located the bulk of the Shoal explosion melt at the base of the chimney and found it to be about 10 meters thick (Hazelton-Nuclear Science, 1965). This implies a very massive glass body that, based solely on geometric considerations, would have a very small specific surface area (on the order of 10^{-6} m^2/g).

There is abundant evidence from other nuclear tests that nuclear melt glass does not solidify as such a cohesive, uniform mass. Rather, it is very heterogeneous and includes blocks of overlying rock that fall into it during chimney formation, and in fact help quench the melt. Melt glass is often noted as being highly vesiculated, presumably as a result of the loss of steam and other gases during cooling (Borg, 1975; Borg *et al.*, 1976). Three glass types were identified for the Rainier nuclear test: a dense, dark glass, high in radioactivity; a light-colored glass, variably vesicular with low radioactivity; and, a highly radioactive dense form found as globules, blebs, smears and coatings along fracture surfaces and drift walls (Schwartz *et al.*, 1984). Glass has also been found outside of explosion cavities. An injected glass seam was found in a fissure between the top of sand stemming and the granite back of the tunnel 2.3 cavity radii from the Piledriver test (Rabb, 1970). Additional seams were also found nearby in the walls of a bypass drift (Borg, 1975). The glass was believed to have been injected during the first two minutes after the explosion along a family of steeply dipping shear zones.

The *in situ* specific surface area of the Shoal nuclear melt glass lies somewhere between the very low surface area projected for the general geometry of the puddle glass and the very high values obtained for finely ground samples from other tests. With a melt thickness of 10 meters, there are undoubtedly large masses of melt that are protected from surface reactions with groundwater. It is also expected that isolated splashes, seams and blebs of glass occur, as well as vesiculated and fractured glass masses that allow contact of groundwater with a greater surface area. The relatively constant specific surface area determined by Essington and Sharp (1968) for the glass fraction above 1000 μm, was selected to conservatively approximate the Shoal melt glass specific surface area. The value used, 0.05 m^2/g, represents the surface area measured pre-equilibration in their experiments (the post-equilibration value was approximately 0.01 m^2/g).

Recent work evaluating the melt glass produced by the Cambric event (W. Bourcier, personal communication, 1998) applied studies of nuclear waste glass surface area to postulate much lower values of specific surface area (approximately 5.2×10^{-5} m^2/g) than that used here. These lower

surface areas, with resultant much slower glass dissolution rates, are used in a sensitivity analysis to determine the impact on transport behavior of this highly uncertain parameter.

6.2.3.4 Dissolution Rate for Shoal Nuclear Melt Glass

The dissolution of radionuclide-bearing glass created by the Shoal test was modeled after the dissolution of volcanic glass using the linear rate equation, a rate constant of 0.87×10^{-15} moles/cm^{2}s, an initial surface exchange of 0.13×10^{-9} moles/cm^2, a specific surface area of 0.05 m^2/g, an initial glass mass of 8750 metric tons, a glass gram formula weight of 60 g/mole, and a glass density of 2.65 g/cm^3. The corresponding release coefficient (the product of the specific surface area and the dissolution rate constant) is 2.3×10^{-6} days^{-1}. The dissolution was calculated iteratively to account for the continual reduction in dissolution as the surface area is reduced. At each time step (of ten years), the amount of dissolution is calculated. That lost mass is then subtracted from the initial mass of that time step to determine the new total mass and related specific surface area to use to determine the amount of mass lost in the next time step. This calculation assumes adequate flow of groundwater such that saturation with amorphous silica is not reached in the water.

Using these parameter values, approximately 2800 years are required to dissolve 90 percent of the glass mass (Figure 6.3). The relationship between the reducing surface area and mass dissolved results in an exponential function, so that most of the mass is lost in early time (50 percent lost in 800 years) with a trailing tail in later years. This predicted timeframe for dissolution is very rapid compared to the history of natural glasses, such as obsidians, basalts, and tektites, which are millions of years old (Jantzen and Plodinec (1984), and even man-made glasses, which have survived for 3500 years (Adams, 1984). It is likely that the dissolution calculations overpredict the process because rate-reducing processes have been neglected, *e.g.*, protection of the glass mass from additional dissolution by the formation of a mantle of reaction products (clays and zeolites), and reduction in internal surface area as interstices are clogged by reaction products (as found in the reduced post-reaction surface area measured by Essington and Sharp, 1965). Using the post-reaction surface area they measured, 0.0168 m^2/g, increases the time to 2500 years for the dissolution of half of the glass mass (and 8500 years for 90 percent). Using the surface area estimate generated for Cambric, 5.2×10^{-5} m^2/g (Bourcier, personal communication, 1998), dissolution of half the glass mass requires almost 900,000 years. The dissolution calculation based on 0.05 m^2/g (shown by the solid line in Figure 6.3) is used as the basis for release of radionuclides for the transport modeling.

6.3 Retardation

Radionuclides that are dissolved in groundwater at Shoal and available for transport are subject to a variety of physical and chemical reactions that can retard their movement relative to the movement of the water. Together, these processes are referred to as retardation and include ion exchange, adsorption, hydrolysis, complexation, and mineral precipitation. The data necessary to consider these individual reactions are not available for most field locations, and Shoal is no exception. Rather, a bulk sorption approach is used here to approximate retardation processes. Only overall partitioning controlled by equilibrium is considered. It should be remembered that kinetic processes, particularly diffusion, can be important in controlling the rate of other retardation

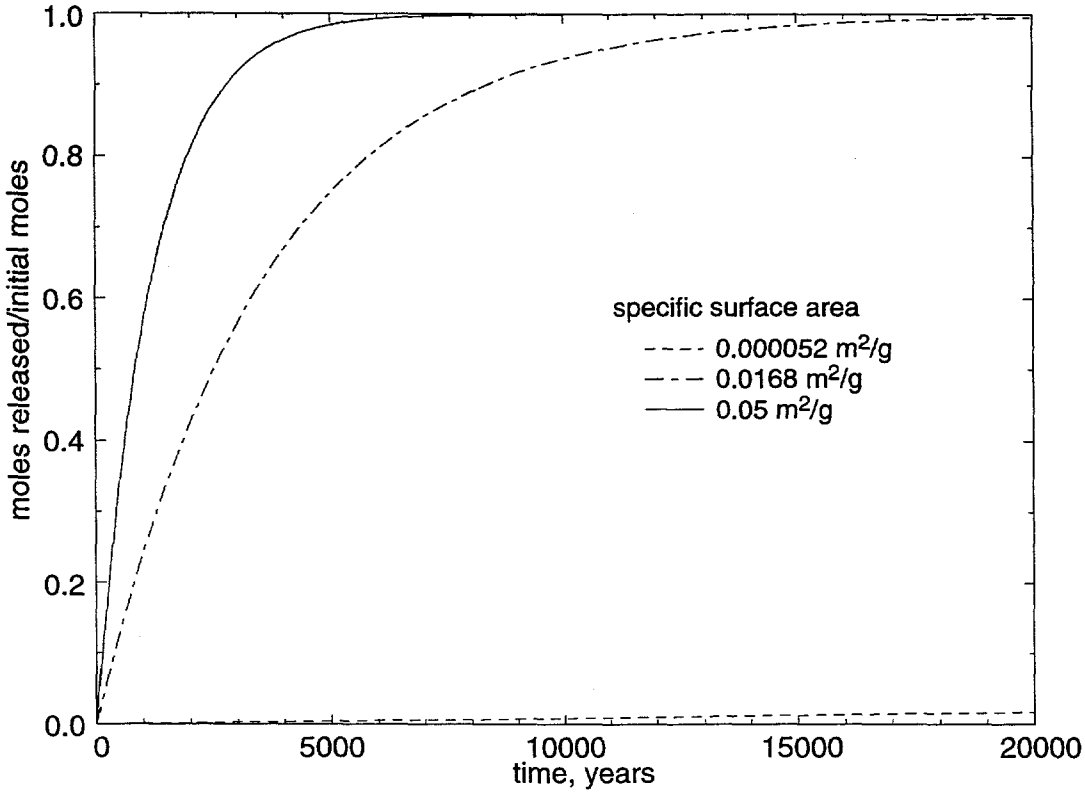

Figure 6.3. Dissolution of Shoal nuclear melt glass, assuming an analog to volcanic glass dissolution, using the parameters described in the text. Also shown are sensitivity calculations for other assumptions of specific surface area. Half of the starting mass is dissolved within approximately 800 years for the base-case estimate of surface area of 0.05 m^2/g. The surface area of 0.0168 m^2/g is the post-reaction surface area measured by Essington and Sharp (1965). Barely visible at the bottom of the graph is the dissolution calculated using a specific surface area of 5.2×10^{-5} m^2/g, the value estimated for the Cambric nuclear melt glass by Bourcier (personal communication, 1998).

processes and may result in additional significant inhibition of radionuclide transport that is not considered here.

The distribution coefficient, K_d, is a measure of partitioning of an ion between the solution and the solid under equilibrium conditions. Many sorption experiments, both batch and column, have been performed on granite materials as a result of interest in radioactive waste disposal in granite terrain (Stenhouse and Pöttinger, 1994; Frick *et al.*, 1991; Werner, 1996; Failor *et al.*, 1982; Beall *et al.*, 1980); unfortunately, by the nature of the reactions being measured, the results are specific to the site mineralogy and hydrochemistry. Values for the distribution coefficient for Sr and Cs in contact with Sand Springs granite are reported by Nork and Fenske (1970) in a compilation of distribution coefficients for varying rock types. They suspended material with a minimum particle diameter of 4000 μm in four parts "deep formation water" for 72 hours. The lack of additional laboratory details (such as pH) limits application of these values to transport calculations. In particular, the specific surface area of the particles is necessary to convert to a surface-related distribution coefficient, K_a, more appropriate for considering sorption on fracture surfaces.

To address the lack of data, equilibrium sorption experiments were conducted using granite from the Shoal site and several types of simulated groundwater. It was impractical to run individual sorption experiments for each of the 26 elements in the source term, plus additional daughter products, especially given the hazardous and controlled nature of many of the elements. Rather, surrogates were identified to approximate the actual source term. Strongly, moderately, and weakly binding cations (lead, cesium, and strontium, respectively) and strongly and weakly binding anions (selenite and chromate, respectively) were evaluated for their affinity for Shoal granite. The laboratory results are summarized below, followed by a discussion of the application of the results to the transport calculations. The details of the sorption experiments may be found in Appendix 7.

6.3.1 Laboratory Results

The adsorbent used in the equilibrium sorption experiments was granite collected from the mining muck pile at the Shoal site. Site restoration work during months immediately preceding sample collection had exposed fresh granite pieces that were mined from the drift and shaft during Project Shoal. The original subsurface position of the collected samples is unknown, but comparison of the characterization results from the muck samples and results from cores analyzed during site characterization in the 1960s indicates that the granite is relatively homogeneous. The granite characterization included x-ray diffraction, solution pH, total carbon and organic carbon, particle size distribution, specific surface area, density, and scanning electron microscopy with energy dispersive x-ray spectroscopy. The detailed results of these analyses can be found in Appendix 7. The granite is comprised of quartz, plagioclase feldspars, chlorite and biotite, with SiO_2 representing the majority of the sample (Table 6.4). In terms of trace elements, the concentrations of Sr (721 ppm) and Zr (418 ppm) were considerable. The granite density was 2.67 g/cm^3. The surface area of the ground fraction used in the experiments (particles passing through a 200-mesh screen (smaller than 75 μm)) was 0.79 m^2/g. The soil solution pH was approximately 8, somewhat high for a granite, but consistent with values measured in groundwater.

The sorption experimental procedures are given in Appendix 7. The experiments typically involved 10 g/L of granite. Most experiments were conducted in a simple 0.01 M $NaNO_3$ matrix, with higher ionic strengths, up to 1.0 M used to investigate the effect of ionic strength on sorption behavior. Three groundwater compositions were also evaluated, HS-1 (ionic strength of 0.0058 M), HC-4 (ionic strength of 0.01 M), and H-2 (ionic strength of 0.6292 M). HC-4 represents groundwater in the immediate test area. HS-1 and H-2 were included to represent water chemistry in potentially downgradient areas to the east and west, respectively. Either lead nitrate ($Pb(NO_3)_2$), cesium nitrate ($CsNO_3$), strontium nitrate ($Sr(NO_3)_2$), potassium chromate (K_2CrO_4), or sodium selenite (Na_2SeO_3) was added as the adsorbate, in concentrations from 10^{-7} to 10^{-4} M. The samples were allowed to equilibrate for 24 hours and the supernatant collected and analyzed to determine the fractional uptake.

Lead displayed a behavior typical of cation sorption on amphoteric oxide surfaces with fractional uptake increasing with increasing pH. Cesium sorption, however, was weakly influenced, if at all, by pH. This indicates the possibility that the sorption of cesium by the granite is not solely

influenced by binding with amphoteric surface sites. For example, the observed cesium uptake may indicate partial sorption on ion-exchange sites of clay minerals present in the granite. Regardless of the particular binding mechanism, the sorption of lead was much stronger than the sorption of cesium by the granite at pH values likely to be encountered in nature. Lead sorption was essentially ionic-strength independent, indicating strong binding and the formation of strong, inner-sphere coordination complexes on the mineral surfaces. Sorption experiments with strontium and the Shoal granite were impossible to perform because of the high strontium content of the rock resulting in significant strontium dissolution (the Sr concentration in the supernatant after equilibration was higher than the Sr concentration added). Similar poor retention of strontium in contact with granite cores from the NTS was found by Failor *et al.* (1982).

Both chromate and selenite displayed behavior typical for anions sorbed on amphoteric oxide surfaces. A maximum in the fractional uptake was usually observed at neutral, or slightly lower, pH. Increased ionic strength tended to increase fractional uptake, attributed to increased screening of the negative oxide surface charge by an increased concentration of positively charged counterions. The effect of ionic strength was not dramatic in most cases.

Using the experimental data, parameters describing both linear and Freundlich isotherms were estimated for a variety of conditions (Table 6.5). Plotting the sorption data as a linear isotherm allows estimation of the distribution coefficient, K_d, a ratio of the mass of sorbate sorbed per mass of sorbent, q_e (g/g), to the concentration of sorbate in equilibrium with the sorbed contaminant, C_e (g/m^3):

$$K_d = \frac{q_e}{C_e} \tag{6.3}$$

The parametric study (involving pH, sorbate concentration, ionic strength, and fluid composition) determined distribution coefficients as a function of these parameters. The linearity of the isotherms was evaluated by estimating parameters for the non-linear Freundlich isotherm:

$$q_e = K_F C_e^{1/n} \tag{6.4}$$

These parameters, K_F and $1/n$, represent the equivalent K_d and the exponent of the equilibrium concentration, respectively. For a linear isotherm, $1/n$ is equal to one.

The results indicate that equilibrium partitioning at the granite-water interface is strongly pH dependent. The linearity of the isotherms was also a function of specific conditions, most notably pH. Under specific conditions, the isotherms were approximately linear, allowing use of a linear isotherm to model equilibrium partitioning. In other cases, there were severe deviations from linearity. In general, the lead and cesium isotherms were more linear than those of the anions.

Table 6.5. Linear and Freundlich Isotherm Parameters.

Ionic Strength (M) or Groundwater Type	pH	K_d (m^3/g)	K_F $(g/g)/(g/m^3)^{1/n}$	1/n (-)
Lead Sorption				
I = 0.01 M	4.0	1.78×10^{-5}	1.85×10^{-5}	0.94
	5.0	4.53×10^{-5}	2.05×10^{-5}	0.74
	6.0	3.56×10^{-4}	1.42×10^{-4}	0.81
	7.0	2.40×10^{-3}	5.44×10^{-4}	0.82
	8.0	9.99×10^{-2}	9.99×10^{-2}	1.00
	9.0	9.99×10^{-2}	9.99×10^{-2}	1.00
HS-1	4.0	4.08×10^{-5}	2.32×10^{-5}	0.87
	5.0	4.49×10^{-5}	1.10×10^{-5}	0.67
	6.0	1.33×10^{-3}	4.67×10^{-4}	0.84
	7.0	9.99×10^{-2}	9.99×10^{-2}	1.00
	8.0	9.99×10^{-2}	9.99×10^{-2}	1.00
	9.0	9.99×10^{-2}	9.99×10^{-2}	1.00
HC-4	6.0	7.33×10^{-4}	2.11×10^{-4}	0.79
	7.0	1.90×10^{-3}	9.30×10^{-3}	0.90
	8.0	4.90×10^{-3}	4.90×10^{-3}	1.00
Chromate Sorption				
I = 0.01 M	4.0	1.00×10^{-4}	2.16×10^{-6}	0.46
	5.0	1.00×10^{-4}	3.96×10^{-6}	0.48
	6.0	9.96×10^{-6}	6.12×10^{-7}	0.35
	7.0	8.89×10^{-6}	4.38×10^{-7}	0.34
	8.0	6.65×10^{-6}	2.53×10^{-7}	0.32
	9.0	5.44×10^{-6}	1.25×10^{-7}	0.28
HS-1	5.0	4.00×10^{-4}	9.53×10^{-6}	0.46
	7.0	1.23×10^{-4}	4.60×10^{-6}	0.46
	8.0	1.79×10^{-5}	2.06×10^{-7}	0.18
	9.0	1.65×10^{-5}	2.15×10^{-7}	0.20
HC-4	9.0	4.25×10^{-6}	2.49×10^{-7}	0.47
Selenite Sorption				
I = 0.01 M	4.0	2.20×10^{-5}	1.46×10^{-5}	0.94
	5.0	3.91×10^{-5}	7.69×10^{-6}	0.78
	6.0	8.20×10^{-5}	4.28×10^{-5}	0.92
	7.0	5.41×10^{-5}	7.06×10^{-6}	0.73
	8.0	2.53×10^{-5}	5.85×10^{-8}	0.25
	9.0	1.39×10^{-5}	1.86×10^{-7}	0.41
HS-1	4.0	2.07×10^{-5}	7.10×10^{-8}	0.23
	5.0	5.38×10^{-5}	8.15×10^{-8}	0.14
	6.0	1.64×10^{-4}	2.31×10^{-6}	0.47
	7.0	1.00×10^{-4}	1.52×10^{-6}	0.46
	8.0	5.66×10^{-5}	5.05×10^{-6}	0.68
	9.0	2.07×10^{-5}	1.27×10^{-6}	0.62
HC-4	4.0	1.51×10^{-5}	6.32×10^{-7}	0.57
	5.0	4.12×10^{-5}	6.17×10^{-7}	0.44
	6.0	2.13×10^{-4}	1.80×10^{-4}	0.98
	7.0	1.00×10^{-4}	2.84×10^{-5}	0.84
	8.0	4.32×10^{-5}	1.89×10^{-6}	0.58
	9.0	2.08×10^{-5}	1.66×10^{-7}	0.34
Cesium Sorption				
HC-4	5.0	3.07×10^{-5}	4.56×10^{-5}	0.85
	6.0	2.75×10^{-5}	3.88×10^{-5}	0.88
	7.0	3.11×10^{-5}	3.62×10^{-5}	0.98
	8.0	4.30×10^{-5}	3.88×10^{-5}	1.07
	9.0	5.46×10^{-5}	4.14×10^{-5}	1.13

6.3.1.1 Limitations

Use of a distribution coefficient to model contaminant partitioning at the mineral-water interface assumes that the isotherm is linear and that sorption is controlled by equilibrium, rather than by kinetics. Use of distribution coefficients without reference to the specific experimental conditions under which they were obtained can also result in significant errors. Use of a linear isotherm imposes limits on the application of the K_d values to conditions similar to those in the experiments. In addition, many of the reactions leading to sorption behavior are strongly pH dependent, and thus require knowledge of pH conditions for application to transport calculations.

The above limitations for using a distribution coefficient approach are not restrictive in the application to Shoal. The lead and cesium isotherms are reasonably linear. The maximum expected lead concentration in solution (as an aqueous $PbCO_3$ species), controlled by lead hydroxide precipitation, is 1.53×10^{-6} m, within the experimental range evaluated. The pH of groundwater within the Sand Springs Range shows little variability (of 12 available pH measurements for groundwater collected from Shoal site wells, three of which are the wells drilled in 1996 and the remainder from the early 1960s, the mean pH is 8.06 with a standard deviation of 0.3). A compilation of data from water samples collected from nuclear cavities and near cavities indicates pH values near neutral to slightly basic, consistent with regional groundwater in the testing areas (Smith *et al.*, 1997).

Batch sorption experiments form the basis of the distribution coefficients reported here because they provide a rapid and economic method of performing parametric studies. However, K_d has been shown to vary with particle size, and new solid-phase surfaces can be created during grinding, both of which can lead to higher batch-derived K_d values than those derived from column studies. For example, sorption of sodium on mylonite (a fracture filling material) was found to be one order of magnitude lower in high-pressure infiltration experiments on core samples, as compared to batch sorption tests (Frick *et al.*, 1991). To some degree, this problem is addressed through the use of a surface-based sorption constant, K_a, to derive the retardation factor (discussed below).

6.3.2 Assignment of Distribution Coefficient

Distribution coefficients were only determined in laboratory tests for the Shoal granite for strontium, cesium, lead, chromate, and selenite. The total radionuclide source (Table 6.4) includes many more elements. Those elements that were not subject to the experiments were assigned K_d values by assuming analogous sorptive behavior to those elements with data. This process required assumptions regarding the likely chemical forms to be found, and obviously includes substantial uncertainty. The resulting sorption assignments are given in Table 6.6.

The laboratory analogue for the weakly binding cation is cesium. The K_d value used was that determined at a pH of 8 for granite in contact with HC-4 groundwater (4.3×10^{-5} m^3/g). The analogue for the strongly binding cation is lead, with a K_d of 4.9×10^{-3} m^3/g. The laboratory analogue for anions is chromium, with a K_d of 2.5×10^{-7} m^3/g. Of the elements assigned a sorption

value, the majority are in the category associated with lead. In comparative studies of laboratory sorption data, lead is generally weaker sorbing, often by an order of magnitude, compared to some of the analogues assigned here (*e.g.*, U, Pu, Np, Am, Th) (Stenhouse and Pottinger, 1994).

Table 6.6. Assignment of Sorption Behavior to Radionuclide Source Elements.

Element	No Sorption	Weakly Sorbing Cation	Strongly Sorbing Cation	Anion Sorbing
H	X			
C	X			
Al	X			
Cl	X			
Ar	X			
K	X			
Ca	X			
Ni		X		
Kr	X			
Sr	X			
Zr			X	
Nb				X
Tc				X
Pd			X	
Cd		X		
Sn		X		
I	X			
Cs		X		
Sm			X	
Eu			X	
Ho			X	
Th			X	
U			X	
Np			X	
Pu			X	
Am			X	

To follow the in-growth of daughters along the decay chains, it is necessary in the modeling process to use the same sorption behavior assigned to the parent for the daughter. In most cases, the expected sorptive properties were similar, but eight daughters are expected to behave differently than the necessary sorption assignment (Table 6.7). Of these, five result in more conservative assignments of K_d (allow less retardation) than expected for the daughter; but in three cases, ^{121}Sb,

^{137}Ba, and ^{134}Ba, these daughters are assigned a retardation equivalent to that of cesium, where very little to no retardation is expected.

Table 6.7. Retardation Coefficients Assigned to Radionuclide Daughter Products that are Contrary to their Expected Transport Behavior. Retardation values were of necessity constant from parent to daughter, resulting variously in over- and under-estimation of sorption for these eight isotopes.

Daughter Isotope	Assigned Retardation	Expected Retardation
Rb-85	1	1.72
In-113	1.72	83.7
Sb-121	1.72	1.0
Ba-137	1.72	1.0
Y-90	1.0	1.72
Zr-90	1.0	83.7
Cu-63	1.72	83.7
Ba-134	1.72	1.0

6.3.3 Calculation of Retardation

The dimensionless retardation factor (R) in fracture flow systems can be represented by the following equation (Freeze and Cherry, 1979; Moreno *et al.*, 1988; Frick *et al.*, 1992):

$$R = 1 + \frac{2K_a}{b} \tag{6.5}$$

where K_a [m] is a surface-based sorption constant ($K_a = K_d/A_{sp}$) and b [m] is the mean fracture aperture. Equation (6.5) is only valid for fractured materials in which the porosity of the solid mass between fractures is insignificant (Freeze and Cherry, 1979).

Tsang (1992) presents three types of fracture aperture calculations, with each being derived from a different process. The three types are b_m, which is the mass balance aperture, b_l, the frictional loss aperture, and b_c, the cubic law aperture. Tsang (1992) showed that in general, $b_m >> b_c >> b_l$. For purposes of the estimation of a retardation calculation, Selroos (1996) suggests that b_l is the most appropriate. There are various methods to estimate b_l, so two independent methods were used to calculate b_l. The b_c was estimated to ensure that the order relations found by Tsang (1992) are found with the Shoal data.

Shapiro and Nicholas (1989) give the following relationship between transmissivity and b_l:

$$b_l = \left[\frac{12T\nu}{g}\right]^{1/3} \tag{6.6}$$

where g is gravitational acceleration [m/s^2], ν is the kinematic viscosity of water [m^2/s] and T is the mean aquifer transmissivity [m^2/day]. Equation (6.6) was used with the aquifer test data and the Shoal groundwater flow model hydraulic data to obtain an estimate of b_l.

The weighted average of a simulated transmissivity was calculated as:

$$T = K\Delta Z \tag{6.7}$$

where K [m/day] is the weighted average of the hydraulic conductivity from each of the fracture classes, and ΔZ [m] is the vertical grid spacing in the groundwater model.

The second approach utilizes the transmissivities estimated from aquifer tests in the new wells (HC-1, HC-2, and HC-4) at the Shoal site. The transmissivity is determined directly from the hydraulic analysis and then Equation (6.6) is used to calculate b_l. The geometric mean of the fracture apertures is then used to estimate the average fracture aperture.

Table 6.8 shows the estimated fracture apertures from each method. Both methods yield nearly identical results.

Table 6.8. Estimated Fracture Apertures.

Method	b_l (m)
Groundwater Model	1.4×10^{-4}
Aquifer Test	1.6×10^{-4}

The cubic law fracture aperture can be calculated from aquifer test data as:

$$b_c = \left[\frac{6\mu Q}{\pi\gamma|\Delta H|} \ln(r_l/r_0) \right]^{1/3} \tag{6.8}$$

where μ is the absolute viscosity of water [Ns/m^2], Q is the well flow rate [m^3/s], γ is the specific weight of water [N/m^3], r_0 is the well casing diameter [m], r_l is the radius of influence [m], and ΔH [m] is the hydraulic head difference $H(r_l) - H(r_0)$. Because a single well test was employed, various values of the radius of influence were investigated to determine the impact on the calculated aperture. Table 6.9 shows the calculated cubic law apertures for the three wells with various values of r_l. The geometric mean of the cubic law aperture is 1.9×10^{-2} m, which is in agreement with the order relationship of Tsang (1992).

The frictional loss aperture of 1.5×10^{-4} m (mean of two estimates) was used to calculate the retardation factor. The lab experiments yielded a surface-based sorption constant of 5.4×10^{-5} m and 6.2×10^{-3} m for cesium and lead, respectively. This was derived by dividing the equilibrium distribution coefficient by the specific surface area of the material used in the experiments (0.79 m^2/g). The resulting retardation coefficients are 1.72 and 83.7, for cesium (weakly sorbing cation) and lead (strongly sorbing cation), respectively. The retardation coefficient calculated for the anion, chromium, was close enough to one that retardation of anions was neglected in the calculations.

Table 6.9. Results from Hydraulic Tests for the Shoal Site.

Well	b_c (mm)	r_0 (m)	r_1 (m)	q (m^3/s)	ΔH (m)
HC-1	18.9	0.076	0.152	3E-05	0.6
HC-1	29.3	0.076	1	3E-05	0.6
HC-1	36.2	0.076	10	3E-05	0.6
HC-1	41.2	0.076	100	3E-05	0.6
HC-1	45.2	0.076	1000	3E-05	0.6
HC-2	5.9	0.076	0.152	1.5E-05	10
HC-2	9.1	0.076	1	1.5E-05	10
HC-2	11.3	0.076	10	1.5E-05	10
HC-2	12.8	0.076	100	1.5E-05	10
HC-2	14.0	0.076	1000	1.5E-05	10
HC-4	11.7	0.076	0.152	3E-05	2.5
HC-4	18.2	0.076	1	3E-05	2.5
HC-4	22.5	0.076	10	3E-05	2.5
HC-4	25.6	0.076	100	3E-05	2.5
HC-4	28.1	0.076	1000	3E-05	2.5

Geometric mean of b_c = 18.9 mm

7.0 Results

The results of each solute transport simulation are provided in three figures. The presentation provides both temporal and spatial information for each solute of interest. In the temporal domain, the mass flux versus time is presented for a downgradient control plane. Spatial information is provided by a contour plot provided at the time of the peak mass flux, along with another plot of the associated standard deviation.

The control plane is aligned with the land exclusion boundary as shown in Figure 7.1 . Figure 7.2 shows the vertical placement of the control plane with respect to the land surface and the model domain. Only a small section of the model domain is shown in the cross-sectional plots such that the control plane captures the entire solute plume. The perspective is such that the viewer is positioned downgradient of the control plane.

The general input parameters for the transport model are given in Table 7.1. A total of seven solute transport cases were simulated separately to include all combinations of retardation, hydraulic and geochemical release types. The seven cases result from the unique combinations of the five release groupings (hydraulic versus glass dissolution release, see Section 6.2.1) and three retardation groupings (no retardation, weakly sorbing cation, strongly sorbing cation, see Section 6.3.2). The specific solute transport parameters for each case are given in Table 7.2. Radioactive decay was calculated for each individual solute concentration in a post-processing mode.

The grid size was identical to the SIS and groundwater flow simulations with $\Delta x=\Delta y=\Delta z=41.9$ m. The volume of one grid block represents the volume of the source area. All simulations utilized

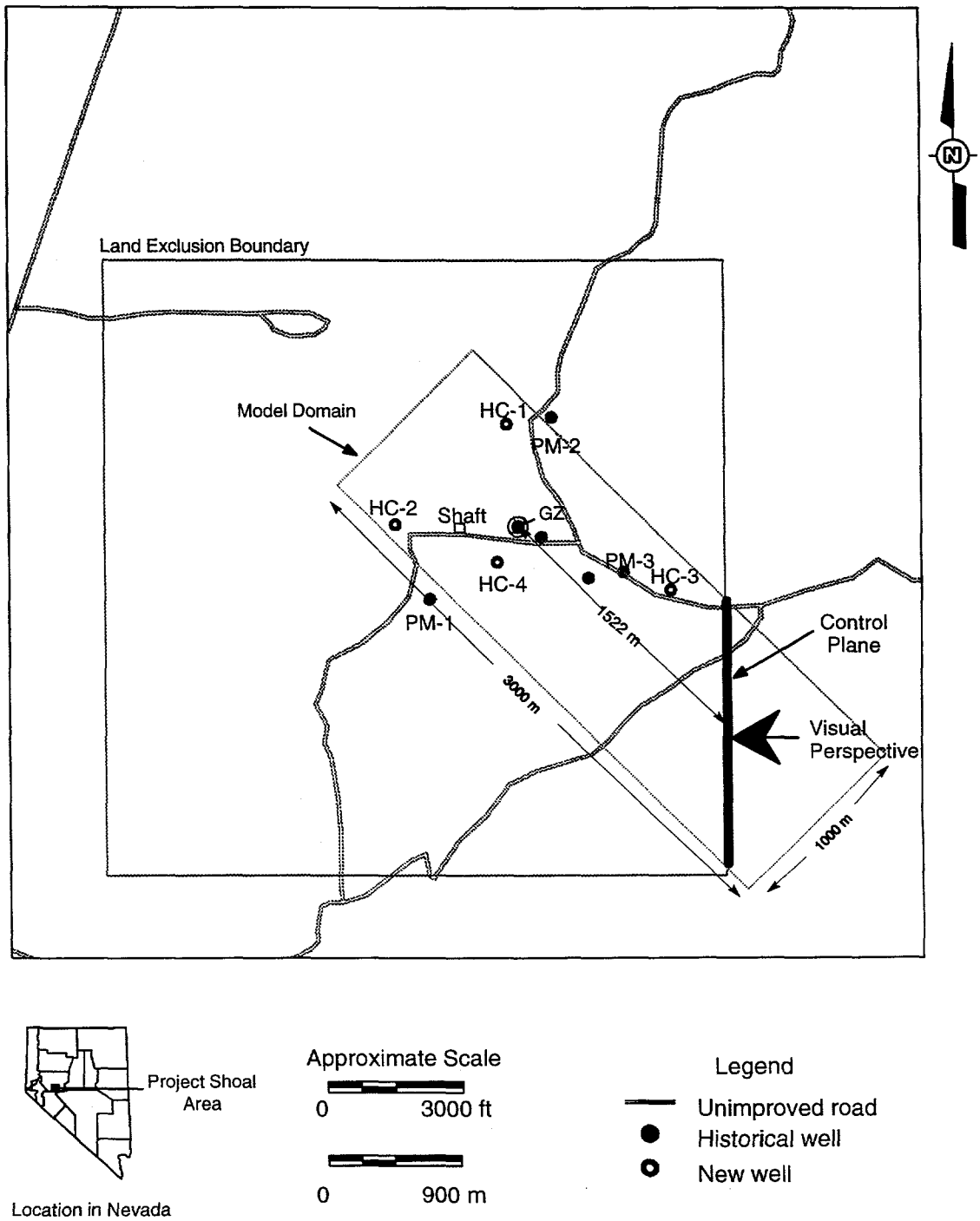

Figure 7.1. Site diagram of the Shoal site showing the areal extents of the model domain and the location of the downgradient control plane.

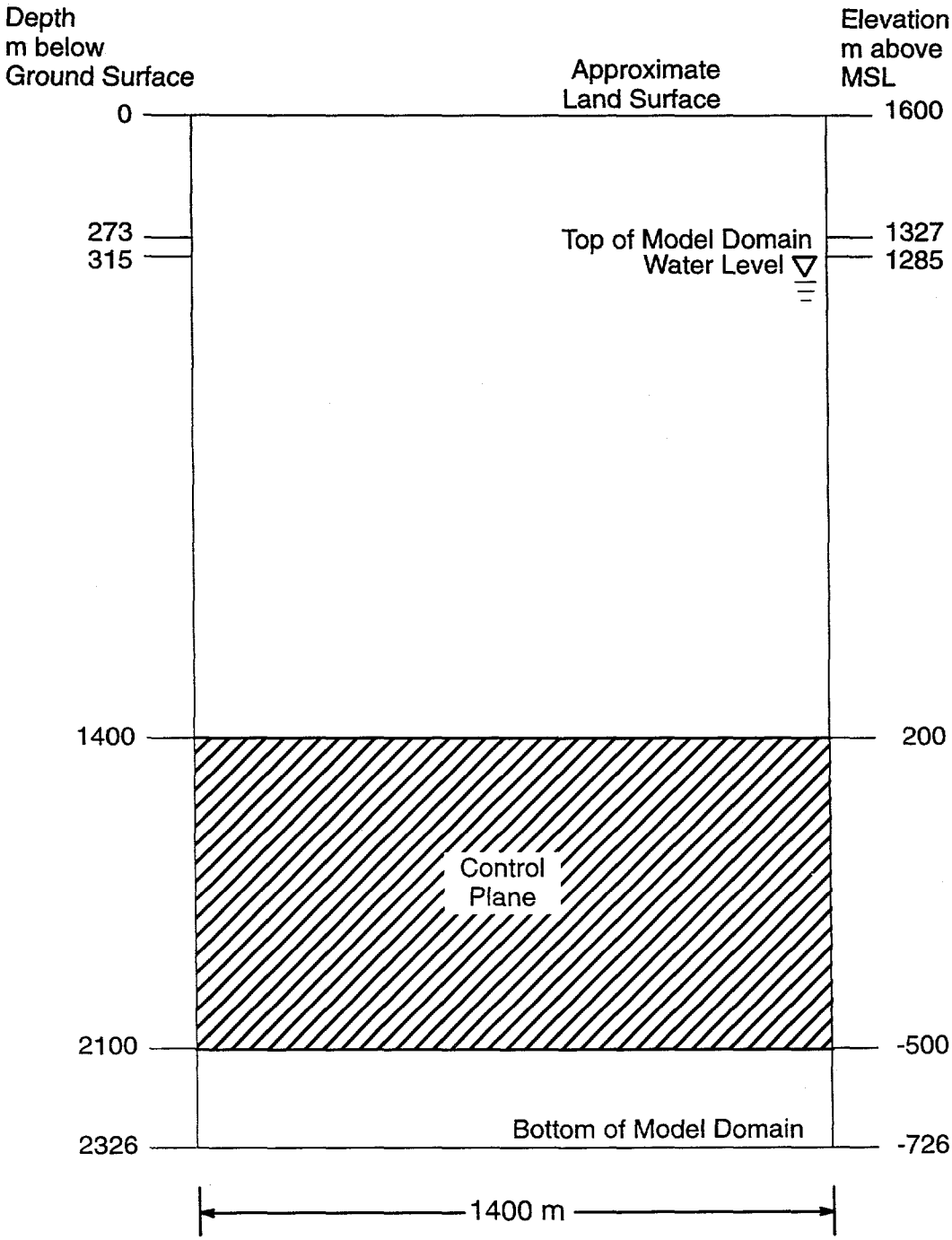

Figure 7.2. Cross section of control plane showing its vertical position.

100,000 particles. Additional test simulations were performed with additional particles with little to no change in transport behavior. The time-step length was chosen such that the cell Courant number was less than one. The microscopic dispersivity values, α_L and α_T, are based on values considered appropriate for the scale of the simulation. One hundred realizations were performed for flow and transport simulations such that stable breakthrough curve statistics could be obtained.

Table 7.1. Values of General Parameters used in Transport Simulations.

Parameter	Value
Source mass (moles)	1
Source diameter (cube) (m)	41.9
Source location - center (Nevada State Plan; West - NAD 27 m)	
Easting	169924
Northing	493818
Elevation (m above MSL)	1232
Number of particles	100000
Longitudinal dispersivity (α_L) (m)	1
Transverse dispersivity (α_T) (m)	1
Diffusion (m^2/day)	0
Effective porosity (m^3/m^3)	0.006
Number of realizations	100

Table 7.2. Case-Specific Transport Parameters.

Parameter	Case 1	Case 2	Case 3	Case 4	Case 5	Case 6	Case 7
Time step (yrs)	3.3	5.7	3.3	3.3	3.3	5.7	275.0
Total simulation time (yrs)	4928	34496	19712	19172	19172	34496	1649938
Retardation factor	1	1.72	1	1	1	1.72	83.7
Hydraulic release percentage/ Geochemical release percentage	100/0	80/20	50/50	40/60	5/95	5/95	5/95
Geochemical release coef. (1/day)	n/a	2.30E-06	2.30E-06	2.30E-06	2.30E-06	2.30E-06	2.30E-06

7.1 Breakthrough Curves

To distinguish between the transport scenarios and examine the effect of different release cases, it is most clear to evaluate the breakthrough curves before applying the decay computations. The final breakthrough curves are strongly influenced by the different half-lives, and thus decay rates, of each radionuclide, and this masks the general behavior resulting from release and retardation. Therefore, in Figure 7.3, the undecayed breakthrough curves are plotted for the seven studied scenarios.

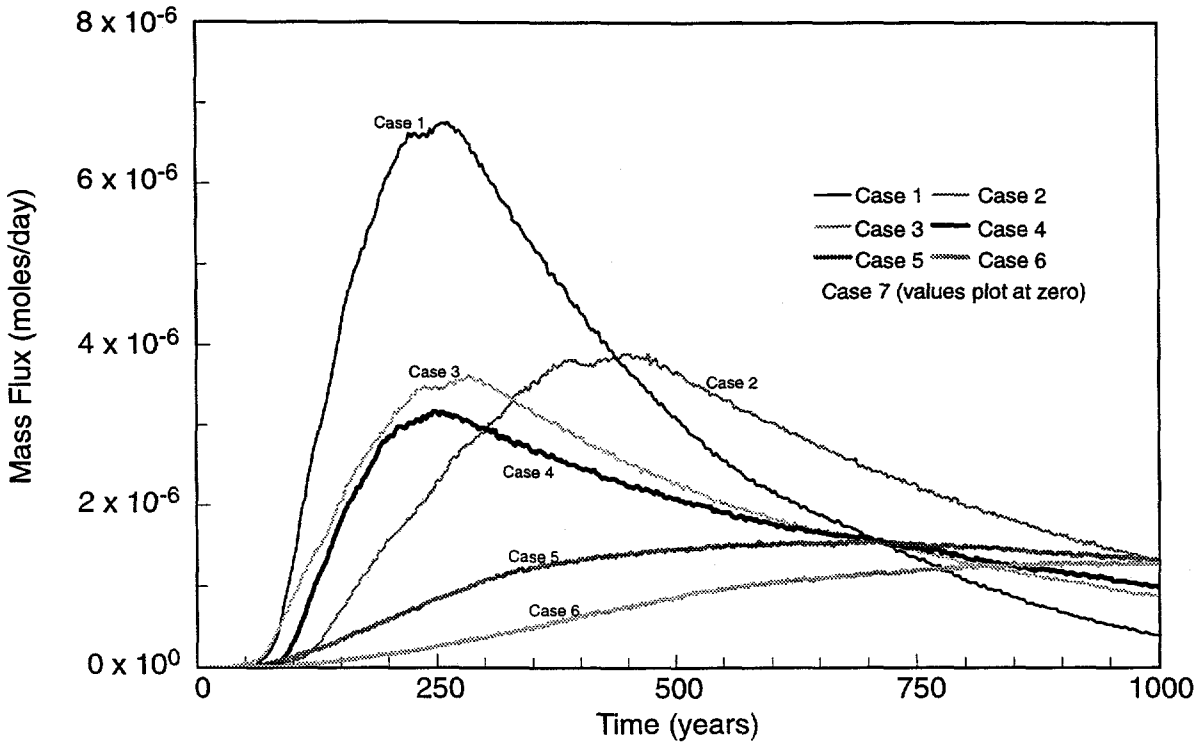

Figure 7.3. Normalized mean mass flux (*i.e.*, assumes unit initial mass with no decay) for the seven transport cases. Case specific input parameters are given in Table 7.2.

The first scenario gives a curve that has the highest peak and the least support, *i.e.*, the plume crosses the control plane in a short period of time with high concentration. This is due to releasing all the mass instantaneously into the cavity which is then subject to the hydraulic release conditions created by the porosity difference. In case 2, there are two parameters different than case 1. The plume has a retardation factor of 1.72 and 20 percent of the initial mass is released slowly according to the chemical release coefficient, k=-2.3e-6. The effect of those two factors is a delayed breakthrough arrival and a reduced peak, since only 80 percent is released to the cavity at time t=infill time. Also the time period during which breakthrough occurs is longer than in case 1 because of the chemical slow release. The third case has no retardation, but has 50 percent of the mass slowly released via the same chemical rate as in case 2. A lower mass flux peak is observed for the breakthrough curve with a much longer tail than case 1. When the ratio between chemical slow release and hydraulic slow release is taken as 40/60 in case 4, the peak of the breakthrough curve is reduced with the arrival time similar to cases 1 and 3.

Case 5 has only 5 percent of the initial mass subject to hydraulic release and 95 percent is subject to the chemical slow release. The resulting breakthrough has a much smaller peak and a much longer tail as compared to the previous four cases. Case 6 is similar to case 5 but with a retardation factor of 1.72. Again this retardation delays the plume arrival at the control plane and slightly

reduces the peak of the breakthrough curve. The final scenario (case 7) is similar to the previous two cases in terms of the release conditions, but the retardation factor is taken as 83.7. Although case 7 is not plotted in Figure 7.7, this large retardation significantly delays the breakthrough and decreases the peak value.

The integration of the breakthrough (area under the curve) is the same for all seven cases (if run to 100 percent completion), which is equivalent to the initial normalized mass. It is concluded from Figure 7.3 that the equilibrium sorption conditions retard the breakthrough and decrease its peak. The chemical slow release produces a long-tail breakthrough with the peak value arriving at the same time as without the chemical slow release for moderate ratios of chemical/hydraulic releases. This is because the peak is dictated by the initial mass released from the cavity. When most of the mass is released via chemical slow release, the peak arrival is delayed since the initial mass released is very small and does not produce a defined peak. The peak occurs at a later time when some additional mass is chemically released into the system.

7.2 Specific Examples

The simulated mean concentration, standard deviation and mass flux at the downgradient control plane is given in Figures 7.4 through 7.6 for tritium, ^{90}strontium and ^{137}cesium, respectively. The spatial distribution of the mean concentration and standard deviation is presented for the time at which the maximum mass flux occurs.

Tritium is derived from transport case 1, with the addition of radioactive decay. The simulations assumed 100 percent hydraulic release and no retardation. The maximum mass flux occurs at 146 years after detonation. The maximum mean concentration is 13,000 pCi/L and the maximum standard deviation is 2,000 pCi/L. Therefore, one would expect that the concentration of tritium at the control plane would be less than 17,000 pCi/L (mean + 2σ).

Strontium-90 is derived from transport case 4, with the addition of radioactive decay. The simulations assumed 40 percent hydraulic/60 percent geochemical releases and no retardation. The maximum mass flux occurs at 154 years after detonation. The maximum mean concentration is 35,000 pCi/L and the maximum standard deviation is 4000 pCi/L. Therefore, one would expect that the concentration of ^{90}Sr at the control plane would be less than 43,000 pCi/L (mean + 2σ).

Cesium-137 is derived from transport case 2. The simulations assume a retardation factor of 1.72 and an 80 percent hydraulic/20 percent geochemical release. The maximum mass flux occurs at 247 years after detonation. The maximum mean concentration is 12,000 pCi/L and the maximum standard deviation is 1800 pCi/L. Therefore, one would expect that the concentration of ^{137}Cs at the control plane would be less than 15,600 pCi/L (mean + 2σ).

Storage space and running time imposed some restrictions on the frequency of saving the output concentrations. We chose to save concentrations every four time steps. As a consequence, the time to the peak concentration may be off by four time steps (4800 days for tritium and ^{90}Sr), especially with the noise associated with the breakthrough curves.

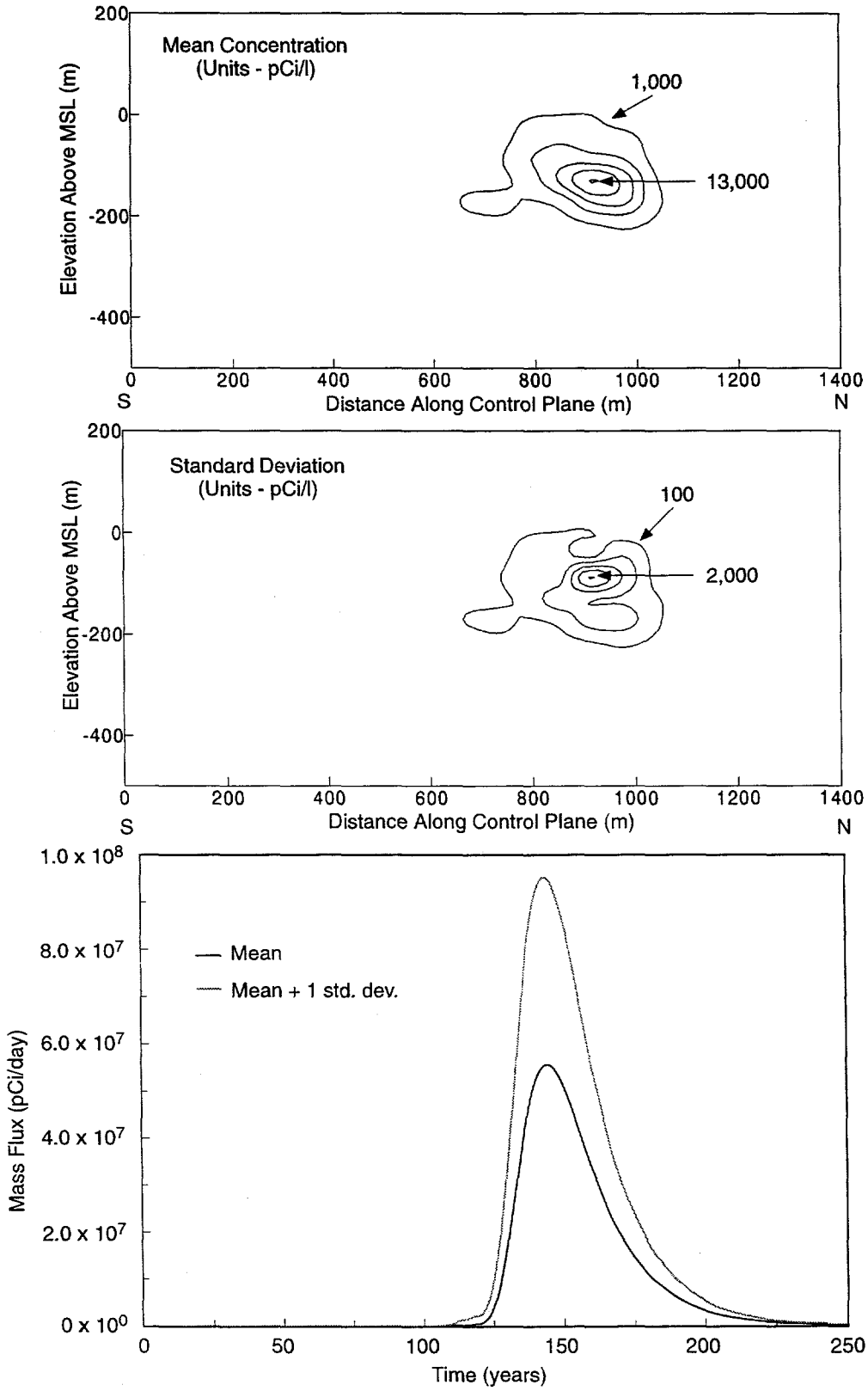

Figure 7.4. Simulated mean tritium concentration, standard deviation and mass flux at the downgradient control plane. Transport parameters: n = 0.006, R = 1.0, half-life = 12.3 yrs and 100% hydraulic release. Source mass = 3.0×10^4 curies.

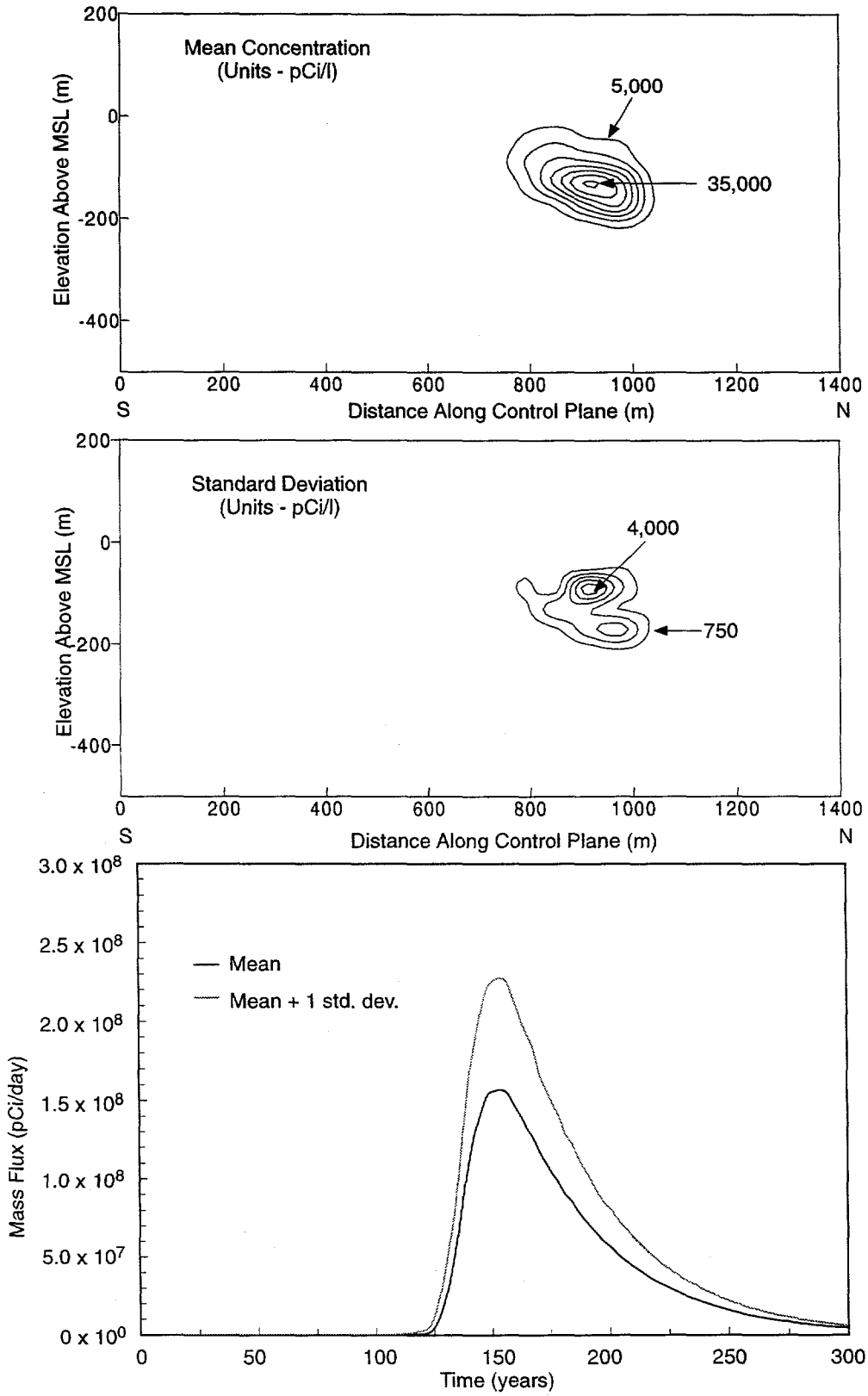

Figure 7.5. Simulated mean ^{90}Sr concentration, standard deviation and mass flux at the downgradient control plane. Transport parameters: n = 0.006, R = 1.0, half-life = 29.1 yrs and 40% hydraulic/ 60% geochemical release (K = 2.3E–6 day^{-1}). Source mass = 1.9 x 10^3 curies.

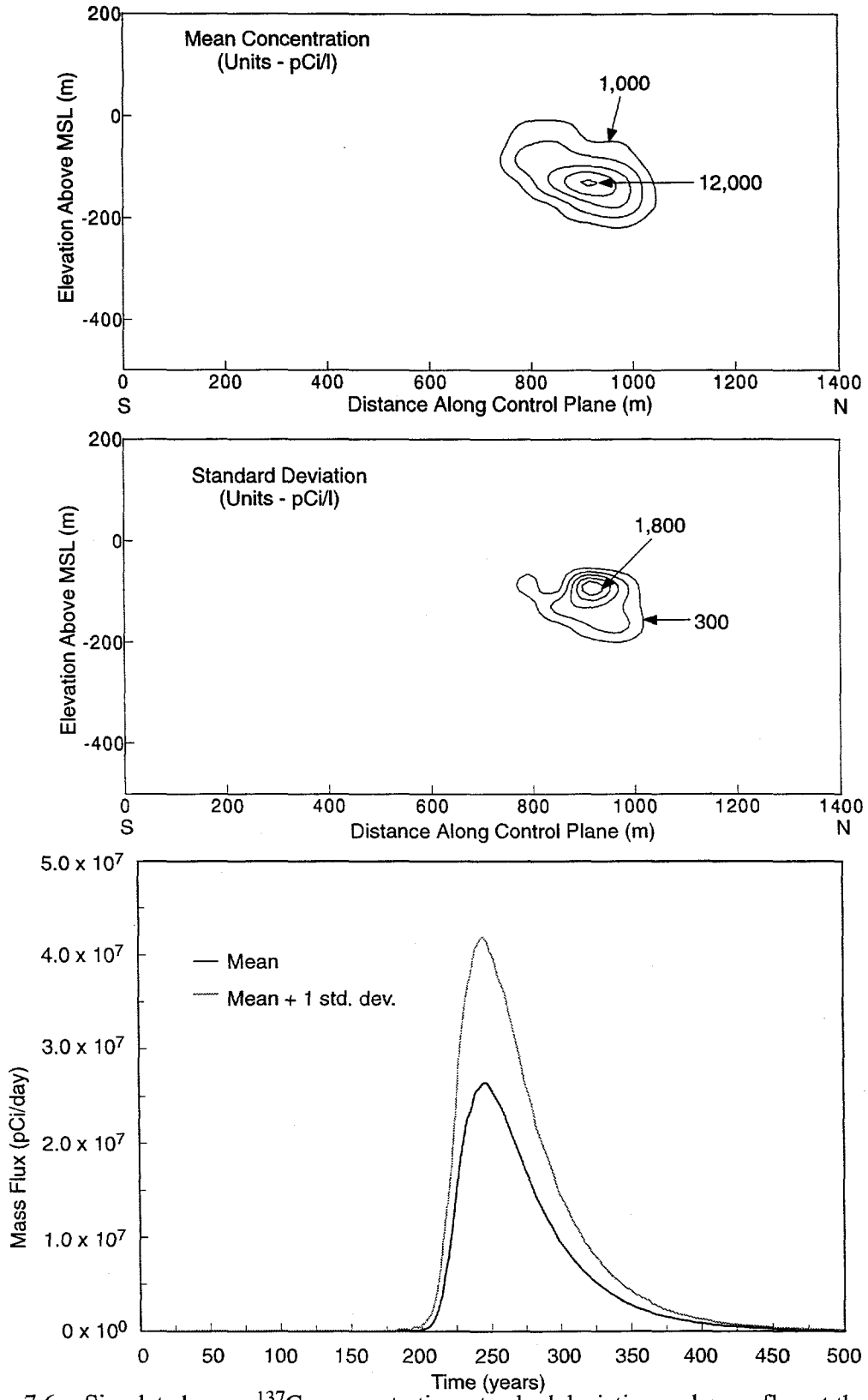

Figure 7.6. Simulated mean ^{137}Cs concentration, standard deviation and mass flux at the downgradient control plane. Transport parameters: n = 0.006, R = 1.72, half-life = 30.2 yrs and 80% hydraulic/ 20% geochemical release (K = 2.3E-6 day^{-1}). Source mass = 2.2 x 10^3 curies.

7.3 Sensitivity and Uncertainty Analysis

All models contain a degree of uncertainty which is manifested as the differences between observed and simulated system behavior. The uncertainty in the simulated output is due to many factors in the modeling process including errors in data collection, scale issues dealing with the transfer of field scale estimates of hydraulic parameters to the scale of the modeling domain and discretization, heterogeneity of the hydraulic and transport properties, incorrect assumptions in the conceptual model and the uncertainty in the boundary condition assignment. Certain components of the input uncertainty (*e.g.*, aquifer heterogeneity) can be quantified directly through the use of stochastic models, but other components need to be addressed with a less rigorous approach to understand how they will impact the simulated system response.

The purpose of a sensitivity analysis is to develop a better understanding of the uncertainty in the model caused by uncertainty in the input parameters. The ASTM Standard Guide for Conducting a Sensitivity Analysis (ASTM, 1994) was used to guide the sensitivity analysis process. The sensitivity analysis is used here to compliment the uncertainty analysis (Monte Carlo) that was performed on the base model. While that analysis provides a quantitative description of the uncertainty caused by the fracture class geometry, it did not account for uncertainties in other input parameters.

The transport behavior was used to compare the impact of various input parameter adjustments. The mass flux (*i.e.*, the time at which the maximum mass flux occurred) was used to identify model sensitivity to a particular input parameter. The sensitivity analysis included an analysis of the geochemical release function, the value of the specified head at the downgradient boundary, retardation, the inclusion of matrix diffusion and, prompt injection, effective porosity, fracture and conductivity heterogeneity and surface recharge.

It should be noted that the parameters/features included in this sensitivity analysis are not exhaustive. For example, the general structure of the boundary conditions was not tested to determine how other plausible boundary conditions might impact the transport results. Because there were no hydraulic head data available downgradient of the HC-3 well there are many other possible boundary condition configurations that could be employed. The impact of the specified head at the lower boundary was investigated, but one might also test the impact of vertical head gradients on this lower boundary.

7.3.1 Geochemical Release Function

The sensitivity of the transport behavior was tested by adjusting the slow release coefficient (the product of the specific surface area and the dissolution rate constant) for ^{90}Sr and ^{99g}Tc. These solutes were chosen such that the impact of radioactive decay in conjunction with the slow release coefficient could be investigated. The slow release coefficient was changed from 2.3×10^{-6} days^{-1} for the base case to 2.4×10^{-9} days^{-1}, which means that a slower release is employed. This reflects a change in the specific surface area from the value of 0.05 m^2/g used in the base case to 5.2×10^{-5} m^2/g, as used at Cambric (see section on glass dissolution). The ^{90}Sr mass was released as 40 percent

hydraulic and 60 percent geochemical slow release, while ^{99g}Tc was released as 5 percent hydraulic and 95 percent geochemical slow release. Both solutes were assumed to be conservative. The results are given in Figures 7.7 and 7.8 for ^{90}Sr and ^{99g}Tc, respectively. In general, the impact of the slow release coefficient is critical for solutes with larger proportions of geochemical release and long half-lives (*e.g.*, ^{99g}Tc). Conversely, the impact is less critical for solutes with shorter half-lives and less apportioned geochemical release. The results of the ^{90}Sr simulation reveal that there is little difference between the two sensitivity simulations, because the peak concentration is attained at early time when 40 percent of the mass is released via hydraulic controls only. Since 40 percent is released hydraulically, releasing the remaining 60 percent slower only affects the tailing limb of the breakthrough curve but not the peak value. Even the tailing limb is minimally affected because radioactive decay removes most of the mass within the first several hundred years. The results of the ^{99g}Tc simulation suggest that there is a large difference between each simulation. With 95 percent of the mass being released according to the geochemical release, the slow release coefficient plays a role in the peak concentration and the tailing limb of the breakthrough curve. Figure 7.8 shows the peak mass flux being over four times larger for the larger slow release coefficient (2.3×10^{-6}). The small peak for the smaller slow release coefficient (2.4×10^{-9}) represents the hydraulic release of five percent of the mass, while no release from glass dissolution is visible over the time span of 2500 years.

7.3.2 Boundary Conditions

A sensitivity analysis was performed on 100 flow and transport realizations to ascertain the impact of changing the value of the specified head on the downgradient model boundary. The uncertainty in the HC-3 water level imparts some uncertainty in the downgradient specified head. For the base simulation, the head at the downgradient boundary was set to 1210 m above MSL, which is about 10 m above the water level in the adjacent Fairview Valley. The water level measured in HC-3 is 1192.7 m, which is lower than the water level in Fairview Valley. A second set of realizations was performed with a specified lower boundary condition of 1100 m. The second value was chosen such that a reasonable level of agreement would be met between all four of the measured water levels (HC-1, HC-2, HC-3, and HC-4). Because the lower boundary condition was changed, the hydraulic conductivity of fracture class 1 had to be changed as well such that the measured versus simulated water levels were in agreement. The conductivity of fracture class 1 was reduced to 1.0×10^{-7} cm/sec (from 4.0×10^{-7} cm/sec). This sensitivity analysis has little physical justification due to arbitrary gradient reversal from Fairview Valley to the edge of the model domain, but it was performed to determine the impact of increased gradients on flow and transport behavior.

Figure 7.9 shows the mean mass flux of tritium at the downgradient control plane for the two gradient conditions. Lowering the boundary head (and lowering the conductivity of fracture class 1) increased the hydraulic gradient and decreased mean velocities (due to lower K value). This in turn led to later arrival times at the control plane and decreased mass fluxes.

Although no water level data exist near the domain boundary, the specified head of 1210 m seems most probable, as the water level in the adjacent Fairview Valley is near 1200 m. The results

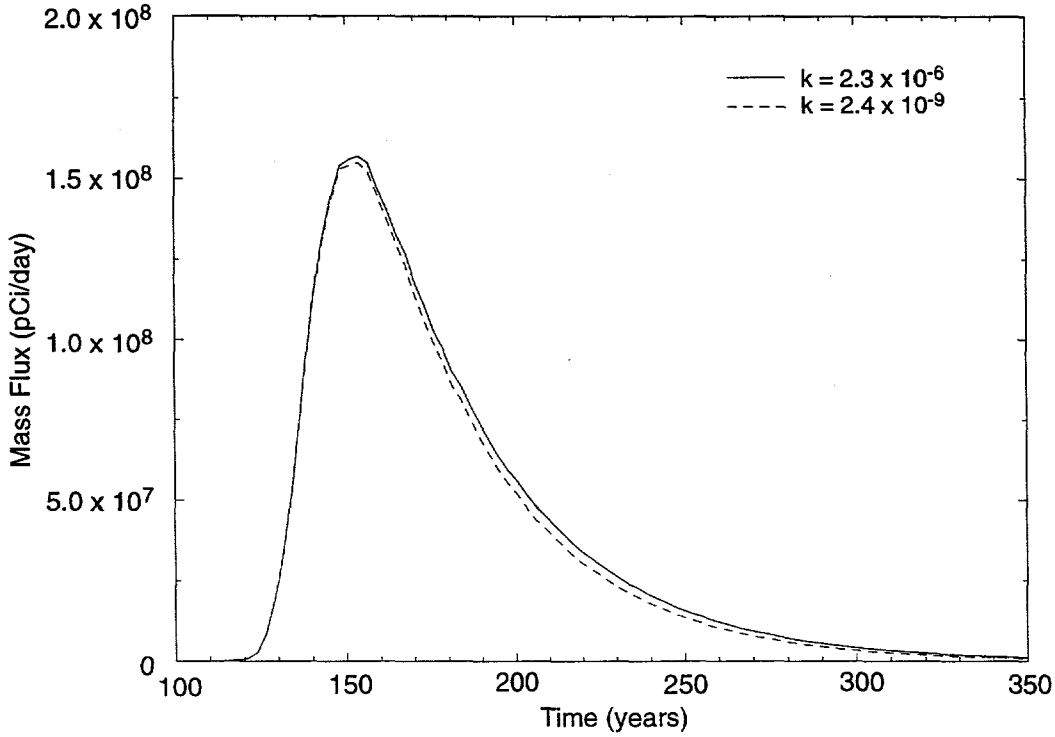

Figure 7.7. Simulated mean ^{90}Sr mass flux for the two values of the geochemical slow release coefficient. Transport parameters: n = 0.006, R = 1.0, half-life = 29.1 yrs and 40% hydraulic/60% geochemical release. Source mass = 1.9 x 10^3 curies.

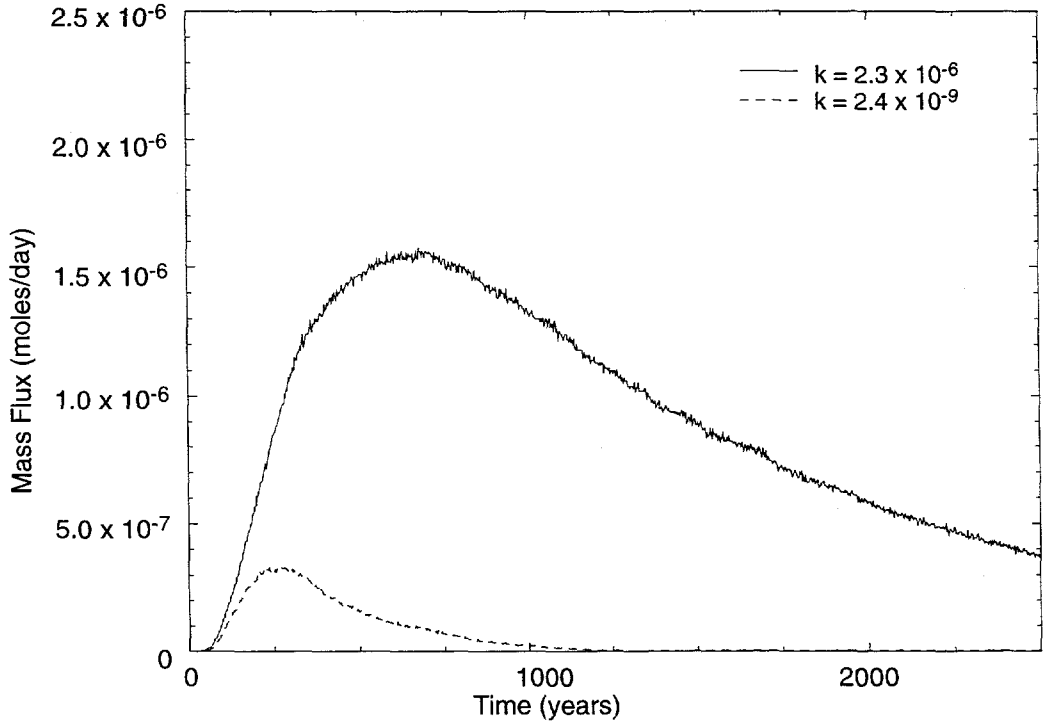

Figure 7.8. Simulated mean ^{99g}Tc normalized mass flux for the two values of the geochemical slow release coefficient. Transport parameters: n = 0.006, R = 1.0, half-life = 2.3 x 10^5 yrs and 5% hydraulic/95% geochemical release. Assumed a unit (1 mole) source mass.

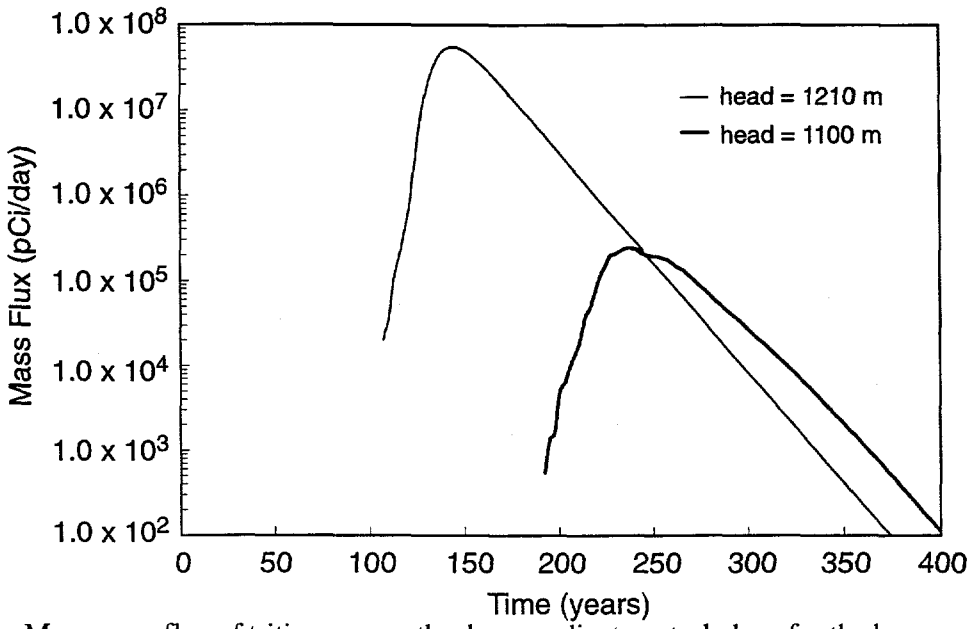

Figure 7.9. Mean mass flux of tritium across the downgradient control plane for the base case (specified head = 1210) and a simulated lower boundary condition of 1100 m above MSL. Transport parameters: n = 0.006, R = 1.00, half-life = 12.3 yrs and 100% hydraulic release. Source mass = 3.0×10^4 curies. Note: $K_1 = 1.0 \times 10^{-7}$ cm/sec for head = 1100 m and $K_1 = 1.0 \times 10^{-7}$ cm/sec for head = 1210 m case.

of this sensitivity analysis suggest that lowering the boundary head (in conjunction with recalibrating) increases travel times to the land exclusion boundary and decreases the mass fluxes. Additional water level data would be required to confirm the downgradient head.

7.3.3 Matrix Diffusion

Matrix diffusion is a potentially important mass transfer process by which solutes are removed from the high-velocity fracture flowpaths into the surrounding rock matrix. With the decay of radionuclides, long residence times in the rock matrix act to eliminate the contaminant, also serving as a "natural remediator." Thus, it is important to determine the effectiveness of the matrix diffusion only within the range of feasible values, since the field data are lacking for any conclusive estimates. This was the strategy followed in the Shoal project, where impact from matrix diffusion is tested on the tritium migration.

The approach utilized is based on the relative dispersion for solute flux framework (Andricevic and Cvetkovic, 1996; 1997), where the source is envisioned as a collection of solute particles that are released slowly (rate depends on difference between the porosity within the source and surrounding media) and transported by groundwater within individual streamtubes (*e.g.*, on the Darcy scale). The results are presented in terms of a total mass flux crossing the control plane downgradient from the source. The solute flux analytical solution provides a useful tool for analyzing the impact on the transport solution coming from different plausible combinations of

parameters that describe the matrix diffusion process. The effect of mass transfer is incorporated analytically using the reaction function $\gamma(t, \tau)$ for matrix diffusion (Cvetkovic and Dagan, 1994):

$$\gamma(t,\tau) = H(t - t_o - \tau)\frac{k * \tau}{2\sqrt{\pi}(t - t_o - \tau)^{3/2}}\exp\left[-\frac{(k * \tau)^2}{4(t - t_o - \tau)}\right] \tag{7.1}$$

where H is the dimensionless Heaviside function, τ (yrs) is the particle travel time, and t_o (yrs) is the injection time. The matrix diffusion parameter ($yr^{-1/2}$) is:

$$k * = \frac{\theta_m\sqrt{DR}}{b} \tag{7.2}$$

where D (m^2/yr) is an effective diffusion coefficient in the rock matrix, b (m) is the effective half-aperture, θ_m (m^3/m^3) is the rock matrix porosity, and R is the dimensionless retardation coefficient in the rock matrix. An effective diffusion coefficient of 2×10^{-4} m^2/yr was based on work for the radioactive waste repository project in Switzerland (NAGRA, 1994), which found that value to be conservative (limiting diffusion) for all radionuclides. For tritium, the retardation is not present and R = 1.

The assumptions inherent in Equation (7.2) are a constant aperture along the streamtube, diffusion only perpendicular to the fracture plane, well-mixed conditions over the cross-sectional area of the fracture, and homogeneous rock matrix with no advection. First-order decay is incorporated by multiplying Equation (7.1) with the expression exp ($-t \ln 2/\omega$); ω being the half-life.

The impact of matrix diffusion was tested using Equation (7.1), which is an analytic expression. It is difficult to directly compare the transport behavior at the Shoal site using analytic tools, as the flow field is more complex. Therefore, only a relative comparison is made to determine the sensitivity of matrix diffusion on the tritium transport behavior. Using the mean flow velocity calculated from the numerical flow model and Equation (7.1), different values of the ratio between matrix porosity and half-aperture were tested. If the true ratio of matrix porosity and half-aperture could range between 0.1 and 0.01, the analytic results suggest only moderate sensitivity. A ratio of 0.01 shows the reduction in the peak mass flux by half, and a ratio of 0.1 shows the peak reduced by a factor of four compared to a case where no matrix diffusion is present. The peak travel time changed only by tens of years. In general, matrix diffusion is not a critical transport parameter for the conditions found at the Shoal site.

7.3.4 Prompt Injection

The high pressure generated by a nuclear explosion fractures the surrounding formation and can impact the distribution of resultant radioactivity. The predicted radius of fracturing for Shoal was 159 m (see Section 2.4.1.4; Beers, 1964), consistent with observed fractures at 135.6 m in USBM-1. A radius of "radiation injection into cracks by particulates and condensates" (Beers, 1964) was also predicted, with an outer limit of 108 m. The minimum radioactive fracture radius predicted was 91.4 m. Those estimates were based on experience from the Rainier and Hardhat tests. Investigations at Piledriver (a 61-kiloton test in granite) found radioactive glass injected 85 and 92

m from the shot point (2.1 to 2.3 cavity radii) (Rabb, 1970; Borg, 1974). These occurrences were in isolated veins, with the 92-m-distance samples found in a fissure between the granite back and sand stemming in a pre-existing drift, and the 85-m samples occurring in seams in the walls of a bypass drift. Injection out of the cavity was inferred to occur along a family of steeply dipping shear zones (Borg, 1974). Any such injection of glass at Shoal is not considered here. During postshot drilling, almost no radioactivity was encountered until near the detonation point (Atkinson, 1964). The volume that could be forced into the formation along fractures is assumed to be very small compared to the mass remaining in the cavity. It is also likely that particulate injection was focused along the least resistive pathways, meaning the mined drift intercepted by the cavity. As the drift runs in the hydraulically upgradient direction from the test, depositing some of the mass along it would primarily result in more dispersion and lower concentrations at the contaminant boundary.

Though the effect of injection of radioactive glass is not analyzed, the prompt injection of gases is considered for the sensitivity analysis. Prompt injection of radioactive gases was observed at Shoal during postshot re-entry into well USBM-1. Specifically, ^{133}Xe, ^{131}I, and a trace of ^{137}Cs were detected (^{137}Cs has a short-lived gaseous precursor, ^{137}Xe) (Atkinson, 1964). Tritium was not recorded at USBM-1, but tritium can migrate as either a gas or vapor at early times. For the sensitivity analysis, injection out the distance of the predicted cracking radius, 159 m, was considered. Solely based on geometric considerations, the bulk of the mass remains in the cavity because the volume of the open fractures is relatively small. The calculations assume that 10 percent of the total tritium mass is injected into the region out to 159 m, while the the remaining 90 percent remains in the cavity.

A case including prompt injection was tested and compared to the base case for tritium. It is assumed that 10 percent of the initial mass was released to the domain at the time of the shot, whereas the remaining 90 percent is still within the initial source boundaries. In the particle tracking approach, 10 percent of the particles is initially located at the surface of a sphere having a center at the source center and with a radius of 159 m. The locations of these particles on the sphere surface are chosen randomly based on a uniform random distribution. This configuration allows some particles to be located upgradient of the source and then propagate with the flow direction such that they may enter the source at a later time. The particles that are promptly injected are allowed to migrate instantaneously once they are released, while the remaining particles will experience the slower hydraulic release conditions as in the base case.

The simulated mean mass flux of tritium at the downgradient control plane with and without the inclusion of prompt injection is shown in Figure 7.10. More dispersion and a higher mass flux peak are observed when prompt injection was included. More dispersion is to be expected since the prompt injection scenario leads to particles occupying more space and experiencing more of the velocity field heterogeneity as compared to the base case. The higher peak is primarily related to the slightly earlier arrival time, driven by both a farther downgradient starting location for some of the particles, as well as their release prior to the hydraulic equilibration of the cavity. The resultant reduced decay increases the mass arriving at the control plane.

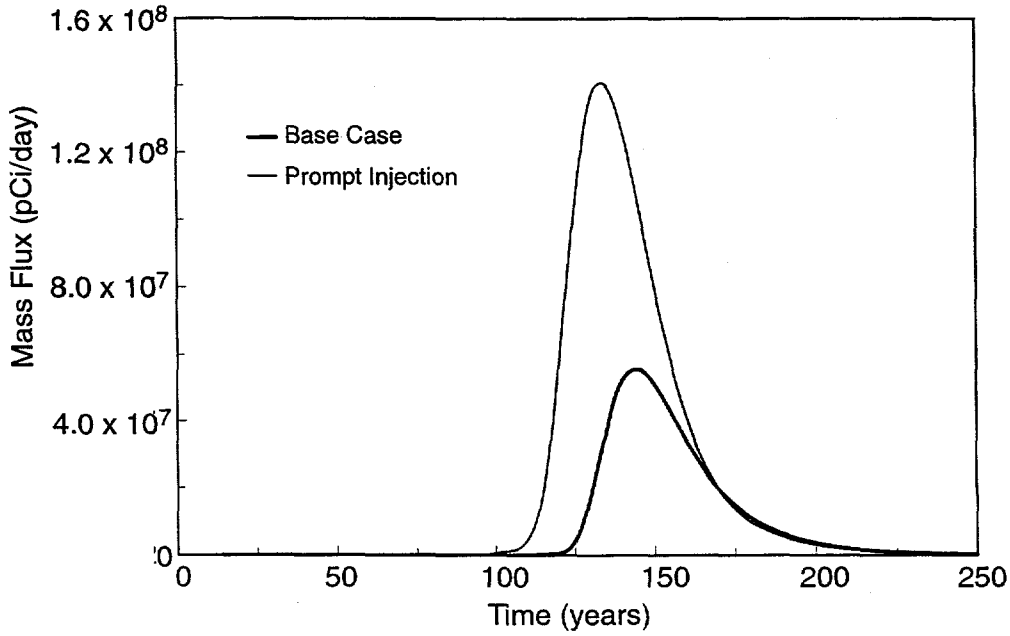

Figure 7.10. Simulated mean mass flux of tritium at the downgradient control plane with and without the inclusion of prompt injection. Transport parameters: n = 0.006, R = 1.0, half-life = 12.3 yrs, and 100% hydraulic release. Source mass = 3.0 x 10^4 curies.

7.3.5 Porosity

Additional simulations were performed to assess the impact of effective porosity on transport behavior. Werner (1996) suggests that the porosity of fractured granite is approximately 0.006, yet there is significant uncertainty in this estimate. Three values of the effective porosity were used in the sensitivity analysis (0.01, 0.006, and 0.0005). This range was determined by values found in the literature for a fractured granite aquifer and secondary numerical analysis of aquifer test data from Shoal. Tritium was used as the solute of interest in each of the simulations. Figure 7.11 shows the mean mass flux of tritium at the downgradient control plane and the mass flux versus time for each of the three porosity values, 0.01, 0.006, and 0.0005.

The inverse relationship between effective porosity and fluid velocity and the large uncertainty in the magnitude of the effective porosity lead to large variations in the tritium mass flux and arrival time. The time of maximum mass flux across the control plane for the 0.01, 0.006 and 0.0005 effective porosity cases is approximately 225, 150 and 25 years, respectively. The impact of effective porosity on arrival time is then magnified due to radioactive decay. The peak mass flux varies by almost six orders of magnitude between the 0.01 and 0.0005 porosity cases. Clearly, effective porosity plays a large role in the transport behavior. Additional data on the effective porosity would be required to reduce this uncertainty.

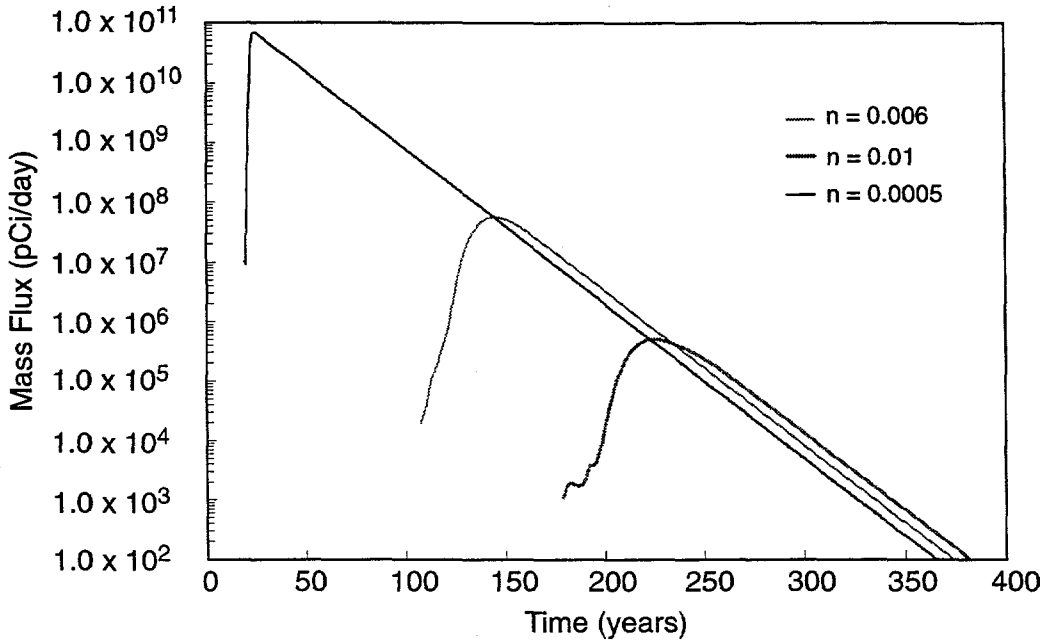

Figure 7.11. Simulated mean mass flux of tritium for the three values of effective porosity. Other transport parameters: R = 1.0, half-life = 12.3 yrs, and 100% hydraulic release. Source mass = 3.0×10^4 curies.

7.3.6 Retardation

The sensitivity of the sorption parameters was not directly simulated, as the impact is similar to the porosity sensitivity. The sorption processes were simulated as a linear function of sorbed versus solute concentration. As such, the sorption directly impacts the effective solute velocity as:

$$v_r = v/R \tag{5.8}$$

where v_r (m/day) is the retarded velocity, v (m/day) is the conservative solute velocity, and R is the dimensionless retardation coefficient. The retardation factor impacts the velocity for transport cases 2, 6 and 7. The uncertainty in R is due to many factors including the estimated fracture aperture, the assumption that sorption is a linear process, the use of surrogates to approximate the actual sorption for solutes that were not included in the lab analysis and the spatial variability in sorption properties. The uncertainty in retardation would most strongly impact the transport case 7, which was assigned a R = 83.7. If, for example, the retardation was one-half the assumed value, then the velocities for case 7 would be twice the current value. This would, in combination with radioactive decay, decrease travel times and increase peak concentrations as was seen in the porosity sensitivity analysis.

7.3.7 Heterogeneity

A sensitivity analysis was performed to determine the impact of various fracture and hydraulic conductivity conceptual models on transport behavior. In all cases, 100 realizations were performed for flow and transport. Tritium mass flux (including decay) at the downgradient control plane was used for comparison purposes. Three cases with different types of fracture and hydraulic conductivity heterogeneity were compared. The input parameters for the base case were exactly the

same as described above. Case 2 utilized the same correlation structure for the SIS (fracture) simulations, but additional hydraulic conductivity variability was included within each fracture class. The conductivity variability was simulated with sequential Gaussian simulation (SGS), similar to the methods of Pohlmann *et al.* (1996). The correlation models were exactly the same as the SIS fracture class simulations. An SGS realization was created for each fracture class and each hydraulic conductivity value (*i.e.*, at each node) is chosen from the SGS realization based upon the simulated SIS fracture class at that node. For the purposes of this numerical experiment the distribution of the hydraulic conductivity was assumed to be ln-normal with the mean being equal to the calibrated conductivity values determined previously and the ln-variance being 1.0. Case 3 was similar to case 2, except the correlation scale along the strike and dip (SGS and SIS) was reduced to 50 m (from 700 m).

Figure 7.12 shows the mass flux for tritium at the downgradient control plane for each sensitivity case. The following transport parameters were used for all cases: n = 0.006, R = 1.0, half-life = 12.3 yrs, and 100 percent hydraulic release. As described earlier, the maximum mass flux (6×10^7 pCi/day) for the base case occurred at 146 years. The inclusion of additional hydraulic conductivity variability (case 2) yielded a later peak mass flux (2×10^5 pCi/day) at 291 years. Decreasing the correlation scale for the SIS and SGS simulations yielded a significant decrease in tritium peak mass flux (7×10^{-4} pCi/day) and a later arrival time of 704 years.

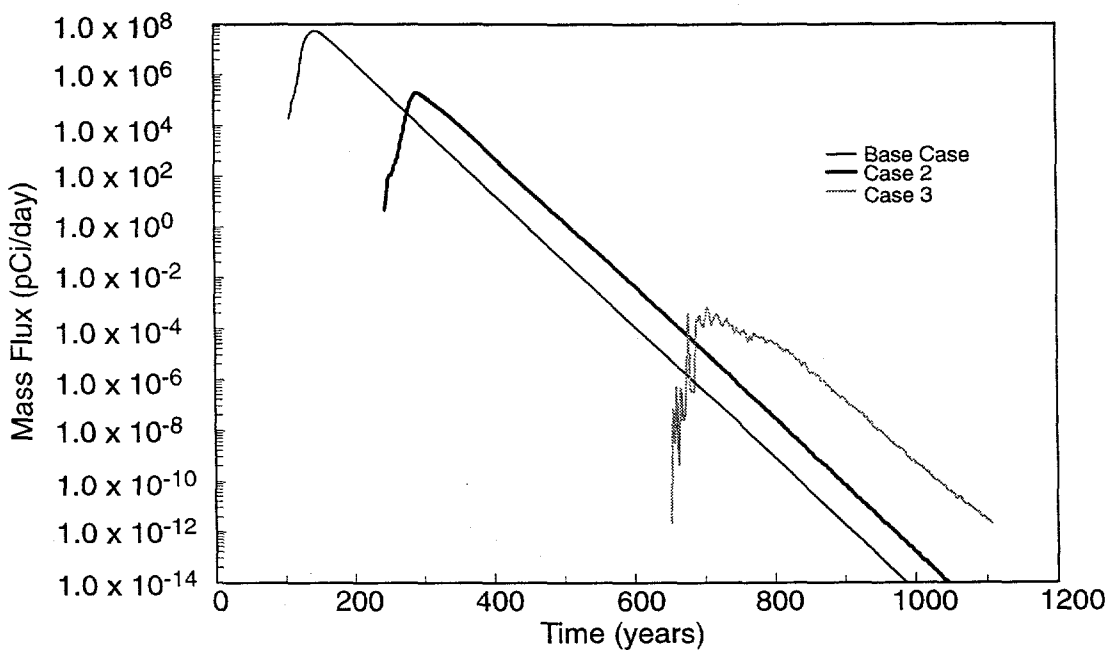

Figure 7.12. Mean mass flux of tritium for three conceptual models of heterogeneity at the downgradient control plane. The base case utilized a single value of conductivity for each fracture class. Case 2 included a ln-normal distribution (ln-variance = 1.0) of conductivity using SGS with the same correlation model as the base case (700 m). Case 3 included a ln-normal distribution (ln-variance = 1.0) of conductivity using SGS with a smaller correlation scale (50 m) for both the SGS and SIS simulations. Other transport parameters were: n = 0.006, R = 1.0, half-life = 12.3 years, and 100% hydraulic release. Source mass = 3.0×10^4 curies.

7.3.8 Recharge

A sensitivity analysis was performed to assess the impact of surface recharge on transport behavior. A comparison of tritium mass flux (no decay) was made between the base case with a surface recharge value of 1.45 cm/yr and a second case with 0.145 cm/yr. To achieve a reasonable level of agreement between the observed and simulated water levels, the second case required an adjustment of the fracture class 1 hydraulic conductivity to 1×10^{-8} cm/sec (from 4×10^{-7} cm/sec). Radioactive decay was not included due to the small velocities and associated large travel times for case 2. For both cases, 100 realizations were performed for both flow and transport simulations.

Figure 7.13 shows the normalized mass flux for tritium. The base case (with no decay) has a peak mass flux of 7×10^{-6} moles/day at 266 years, while the reduced recharge simulation has a peak mass flux of 4×10^{-7} moles/day at 6445 years. The inclusion of radioactive decay for tritium would only amplify the differences in the transport behavior.

Although the location of the plume was not plotted, the plumes for both cases intersect the control plane at nearly identical locations. This indicates that decreasing the recharge, with a simultaneous decrease in the magnitude of conductivity continues to yield flux fields with a significant downward component as found in the base case.

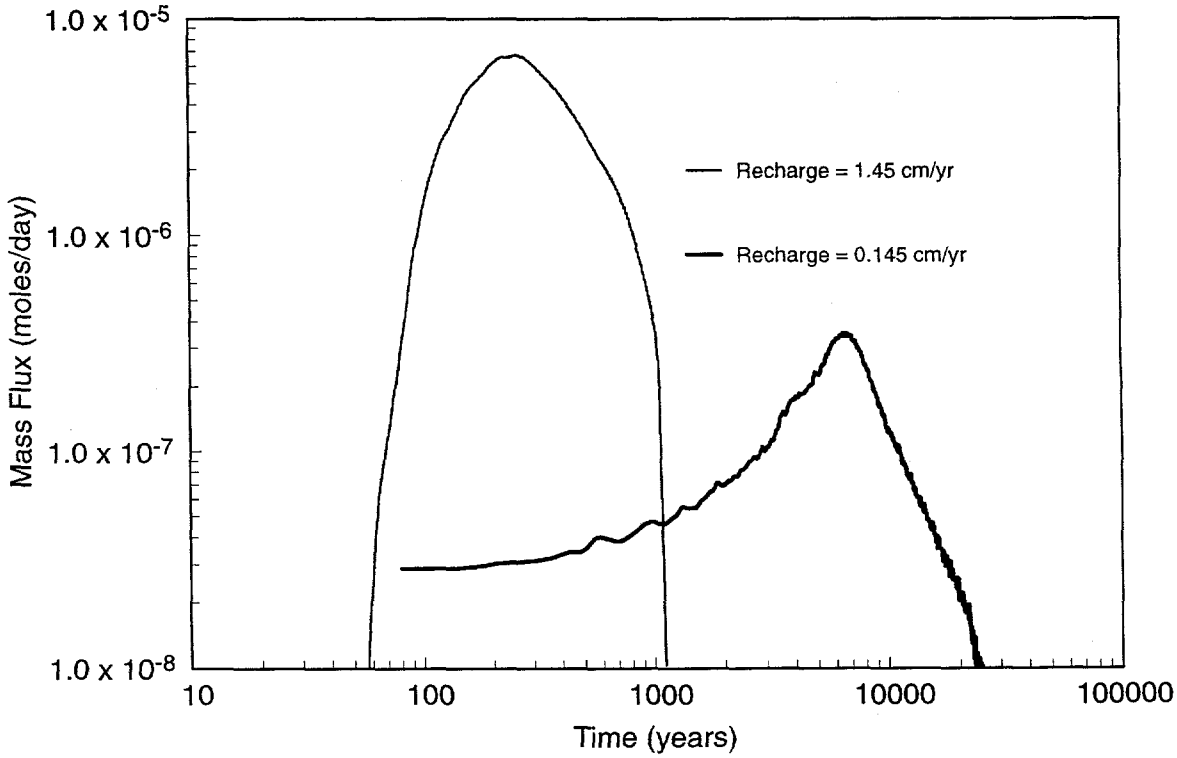

Figure 7.13. Normalized mean mass flux of tritium (unit initial mass and no decay) at the downgradient control plane for two values of surface recharge. Other transport parameters were: n = 0.006, R = 1.0, half-life = 12.3 years, and 100% hydraulic release. Source mass = 3.0×10^4 curies.

8.0 Discussion

8.1 Summation of Tritium, Strontium and Cesium

The simulated mean concentration, standard deviation and mass flux were presented separately at the downgradient control plane for tritium, ^{90}Sr, and ^{137}Cs based on unclassified estimates of initial mass. The migration behavior for each solute is essentially the same, with the differences in the magnitude of the mean concentration, standard deviation and mass flux due to differing initial masses, half-lives, and retardation (in the case of ^{137}Cs). The plumes show very little transverse dispersion with the majority of the solutes confined to an area of approximately 10^5 m^2 with the center of mass nearly 1800 m below ground surface. The limited dispersion is likely due to the scale of heterogeneity being at the same scale as the source. The significant vertical movement of the plume is due to the application of surface recharge.

The maximum mean concentration was estimated to be 13,000, 35,000 and 12,000 pCi/L for tritium, ^{90}Sr and ^{137}Cs, respectively. The magnitude of the standard deviation is 2000, 4000 and 1800 pCi/L for tritium, ^{90}Sr and ^{137}Cs. The bounding concentration ($\mu+2\sigma$) is 17,000, 43,000 and 15,600 pCi/L for tritium, ^{90}Sr and ^{137}Cs, respectively. The maximum mass flux occurs at 146, 154 and 247 years for tritium, ^{90}Sr and ^{137}Cs, respectively.

8.2 Impact of Sensitivity Analysis

Groundwater flow and transport modeling is a tool that combines all of the information collected into a single "model" of how the groundwater system behaves. The parameters used in the model contain a certain amount of uncertainty due to imperfections in the data collection and in the modeling structure. Some of the uncertainty can be addressed directly with powerful tools such as Monte Carlo analysis, which quantifies the uncertainty. Not all of the uncertain parameters can be included in the analysis. Some of these were addressed indirectly through sensitivity analysis, which involves the adjustment of the input parameters with an analysis of the associated impact on the transport behavior. In this case, the effective porosity and value of the specified head at the lower boundary condition impact the transport behavior significantly. For example, the peak mass flux across the downgradient control plane varied by six orders of magnitude with an adjustment of only 1.5 orders of magnitude in the porosity. The impact of the lower boundary condition was less pronounced with a 110-m decrease in the boundary head, causing the peak mass flux to decrease by 3 orders of magnitude due to a required reduction in hydraulic conductivity. One could argue that the uncertainty in the sorption properties plays a role in the transport similar to the porosity, as it has a direct impact on the relative plume velocity. Lastly, the characterization of subsurface heterogeneity is critical in terms of the simulated transport behavior. Most of this uncertainty was accounted for in the Monte Carlo analysis through the simulation of equiprobable fracture class fields and their associated flow fields. The analysis assumed that the geometry of the fracture classes represented the majority of the spatial variability and that a single hydraulic conductivity value could be assigned to each fracture class. The field data support this methodology, but as with all methods there are limitations. Specifically, a thermal flowmeter was used to identify the hydraulic conductivity values. Other methods (such as packer tests) may have allowed characterization of the

ranges in hydraulic conductivity that would significantly increase the spatial variability modeled in the flow system.

There are significant uncertainties that were not quantitatively examined through the sensitivity analysis, principally those that relate to the representation of the radionuclide source and its transport properties. These include the apportioning of radionuclides between glass and surface deposits, the release of surface-deposited materials, sorption and precipitation reactions, and colloidal transport. Ongoing research of underground tests at the Nevada Test Site has identified situations of unexpectedly retarded radionuclide transport, as well as surprisingly enhanced transport. Possible mechanisms being investigated include the role of iron oxide coatings and their distribution, colloids, and organic complexes. Findings from these studies will be applied to Shoal as they become available.

The results of the sensitivity analysis must be placed within the context of all the data collected such that a broad understanding of the groundwater flow and transport can be obtained. The most important data are those which relate to the fluid velocities. Other researchers made estimates of the fluid velocities based on indirect evidence. Hazelton-Nuclear Science (1965) estimated the mean fluid velocity to be 3 to 6 m/yr, while Gardner and Nork (1970) broadened the range to 0.3 to 30 m/yr. The flow modeling presented herein (Section 5.5.5), indicates a mean horizontal fluid velocity of 5 m/yr with the range being from essentially zero to 60 m/yr.

The hydrochemical evidence presented (Section 2.4.2) indicates that the travel times are very low. The absence of tritium and relatively old water in HC-1 (6000 years) and HC-2 (12,500 years) suggest very slow migration. It is difficult to estimate a groundwater velocity from its age alone, as the fluid path is not known. If one assumes that the flowpath begins on the topographic divide and the "clock" begins near the surface, then the maximum travel length to either HC-1 or HC-2 is approximately 800 m. About 300 m of this flowpath is in the vadose zone, where the estimated travel time (from recharge estimate) is approximately 100 years. Once in the groundwater, the fluid must travel the remaining 500 m in multiple thousands of years. Therefore, the velocities (assuming at least a 6000-year travel time) would be less than 0.1 m/yr, which is approximately 1.5 orders of magnitude smaller than the simulated values for the base case simulation.

There is a large degree of uncertainty associated with the velocities calculated via the ^{14}C approach. Age dating can be directly transferred to a groundwater velocity only if the system is closed to atmospheric CO_2 and if the flowpath is known. The degree of closure to atmospheric CO_2 in the Shoal unsaturated zone is unknown, and input of modern ^{14}C along the entire upper model domain may occur as a result of recharge. In addition, flow at Shoal has a strong vertical component that invalidates considering only lateral flowpaths. Perhaps most importantly, matrix diffusion and possibly isotopic exchange reactions, can retard ^{14}C as compared to groundwater velocities. These processes are expected to be relatively unimportant in the Shoal environment due to the very low granite block porosity and general lack of carbonate minerals, but they may account for some of the discrepancy with the calculated flow velocities.

Although there is a large discrepancy in the velocities estimated via the ^{14}C approach and the base case groundwater model, the results of the sensitivity analysis suggests that there are other possible configurations of the groundwater model that would decrease the apparent discrepancy. Specifically, decreasing the correlation scale of the fracture connectivities, reducing the surface recharge, and increasing the effective porosity yield velocities that are of the same magnitude as estimated via the ^{14}C approach.

The recharge estimate is critical in this analysis, as decreasing the recharge by one order of magnitude would delay the vadose zone travel time to at least 1000 years. A reduction in recharge would have resulted in a lower calibrated hydraulic conductivity for fracture class 1, which would reduce the mean groundwater velocity, possibly to the point of reducing the discrepancy between the numerical and isotopic results. The lack of significant heterogeneity found in the field campaign may also explain the differences between the hydrochemical and numerical model evidence.

The chemical and isotopic differences found between the granitic wells and Fairview Valley also suggest very slow velocities. If the velocities were large and flow volumes significant, then the water composition in the adjacent valley would be similar. This evidence suggests that the source of water in Fairview Valley is either from surface infiltration and/or pluvial recharge from the Sand Springs Range, but not recently recharged water from near the Shoal site.

8.3 Contamination Boundaries

The purpose of the modeling effort is to aid in characterizing groundwater flow and transport at Shoal. Ultimately, however, the calculations will support development of the CADD and provide a foundation for establishing areas that may contain contaminated groundwater. Appendix VI of the FFACO calls for establishing contaminant boundaries that define the aggregate maximum extent of contaminant transport at or above a concentration of concern, and in addition express modeling uncertainty through inclusion of a confidence interval in the boundary determination.

Simulations were performed to identify spatial boundaries within a given solute concentration. Tritium was selected to determine the maximum extent at which solute concentrations might exceed the EPA drinking water standard (20,000 pCi/L). The location of the boundary was determined through 100 groundwater flow and transport simulations to identify the 50th percentile (*i.e.*, median) probability of an area that would be located within such a boundary. For each simulation and at each time step, the concentration level is determined for each model grid cell. If the concentration exceeds the specified limit at any one vertical location, then a "hit" is recorded for that x-y location (areal perspective). Each of the x-y locations (72 x 24 = 1728 grid locations) is scanned to determine if the threshold is exceeded. This process is repeated for all simulation time or until one of the following criteria is met: 1) all of the simulated cell concentrations are less than the specified limit, or 2) if the total simulation time exceeds 1000 years. The simulations are performed in a Monte Carlo environment such that 100 equiprobable simulations are created. The 50th percentile boundary is determined by simply counting the number of realizations whereby the x-y cell location exceeded the threshold. The boundary is drawn around all cells that have at least 50 realizations that exceed

the limit. The process could be repeated for any confidence level. For example, if one wanted the 95 percent confidence level, then only 5 realizations would be required.

To illustrate the vertical location of the tritium plume, the same process was repeated, but the x-z plane was used as a spatial reference (72 x 49 = 3528). At each x-z cell position, all cells in the y direction were scanned and the cell was recorded as a hit if any one cell exceeded the threshold.

These boundaries are not snapshots in time. Rather, the boundary probabilistically represents all the locations the plume may encounter during the entire migration period. The plume boundary at any one point in time would be much smaller than the boundary presented.

The 50th percentile 20,000 pCi/L boundary for tritium in the areal plane is shown in Figure 8.1. The boundary extends downgradient beyond the land exclusion area. The width of the boundary diminishes downgradient, as this zone represents the leading edge of the plume. Radioactive decay reduces the concentration below the threshold by the time the trailing edge of the plume encounters the land exclusion boundary. The 50th percentile 20,000 pCi/L boundary extends beyond the downgradient control plane, yet maximum concentrations at the control plane were less than 20,000 pCi/L. This apparent discrepancy is due to differences in the calculation of the ensemble mean versus the concentrations found for the individual realizations. The ensemble mean concentration is presented at the time of peak mass flux, but the peak concentration at an individual model cell may not occur at the same time. Therefore, peak concentration for individual realizations may be larger than the ensemble mean.

The 50th percentile 20,000 pCi/L boundary along A-A' is shown in Figure 8.2. The strong vertical gradients cause the tritium to move downward hundreds of meters below ground surface. The downgradient edge of the boundary is nearly 1700 m below ground surface.

8.4 Interpretation of Contaminant Concentration Predictions

The mean radionuclide concentrations presented at the control plane, as well as the spatial distribution of concentration levels given in the preceding section, are subject not only to the data uncertainties examined in the sensitivity analysis, but also to the irreducible uncertainty caused by our imperfect knowledge of the heterogeneous aquifer through which flow and transport occurs. The level of this uncertainty is reflected in the standard deviation of the concentrations, which is generally of the same magnitude as the mean itself. This is problematic for attempts to validate predictions of contaminant concentrations with field measurements.

In addition, the procedures for measurement of concentration in the field itself affects resultant values and must be consistent with the scale of the model for meaningful comparison. The contaminant concentrations presented here are representative of concentrations averaged over the volume of water contained in one model grid cell, 4.4×10^5 liters, thus, observations of solute concentration must be on the same scale for comparison. Solute concentrations measured in groundwater are volume averages of local concentration, and various sampling methods result in different amounts of mixing of solute mass in sampled water volume. The observation procedure

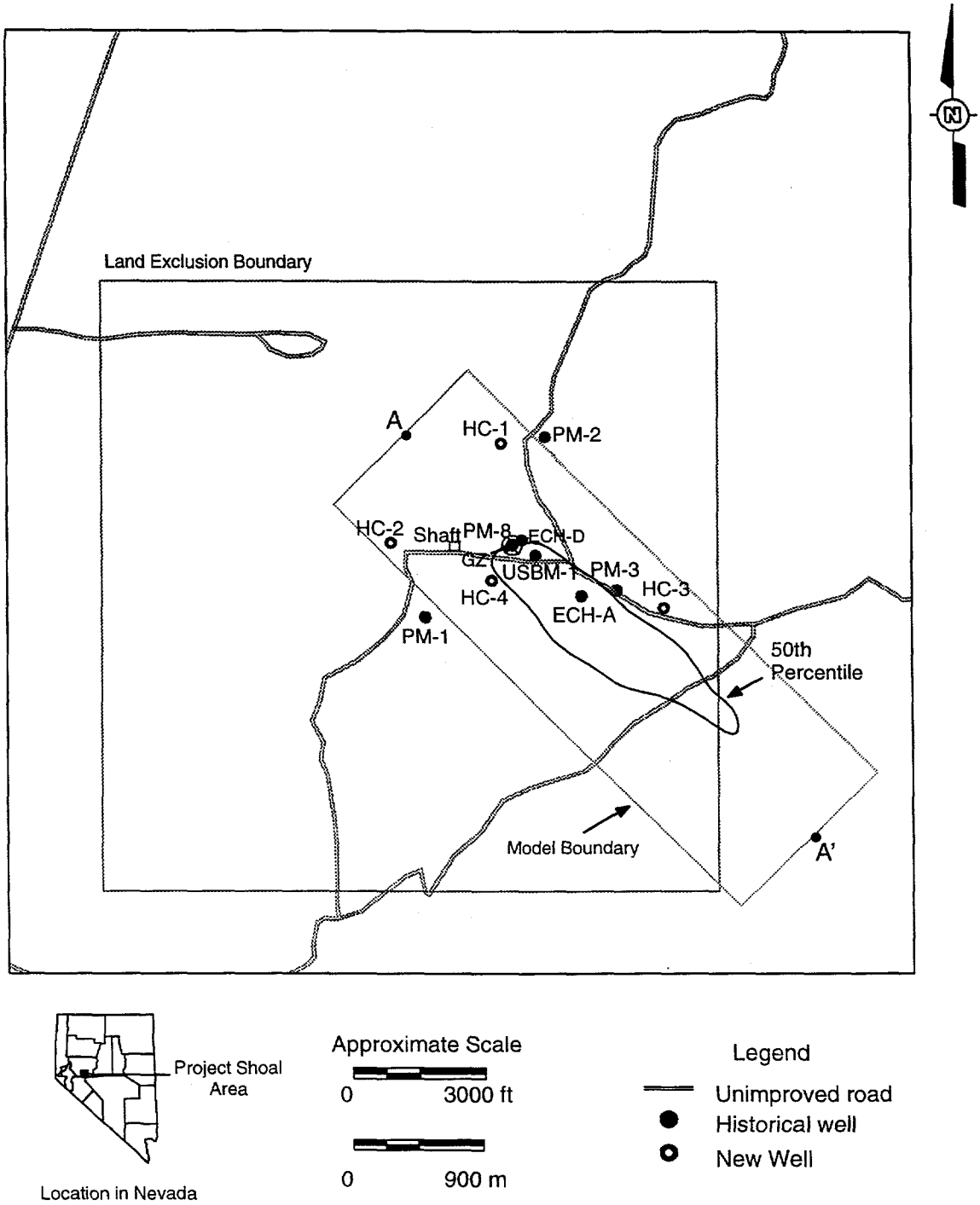

Figure 8.1. Map of the Shoal site with the simulated boundary (50th percentile) for tritium at 20,000 pCi/L. Transport parameters: n = 0.006, R = 1.0, half-life = 12.3 years, and 100% hydraulic release. Source mass = 3.0 x 10^4 curies.

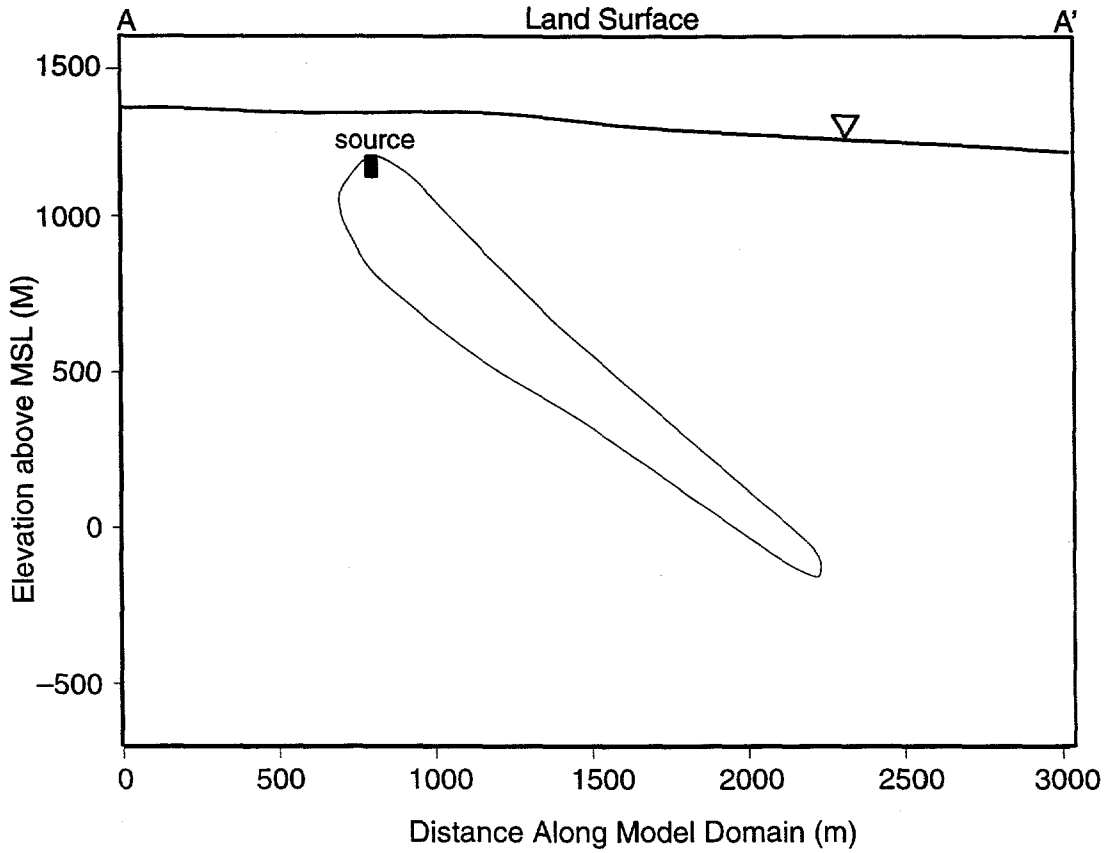

Figure 8.2. Cross section of the Shoal site with the simulated boundary (50th percentile) for tritium at 20,000 pCi/L.

additionally greatly influences the variance of locally measured solute concentrations (Destouni and Graham, 1997).

Aquifer pumping for a supply well necessarily introduces groundwater mixing, as well as causes perturbations to the flow field that will affect transport. As a result, concentrations that could conceivably be produced through a well and supplied to people, whether for agricultural, industrial, or domestic purposes, cannot be directly related to the predictions of *in situ* aquifer concentrations presented here.

9.0 Conclusions

Groundwater flow at Shoal is controlled by two sets of dipping fractures in competent granite. The site is in a recharge area, and a groundwater divide occurs west of the underground nuclear test so that flow is southeast towards Fairview Valley. The flow field is primarily controlled by the distribution and hydraulic conductivity of the fractures, and also by surface recharge. Significant uncertainties derive from the lack of successful field testing in the low hydraulic conductivity range that lead to a small range in modeled conductivity values, from uncertainty in the recharge rate, and from a lack of reliable hydraulic head values near the downgradient boundary. Additional large uncertainty is introduced by the effective porosity value necessary for transport simulations. Based

on the available data and flow model results, the mean groundwater velocity across the Shoal site is estimated at 5 m/day, a value that appears high in view of interpretations based on groundwater chemical and isotopic data. Although there is a large discrepancy in the velocities estimated from the chemical and isotopic data and the base case groundwater model, the results of the sensitivity analysis suggest that there are other possible configurations of the groundwater model that would decrease the apparent discrepancy. These include decreasing the correlation scale of the fracture connectivities, reducing the surface recharge, and increasing the effective porosity. Additional data would be required to verify both the groundwater model and the groundwater velocities derived from the isotopic data.

Release of contaminants from the nuclear test cavity relies on assumptions of radionuclide distribution between surface deposits and volume deposits in nuclear melt glass, and calculations of hydraulic release and glass dissolution rates. Non-retarded contaminants (transport case 1) without radioactive decay, are predicted to begin crossing the downgradient control plane 96 years (2059 AD) after the nuclear test, with the maximum mass flux occurring after 181 years (2144 AD) and all of the mass migrating beyond the control plane after 825 years (2788 AD). Significant downward migration occurs, driven by the recharge component. There is minimal plume spreading as a result of the alignment of conductive pathways along fracture trends, and as a result of the scale of hydraulic heterogeneity coinciding with the cavity size. Retardation, based on laboratory measurements of distribution coefficients, significantly delays migration of some reactive contaminants. The mass-reducing action of radioactive decay increases the sensitivity of the calculations to time-dependent processes such as retardation and release rates. Standard deviations of solute concentrations are on the same order as the mean value, quantifying some of the uncertainty discussed above.

Unclassified estimates of tritium, ^{90}Sr, and ^{137}Cs mass can be used to estimate contaminant migration to the downgradient control plane, along the site boundary. The peak mean concentration of the conservative solute, tritium, at the control plane is 13,000 pCi/l, which passes 146 years after the nuclear test. Due to the relatively high natural strontium in the granite, no retardation of ^{90}Sr was included in the calculations, with a resultant peak concentration of 35,000 pCi/l passing the boundary at 154 years. Cesium-137 is subject to retardation, which delays the arrival of the peak concentration of 12,000 pCi/l until 247 years after the test. These estimates are subject to significant uncertainties both in the flow and transport parameters.

The transport calculations are sensitive to many flow and transport parameters. Sensitivity analysis was performed to determine the relative sensitivity of each uncertain input parameter on model output. Mass flux at the downgradient control plane was used to compare the relative sensitivity for most of the uncertain parameters. The parameters include: effective porosity, hydraulic head (downgradient of the source), geologic heterogeneity (fractures and hydraulic conductivity), recharge, glass dissolution rates, and retardation.

There are no direct measurements of porosity and as such there is a wide range of values that may exist. The effective porosity drives the groundwater flow velocity which then impacts transport

behavior. This impact is amplified for radioactive solutes with short half-lives such as tritium. The sensitivity analysis indicates that uncertainty in almost 1.5 order of magnitude of porosity causes an uncertainty of about six orders of magnitude in the peak mass flux of tritium.

The hydraulic head downgradient of the source is not well defined, which causes large uncertainty in the specified boundary conditions of the groundwater model. The specified head for the base model was determined from the adjacent water levels in Fairview Valley. The water level in HC-3 is uncertain due to problems with the well installation, but the water level at HC-3 is lower than in Fairview Valley, suggesting steeper gradients. Sensitivity simulations with a specified head boundary condition of 1100 m (compared to 1210 m for the base case), increases the hydraulic gradient. To achieve reasonable water levels the hydraulic conductivity of the fracture class 1 was reduced to 1.0×10^{-7} cm/sec (from 4.0×10^{-7} cm/sec). Therefore, the net effect of lowering the boundary condition head was to decrease the mean velocities, decrease the peak mass flux and delay the arrival times.

The impact of fracture and hydraulic conductivity heterogeneity on transport behavior is critical. As shown in the heterogeneity sensitivity analysis, the fracture connectivity is more important than the variability in conductivity within a fracture class. Decreasing the correlation scale from 700 m to 50 m along the strike and dip decreased the peak mass flux by more than 10 orders of magnitude with the arrival time being more than 500 years greater than the base case. The hydraulic conductivity variation is uncertain due to the limits of the hydraulic testing. It is possible that there is more variability than was included in the flow simulations which will alter the transport behavior. Sensitivity analysis with increased conductivity variability indicates a later arrival time and decreased peak mass flux for tritium. The hydraulic testing and surface fracture mapping provide a subjective measure of the fracture aperture, and less so the fracture connectivity. The discrete hydraulic tests measure only a small volume of the aquifer, which does not provide a good measure of the fracture connectiveness. Surface fracture maps were used to quantify how the fractures persist spatially, but this is only secondary evidence of the fracture connection network. A more rigorous approach would be to use geophysics and/or cross-hole pressure tests to determine hydraulic properties over a larger volume. These types of tests will be evaluated as potential techniques to quantify the hydraulic characteristics of the fractured granite aquifer.

The sensitivity of the model to surface recharge was also tested. Although an independent estimate of recharge was made via thermal profiles, there is still a certain degree of uncertainty in the recharge estimate. There are many possible configurations of recharge and hydraulic conductivity that would provide equiprobable flow systems, but each would have its own unique transport behavior. Decreasing the surface recharge by one order of magnitude (0.145 cm/yr) also required a decrease in the hydraulic conductivity to achieve a reasonable level of agreement between the observed and simulated water levels. The base case (with no decay) has a peak mass flux of 7×10^{-6} moles/day at 266 years, while the reduced recharge simulation has a peak mass flux of 4×10^{-7} moles/day at 6445 years. The inclusion of radioactive decay for tritium would only amplify the differences in the transport behavior. The plumes for both cases intersect the control plane at nearly identical locations. This indicates that decreasing the recharge, with a simultaneous decrease in the

magnitude of conductivity, continues to yield flux fields with a significant downward component as found in the base case.

The impact of the glass dissolution is more pronounced for species that are trapped in the puddle glass (*e.g.*, ^{99g}Tc). Decreasing the release rate from 2.3 x 10^{-6} day^{-1} to 2.4 x 10^{-9} day^{-1} for ^{90}Sr (60 percent glass dissolution) causes little difference in the peak mass flux, while for ^{99g}Tc (95 percent glass dissolution) the peak mass flux increases by four times.

The retardation is important for transport cases 2, 6 and 7. The uncertainty in retardation is due to many factors including the estimated fracture aperture, the assumption that sorption is a linear process, the use of surrogates to approximate the actual sorption and the spatial variability in sorption properties. The uncertainty in retardation would most strongly impact transport case 7, which was assigned a R = 83.7.

The large uncertainties in the parameters supporting this model indicate that additional field characterization may be necessary. This model will be used in conjunction with a data decision analysis (DDA) to identify parameters that yield the most modeling uncertainty. After the completion of the DDA, critical input parameters will be identified and additional field characterization will be performed. Once additional data are collected a second groundwater model will be constructed with the new data. The second phase of the modeling effort will support the development of the CADD for the site.

10.0 Recommendations for Future Work

The model sensitivity to many of the input parameters was addressed in previous sections (section 7.3 and 9.0), but the analysis was focused on sensitivity, not the reduction of uncertainty that could be gained by collecting additional data. Recommendations for additional field work will be proposed after a DDA is performed. The eight parameters identified as uncertain will be investigated:

- Effective porosity
- Hydraulic head (mostly downgradient of the source)
- Hydraulic conductivity (mean and variance)
- Recharge
- Fracture connectivities (*i.e.*, correlation scales)
- Fracture orientation
- Glass dissolution rates
- Retardation

The analysis methodology will differ from a standard uncertainty analysis by focusing on the relationship of uncertainty reduction as a function of data collected. The results will focus any data

collection activities. Each uncertain parameter will be evaluated separately with a detailed analysis of how the model uncertainty will be reduced as additional data are collected. This information will be used to decide how much additional data are required for each of the eight parameters listed above. There are a variety of measurement techniques possible for data collection for each parameter in question. Each technique will be evaluated for data worth (via the data decision analysis), accuracy, feasibility, and cost. After additional data collection, a second groundwater model will be constructed and provide an improved evaluation of groundwater flow and transport at the Shoal Site.

11.0 Bibliography

Adams, P.B., 1984. Glass corrosion: A record of the past? A predictor of the future? *J. Non–Crystalline Solids 67*:193–205.

Allison, G.B., C.J. Barnes, M.W. Hughes and F.W. Leaney, 1984. Effect of climate and vegetation on oxygen-18 and deuterium profiles in soils. International Atomic Energy Agency, IAEA-SM-270/20, pp. 105-123.

Allison, G.B. and M.W. Hughes, 1978. The use of environmental tritium and chloride to estimate total recharge to an unconfined aquifer. *Aust. J. Soil Res.*, 16:181-195.

American Society for Testing and Materials, 1995. The Standard Guide for Calibrating a Groundwater Flow Model Application, Section D18.21.10, Designation C-7, Draft No. 4, September 21.

Andricevic, R., 1990. A real-time approach to management and monitoring of groundwater hydraulics. *Water Resources Research,* 26(11):2747-2755.

Andricevic, R., 1993. Coupled withdrawal and sampling designs for groundwater supply models. *Water Resources Research,* 29(1):5-16.

Andricevic, R., J. Daniels and R. Jacobson, 1994. Radionuclide migration using a travel time transport approach and its application in risk analysis. *Journal of Hydrology,* 163:125-145.

Andricevic, R. and V. Cvetkovic, 1996. Evaluation of risk from contaminants migrating by groundwater. *Water Resources Research,* 32(3):611-621.

Andricevic, R. and V. Cvetkovic, 1997. Relative dispersion for solute flux in aquifers. *Journal of Fluid Mechanics* (in press).

Arsham, H., 1989. On the inverse problem in Monte Carlo experiments. *Inverse Problems,* 5:927-934.

ASTM, 1994. Standard Guide for Conducting a Sensitivity Analysis for a Ground-Water Flow Model Application. ASTM, Philadelphia, PA.

ASTM, 1995. Standard Guide for Calibrating a Ground-Water Flow Model Application. ASTM, Philadelphia, PA.

Atkinson, C.H., 1964. Subsurface Fracturing from Shoal Nuclear Detonation. U. S. Department of Interior, Bureau of Mines, PNE–3001, 30p.

Ayers, J.F., 1989. Application and Comparison of Shallow Seismic Methods in the Study of an Alluvial Aquifer. *Groundwater,* 27(4):550-563.

Barnes, C.J. and G.B. Allison, 1983. The distribution of deuterium and ^{18}O in dry soils, 1, Theory. *J. Hydrol.*, 60:141-156.

Bateman, R.L. and J.W. Hess, 1978. Hydrologic Inventory and Evaluation of Nevada Playas. Desert Research Institute, Water Resources Center, Project Report No. 49.

Beall, G.W., G.D. O'Kelley and B. Allard, 1980. An Autoradiographic Study of Actinide Sorption on Climax Stock Granite. Oak Ridge National Laboratory, ORNL–5617, 27p.

Bedford, R.G. and D.D. Jackson, 1965. Volatilities of the Fission Product and Uranium Oxides. Lawrence Livermore National Laboratory, UCRL–12314, 37 p.

Beers, R.F., Inc., 1964. Analysis of Shoal Data on Ground Motion and Containment. U. S. Atomic Energy Commission, Vela Uniform Project Shoal, VUF–1013, 112 p.

Benson, L.V. and R.S. Thompson, 1987. Lake-level Variation in the Lahontan Basin for the past 50,000 years. *Quaternary Research*. V. 28, 69-85.

Bibby, R., 1981. Mass transport of solutes in dual-porosity media. *Water Resources Research,* 17(4):1075-1081.

Borg, I.Y., 1975. Radioactivity trapped in melt produced by a nuclear explosion. *Nuclear Technology, 26*:88–100.

Borg, I.Y., R. Stone, H.B. Levy and L.D. Ramspott, 1976. Information Pertinent to the Migration of Radionuclides in Ground Water at the Nevada Test Site, Part 1: Review and Analysis of Existing Information. Lawrence Livermore National Laboratory, UCRL–52078 Pt. 1, 216 p.

Bredehoeft, J.D. and I.S. Papadopulos, 1965. Rates of vertical groundwater movement estimated from the earth's thermal profile. *Water Resources Research*, 1(2):325-328.

Brutsaert, W., 1982. Evaporation into the atmosphere, Kluwer Academic Publishers, London, 299 p.

Bryant, E.A. and J. Fabryka–Martin, 1991. Survey of Hazardous Materials used in Nuclear Testing. Los Alamos National Laboratory, LA–12014–MS, 12 p.

Bryant, E.A. and S. Papadopulos, 1980. A method for determining the hydraulic properties of tight formations. *Water Resources Research,* 16(1):233-238.

Cacas, M., E. Ledoux, G. de Marsily, B. Tillie, A. Barbreau, E. Durand and B. Feuga, 1990. Modeling fracture flow with a stochastic discrete fracture network: calibration and validation 1. The flow model. *Water Resources Research,* 26(3):479-489.

Chapman, J. and S. Hokett, 1991. Evaluation of Groundwater Monitoring at Offsite Nuclear Test Areas. Desert Research Institute, Water Resources Center, Publication No. 45085. 24 p.

Chapman, J., T. Mihevc and A. McKay, 1994a. Groundwater Flow near the Shoal Site, Sand Springs Range, Nevada: Influence of Density Driven Flow. Desert Research Institute, Water Resources Center, Publication No. 45130. 24 p.

Chapman, J.B., S.W. Tyler, M.L. Davisson, and C.A. Shadel, 1994b. Carbon-14 Age Dating of Soil Water from a Thick Vadose Zone in Southern Nevada, Geological Society of America, Abstracts with Program, p. 391.

Chapman, J., K. Pohlmann and R. Andricevic, 1995. Exposure Assessment of Groundwater Transport of Tritium from the Shoal Site. Desert Research Institute, Water Resources Center, Publication No. 45132. 30 p.

Chin, D. and T. Wang, 1992. An investigation of the validity of first-order stochastic dispersion theories in isotropic porous media. *Water Resources Research,* 28(6):1531-1542.

Claassen, H.C. and E.H. Cordes, 1975. Two-well recirculating tracer test in fractured carbonate rock, Nevada. *Hydrological Sciences Bulletin*, 20(3).

Cohen, P. and D. Everett, 1963. A brief appraisal of the ground-water hydrology of the Dixie-Fairview Valley area, Nevada. Ground-water Resources Reconnaissance Series, Vol. 23. Carson City: State of Nevada, Department of Conservation and Natural Resources. 40 p.

Cooper, H. J., J. Bredehoeft and I. Papadopulos, 1967. Response of a finite-diameter well to an instantaneous charge of water. *Water Resources Research,* 3(1)::263-269.

Cvetkovic, V. and A. Shapiro, 1990. Mass arrival of sorptive solute in heterogeneous porous media. *Water Resources Research,* 26(9):2057-2067.

Cvetkovic, V. and G. Dagan, 1994. Transport of kinetically sorbing solute by steady random velocity in heterogeneous porous formation. *Journal of Fluid Mechanics*, 265:189–215.

Dagan, G., V. Cvetkovic and A. Shapiro, 1992. A solute flux approach to transport in heterogeneous formations 1. The general approach. *Water Resources Research,* 28(5):1369-1376.

Datta-gupta, A., D. Vasco and J. Long, 1997. On the sensitivity and spatial resolution of transient pressure and tracer data for heterogeneity characterization. *SPE Formation Evaluation* (June):137-144.

Derlich, S., 1970. Underground Nuclear Explosion Effects in Granite Rock Fracturing. Proc. Symp. Engineering with Nuclear Explosives, CONF–700101, Vol. 1:505–518.

Destouni, G. and W. Graham, 1997. The influence of observation method on local concentration statistics in the subsurface. *Water Resources Research*, 33(4):663–676.

Deutsch, C.V. and A.G. Journel, 1992. GSLIB, Geostatistical Software Library and User's Guide, Oxford University Press, New York, 340 p.

Domenico, P.A. and F.W. Schwartz, 1990. Physical and Chemical Hydrogeology. John Wiley & Sons, New York.

Driscoll, F.G, 1986, Groundwater and Wells, Johnson Screens, St. Paul, Minnesota, 1089 pp.

Dupuis, M., 1970. Distribution and Evolution of Radioelements After a Nuclear Explosion. Bull. Infor. Sci. Tech., 149: Lawrence Livermore National Laboratory, 1972, UCRL–Trans–10617–5.

Duffy, C. and S. Al-Hassan, 1988. Groundwater circulation in a closed desert basin: Topographic scaling and climatic forcing. *Water Resources Research,* 24(10):1675-188.

Dverstorp, B., J. Andersson and W. Nordqvist, 1992. Discrete fracture network interpretation of field tracer migration in sparsely fractured rock. *Water Resources Research,* 28(9):2327-2343.

Earman, S. and G. Pohll, 1997. Shoal Field Operations, unpublished letter report to the U.S. Department of Energy, Nevada Operations Office, Las Vegas, Nevada.

Endo, H., J. Long, C. Wilson and P. Witherspoon, 1984. A model for investigating mechanical transport in fracture networks. *Water Resources Research,* 20(10):1390-1400.

Essington, E.H. and J.V.A. Sharp, 1968. Some Aspects of Ground–Water Solution Chemistry, Underground Nuclear Explosion Zones, Nevada Test Site. In Eckel, E.B., Nevada Test Site, Geological Society of America Memoir 110, pp.263–273.

Failor, R., D. Isherwood, E. Raber and T. Vandergraaf, 1982. Laboratory Studies of Radionculide Transport in Fractured Climax Granite. Lawrence Livermore National Laboratory, UCRL–53308, 73p.

Failor, R.A., D.G. Coles and J.H. Rego, 1983. A Leaching Study of Nuclear Melt Glass: Part I. Lawrence Livermore National Laboratory, UCRL–ID–19729, 71 p.

Faure, G, 1977. Radioactive Decay and Growth. Principles of Isotope Geology-Second Edition. John Wiley & Sons, Inc., 38-47.

Freeze, R.A. and J.A. Cherry, 1979. Groundwater, Prentice-Hall, Inc., Englewood Cliffs, New Jersey.

Frick, U., W. Alexander, B. Baeyens, P. Bossart, M.H. Bradbury, Ch. Bühler, J. Eikenberg, Th. Fierz, W. Heer, E. Hoehn, I.G. McKinley and P.A. Smith, 1991. Grimsel Test Site - The Radionuclide Migration Experiment - Overview of Investigations 1985-1990. National Cooperative for the Disposal of Radioactive Waste Technical Report 91–94.

Fried, J.J., P.C. Leveque, D. Poitrinal and J. Severac, 1974. Local studies of miscible pollutions of groundwater: the single well pulse technique. Groundwater Pollution in Europe, ed. J.A. Cole. Water Information Center, Port Washington, N.Y., pp.388-406.

Fried, J.J. 1976. Groundwater Pollution, Elsevier, Amsterdam, 330 p.

Furbish, D.J., 1991. The response of water level in a well to a time series of atmospheric loading under confined conditions. *Water Resources Research*, 27(4):557-568.

Gardner, M. and W. Nork, 1970. Evaluation of the Project Shoal Site, Fallon, Nevada, for Disposition, Including Identification of Restrictions, Part I. Palo Alto, CA. Teledyne Isotopes. 42p.

Gelhar, L., 1993. Stochastic Subsurface Hydrology. Englewood Cliffs, New Jersey. Prentice Hall.

Gendzwill, D. J. and M. R. Stauffer, 1981. Analysis of triaxial ellipsoids: Their shapes, plane sections, and plane projections. *Mathematical Geology,* 13(2):135-152.

Gislason, S.R. and H.P. Eugster, 1987a. Meteoric water–basalt interactions. I: A laboratory study. *Geochim. et Cosmochim. Acta 51*:2827–2840.

Gislason, S.R. and H.P. Eugster, 1987b. Meteoric water–basalt interactions. II: A field study in N.E. Iceland. *Geochim. et Cosmochim. Acta 51*:2841–2855.

Glancy, P. and Katzer, 1975. Water Resources Appraisal of the Carson River Basin, Western Nevada, Water Resources - Reconnaissance Series, Vol. 59. Carson City, State of Nevada, Department of Conservation and Natural Resources. 126 p.

Glass, B.P., 1984. Solution of Naturally–Occurring Glasses in the Geological Environment. *J. Non–Crystalline Solids 67*:265–286.

Goishi, W., B. Esser, J. Meadows, N. Namboodiri, D. Smith, J. Wild, S. Bowen, P. Baca, L. Olivas, C. Geoffrion, J. Thompson and C. Miller, 1994. Total Radionuclide Inventory Associated with Underground Nuclear Tests Conducted at the Nevada Test Site 1955–1992. Los Alamos National Laboratory, LA–CP–94–0222, 242 p., Secret–Restricted Data.

Goishi, W., J.W. Meadows, N. Namboodiri, D.K. Smith and J.F. Wild, 1995. Radionuclide Inventory for U.S. Nuclear Tests Conducted Off the NTS and Hydronuclear and Safety Experiments Conducted on the NTS, Lawrence Livermore National Laboratory, UCRL–ID–121901, Secret–Restricted Data.

Grove, D.B. and W.A. Beetem, 1971. Porosity and dispersion constant calculations for a fracture carbonate aquifer using the two well tracer method. *Water Resources Research*, 7(1):128-134.

Hampton, C.M. and D.K. Bailey, 1984. Gas Extraction experiments on volcanic glasses. *J. Non–Crystalline Solids, 67*:147–168.

Hardman, G. and H.G. Mason, 1949. Irrigated lands of Nevada. Nevada University Agr. Sta. Bulletin 183, 56 pp.

Hazelton–Nuclear Science Corp., 1965. Post–Shot Hydrologic Safety, Project Shoal Final Report. U.S. Atomic Energy Commission, Vela Uniform Project Shoal, VUF–1014, 50 p.

Hershey, R.L., B.F. Lyles and J.W. Hess, 1989. Delineation of Mountain Block Recharge Using Carbon Isotopes in the Spring Mountains, Nevada. In 28th International Geological Congress Abstracts, Vol. 2, Washington D.C.

Hill, M.C., 1990. Preconditioned Conjugate-Gradient 2 (PCG2), A computer program for solving ground-water flow equations. U.S. Geological Survey, Denver, Colorado.

Hoehn, E., T. Fierz and P. Thorne, 1989. Hydrogeological Characterization of the Migration Experimental Area at the Grimsel Test Site. NAGRA.

Hoeksema, R. and P. Kitanidis, 1985. Analysis of spatial structure of properties of selected aquifers. *Water Resources Research,* 21(2):563-572.

Hsieh, P.A., S.P. Neuman and E.S. Simpson, 1983. Pressure testing of fractured rocks - A methodology employing three-dimensional cross-hole tests, NUREG/CR-3213.

Hsieh, P. and S. Neuman, 1985. Field determination of the three-dimensional hydraulic conductivity tensor of anisotropic media, 1. Theory. *Water Resources Research,* 21(11):1655-1665.

Huyakorn, P.S., B.H. Lester and J.W. Mercer. 1983. An efficient finite element technique for modeling transport in fractured porous media, 1. Single species transport. *Water Resources Research,* 19(3):841-854.

Huyakorn, P.S., S. Neuman and E. Simpson, 1983. Pressure Testing of Fractured Rocks - A Methodology Employing Three-Dimensional Cross-Hole Tests. University of Arizona. 176 p.

Huyakorn, P.S., S. Neuman, G. Stiles and E. Simpson, 1985. Field determination of the three-dimensional hydraulic conductivity tensor of anisotropic media, 2. Methodology and application to fractured rocks. *Water Resources Research,* 21(11):1667-1676.

Jacobson, R.L., N.L. Ingraham and M.E. Campana, 1983. Isotope Hydrology of a Basin and Range Geothermal System. Desert Research Institute, Water Resources Center Publication No. 41087, 18p.

Jankovic, I. and R. Andricevic, 1996. Spatial and temporal analysis of groundwater recharge with application to sampling design. *Stochastic Hydrology and Hydraulics,* 10:39-63.

Jantzen, C.M. and M.J. Plodinec, 1984. Thermodynamic model of natural, medieval and nuclear waste glass durability. *J. Non–Crystalline Solids 67*:207–223.

Jerome, S.E., 1965. Geologic Mapping and Guidance, in University of Nevada, Geological, Geophysical, Chemical and Hydrological Investigations of the Sand Springs Range, Fairview Valley and Fourmile Flat, Churchill County Nevada. VUF-1001, pp155-159.

Jury, W.A., W.R. Gardner and W.H. Gardner, 1991. Soil Physics, John Wiley and Sons, Inc., New York, 328 p.

Kemblowski, M. and C. Klein, 1988. An automated numerical evaluation of slug test data. *Ground Water,* 26(4):435-438.

Kersting, A.B., 1996. The State of the Hydrologic Source Term. Lawrence Livermore National Laboratory, UCRL–ID–126557, 30 p.

Koltermann, C. and S. Gorelick, 1996. Heterogeneity in sedimentary deposits: A review of structure-imitating, and descriptive approaches. *Water Resources Research,* 32(9):2617-2658.

Kool, J., J. Parker and M. T. van Genuchten, 1987. Parameter estimation for unsaturated flow and transport models - A review. *Water Resources Research,* 91:255-293.

Krikorian, O.H., 1981. Predictive Calculations of Volatilities of Metals and Oxides in Steam–Containing Environments. Lawrence Livermore National Laboratory, UCRL–85553, 27 p.

Landmeyer, J.E., 1996. Aquifer Response to Record Low Barometric Pressures in the southeastern United States. *Groundwater*, 34(5):917.

Lassey, K., 1988. Unidimensional solute transport incorporating equilibrium and rate-limited isotherms with first-order loss, 1. Model conceptualizations and analytic solutions. *Water Resources Research,* 24(3):343-350.

Lassey, K., 1988. Unidimensional solute transport incorporating equilibrium and rate-limited isotherms with first-order loss, 2. an approximated simulation after a pulsed input. *Water Resources Research,* 24(3):351-355.

LaVenue, A. M. and J. Pickens, 1992. Application of a coupled adjoint sensitivity and kriging approach to calibrate a groundwater flow model. *Water Resources Research,* 28(6):1543-1569.

Lebbe, L. and W. De Breuck, 1995. Validation of an inverse numerical model for interpretation of pumping tests and a study of factors influencing accuracy of results. *Journal of Hydrology,* 172, 61-85.

Long, J.C.S., P. Gilmour and P.A. Witherspoon, 1985. A model for steady fluid flow in random 3-D network of disc shaped fractures. *Water Resources Research*, 21(8):1105-1115.

Long, J., K. Karasaki, A. Davey, J. Peterson, M. Landsfeld, J. Kemeny and S. Martel, 1991. An inverse approach to the construction of fracture hydrology models conditioned by geophysical data. *International Journal of Rock Mechanics, Mining Science and Geomechanical Abstracts*, 28(2/3):121-142.

Long, J., C. Remer, P. Wilson and P. Witherspoon, 1982. Porous media equivalents for networks of discontinuous fractures. *Water Resources Research,* 18(3):645-658.

Lyles, B., 1994. Increased thermal-pulse flowmeter resolution by adding a packer and computer. *Ground Water Monitoring and Remediation* (Fall).

Maxey, G. and T. Eakin, 1949. Ground water in the White River Valley, White Pine, Nye, and Lincoln Counties, Nevada, Water Resources Bulletin, vol. 8. Carson City, Nevada: State of Nevada, Office of the State Engineer. 59 p.

McDonald, M.G. and A.W. Harbaugh, 1988. A Modular Three-Dimensional Finite-Difference Ground-Water Flow Model (MODFLOW): Chapter A1–Book 6. U.S. Geological Survey, Water Resources Investigations.

McDonald, M.G., A.W. Harbaugh, B.R. Orr and D.J. Ackerman, 1991. A method of converting no-flow cells to variable-head cells for the U.S. Geological Survey Modular Finite-Difference Ground-Water Flow Model. U.S. Geological Survey Open-File Report 91–536.

McKee, C. and M. Hanson, 1975. Explosively created permeability from single charges. *Society of Petroleum Engineers Journal,* 12:495-501.

Michel, J. and M. Jordana, 1987. Nationwide Distribution of Radium-228, Radium-226, Radon-222, and Uranium in Groundwater. In Radon, Radium, and Other Radioactivity in Ground Water, Barbara Graves, editor, Lewis Publishers, Chelsea, Michigan, pp. 227-240.

Molz, F., R. Morin, A. Hess, J. Melville and O. Guven, 1989. The impeller meter for measuring aquifer permeability variations: Evaluation and comparison with other tests. *Water Resources Research,* 25(7):1677-1683.

Moody, J.B., 1982. Radionuclide Migration/Retardation: Research and Development Technology Status Report. Office of Nuclear Waste Isolation, ONWI–321, 61p.

Mook, W.G., 1980. Carbon–14 in Hydrogeological Studies. In Handbook of Environmental Isotope Geochemistry, Vol. 1 (P. Fritz and J. Ch. Fontes, Eds.), Elsevier Pub. Co. Amsterdam, pp.49–71.

Moreno, L., Y. Tsang, C. Tsang, F. Hale and I. Neretnieks, 1988. Flow and tracer transport in a single fracture: A stochastic model and its relation to some field observations. *Water Resources Research,* 24(12):2033-2048.

Moreno, L. and C. Tsang, 1994. Flow channeling in strongly heterogeneous porous media: A numerical study. *Water Resources Research,* 30(5):1421-1430.

Mosegaard, K. and A. Tarantola, 1995. Monte Carlo sampling of solutions to inverse problems. *Journal of Geophysical Research,* 100(B7):12431-12447.

NAGRA (National Cooperative for the Disposal of Radioactive Waste), 1994. Kristallin–I Safety Assessment Report. National Cooperative for the Disposal of Radioactive Waste, Technical Report 93–22, 396p.

Neretnieks, I., 1980. Diffusion in the rock matrix: An important factor in radionuclide retardation. *Journal of Geophysical Research,* 85(B8):4379-4397.

Neuman, S.P. and S. Joseph, 1988. Use of variable-scale pressure test data to estimate the log hydraulic conductivity covariance and dispersivity of fractured granites near Oracle, Arizona. *Water Resources Research,* 102:475-501.

Neuzil, C., 1982. On conducting the modified slug test in tight formations. *Water Resources Research,* 18(2):439-441.

Nordqvist, A.W., Y. Tsang, C. Tsang, B. Dverstorp and J. Andersson, 1992. A variable aperature fracture network model for flow and transport in fractured rocks. *Water Resources Research,* 28(6):1703-1713.

Nork, W.E. and P.R. Fenske, 1970. Radioactivity in Water – Project Rulison. U.S. Atomic Energy Commission, Nevada Operation Office Report NVO–1229–131, 14p.

Novakowski, K., 1990. Analysis of aquifer tests conducted in fractured rock: A review of the physical background and the design of a computer program for generating type curves. *Ground Water,* 28(1):99-107.

Paillet, F.L. and J.D. Olson, 1991. Analysis of the results of hydraulic-fracture simulation of two crystalline bedrock boreholes, Grand Portage, Minnesota. U.S. Geological Survey, WRI 94-4044, 45 p.

Papadopulos, I. and H. Cooper, Jr., 1967. Drawdown in a well of large diameter. *Water Resources Research,* 3(1):241-244.

Papadopulos, S., J. Bredehoeft and H.J. Cooper, 1973. On the analysis of 'slug test' data. *Water Resources Research,* 9(4):1087-1089.

Percious, D. J., 1969. Aquifer dispersivity by recharge-discharge of a fluorescent dye tracer through a single well. Unpublished M.S. Thesis, University of Arizona.

Phillips, F.M., J.L. Mattick, T.A. Duval, D. Elmore and P.W. Kubick, 1988. Chlorine-36 and tritium from nuclear-weapons fallout as tracer for long-term liquid and vapor movement in desert soils. *Water Resources Research,* 24:1877-1891.

Plata, A., 1990. Parameters of carbonate rock aquifers from tracer methods. Hydrogeological Processes in Karst Terranes.

Plummer, L.N., B.F. Jones and A.H. Truesdell, 1976. WATEQF – A FORTRAN IV Version of WATEQ, A Computer Program for Calculating Chemical Equilibrium of Natural Waters. U.S. Geological Survey, Water-Resources Investigations 76-13, 63 p.

Pohll, G. and K. Pohlmann, 1996, Evaluation of the radionuclide tracer test conducted at the project Gnome underground nuclear test site, New Mexico, Desert Research Institute, Water Resources Center Publication #45141.

Pohlmann, K. and R. Andricevic, 1994. Identification of Potential Groundwater Flowpaths Using Geological and Geophysical Data. Desert Research Institute, Water Resources Center, Publication No. 45128, 23 p.

Pohlmann, K., C. Shirley and R. Andricevic, 1996. Near-Field Modeling in Frenchman Flat, Nevada Test Site. Desert Research Institute, Water Resources Center, Publication No. 45154, 24 p.

Rabb, D.D., 1970. Particle–Size Distribution Study: Piledriver Event. Proc. Symp. Engineering with Nuclear Explosives, CONF–700101, Vol. 2, pp.888–908.

Ramspott, L.D., J.D. Tewhey, D.G. Coles, H.C. Weed, J.S. Schweiger and R. Stone, 1979. FY78 Annual Technical Report of Lawrence Livermore Laboratory's Participation in the DOE–NV Project: Radionuclide Migration in the Ground. Lawrence Livermore National Laboratory, UCID–18259–78, 29 p.

Raven, K., K. Novakowski and P. Lapcevic, 1988. Interpretation of field tracer tests of single fracture using a transient solute storage model. *Water Resources Research,* 24(12):2019-2032.

Raven, K., L. Smith and R.A. Freeze, 1992. Hydrogeological scoping calculations on radionuclide transport to the biosphere. Report of the Subsurface Advisory Team to Environment Canada on the Canadian Nuclear Fuel Waste Disposal Concept, Tech. Appendix 2.

Raven, K., L. Smith and R.A. Freeze, 1993. Radionuclide transport to the biosphere. Report of the Subsurface Advisory Team to Environment Canada on the Canadian Nuclear Fuel Waste Disposal Concept, Tech. Appendix 8.

Rehfeldt, K., J. Boggs and L. Gelhar, 1992. Field study of dispersion in a heterogeneous aquifer, 3. Geostatistical analysis of hydraulic conductivity. *Water Resources Research,* 28(12):3309-3324.

Schilling, J.H., 1965. Exposure of Minerals and Other Substances to High–Pressure Shock–Waves. In University of Nevada, Geological, Geophysical, Chemical, and Hydrological Investigations of the Sand Springs Range, Fairview Valley, and Fourmile Flat, Churchill County, Nevada. U. S. Atomic Energy Commission, Vela Uniform Project Shoal, VUF–1001, pp. 193–202.

Schwartz, F.W., L. Smith and A. Crowe, 1983. A stochastic analysis of macroscopic dispersion in fractured media. *Water Resources Research,* 19(5):1253-1265.

Schwartz, L., A. Piwinskii, F. Ryerson, H. Tewes and W. Beiriger, 1984. Glass produced by underground nuclear explosions. *J. Non–Crystalline Solids 67*:559–591.

Schwartz, F.W. and L. Smith, 1988. A continuum approach for modeling mass transport in fractured media. *Water Resources Research*, 24(8):1360-1372.

Selroos, J., A. Winberg and V. Cvetkovic, 1994. Design constraints and process discrimination for the detailed scale tracer experiments at Aspo – multiple well tracer experiment and matrix diffusion. SKB, International Cooperation Report 94–04.

Selroos, J. and V. Cvetkovic, 1994. Mass flux statistics of kinetically sorbing solute in heterogeneous aquifers: Analytical solution and comparison with simulations. *Water Resources Research,* 30(1):63-69.

Selroos, J., 1996. Contaminant Transport by Groundwater: Stochastic Travel Time Analysis and Probabilistic Safety Assessment, Diss. Stockholm, Sweden: Royal Institute of Technology, 50 p.

Shapiro, A.M. and J. Anderson, 1985. Simulation of steady-state flow in three-dimensional networks using the boundary element methods. *Water Resources Research*, 8:106-110.

Shapiro, A. and J. Nicholas, 1989. Assessing the validity of the channel model of fracture aperture under field conditions. *Water Resources Research,* 25(5):817-828.

Shirley, C., K. Pohlmann and R. Andricevic, 1996. Three-dimensional Mapping of Equiprobable Hydrostratigraphic Units at the Frenchman Flat Corrective Action Unit, Nevada Test Site. Desert Research Institute, Water Resources, Publication No. 45152.

Smith, D.K., 1993. A Review of Literature Pertaining to the Leaching and Sorption of Radionuclides Associated with Nuclear Explosive Melt Glasses. Lawrence Livermore National Laboratory, UCRL–ID–113370, 26 p.

Smith, D.K., B.K. Esser and J.L. Thompson, 1995. Uncertainties Associated with the Definition of a Hydrologic Source Term for the Nevada Test Site. Lawrence Livermore NAtional Laboratory, UCRL–ID–120322, 21 p.

Smith, D.K., 1995. Characterization of nuclear explosive melt debris. *Radiochimica Acta,* 69:157–167.

Smith, D.K., A.B. Kersting, J.M. Kenneally, J.H. Rego and J.L. Thompson, 1997. Hydrologic Resources Management Program FY 1996 Progress Report. Lawrence Livermore National Laboratory, UCRL–ID–126886, 40 p.

Stallman, R.W., 1960. Notes on the use of temperature data for computing ground-water velocity: Nancy, France, 6th Assembly on Hydraulics Societe Hydrotechnique de France, Quest. 1, rapp. 3, p. 1–7.

Stallman, R.W., 1965. Steady one-dimensional fluid flow in a semi-infinite porous medium with sinusoidal surface temperature. *Journal of Geophysical Research,* 70(12):2821–2827.

Stanfors, R., M. Erlstrom and I. Markstrom, 1991. *Aspo Hard Rock Laboratory. Overview of the Investigations 1986-1990,* SKB Technical Report, vol. 91-20. Stockholm, Sweden: Swedish Nuclear Fuel and Waste Management Co.

Stenhouse, M.J. and J. Pottinger, 1994. Comparison of sorption databases used in recent performance assessments involving crystalline host rock. *Radiochemical Acta,* 66/67:267-275.

SwedPower/SKB, 1991. Instrumentation for site characterization brochure.

Teng, H. and D.E. Grandstaff, 1994. The dissolution of volcanic glass: The effect of pH and organic acids. *EOS 75(16)*:140.

Thorstenson, D.C., E.P. Weeks, H. Haas and D.W. Fisher, 1983. Distribution of gaseous $12CO_2$, $13CO_2$, $14CO_2$ in the subsoil unsaturated zone of the western United States. *Radiocarbon* 25(2):315-346.

Tompson, A.F.B., E.G. Vomvoris and L.W. Gelhar, 1988. Numerical simulation of solute transport in randomly heterogeneous porous media: Motivation, model development, and application. Technical Report Number 316, R.M. Parsons Laboratory, Department of Civil Engineering, M.I.T., Cambridge, Massachusetts.

Tompson, A.F.B. and L.W. Gelhar, 1990. Numerical simulation of solute transport in three-dimensional randomly heterogeneous porous media. *Water Resources Research,* 26(10):2541–2562.

Toth, J., 1963. A theoretical analysis of groundwater flow in small drainage basins. *Journal of Geophysical Research,* 68:4795-4812.

Tsang, Y., 1992. Usage of equivalent apertures for rock fractures as derived from hydraulic and tracer tests. *Water Resources Research,* 28(5):1451-1455.

Tsang, Y., C. Tsang, F. Hale and B. Dverstorp, 1996. Tracer transport in a stochastic continuum model of fractured media. *Water Resources Research,* 32(10):3077-3092.

Tsang, Y., C. Tsang, I. Neretnieks and L. Moreno, 1988. Flow and tracer transport in fractured media: A variable aperture channel model and its properties. *Water Resources Research*, 24(12):2049-2060.

U.S. Atomic Energy Commission, 1964. Project Manager's Report Project Shoal. Reynolds Electrical and Engineering Co., Inc., U.S. AEC, Nevada Operations Office, NVO–11, 82 p.

U.S. Atomic Energy Commission, 1970. Site Disposal Report, Fallon Nuclear Test Site (Shoal): Churchill County, Nevada, NVO-73, 40 p.

U.S. Department of Commerce, 1963. Maximum Permissible Body Burdens and Maximum Permissible Concentrations of Radionuclides in Air and in Water for Occupational Exposure. National Bureau of Standards Handbook 69, National Committee on Radiation Protection Report No. 22, issued in 1959 and amended in 1963, 95p.

U.S. Department of Energy, 1984. Long-Term Hydrologic Monitoring Program Project Shoal Site, NVO – 276. 21p.

U.S. Department of Energy, 1993. Announced United States Nuclear Tests July 1945 through December 1992. DOE/NV–209 (Rev. 13), 104 p.

U.S. Department of Energy, 1996. Corrective Action Investigation Plan for Project Shoal Area, 62 p.

U.S. Department of Energy, 1998. Data Report, Project Shoal Area, Churchill County, Nevada, Environmental Restoration Division, Nevada Operations Office.

U.S. Environmental Protection Agency, 1976. National Interim Primary Drinking Water Regulations. EPA–570/9–76–003, 159p.

U.S. Environmental Protection Agency, 1979. Off-Site Environmental Monitoring Report for the Nevada Test Site and other Test Areas used for Underground Nuclear Detonations. Las Vegas, NV. 136 p.

University of Nevada, 1965. Geological, Geophysical, Chemical, and Hydrological Investigations of the Sand Springs Range, Fairview Valley, and Fourmile Flat, Churchill County, Nevada. U.S. Atomic Energy Commission, Vela Uniform Report, vol. 1001. 369 p.

University of Nevada, 1980. Environmental Isotope Hydrology of the Dixie Valley Geothermal System. In Geothermal Reservoir Assessment Case Study, Northern Basin and Range Province, Northern Dixie Valley, Nevada, Vol. III, pp.C–1 to C–26.

Van Kote, F. and F. Balard, 1972. Distribution de la Radioactivité dans l'Environment d'une Explosion Nucléaire Souterraine. Commissariat à l'Energie Atomique, CEA–R–4287.

Webster, D., J. Proctor and I. Marine, 1970. Two-well Tracer Test in Fractured Crystalline Rock, U.S. Geological Survey Water-Supply Paper, vol. 1544-I. Washington.

Werner, K., 1996. Literature Review and Scoping Calculations for the Tracer Retention Understanding Experiments at Aspo Hard Rock Laboratory, diss. Stockholm, Sweden: Royal Institute of Technology, 81 p.

White, A.F., 1983. Surface chemistry and dissolution kinetics of glassy rocks at 25° C. *Geochim. et Cosmochim. Acta,* 47:805–815.

Wolfsberg, K., 1978. Sorption–Desorption Studies of Nevada Test Site Alluvium and Leaching Studies of Nuclear Test Debris. Los Alamos National Laboratory, LA–7216–MS, 32 p.

Woodbury, A. and L. Smith, 1988. Simultaneous inversion of hydrogeologic and thermal data, 2. Incorporation of thermal data. *Water Resources Research,* 24(3):356-372.

Xian-Huan, W., J. Gomez-Hernandez, J. Capilla and A. Sahuquillo, 1996. Significance of conditioning to piezometric head data for predictions of mass transport in groundwater modeling. *Mathematical Geology,* 28(7):951-968.

Xian-Huan, W. and C. Kung, 1993. Stochastic simulation of solute transport in heterogeneous formations: A comparison of parametric and nonparametric approaches. *Ground Water,* 31(6):953-965.

Xie, L., 1995. *Convective Transport Coupled with Nonlinear Kinetic Sorption.* Royal Institute of Technology.

Young, D., 1987. Indicator kriging for unit vectors: Rock joint orientations. *Mathematical Geology,* 19(6):481-501.

Young, D., 1987. Random vectors and spatial analysis by geostatistics for geotechnical applications. *Mathematical Geology,* 19(6):467-479.

Zimmerman, U., D. Ehhalt and K.O. Munnich, 1967. Soil water movement and evapotranspiration: changes in the isotopic composition of the water, in Proceedings of the IAEA Symposium on Isotope Hydrology, Int. Atomic Energy Agency, Vienna.

Zones, C., 1957. Changes in hydrologic conditions in the Dixie Valley and Fairview Valley areas, Nevada, after the earthquake of December 16, 1954. *Bulletin of the Seismological Society of America,* 387-397.

APPENDIX 1

SHOAL WATER LEVELS

After each newly installed well (HC-1, HC-2, HC-3, HC-4) was completed, the depth to water was verified with Desert Research Institute's Chem-tool, which is accurate to +-0.01 ft (.003 m). A calibrated (100 ft water range) pressure transducer was installed and the water level was monitored on an hourly basis. The borehole deviation logs (Century Geophysical) and surveyed wellhead elevations (IT Corp) were used to properly calculate the elevation of the water table. Periodic measurements of the depth to water were taken to verify the accuracy of the pressure transducer.

During the monitoring period hydraulic tests (pumping test, slug tests and thermal flow meter tests) were performed and water level monitoring ceased. The data presented in Figures 1-1 - 1-4 represent quasi-equilibrium conditions such that water levels that were impacted by the testing procedures are not included. Temporally varying water levels due to drilling induced impacts immediately after initial transducer installation are included.

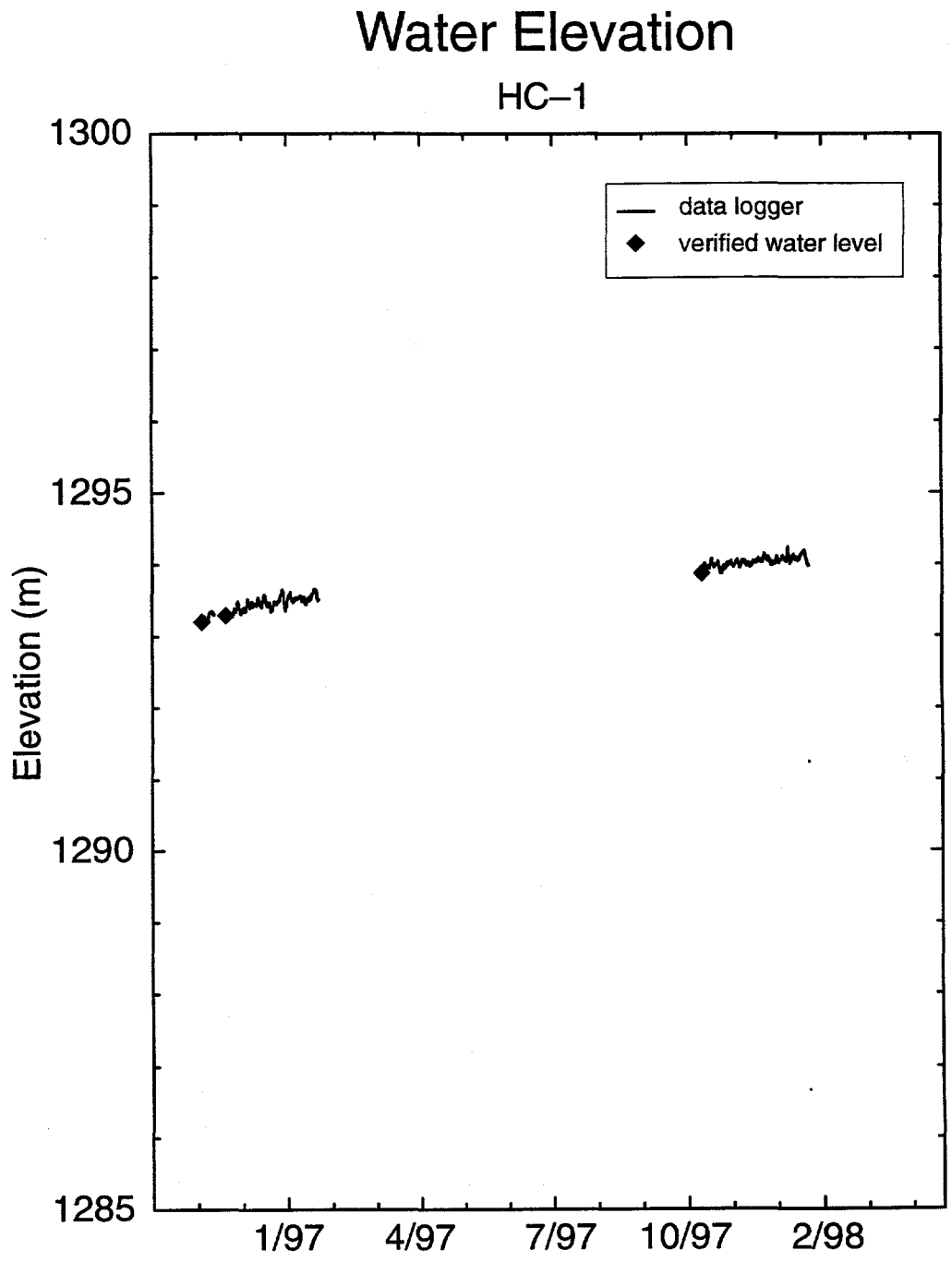
Water Elevation
HC–1
1300
1295
1290
1285
Elevation (m)
1/97
4/97
7/97
10/97
2/98
data logger
verified water level

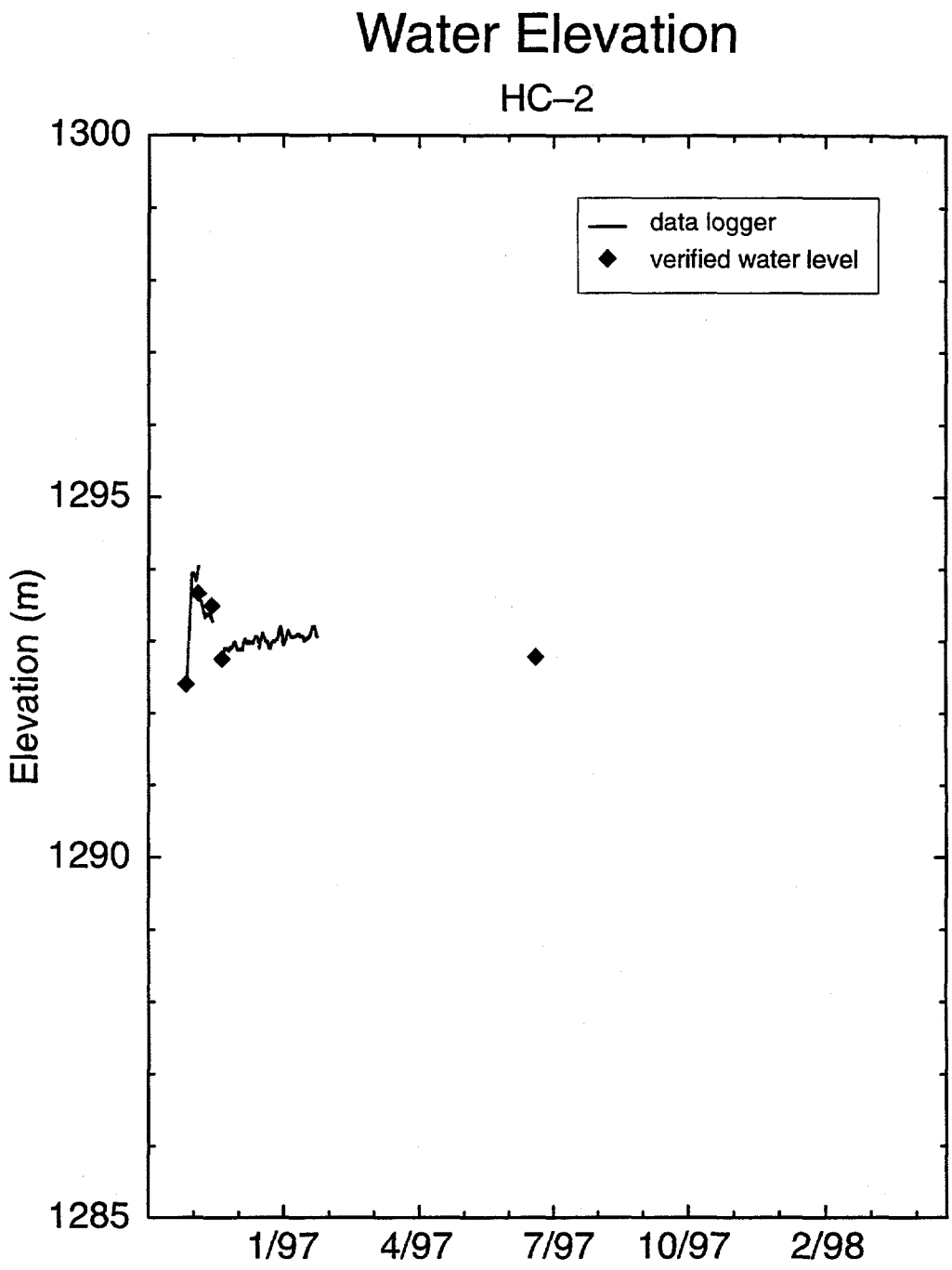
Water Elevation
HC–2
1300
1295
1290
1285
Elevation (m)
1/97
4/97
7/97
10/97
2/98
data logger
verified water level

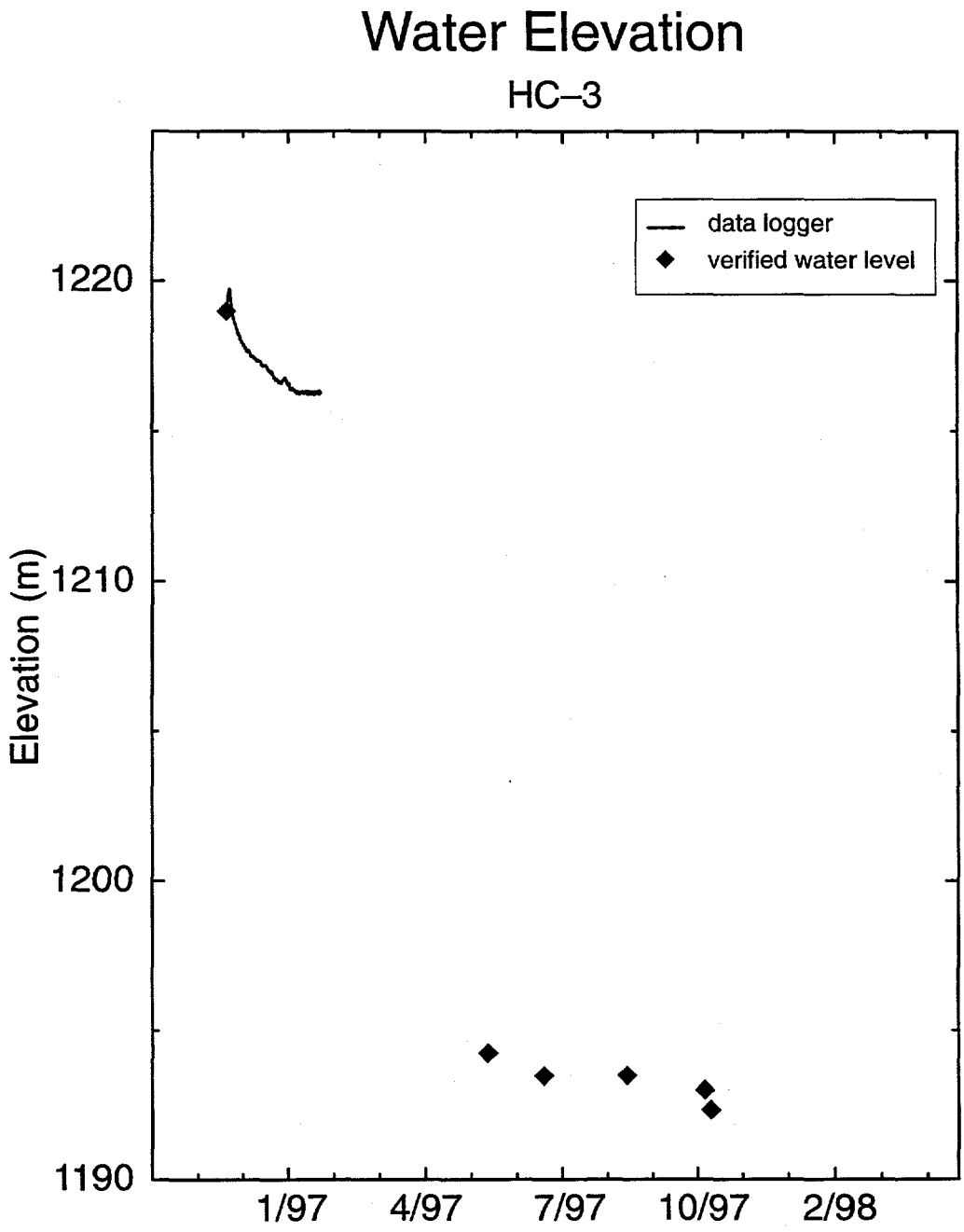
Water Elevation
HC–3
data logger
verified water level
Elevation (m)
1220
1210
1200
1190
1/97
4/97
7/97
10/97
2/98

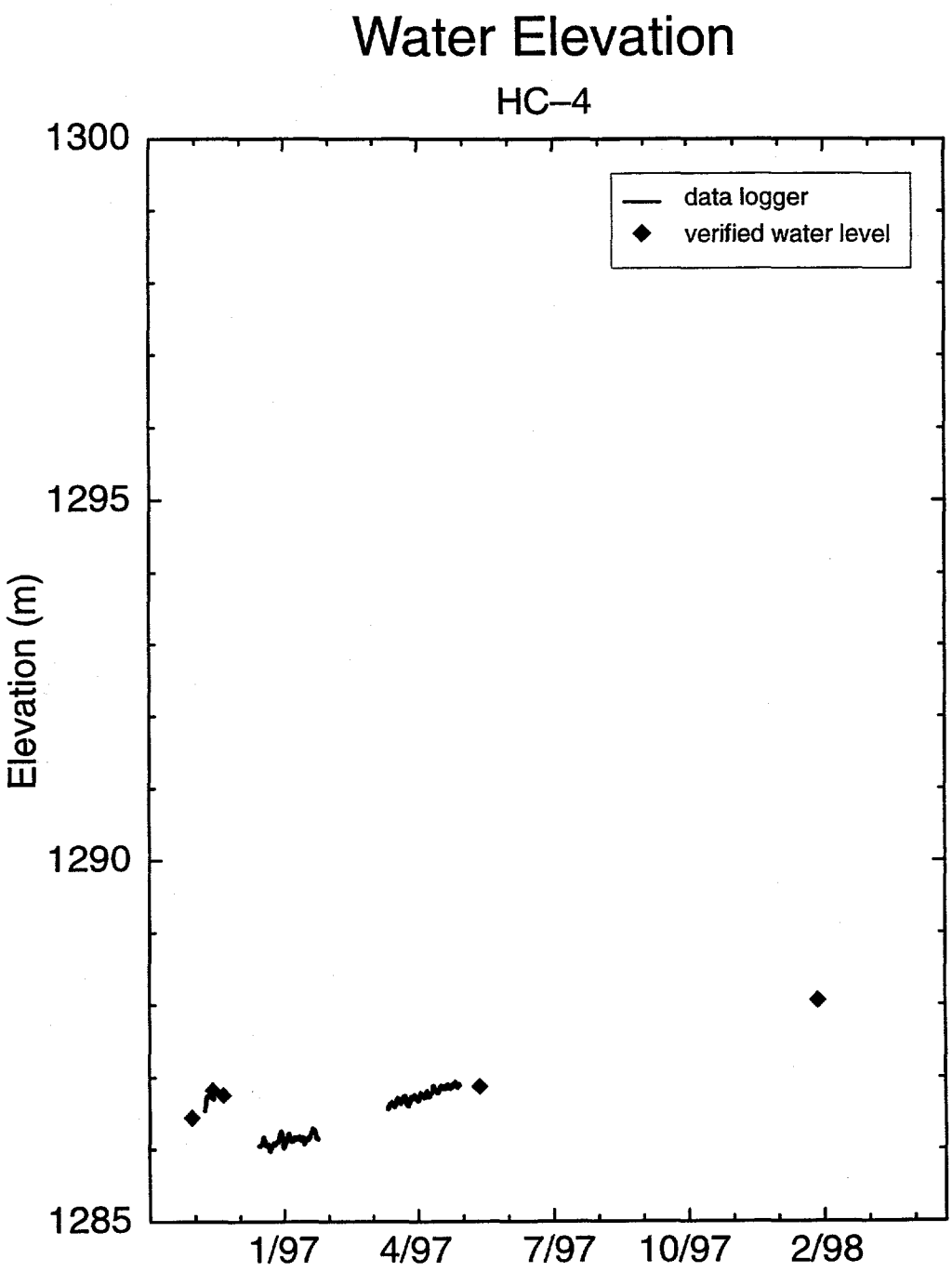
Water Elevation
HC–4
1300
1295
1290
1285
Elevation (m)
1/97
4/97
7/97
10/97
2/98
data logger
verified water level

This page intentionally left blank

APPENDIX 2

VERTICAL CONDUCTANCE

MODFLOW has an option to create quasi-three-dimensional simulations such that one would not have to explicitly simulate semi-confining layers. With this option, semi-confining layers are eliminated from the computational matrix by essentially averaging the hydraulic conductivity of the semi-confining layer into a vertical conductance term. This option led to fewer nodes in the model domain which was critical on older and slower computers. With faster computer capabilities, this is not necessary. To simulate the fully three-dimensional finite difference approximation to the continuity equation (Eq. 4), one must average the conductivities between to adjacent block centered nodes to estimate the flux between nodes. MODFLOW uses a harmonic mean to calculate conductivity between two adjacent nodes. To illustrate the differences between the quasi-and fully-three-dimensional approach, one can compare the calculation of the VCONT term for each type as:

$$\mathrm{VCONT}_{Q3D} = \left[\frac{\Delta z_u/2}{K_{z_u}} + \frac{\Delta z_c}{K_{z_c}} + \frac{\Delta z_L/2}{K_{z_L}} \right]^{-1} \tag{2}$$

$$\mathrm{VCONT}_{3D} = \left[\frac{\Delta z_u/2}{K_{z_u}} + \frac{\Delta z_L/2}{K_{z_L}} \right]^{-1} \tag{3}$$

where VCONT_{Q3D} = vertical conductance for the quasi-three-dimensional model (L^2/T),
VCONT_{3D} = vertical conductance for the fully three-dimensional model (L^2/T),
Δz_u = thickness of the upper model layer (L),
z_c = thickness of the semi-confining layer (L),
Δz_L = thickness of the lower model layer (L),
K_{z_u} = hydraulic conductivity of the upper model cell (L/T),
K_{z_c} = hydraulic conductivity of the semi-confining unit (L/T),
K_{z_L} = hydraulic conductivity of the lower model cell (L/T).

The harmonic mean of adjacent nodes in the two lateral directions (x and y) is calculated internally by MODFLOW. Eq. (6) was used to calculate the vertical conductance for all simulations.

This page intentionally left blank

APPENDIX 3

FRACTURE CODE PLOTS

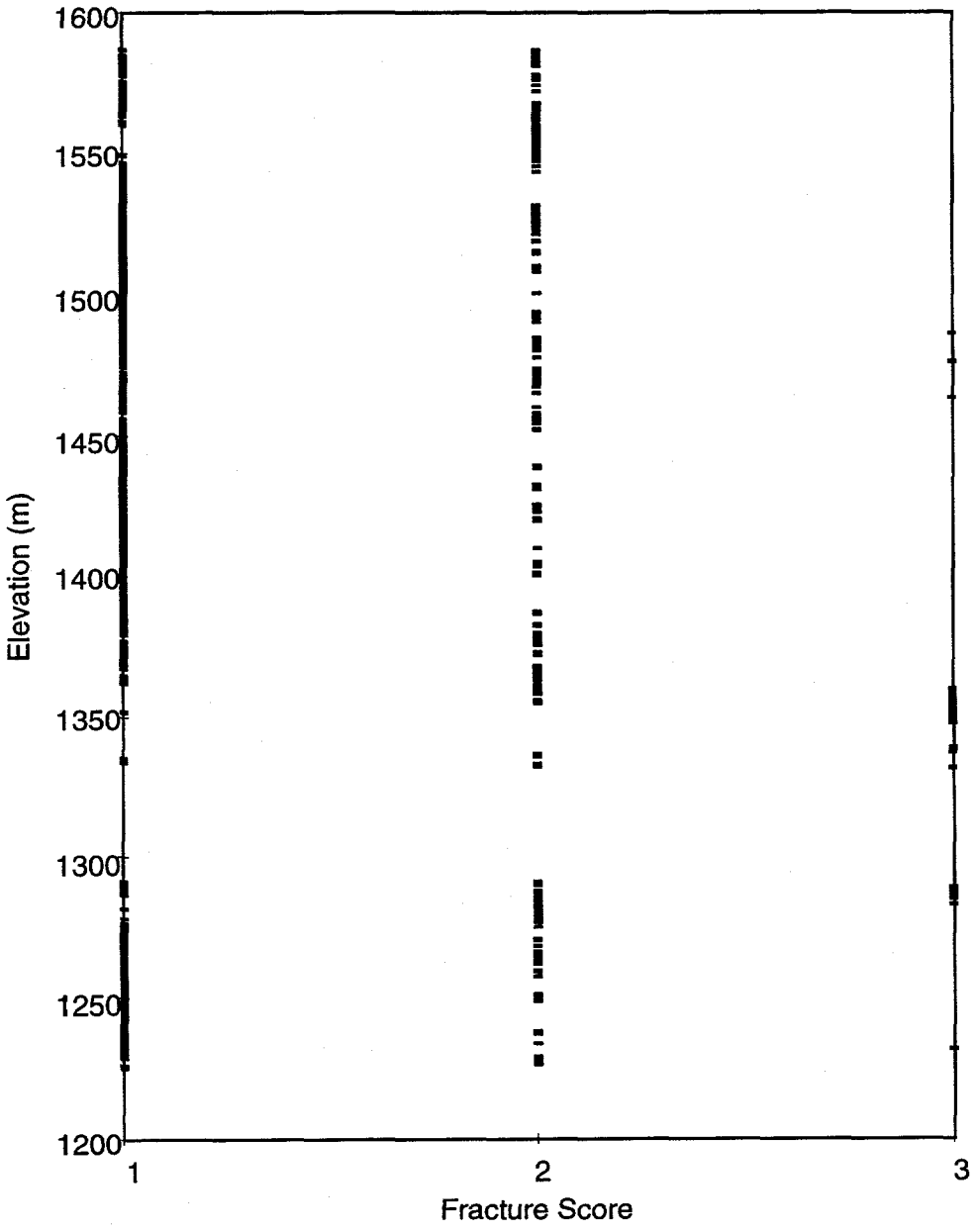

Figure 3–1. HC-1 fracture score.

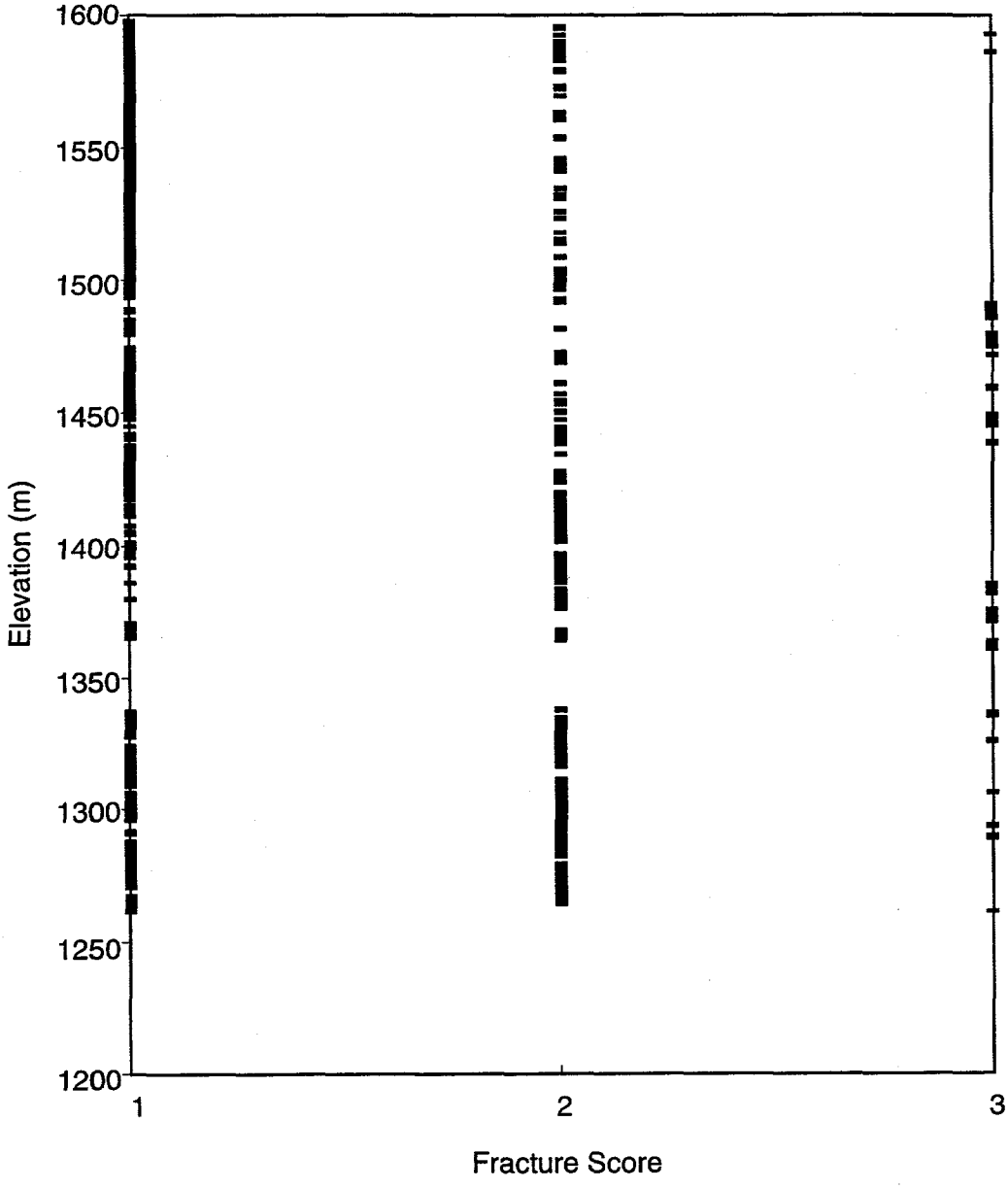

Figure 3–2. HC-2 fracture score.

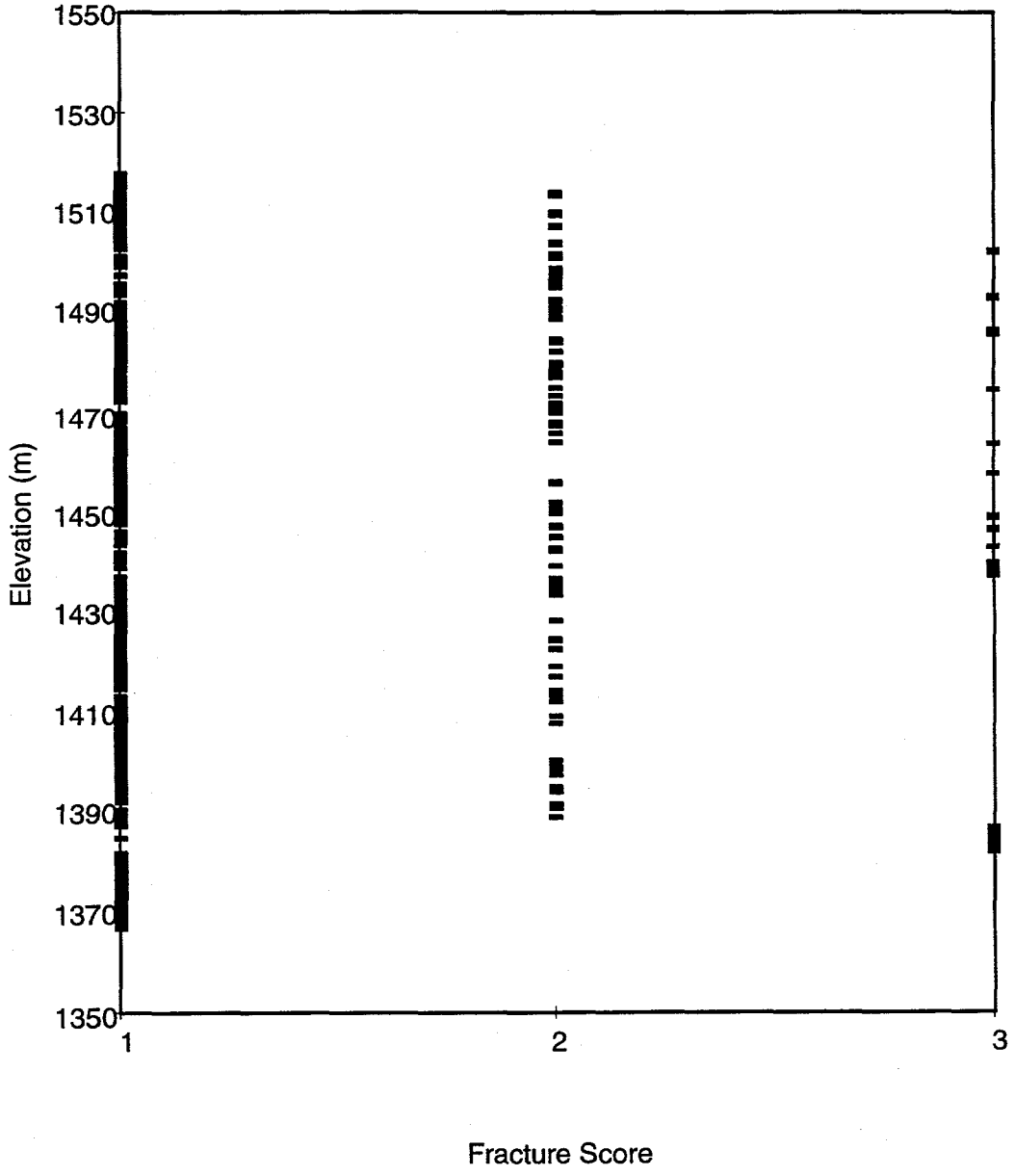

Figure 3–3. HC-3 fracture score.

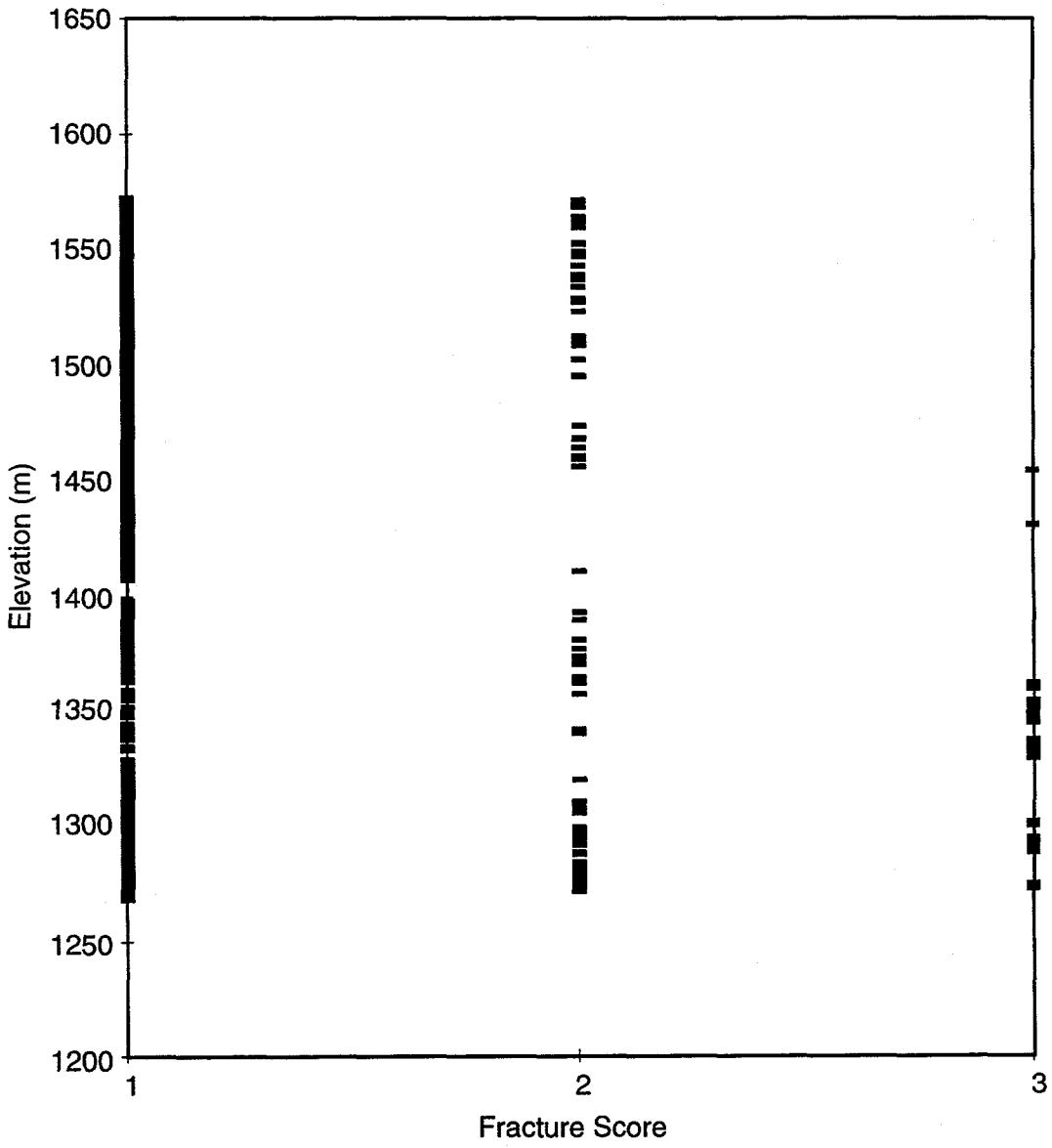

Figure 3–4. HC-4 fracture score.

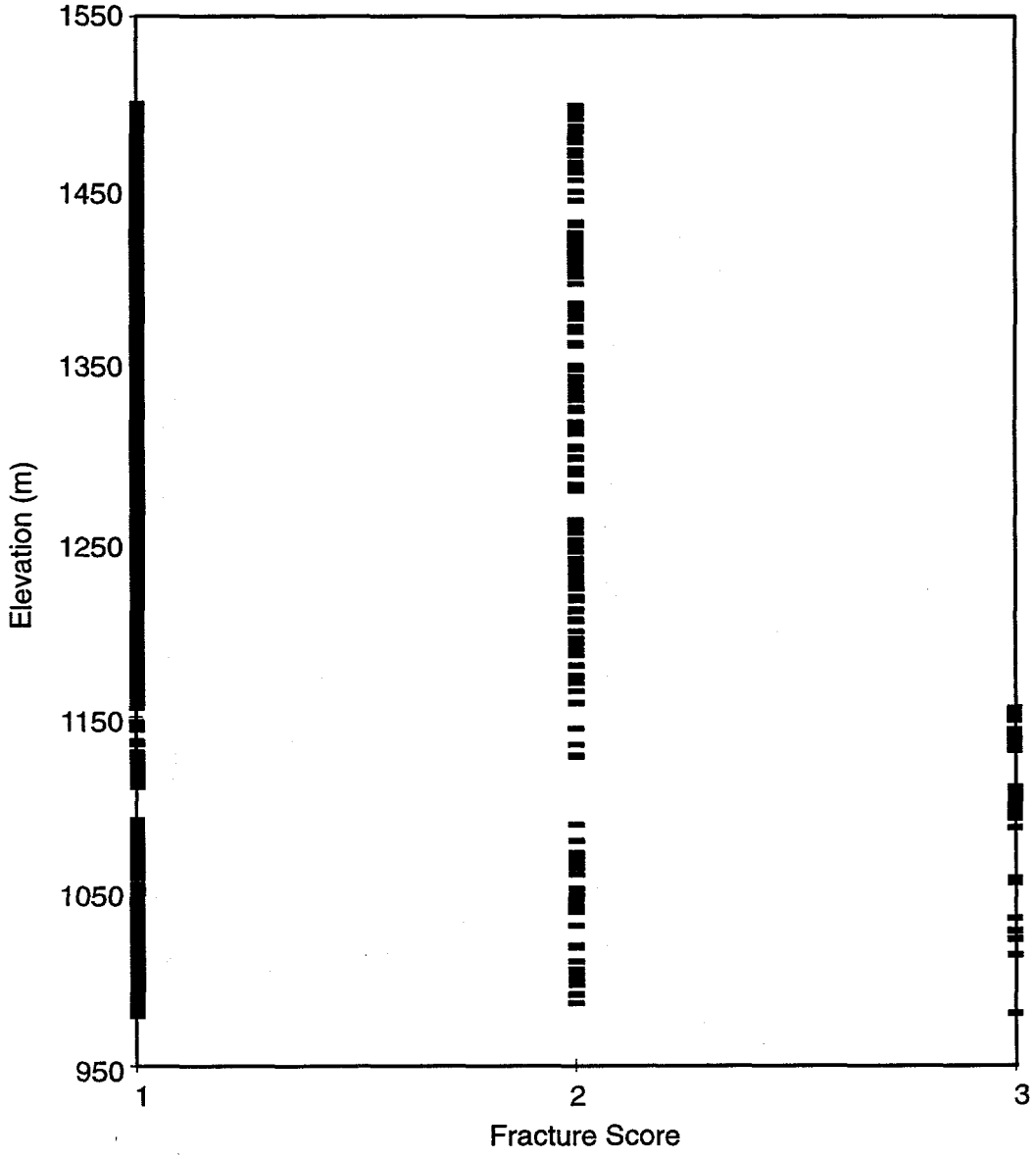

Figure 3–5. ECH-D fracture score.

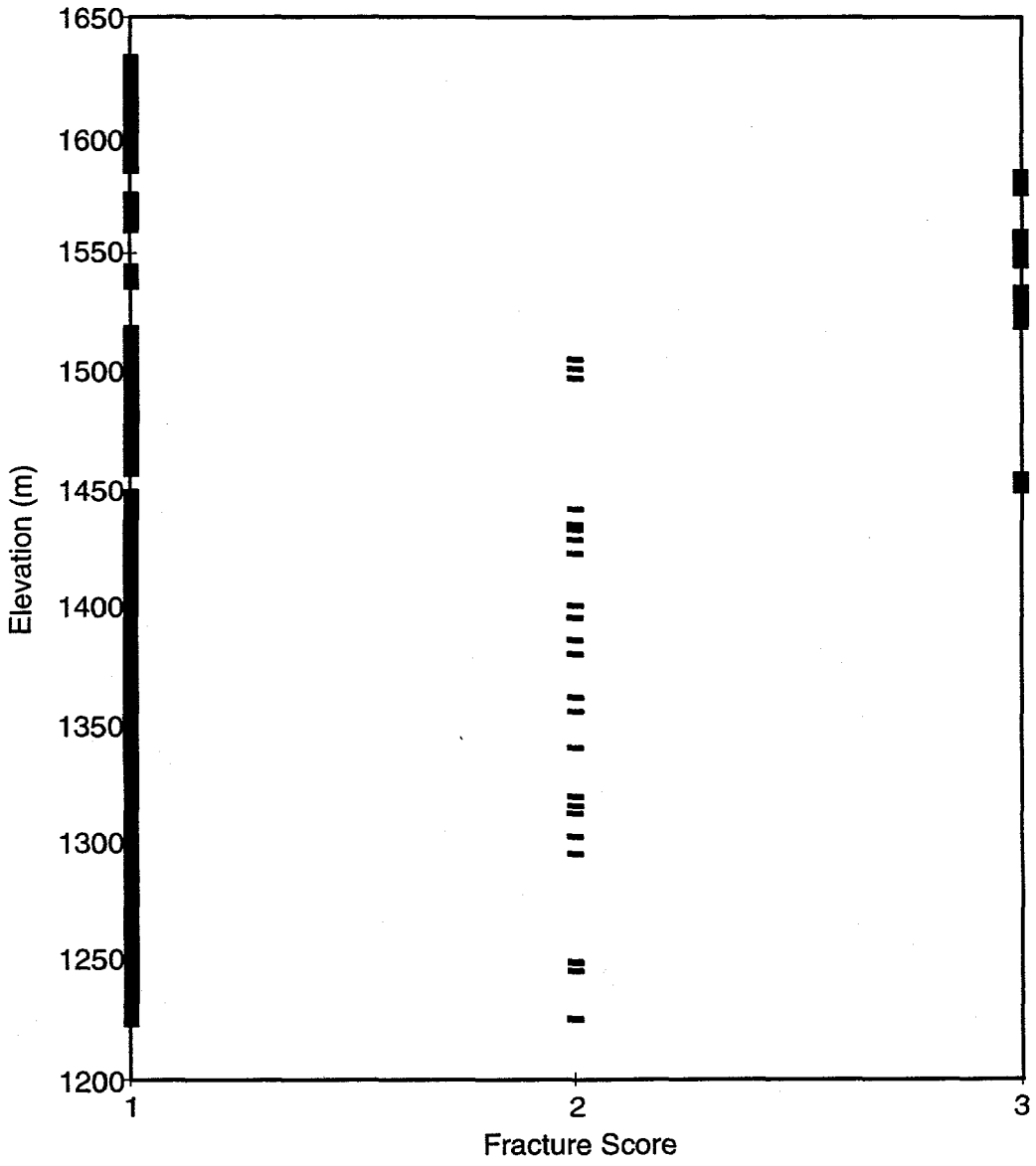

Figure 3–6. PM-1 fracture score.

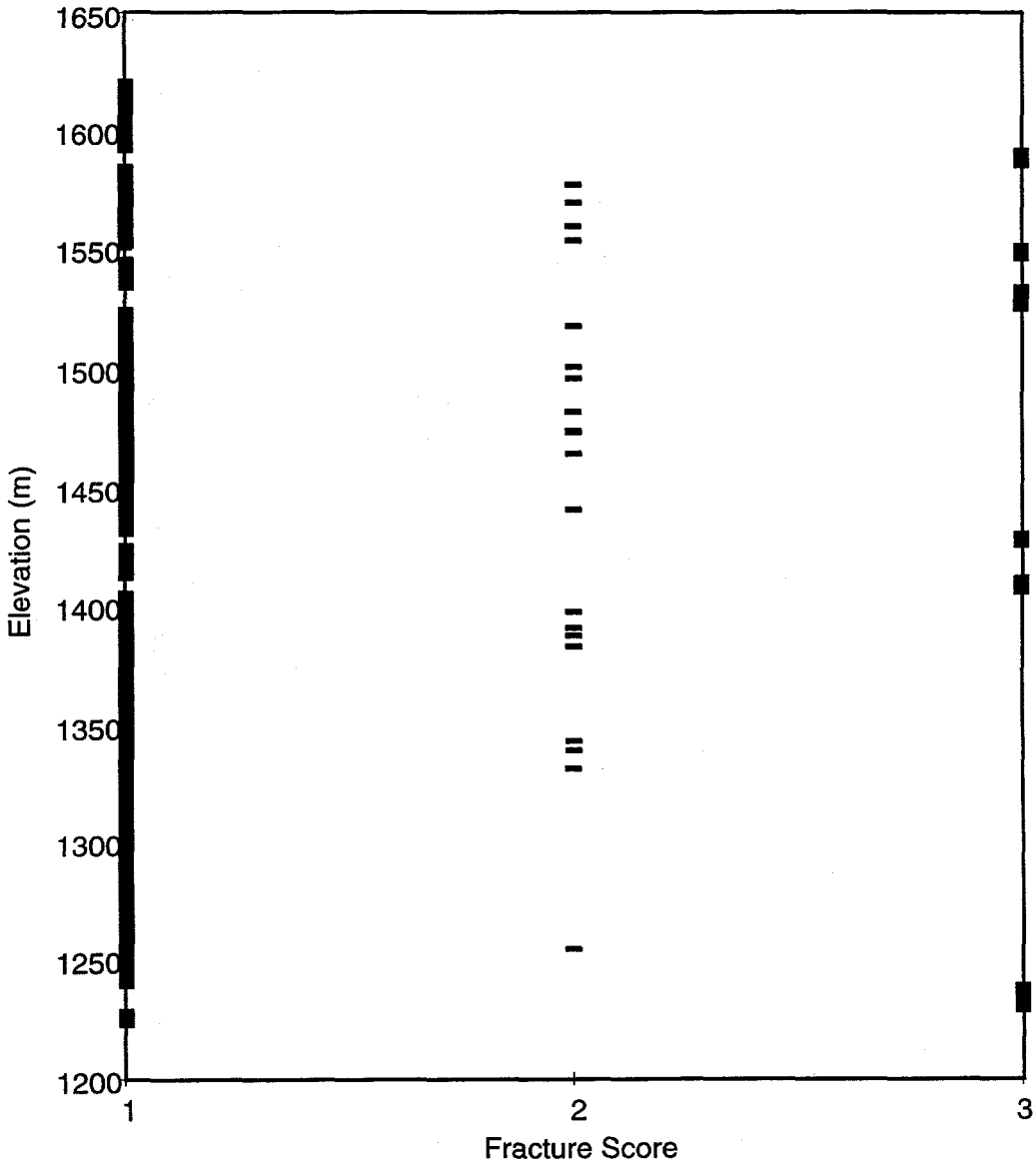

Figure 3–7. PM-2 fracture score.

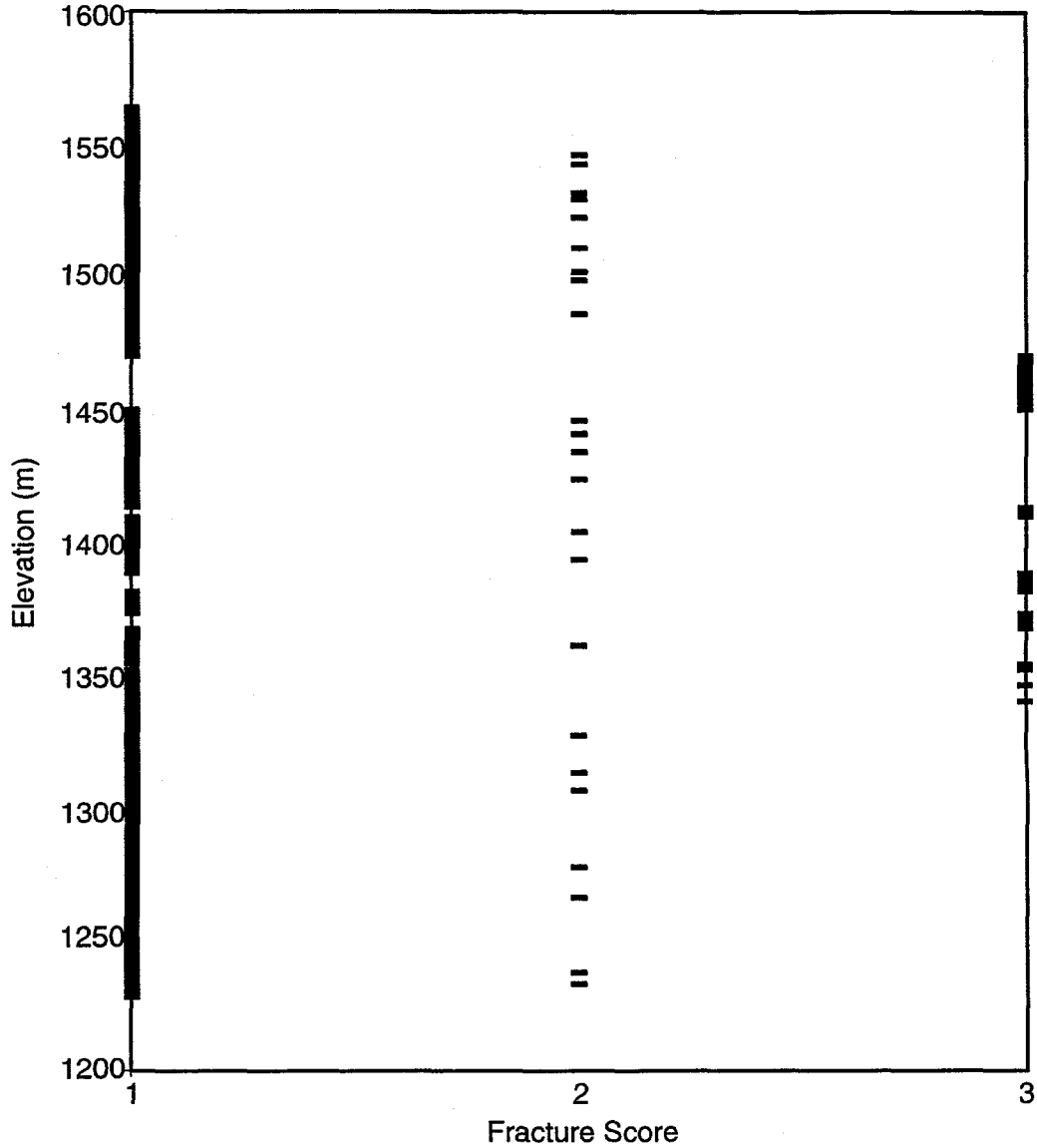

Figure 3–8. PM-3 fracture score.

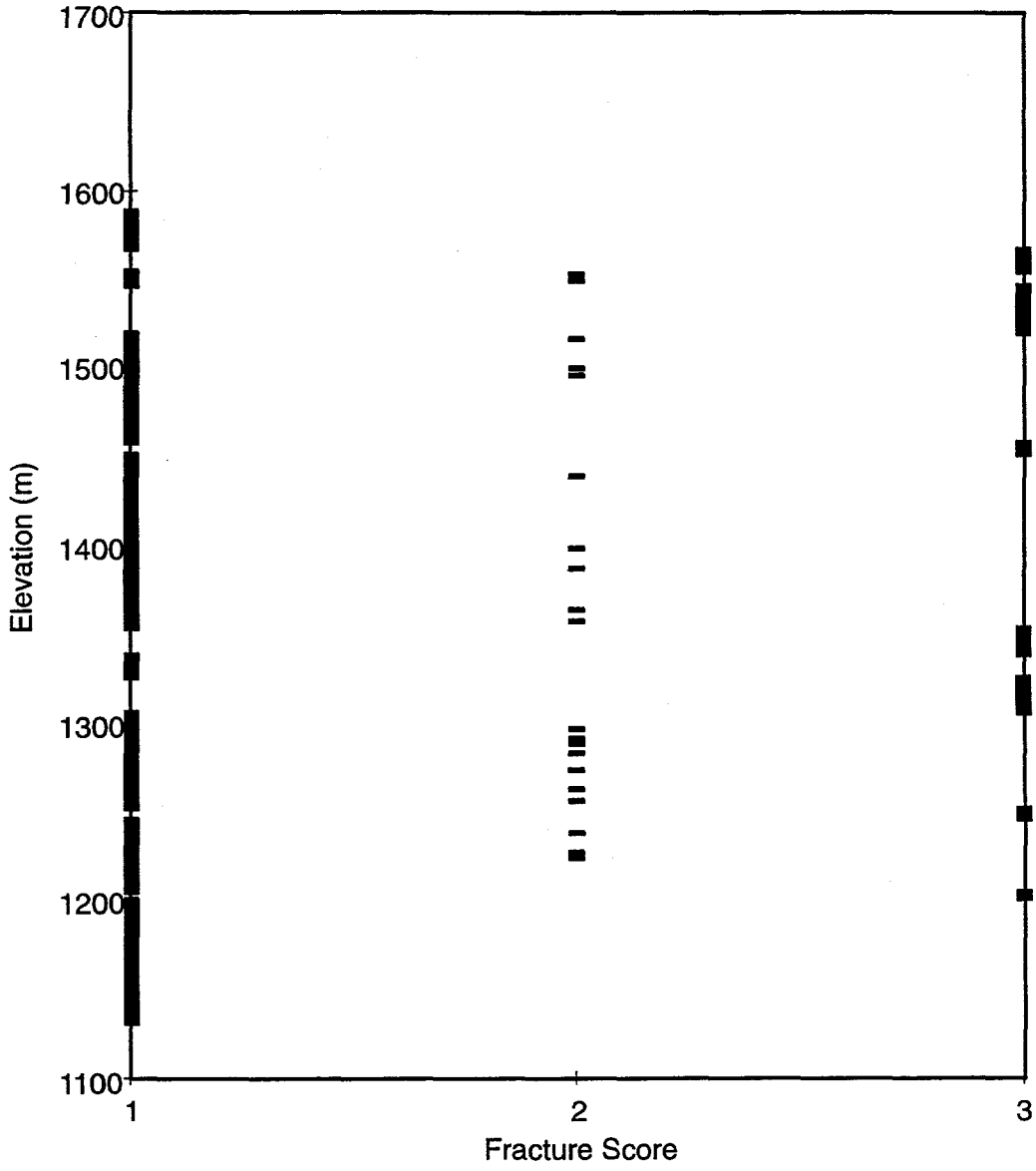

Figure 3–9. USBM-1 fracture score.

APPENDIX 4

Letter Report

Shoal Field Operations

prepared by

Sam Earman and Greg Pohll
Water Resources Center
Desert Research Institute
University and Community College System of Nevada

submitted to

Nevada Operations Office
U.S. Department of Energy
Las Vegas, Nevada

June 1997

The work upon which this report is based was supported by the U.S. Department of Energy under Contract #DE–AC08–95NV11508.

CONTENTS

FIGURES iii

TABLES iii

INTRODUCTION 1
Scope of Work 1

GENERAL TESTING AND SAMPLING PROCEDURE 1

SUMMARY OF OPERATIONS, WELL HC-1 5

SUMMARY OF OPERATIONS, WELL HC-2 7

SUMMARY OF OPERATIONS, WELL HC-4 8

SUMMARY OF HYDRAULIC TESTING 10
Numerical Analysis of Hydraulic Properties (HC-1) 11

FLUID MANAGEMENT 12

REFERENCES 15

APPENDICES
APPENDIX A – Bromide Concentrations During Well Purging A-1
APPENDIX B – Time Drawdown Data for HC-1 ..... B-1
APPENDIX C – Time Drawdown Data for HC-2 ..... C-1
APPENDIX D – Time Drawdown Data for HC-4 ..... D-1
APPENDIX E – Shoal Water Quality and Stable Isotope Analysis E-1

FIGURES

1. Project Shoal well location map. 2
2. Drawdown vs. time for the HC-1 pump test. 5
3. Drawdown vs. time for the HC-2 pump test. 7
4. Drawdown vs. time for the HC-4 pump test. 10
5. Measured and simulated drawdown for HC-1. 12

TABLES

1. Summary of Br^- Concentrations 4
2. Water Sampling Procedure Descriptions. 4
3. HC-1 Flow Rate, Hydraulic Head and Drawdown. 6
4. HC-2 Flow Rate, Hydraulic Head and Drawdown. 8
5. HC-4 Flow Rate, Hydraulic Head and Drawdown. 9
6. Summary of Hydraulic Conductivity Measurements 11
7. Summary of Fluid Discharges to Sumps 13
8. Project Shoal Fluid Management Data 14

This page intentionally left blank

INTRODUCTION

This report summarizes the activities conducted by the Desert Research Institute (DRI) at the Project Shoal site in west-central Nevada, pursuant to the *Corrective Action Investigation Plan (CAIP) for the Project Shoal Area, CAU No. 416* (U.S. DOE, 1996). The majority of this work, which involved aquifer testing and water sampling for chemical, radiochemical, and stable isotopic analysis from three wells at the Shoal site, took place from February 19 through February 26, 1997, with some additional work performed on March 23 and March 24, 1997.

Project Shoal involved the detonation of a 12-kiloton nuclear device approximately 366 m below ground surface (BGS) on October 26, 1963. The test was conducted to aid in the detection of nuclear detonations in active seismic zones. The site is located approximately 48 km east-southeast of Fallon, Nevada in the Sand Spring Range.

Scope of Work

Four wells (HC-1, HC-2, HC-3, and HC-4; Figure 1) were constructed at the site between September 26 and November 10, 1996, with all but HC-3 producing water. A detailed description of these wells and their construction is provided by the Department of Energy (1997). The drilling and completion process was designed to have the minimum possible impact on the formation. During drilling, air was used as the circulation medium, and fluid (foam) was added sparingly. Even so, some drilling fluid was assumed to be left in the wells after completion, thus making purging of the wells necessary to collect samples representative of formation water. In conjunction with the purging process, discharge and drawdown were monitored to provide data regarding aquifer characteristics. To this end, water levels were also monitored during the recovery period following the cessation of pumping. The pumping and recovery data were analyzed to determine mean values for the hydraulic conductivity of the aquifer. Water samples were collected from each of the producing wells for various chemical, radiochemical, and isotopic analyses. All of these data will be used to support contaminant transport predictions for the Shoal site.

GENERAL TESTING AND SAMPLING PROCEDURE

Although certain details differ from well to well, as described in following sections, the same general operations were carried out at each well during the testing and sampling process. This general procedure is outlined here to avoid redundancy in the description of activities at individual wells. The description provided below is only a brief summary of the activities performed at the Shoal site. All field activities were carried out in accordance with the following DRI standard operating procedures (SOPs):

- Shipping and Control of Groundwater Samples
- Decontamination of Field Equipment
- Calibration and Use of Portable pH and Temperature Meter
- Calibration and Use of Portable Electrical Conductivity Meter
- Installing Pressure Transducers
- Recording Field Activities
- Calibrating Pressure Transducers
- Single Well Slug Test
- Collection of Groundwater Samples
- Determination of Groundwater Levels

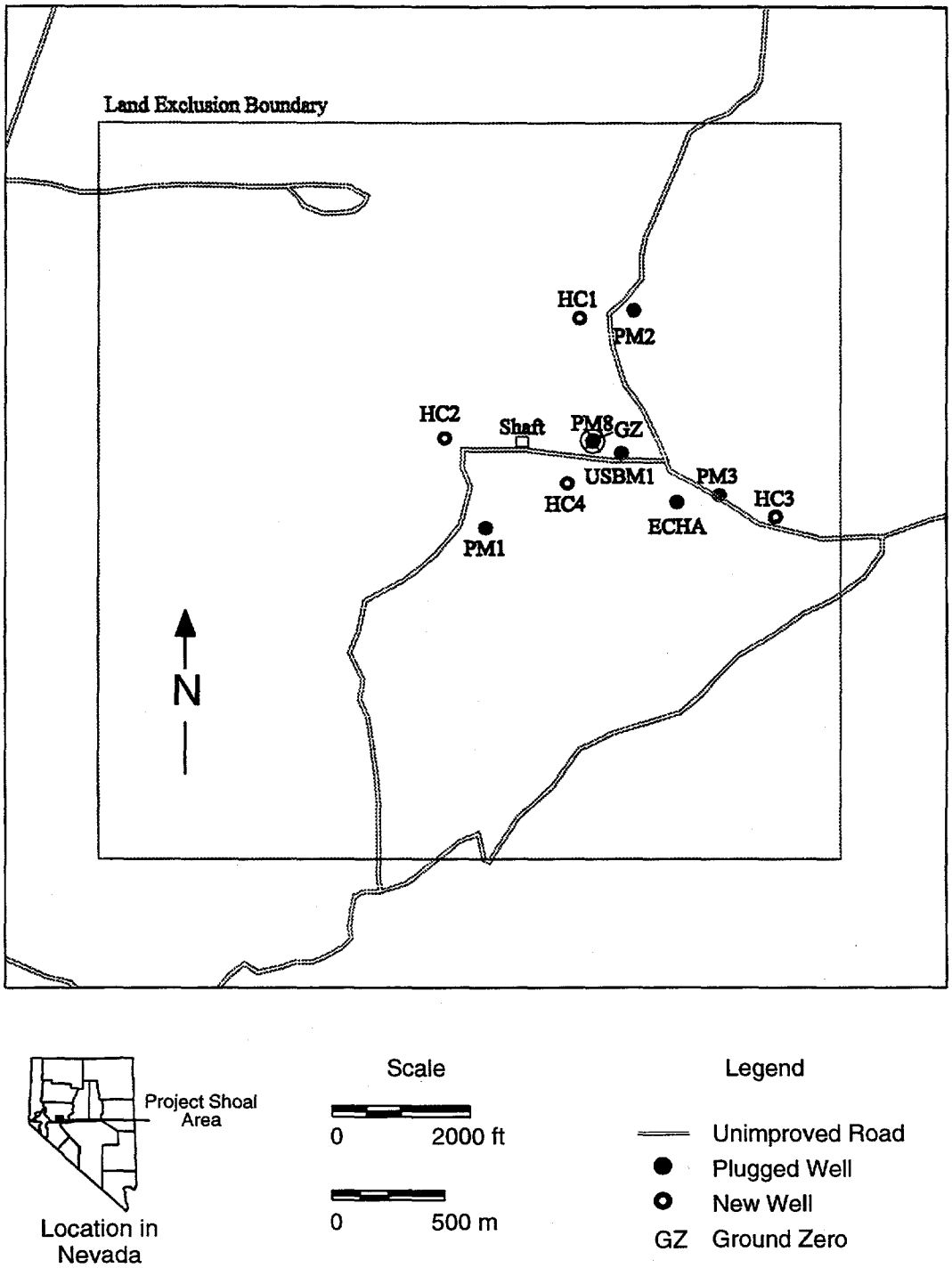

Figure 1. Project Shoal well location map.

These SOPs provide more complete descriptions of the procedures followed during field work, and are permanently maintained by DRI, along with copies of field notes, field data sheets, digital versions of information recorded via datalogger, and chain-of-custody records for samples taken at the Shoal site.

Upon arrival at a well pad, the lid was removed from the protective casing for the well. The dedicated pressure transducer in place was removed to avoid entanglement during the downhole insertion of the pump and associated tubing. A Bennett model 180 pump was lowered down the hole, with the pressure transducer attached to the tubing bundle just above the top of the pump housing. Electrical tape was used to secure the transducer to the tubing bundle, and plastic "zip" style cable ties were used to secure the transducer cable to the pump tubing every 15.24 m. Before being lowered downhole, the pump was wiped clean, and allowed to pump approximately 12 L of distilled water. A sounding circuit in the pump designed to indicate water contact was turned on, alerting DRI personnel when the pump was submerged. After contacting water, the pump was lowered an additional 4.6 to 7.6 m downhole in an effort to keep the pump submerged during the period of drawdown. Depth to water and transducer depth below the potentiometric surface were recorded. A visual estimate of the depth of existing water in the sump to which discharge was to be routed was made prior to the start of pumping.

Shortly after water discharge from the pump outlet hose began at the surface, the rate of discharge was measured using a stopwatch and a bucket of known volume. Discharge rate and water level were subsequently recorded manually each hour until the cessation of pumping. Water level was measured in one-minute intervals for the duration of the test, with data recorded by datalogger. The hourly values recorded in the field were read from the datalogger to insure drawdown did not dewater the hole to pump level. Every four hours, the electrical conductivity (EC), pH, and temperature of the discharge were measured, and a 237-mL sample was collected in a polyethylene bottle for Br^- (bromide) analysis. After one well volume had been purged, the field parameters were measured every 30 minutes. When EC and pH showed three consecutive stable measurements (EC within five percent of the other measurements, pH within 0.1 standard units of the other measurements), water sampling activities were begun. Water temperature was not used as an indicator of stabilization because weather conditions caused significant changes in water temperature as ambient temperature and sunlight conditions changed.

The Br^- samples were analyzed (see Appendix A for a complete listing of bromide concentrations and cumulative purging volumes) at the DRI Water Analysis Laboratory to serve as an additional check that purging was adequate to insure a representative sample. Br^- was used as an indicator because the wells were being pumped for the first time since construction, and a LiBr solution had been introduced into the drilling fluid. For each of the newly drilled holes at the Shoal site, DOE (1997) reports 50 to 150 measurements of Br^- concentrations in the drilling fluid, and various control samples, over time. Using an average concentration of Br^- for each hole, and a background value for Br^- in the aquifer (Table 1), it is possible to compute the percent of drilling fluid in a water sample for which a Br^- concentration is known. The background concentration was assumed to be 0.25 mg/L, based on a value from Smith-James Spring (Chapman et al., 1994).

Average values of Br^- concentration should be regarded as approximations, due to the irregular temporal spacing of measurements, the high range in values, and the lack of data regarding concentration behavior between measurements. It was assumed that purging was adequate when pumped water was composed of five percent or less drilling fluid, as suggested by Br^- concentration.

TABLE 1. SUMMARY OF Br^- CONCENTRATIONS. Br^- in groundwater was assumed to be 0.25 mg/L, based on a nearby spring (Chapman et al., 1994).

	Number of Br^- Measurements During Drilling	Average Br^- Concentration (mg/L)	Standard Deviation Br^- (mg/L)	Minimum Br^- Concentration (mg/L)	Maximum Br^- Concentration (mg/L)	Final Pumped Br^- Concentration (mg/L)	% Native Groundwater (mg/L)
HC-1	119	38	15.5	2.71	82.4	0.7	99
HC-2	43	26	5.1	0.9	34.6	0.6	99
HC-4	47	30	5.4	20.4	46.4	1.7	95

Water samples were collected and preserved (if needed) as described in Table 2. Chain-of-custody procedures were followed, and each sample was conveyed to the laboratory performing the analysis (Table 2). In the case of ^{14}C, field precipitation of carbon was performed to minimize atmospheric interaction with the samples, and possible contamination with modern carbon. A method devised by Haas (Hass, H., DRI, personal communication, 1997) was used. This method involves the collection of water in two 18.9-L carboys. Immediately after collection, approximately 50 mL of NaOH was added to each carboy, and dissolved by vigorous agitation, acting to fix the carbon. After dissolution of the NaOH was accomplished, approximately 60 mL of $SrCl_2$ was added and dissolved, causing the carbon to precipitate out of solution. This was followed by the addition and dissolution of approximately 30 mL of $FeSO_4$, which acted to flocculate the precipitate. The carboys were then fitted with lids equipped with a stopcock, and inverted in specially designed stands. The precipitate was allowed to settle for 20 to 30 minutes before being collected in HDPE bottles.

TABLE 2. WATER SAMPLING PROCEDURE DESCRIPTIONS.

Analyte	Container Description	Preservative	Organization/Laboratory Performing Analysis
Tritium	1 L Glass (PSL)	None	DRI
Tritium	1 L Glass (PSL)	None	EPA
Gross Alpha and Beta	3.79 L Polyethylene	HNO_3	EPA
Gamma Scan	3.79 L Polyethylene	HNO_3	EPA
Major Anions*	500 mL Polyethylene	None	DRI
Major Cations	250 mL Polyethylene	HNO_3	DRI
Carbon-13	1 L Glass	None	DRI
Carbon-14	2x18.9 L Polyethylene**	Field Precipitated	DRI
Oxygen-18 and Deuterium	500 mL Glass (PSL)	None	DRI

PSL = polyseal lid
HNO_3 = Nitric acid added to sample until pH was less than 2.0
*This sample also used to determine pH, silica, electrical conductivity, and alkalinity
**Sample water initially collected in two 18.9 L carboys. Field precipitation of carbonate allowed the precipitate to be collected in two to three 1.89 L polyethylene bottles for transport to the laboratory

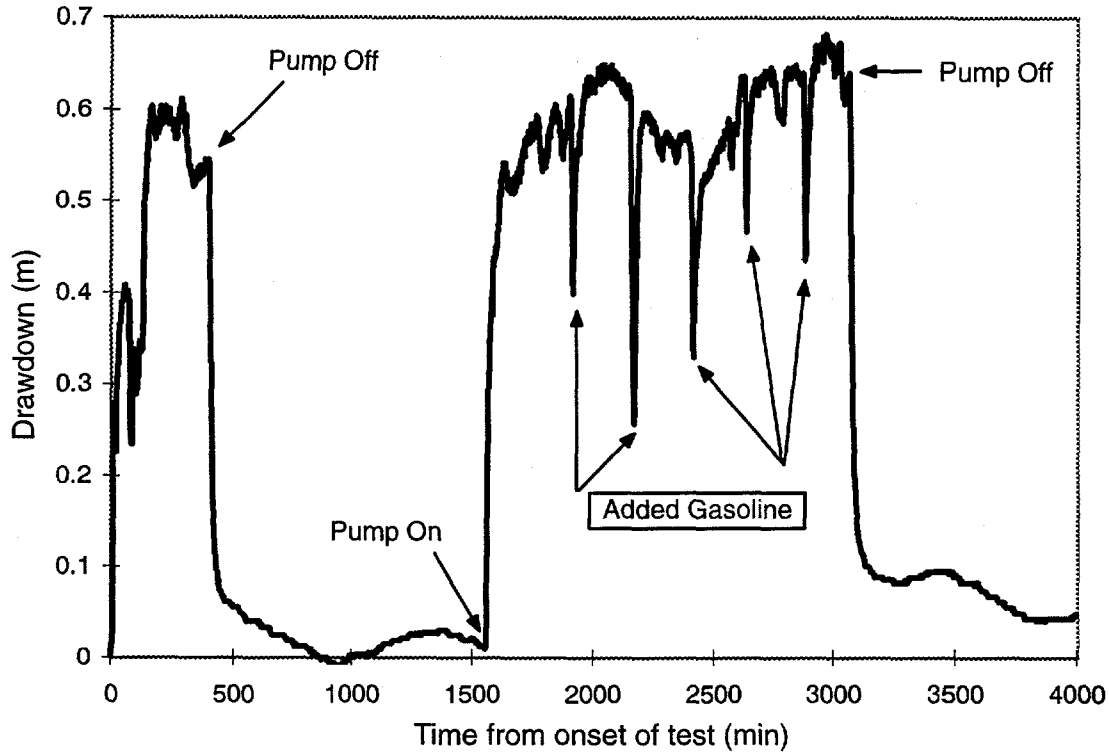

Figure 2. Drawdown vs. time for the HC-1 pump test. The data are tabulated in Table 3 and Appendix B.

Upon the conclusion of sampling, pumping was stopped, and water level in the well was monitored until such a time as recovery was complete, or enough data were collected to allow for adequate recovery interpretation. The pump and pressure transducer were pulled from the hole and separated. The pressure transducer was then re-inserted to allow for water level monitoring, and the lid was replaced and locked onto the protective casing.

SUMMARY OF OPERATIONS, WELL HC-1

Sampling activities were begun at HC-1 on February 19, 1997, with pumping commencing at 13:11 PST. A plot of drawdown versus time is displayed in Figure 2, and field data for pumping rate and drawdown are shown in Table 3 (see Appendix B for a comprehensive listing). A major interruption in pumping took place at 19:00 on February 19, due to an air compressor malfunction. Pumping did not resume until a new compressor was brought to the site at 15:20 on February 20. From that point on, several minor (approximately 5 min) interruptions to pumping took place when the backup compressor was shut down to add gasoline. Sample collection took place shortly after 14:00 on February 21, based on volume pumped (1.16 well volumes), EC, and pH measurements. Later Br^- analysis determined that the sample consisted of 99 percent native groundwater (Table 1). Water chemistry analyses are reported in Appendix E. The pump and pressure transducer were left downhole overnight to allow early-time recovery data to be collected.

TABLE 3. HC-1 FLOW RATE, HYDRAULIC HEAD AND DRAWDOWN. Detailed drawdown data can be found in Appendix B.

Date	Time	Flow Rate (gpm)	Flow Rate (L/min)	Head (ft)	Drawdown (ft)	Drawdown (m)
02/19/97	13:46	start	–	21.55	0.00	0.00
02/19/97	14:00	0.25	0.95	20.39	1.16	0.35
02/19/97	15:00	0.20	0.76	–	–	–
02/19/97	16:00	0.50	1.89	19.70	1.85	0.56
02/19/97	17:00	0.50	1.89	19.71	1.84	0.56
02/19/97	18:00	0.50	1.89	19.72	1.83	0.56
02/19/97	19:00	0.46	1.74	19.89	1.66	0.51
02/19/97	19:00	stop	0.00	–	–	–
02/20/97	15:20	start	0.00	21.60	0.00	0.00
02/20/97	16:00	0.43	1.63	20.18	1.37	0.42
02/20/97	17:00	0.44	1.67	19.97	1.58	0.48
02/20/97	18:00	0.46	1.74	19.81	1.74	0.53
02/20/97	19:00	0.44	1.67	19.82	1.73	0.53
02/20/97	20:00	0.46	1.74	19.65	1.90	0.58
02/20/97	21:00*	0.46	1.74	19.61	1.94	0.59
02/20/97	22:00	0.46	1.74	19.60	1.95	0.59
02/20/97	23:00	0.46	1.74	19.58	1.97	0.60
02/21/97	00:00	0.46	1.74	19.58	1.97	0.60
02/21/97	01:00*	0.46	1.74	19.60	1.95	0.59
02/21/97	02:00	0.45	1.70	19.70	1.85	0.56
02/21/97	03:00	0.45	1.70	19.72	1.83	0.56
02/21/97	04:00	–	–	–	–	–
02/21/97	05:00*	0.45	1.70	19.77	1.78	0.54
02/21/97	06:00	0.43	1.63	19.98	1.57	0.48
02/21/97	07:00	0.42	1.59	19.85	1.70	0.52
02/21/97	08:00	0.47	1.78	19.70	1.85	0.56
02/21/97	09:00*	0.47	1.78	19.60	1.95	0.59
02/21/97	10:00	0.46	1.74	19.60	1.95	0.59
02/21/97	11:00	0.46	1.74	19.60	1.95	0.59
02/21/97	12:00	0.48	1.82	19.70	1.85	0.56
02/21/97	13:00	0.46	1.74	19.60	1.95	0.59
02/21/97	14:00	0.48	1.82	19.50	2.05	0.62
02/21/97	15:00	0.48	1.82	19.45	2.10	0.64
02/21/97	16:00	0.48	1.82	19.45	2.10	0.64
02/21/97	16:30	0.48	1.82	19.41	2.14	0.65
02/21/97	16:30	stop	–	–	–	–

*Hours during which pumping was stopped for the gas tank on the air compressor to be filled.

SUMMARY OF OPERATIONS, WELL HC-2

Pumping began at 17:15 PST on February 24, 1997, and continued uninterrupted until sampling took place at 12:00 on February 25, 1997. A plot of drawdown versus time is displayed in Figure 3, and field data for pumping rate and drawdown are shown in Table 4 (see Appendix C for a comprehensive listing). The pump and pressure transducer were left downhole until sufficient recovery data were gathered. Laboratory analysis of Br^- later indicated that the concentration at the time of sampling (total pumping equal to 1.10 well volumes) was above 4 mg/L (4 mg/L of Br^- indicates a mixture of approximately 15 percent drilling fluid and 85 percent formation water), deemed too high for a representative sample. The pump was reinstalled in the hole on March 18, 1997, and approximately 0.87 additional well volumes were pumped in an effort to purge the remaining drilling fluid, making the total purged volume about two well volumes. Samples were collected at 15:00 PST on March 19, 1997, at which time the Br^- concentration was 0.59 mg/L. Using an average Br^- concentration in HC-2 drilling fluid of 26 mg/L, this suggests the samples contain approximately one percent drilling fluid (Table 1). The second set of samples was submitted for laboratory analysis; the water from the first set of samples was disposed of in accordance with pertinent regulations. Water chemistry analyses are reported in Appendix E.

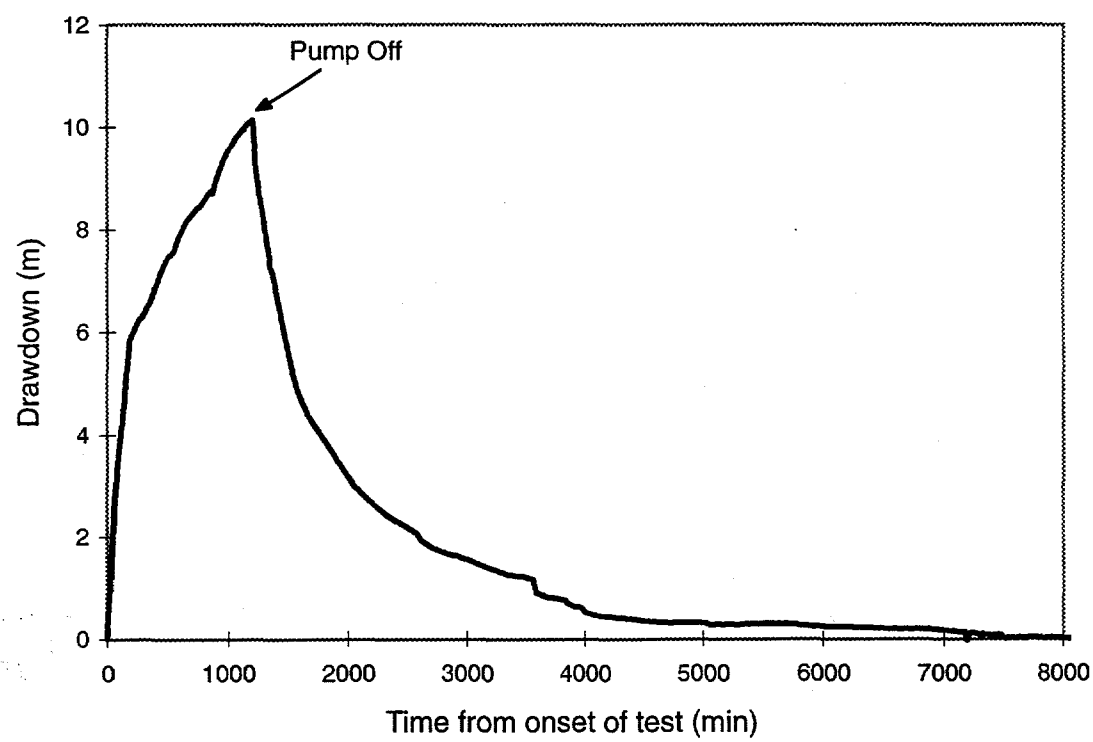

Figure 3. Drawdown vs. time for the HC-2 pump test. The data are tabulated in Table 4 and Appendix C.

TABLE 4. HC-2 FLOW RATE, HYDRAULIC HEAD AND DRAWDOWN. Detailed drawdown data can be found in Appendix C.

Date	Time	Flow Rate (gpm)	Flow Rate (L/min)	Head (ft)	Drawdown (ft)	Drawdown (m)
02/24/97	17:06	start	–	26.3	0.00	0.00
02/24/97	18:00	0.44	1.67	18.50	6.21	1.89
02/24/97	19:00	0.46	1.74	13.16	11.55	3.52
02/24/97	20:00	0.44	1.67	7.67	17.04	5.19
02/24/97	20:15	0.44	1.67	–	–	–
02/24/97	20:30	0.29	1.10	7.10	17.61	5.37
02/24/97	21:00	0.29	1.10	6.47	18.24	5.56
02/24/97	22:00	0.29	1.10	5.64	19.07	5.81
02/25/97	02:00	0.26	0.98	11.98*	23.08	7.03
02/25/97	06:00	0.26	0.98	8.98	26.08	7.95
02/25/97	08:00	0.32	1.21	7.96	27.10	8.26
02/25/97	09:30	0.30	1.14	6.00	29.06	8.86
02/25/97	10:00	0.29	1.10	5.26	29.80	9.08
02/25/97	10:30	0.29	1.10	4.84	30.22	9.21

*To avoid drawdown below the pump, pump and transducer were lowered 10.35 ft at 22:20 on February 24, 1997.

SUMMARY OF OPERATIONS, WELL HC-4

Sampling operations began at HC-4 on February 22, 1997, with pump start-up occurring at 17:58 PST. Field data for pumping rate and drawdown are shown in Table 5 (see Appendix D for a comprehensive listing) and a plot of drawdown versus time is displayed in Figure 4. Pumping continued until approximately 08:00 on February 24, 1997, when frozen water vapor in an air line caused pump failure. Pumping resumed at 12:45 on February 24, and sampling was carried out at 14:00, when 1.70 well volumes had been pumped. The pump was shut down at 15:00. Br^- analysis showed a concentration of 1.67 mg/L, which, based on an average drilling fluid Br^- concentration of 30 mg/L, indicates that it contains 95 percent native groundwater (Table 1). Water chemistry analyses are reported in Appendix E. The period of pump failure on February 24 provided sufficient recovery data for analysis, allowing the pump and transducer to be removed from the hole upon the conclusion of sampling.

TABLE 5. HC-4 FLOW RATE, HYDRAULIC HEAD AND DRAWDOWN. Detailed drawdown data can be found in Appendix D.

Date	Time	Flow Rate (gpm)	Flow Rate (L/min)	Head (ft)	Drawdown (ft)	Drawdown (m)
02/22/97	17:58	start	–	24.71	0.00	0.00
02/22/97	19:00	0.31	1.17	23.42	1.29	0.39
02/22/97	20:00	0.38	1.44	22.54	2.17	0.66
02/22/97	21:00	0.43	1.63	22.00	2.71	0.83
02/22/97	22:00	0.44	1.67	21.45	3.26	0.99
02/22/97	23:00	0.46	1.74	21.01	3.70	1.13
02/23/97	00:00	0.46	1.74	20.69	4.02	1.23
02/23/97	01:00	0.48	1.82	20.40	4.31	1.31
02/23/97	02:00	–	–	–	–	–
02/23/97	03:00	–	–	–	–	–
02/23/97	04:00	0.48	1.82	19.83	4.88	1.49
02/23/97	05:00	0.47	1.78	19.60	5.11	1.56
02/23/97	06:00	0.44	1.67	19.46	5.25	1.60
02/23/97	07:00	0.44	1.67	19.26	5.45	1.66
02/23/97	08:00	0.45	1.70	19.11	5.60	1.71
02/23/97	09:00	0.46	1.74	18.91	5.80	1.77
02/23/97	10:00	0.50	1.89	18.49	6.22	1.90
02/23/97	11:00	0.46	1.74	18.40	6.31	1.92
02/23/97	12:00	0.46	1.74	18.37	6.34	1.93
02/23/97	13:00	0.47	1.78	18.12	6.59	2.01
02/23/97	14:00	0.50	1.89	17.97	6.74	2.05
02/23/97	15:00	0.50	1.89	17.78	6.93	2.11
02/23/97	16:00	0.50	1.89	17.64	7.07	2.15
02/23/97	17:00	0.50	1.89	17.54	7.17	2.19
02/23/97	18:00	0.50	1.89	17.34	7.37	2.25
02/23/97	19:00	0.48	1.82	17.20	7.51	2.29
02/23/97	20:00	0.48	1.82	17.06	7.65	2.33
02/23/97	21:00	0.48	1.82	16.88	7.83	2.39
02/23/97	22:00	0.49	1.85	16.76	7.95	2.42
02/23/97	23:00	0.50	1.89	16.61	8.10	2.47
02/24/29	00:00	0.50	1.89	16.41	8.30	2.53
02/24/29	01:00	0.50	1.89	16.33	8.38	2.55
02/24/29	02:00	–	–	–	–	–
02/24/29	03:00	–	–	–	–	–
02/24/29	04:00	0.49	1.85	16.04	8.67	2.64
02/24/29	05:00	0.48	1.82	16.00	8.71	2.65
02/24/29	06:00	0.47	1.78	15.98	8.73	2.66
02/24/29	07:00	0.46	1.74	15.98	8.73	2.66
02/24/29	08:00	stop	–	17.40	7.31	2.23
02/24/29	12:45	start	–	–	–	–
02/24/29	13:00	0.46	1.74	–	–	–
02/24/29	14:00	0.46	1.74	–	–	–
02/24/29	15:00	stop	–	–	–	–

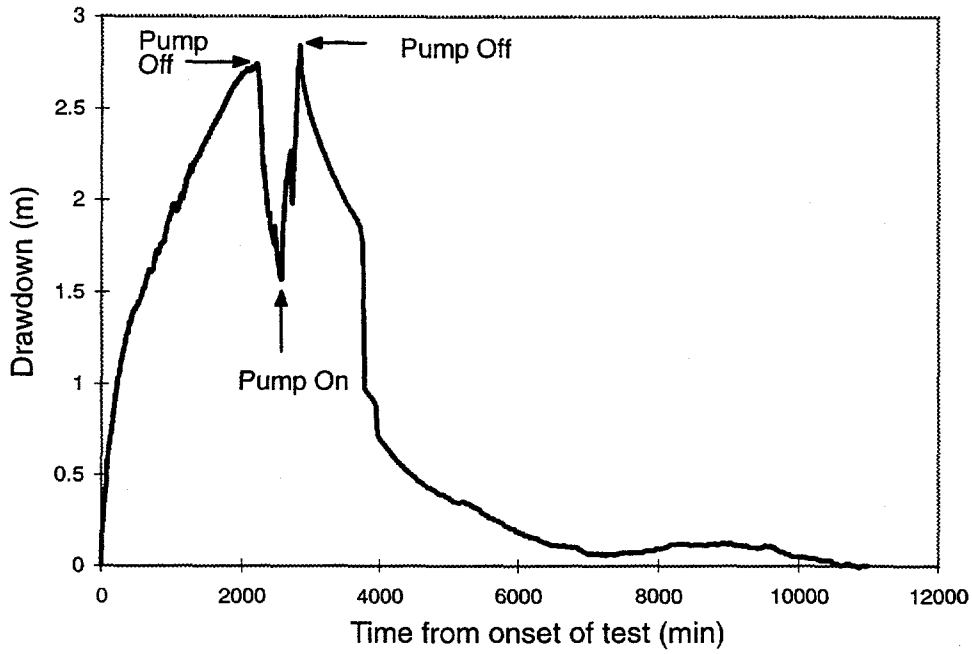

Figure 4. Drawdown vs. time for the HC-4 pump test. The data are tabulated in Table 5 and Appendix D.

SUMMARY OF HYDRAULIC TESTING

Pumping and recovery data were analyzed to make gross estimates of hydraulic conductivity values for the area of the formation surrounding each well. Estimations of hydraulic parameters for the site will be refined based on future field work scheduled to take place in 1997. The pumping test data were analyzed as described by Mcelwee (1980), and the recovery data were examined using the methods outlined by Kemblowski and Klein (1988) and Bouwer and Rice (1976). There are several major assumptions underlying one or both of these analyses, including a constant pumping rate, a drawdown which is small compared to the aquifer's saturated thickness for the pumping test, a constant well radius, and a homogeneous, isotropic aquifer. Although some assumptions were not met (most notably that the pumping rate was constant, and the aquifer is homogeneous and isotropic), the preliminary nature of these estimates obviates the need for strict adherence to all assumptions.

Hydraulic conductivity values determined from the tests are given in Table 6. Graphs of the drawdown and recovery versus time for each well appear in Figures 2, 3, and 4, with complete listings of water levels recorded by the datalogger at one-minute intervals in Appendices B, C, and D. In the case of the recovery tests, an abridged version of the data was used to determine conductivity, focusing on the portion of the curve where little disturbance was found.

Conductivity values range from 9.97×10^{-7} to 5.60×10^{-5} cm/sec, with the mean of the two measurements for each hole ranging from 1.48×10^{-6} to 4.70×10^{-5} cm/sec. These values are in good agreement with values determined as part of Project Shoal, which showed a range of conductivity values from 10^{-6} to 10^{-5} cm/sec, with 10^{-5} cm/sec given as an average value (Hazelton-Nuclear Science Corporation, 1966).

TABLE 6. SUMMARY OF HYDRAULIC CONDUCTIVITY MEASUREMENTS.

Well	Hydraulic Conductivity (Pumping) (cm/sec)	Hydraulic Conductivity (Recovery) (cm/sec)	Mean (cm/sec)	Numerical Analysis (cm/sec)
HC-1	3.79E–05	5.60E–05	4.70E–05	8.60E–05
HC-2	1.96E–06	9.97E–07	1.48E–06	—
HC-4	3.83E–06	1.18E–06	2.51E–06	—

Numerical Analysis of Hydraulic Properties (HC-1)

A more rigorous approach was taken to analyze the pumping test results at HC-1. The analytical methods of Mcelwee (1980), Kemblowski and Klein (1988) and Bouwer and Rice (1976) do not account for borehole storage or changes in saturated thickness due to drawdown. To account for borehole storage and unsaturated conditions, a variably saturated groundwater flow model SWMS_2D (Simunek et al., 1994) was used to estimate the hydraulic conductivity and porosity with more accuracy than the analytical methods.

The model geometry was setup to represent the borehole conditions and initial water level. The flow domain was simulated as a two-dimensional axisymmetric flow domain to represent the radial flow to the well bore. The axis of symmetry was simulated as no flow, as was the upper and lower boundaries. The outer boundary parallel to the axis of symmetry was represented as a constant pressure boundary, with pressures set to initial conditions. The pumping was represented as a flux boundary at all nodes within the borehole located beneath the pump intake elevation. Although the fractured granite aquifer is highly heterogeneous, the model domain was represented with a single homogenous hydraulic conductivity. The hydraulic conductivity was used as a calibration parameter such that measured water levels were in agreement with simulated values. To account for borehole storage, the porosity (assumed to be equal to specific yield) of the borehole was assigned a value of 1.0. The porosity of the remaining aquifer was also used as a calibration parameter.

The temporally varying pumping rate was input to the model and each simulation was performed for a 2.5-day period which corresponds to the entire drawdown and recovery period. The calibration parameters (hydraulic conductivity and porosity) were adjusted until a reasonable level of agreement was obtained between the pressure at the installed pressure transducer location (approximately 1 m above the pump intake) and simulated pressures.

Figure 5 shows the measured and simulated drawdowns for the calibrated simulation. The "best fit" was obtained with a hydraulic conductivity of 8.6×10^{-5} cm/sec, which is approximately twice the value obtained via analytical methods. The value obtained from numerical methods is considered more accurate as the analytical methods may underestimate hydraulic conductivity and overestimate porosity because these methods do not account for borehole storage. The "best-fit" porosity for the numerical simulation was 0.0005, which is slightly lower than the range (0.001 - 0.01) reported by Hazelton-Nuclear Science Corporation (1966).

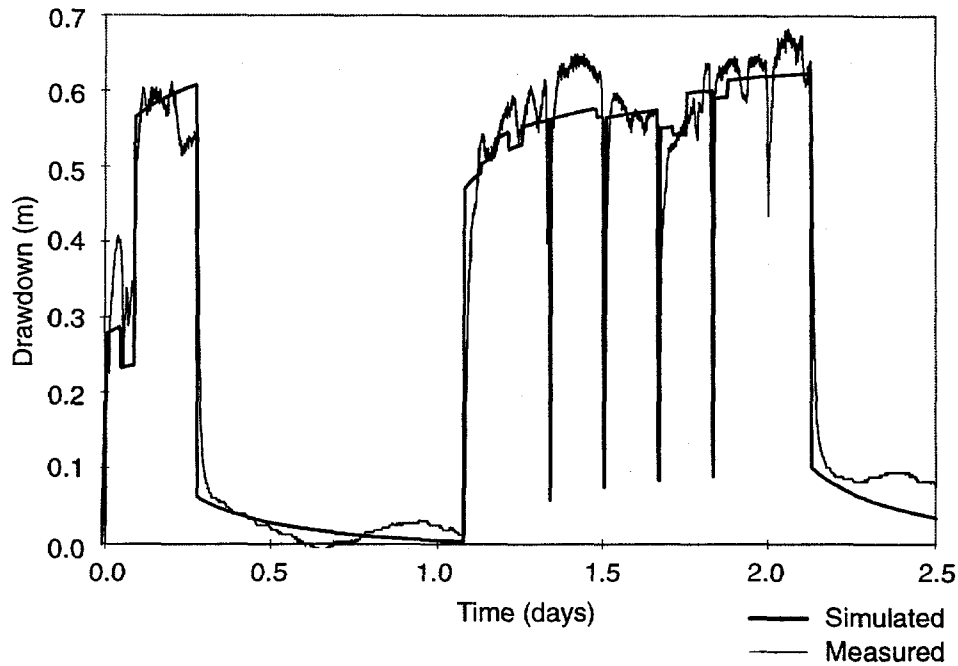

Figure 5. Measured and simulated drawdown for HC-1.

The relatively small hydraulic conductivities found in the HC-2 and HC-4 wells made simulation impossible because the model would not converge with such small hydraulic conductivity values. As such, these wells were not analyzed with numerical methods.

FLUID MANAGEMENT

Water pumped during the purging operations was placed in the double-lined sump present at each well pad, the construction of which is described by DOE (1997). At the conclusion of the initial sampling operations in February, 1997, two 1.89-L water samples from each of these sumps were collected for laboratory analysis. These samples were sent, under chain of custody, to Quanterra Laboratories in Missouri for gross alpha/beta, tritium and RCRA metals. International Technology (IT) Corporation, which is responsible for the sumps, was designated as the organization that would receive the analysis results from Quanterra. Table 7 provides information on the total volume of water placed in each sump, and the total percentage of sump volume filled by this water. The percentage of sump volume filled was calculated based on field discharge measurements, and sump volumes provided by DOE (1997). Prior to any purging activities, each of the sumps was filled to a depth of at least 0.3 m with water, apparently deposited by precipitation events. In addition, the sumps contain appreciable amounts of sand and gravel, most likely deposited by the strong winds often present at the site. Table 8 provides information on the sump water quality, provided by IT Corporation.

TABLE 7. SUMMARY OF FLUID DISCHARGES TO SUMPS.

Well	Volume Pumped (m^3)	Percent of Sump Capacity Filled*
HC-1	3.07	1.2
HC-2	2.16	1.0
HC-4	4.17	1.9

*Percent capacity filled was calculated based on a total sump capacity of 219 m^3 (DOE, 1997).

TABLE 8. PROJECT SHOAL FLUID MANAGEMENT DATA (from IT Corporation). Samples were collected from the sumps used during aquifer testing and sampling.

Sample #	Location	Date	Matrix	Arsenic (µg/L)	Barium (ug/L)	Cadmium (ug/L)	Chromium (ug/L)	Lead (ug/L)	Mercury (ug/L)	Selenium (ug/L)	Silver (ug/L)	Gross Alpha (pCi/L)	Gross Beta (pCi/L)	Tritium (pCi/L)
PSX00001	HC–1	11/3/96	Liquid	2.6	160	0.6	10.6	4.6	0.1	4.3	1.5	14.2	8.11	–2
PSX00002	HC–1	3/3/97	Liquid	1.8	18.6	0.8	1.2	0.8	0.1	1.9	2.5	1.59	2.21	32
PSX00003	HC–2	3/397	Liquid	1.8	16.8	0.8	1.2	0.8	0.1	1.9	2.5	1.68	1.64	215
PSX00005	HC–4	3/397	Liquid	1.8	11.2	0.8	1.2	0.8	0.1	1.9	2.5	12.8	3.47	252
PSF00001	HC–1	10/5/96	Liquid	8.6	52.6	3.0	4.4	1.3	0.1	4.0	6.6	4.6	9.64	22
PSF00002	HC–2	10/20/96	Liquid	62.1	55.6	3.0	4.4	7.4	0.25	3.1	6.6	6.15	6.61	13
PSF00005	HC–3	11/12/96	Liquid	1.8	138	0.6	3.2	4.9	0.16	2.8	1.5	17.5	6.62	–30
PSF00007	HC–4	10/24/96	Liquid	10.1	670	0.6	6.1	10.3	0.10	2.8	1.5	5.24	5.15	11

REFERENCES

Bouwer, H. and R. C. Rice, 1976. A slug test for determining hydraulic conductivity of unconfined aquifers with completely or partially penetrating wells, *Water Resources Research*, vol. 12, pp. 423–428.

Chapman, J., T. Mihevc and A. McKay, 1994. Groundwater flow near the Shoal site, Sand Springs Range, Nevada: Impact of density–driven flow, Desert Research Institute, Water Resources Center Report #45130, DOE/NV/10845–51.

Hazelton-Nuclear Science Corporation, 1966. Project Shoal Final Report: Post-shot Hydrologic Safety, Earth Sciences Division, Hazelton-Nuclear Science Corporation, Palo Alto, California, VUF–1014.

Kemblowski, M. W. and C. L. Klein, 1988. An automated numerical investigation of slug test data, *Ground Water* 26 (4), 435–438.

Mcelwee, C. D., 1980. The thesis equation: Evaluations, sensitivity to storage and transmissivity, and automated fit of pump test data, Groundwater Series 3, Kansas Geological Survey.

Simunek, J., T. Vogel and M. T. van Genuchten, 1994. The SWMS_2D code for simulating water flow and solute transport in two–dimensional variably saturated media Version 1.2, U.S. Salinity Laboratory/ARS/USDA, Riverside, California.

U. S. Department of Energy, 1996. Corrective Action Investigative Plan for Project Shoal area, CAU No. 416.

U.S. Department of Energy, 1997. Data Report: Project Shoal Area, Churchill County, Nevada (Draft).

This page intentionally left blank

APPENDIX A

BROMIDE CONCENTRATIONS DURING WELL PURGING

Well	Date	Time	Br^- (mg/L)	Cumulative Volume Purged m^3
HC–1	20–Feb–97	18:00	1.1	0.87
	21–Feb–97	02:00	1.0	1.70
		06:00	0.8	2.09
		10:00	0.7	2.50
		14:09	0.7	2.85
		15:30	0.7	3.07
HC–2	24–Feb–97	18:00	11.4	0.18
		22:00	11.4	0.66
	25–Feb–97	02:00	11.2	0.89
		06:00	8.78	1.04
		09:30	5.31	1.17
		10:00	4.97	1.21
		10:30	4.52	1.24
	19–Mar–97	15:00	0.59	2.16
HC–4	22–Feb–97	19:26	3.5	0.16
	23–Feb–97	00:00	3.5	0.67
		04:00	3.2	1.10
		08:00	2.7	1.51
		12:00	2.6	1.94
		16:00	2.4	2.39
		20:00	2.2	2.83
	24–Feb–97	04:00	1.65	3.73
		15:00	1.67	4.17

This page intentionally left blank

APPENDIX B

TIME DRAWDOWN DATA FOR HC-1

Date	Time Since Onset of Pumping (min)	Hour	Head (m)	Drawdown (m)
2/19/97	0	1311	6.6050	0.0000
2/19/97	10	1321	6.3459	0.2591
2/19/97	20	1331	6.3612	0.2438
2/19/97	30	1341	6.2758	0.3292
2/19/97	40	1351	6.2271	0.3780
2/19/97	50	1401	6.2088	0.3962
2/19/97	60	1411	6.2057	0.3993
2/19/97	70	1421	6.2149	0.3901
2/19/97	80	1431	6.3612	0.2438
2/19/97	90	1441	6.2850	0.3200
2/19/97	100	1451	6.3002	0.3048
2/19/97	110	1501	6.2819	0.3231
2/19/97	120	1511	6.2606	0.3444
2/19/97	130	1521	6.1996	0.4054
2/19/97	140	1531	6.0960	0.5090
2/19/97	150	1541	6.0289	0.5761
2/19/97	160	1551	6.0076	0.5974
2/19/97	170	1601	6.0137	0.5913
2/19/97	180	1611	6.0259	0.5791
2/19/97	190	1621	6.0198	0.5852
2/19/97	200	1631	6.0015	0.6035
2/19/97	210	1641	6.0046	0.6005
2/19/97	220	1651	6.0015	0.6035
2/19/97	230	1701	6.0168	0.5883
2/19/97	240	1711	6.0137	0.5913
2/19/97	250	1721	6.0259	0.5791
2/19/97	260	1731	6.0228	0.5822
2/19/97	270	1741	6.0320	0.5730
2/19/97	280	1751	6.0076	0.5974
2/19/97	290	1801	5.9985	0.6066
2/19/97	300	1811	6.0259	0.5791
2/19/97	310	1821	6.0442	0.5608
2/19/97	320	1831	6.0655	0.5395
2/19/97	330	1841	6.0747	0.5304
2/19/97	340	1851	6.0838	0.5212
2/19/97	350	1901	6.0838	0.5212

2/19/97	360	1911	6.0808	0.5243
2/19/97	370	1921	6.0686	0.5364
2/19/97	380	1931	6.0655	0.5395
2/19/97	390	1941	6.0625	0.5425
2/19/97	400	1951	6.0747	0.5304
2/19/97	410	2001	6.3520	0.2530
2/19/97	420	2011	6.4648	0.1402
2/19/97	430	2021	6.5105	0.0945
2/19/97	440	2031	6.5258	0.0792
2/19/97	450	2041	6.5319	0.0732
2/19/97	460	2051	6.5380	0.0671
2/19/97	470	2101	6.5441	0.0610
2/19/97	480	2111	6.5441	0.0610
2/19/97	490	2121	6.5471	0.0579
2/19/97	500	2131	6.5502	0.0549
2/19/97	510	2141	6.5502	0.0549
2/19/97	520	2151	6.5502	0.0549
2/19/97	530	2201	6.5562	0.0488
2/19/97	540	2211	6.5593	0.0457
2/19/97	550	2221	6.5623	0.0427
2/19/97	560	2231	6.5654	0.0396
2/19/97	570	2241	6.5654	0.0396
2/19/97	580	2251	6.5654	0.0396
2/19/97	590	2301	6.5654	0.0396
2/19/97	600	2311	6.5654	0.0396
2/19/97	610	2321	6.5654	0.0396
2/19/97	620	2331	6.5715	0.0335
2/19/97	630	2341	6.5715	0.0335
2/19/97	640	2351	6.5715	0.0335
2/20/97	650	2	6.5745	0.0305
2/20/97	660	12	6.5806	0.0244
2/20/97	670	22	6.5806	0.0244
2/20/97	680	32	6.5806	0.0244
2/20/97	690	42	6.5806	0.0244
2/20/97	700	52	6.5806	0.0244
2/20/97	710	102	6.5806	0.0244
2/20/97	720	112	6.5837	0.0213
2/20/97	730	122	6.5867	0.0183
2/20/97	740	132	6.5867	0.0183
2/20/97	750	142	6.5867	0.0183
2/20/97	760	152	6.5898	0.0152
2/20/97	770	202	6.5928	0.0122
2/20/97	780	212	6.5928	0.0122
2/20/97	790	222	6.5928	0.0122
2/20/97	800	232	6.5928	0.0122
2/20/97	810	242	6.5928	0.0122
2/20/97	820	252	6.5959	0.0091
2/20/97	830	302	6.5959	0.0091
2/20/97	840	312	6.6020	0.0030

2/20/97	850	322	6.6020	0.0030
2/20/97	860	332	6.6050	0.0000
2/20/97	870	342	6.6081	–0.0030
2/20/97	880	352	6.6050	0.0000
2/20/97	890	402	6.6081	–0.0030
2/20/97	900	412	6.6081	–0.0030
2/20/97	910	422	6.6111	–0.0061
2/20/97	920	432	6.6111	–0.0061
2/20/97	930	442	6.6142	–0.0091
2/20/97	940	452	6.6142	–0.0091
2/20/97	950	502	6.6142	–0.0091
2/20/97	960	512	6.6111	–0.0061
2/20/97	970	522	6.6111	–0.0061
2/20/97	980	532	6.6081	–0.0030
2/20/97	990	542	6.6050	0.0000
2/20/97	1000	552	6.6050	0.0000
2/20/97	1010	602	6.6050	0.0000
2/20/97	1020	612	6.6020	0.0030
2/20/97	1030	622	6.6020	0.0030
2/20/97	1040	632	6.6020	0.0030
2/20/97	1050	642	6.6020	0.0030
2/20/97	1060	652	6.6020	0.0030
2/20/97	1070	702	6.6020	0.0030
2/20/97	1080	712	6.6020	0.0030
2/20/97	1090	722	6.5989	0.0061
2/20/97	1100	732	6.5989	0.0061
2/20/97	1110	742	6.5959	0.0091
2/20/97	1120	752	6.5959	0.0091
2/20/97	1130	802	6.5898	0.0152
2/20/97	1140	812	6.5898	0.0152
2/20/97	1150	822	6.5898	0.0152
2/20/97	1160	832	6.5898	0.0152
2/20/97	1170	842	6.5867	0.0183
2/20/97	1180	852	6.5867	0.0183
2/20/97	1190	902	6.5867	0.0183
2/20/97	1200	912	6.5867	0.0183
2/20/97	1210	922	6.5837	0.0213
2/20/97	1220	932	6.5837	0.0213
2/20/97	1230	942	6.5837	0.0213
2/20/97	1240	952	6.5806	0.0244
2/20/97	1250	1002	6.5806	0.0244
2/20/97	1260	1012	6.5806	0.0244
2/20/97	1270	1022	6.5806	0.0244
2/20/97	1280	1032	6.5806	0.0244
2/20/97	1290	1042	6.5806	0.0244
2/20/97	1300	1052	6.5776	0.0274
2/20/97	1310	1102	6.5776	0.0274
2/20/97	1320	1112	6.5776	0.0274
2/20/97	1330	1122	6.5776	0.0274

2/20/97	1340	1132	6.5776	0.0274
2/20/97	1350	1142	6.5776	0.0274
2/20/97	1360	1152	6.5745	0.0305
2/20/97	1370	1202	6.5745	0.0305
2/20/97	1380	1212	6.5745	0.0305
2/20/97	1390	1222	6.5745	0.0305
2/20/97	1400	1232	6.5776	0.0274
2/20/97	1410	1242	6.5806	0.0244
2/20/97	1420	1252	6.5806	0.0244
2/20/97	1430	1302	6.5806	0.0244
2/20/97	1440	1312	6.5806	0.0244
2/20/97	1450	1322	6.5806	0.0244
2/20/97	1460	1332	6.5837	0.0213
2/20/97	1470	1342	6.5867	0.0183
2/20/97	1480	1352	6.5867	0.0183
2/20/97	1490	1402	6.5867	0.0183
2/20/97	1500	1412	6.5837	0.0213
2/20/97	1510	1422	6.5867	0.0183
2/20/97	1520	1432	6.5898	0.0152
2/20/97	1530	1442	6.5898	0.0152
2/20/97	1540	1452	6.5928	0.0122
2/20/97	1550	1502	6.5928	0.0122
2/20/97	1560	1512	6.5227	0.0823
2/20/97	1570	1522	6.2972	0.3078
2/20/97	1580	1532	6.2179	0.3871
2/20/97	1590	1542	6.1692	0.4359
2/20/97	1600	1552	6.1570	0.4481
2/20/97	1610	1602	6.1204	0.4846
2/20/97	1620	1612	6.0990	0.5060
2/20/97	1630	1622	6.0655	0.5395
2/20/97	1640	1632	6.0747	0.5304
2/20/97	1650	1642	6.0838	0.5212
2/20/97	1660	1652	6.0960	0.5090
2/20/97	1670	1702	6.0869	0.5182
2/20/97	1680	1712	6.0899	0.5151
2/20/97	1690	1722	6.0777	0.5273
2/20/97	1700	1732	6.0594	0.5456
2/20/97	1710	1742	6.0533	0.5517
2/20/97	1720	1752	6.0411	0.5639
2/20/97	1730	1802	6.0381	0.5669
2/20/97	1740	1812	6.0411	0.5639
2/20/97	1750	1822	6.0350	0.5700
2/20/97	1760	1832	6.0289	0.5761
2/20/97	1770	1842	6.0137	0.5913
2/20/97	1780	1852	6.0503	0.5547
2/20/97	1790	1902	6.0716	0.5334
2/20/97	1800	1912	6.0564	0.5486
2/20/97	1810	1922	6.0442	0.5608
2/20/97	1820	1932	6.0320	0.5730

2/20/97	1830	1942	6.0137	0.5913
2/20/97	1840	1952	6.0107	0.5944
2/20/97	1850	2002	6.0076	0.5974
2/20/97	1860	2012	6.0168	0.5883
2/20/97	1870	2022	6.0533	0.5517
2/20/97	1880	2032	6.0442	0.5608
2/20/97	1890	2042	6.0289	0.5761
2/20/97	1900	2052	6.0015	0.6035
2/20/97	1910	2102	6.0046	0.6005
2/20/97	1920	2112	6.1448	0.4602
2/20/97	1930	2122	6.0625	0.5425
2/20/97	1940	2132	6.0442	0.5608
2/20/97	1950	2142	6.0168	0.5883
2/20/97	1960	2152	5.9985	0.6066
2/20/97	1970	2202	5.9802	0.6248
2/20/97	1980	2212	5.9741	0.6309
2/20/97	1990	2222	5.9802	0.6248
2/20/97	2000	2232	5.9741	0.6309
2/20/97	2010	2242	5.9802	0.6248
2/20/97	2020	2252	5.9741	0.6309
2/20/97	2030	2302	5.9710	0.6340
2/20/97	2040	2312	5.9588	0.6462
2/20/97	2050	2322	5.9619	0.6431
2/20/97	2060	2332	5.9649	0.6401
2/20/97	2070	2342	5.9588	0.6462
2/20/97	2080	2352	5.9619	0.6431
2/21/97	2090	3	5.9649	0.6401
2/21/97	2100	13	5.9680	0.6370
2/21/97	2110	23	5.9741	0.6309
2/21/97	2120	33	5.9832	0.6218
2/21/97	2130	43	5.9802	0.6248
2/21/97	2140	53	5.9832	0.6218
2/21/97	2150	103	5.9802	0.6248
2/21/97	2160	113	6.1539	0.4511
2/21/97	2170	123	6.3398	0.2652
2/21/97	2180	133	6.1539	0.4511
2/21/97	2190	143	6.0503	0.5547
2/21/97	2200	153	6.0198	0.5852
2/21/97	2210	203	6.0137	0.5913
2/21/97	2220	213	6.0168	0.5883
2/21/97	2230	223	6.0168	0.5883
2/21/97	2240	233	6.0137	0.5913
2/21/97	2250	243	6.0259	0.5791
2/21/97	2260	253	6.0320	0.5730
2/21/97	2270	303	6.0442	0.5608
2/21/97	2280	313	6.0411	0.5639
2/21/97	2290	323	6.0442	0.5608
2/21/97	2300	333	6.0381	0.5669
2/21/97	2310	343	6.0381	0.5669

2/21/97	2320	353	6.0411	0.5639
2/21/97	2330	403	6.0381	0.5669
2/21/97	2340	413	6.0564	0.5486
2/21/97	2350	423	6.0442	0.5608
2/21/97	2360	433	6.0411	0.5639
2/21/97	2370	443	6.0320	0.5730
2/21/97	2380	453	6.0320	0.5730
2/21/97	2390	503	6.0289	0.5761
2/21/97	2400	513	6.0411	0.5639
2/21/97	2410	523	6.1600	0.4450
2/21/97	2420	533	6.2118	0.3932
2/21/97	2430	543	6.1539	0.4511
2/21/97	2440	553	6.1234	0.4816
2/21/97	2450	603	6.0808	0.5243
2/21/97	2460	613	6.0777	0.5273
2/21/97	2470	623	6.0777	0.5273
2/21/97	2480	633	6.0747	0.5304
2/21/97	2490	643	6.0655	0.5395
2/21/97	2500	653	6.0594	0.5456
2/21/97	2510	703	6.0533	0.5517
2/21/97	2520	713	6.0472	0.5578
2/21/97	2530	723	6.0442	0.5608
2/21/97	2540	733	6.0381	0.5669
2/21/97	2550	743	6.0320	0.5730
2/21/97	2560	753	6.0137	0.5913
2/21/97	2570	803	6.0594	0.5456
2/21/97	2580	813	6.0411	0.5639
2/21/97	2590	823	6.0259	0.5791
2/21/97	2600	833	6.0137	0.5913
2/21/97	2610	843	5.9802	0.6248
2/21/97	2620	853	5.9741	0.6309
2/21/97	2630	903	5.9680	0.6370
2/21/97	2640	913	6.0808	0.5243
2/21/97	2650	923	6.0228	0.5822
2/21/97	2660	933	5.9893	0.6157
2/21/97	2670	943	5.9863	0.6187
2/21/97	2680	953	5.9741	0.6309
2/21/97	2690	1003	5.9710	0.6340
2/21/97	2700	1013	5.9710	0.6340
2/21/97	2710	1023	5.9710	0.6340
2/21/97	2720	1033	5.9649	0.6401
2/21/97	2730	1043	5.9649	0.6401
2/21/97	2740	1053	5.9649	0.6401
2/21/97	2750	1103	5.9619	0.6431
2/21/97	2760	1113	5.9863	0.6187
2/21/97	2770	1123	6.0107	0.5944
2/21/97	2780	1133	6.0168	0.5883
2/21/97	2790	1143	6.0107	0.5944
2/21/97	2800	1153	5.9771	0.6279

2/21/97	2810	1203	5.9649	0.6401
2/21/97	2820	1213	5.9619	0.6431
2/21/97	2830	1223	5.9588	0.6462
2/21/97	2840	1233	5.9588	0.6462
2/21/97	2850	1243	5.9710	0.6340
2/21/97	2860	1253	5.9710	0.6340
2/21/97	2870	1303	5.9710	0.6340
2/21/97	2880	1313	6.1051	0.4999
2/21/97	2890	1323	6.0747	0.5304
2/21/97	2900	1333	6.0259	0.5791
2/21/97	2910	1343	5.9710	0.6340
2/21/97	2920	1353	5.9710	0.6340
2/21/97	2930	1403	5.9527	0.6523
2/21/97	2940	1413	5.9375	0.6675
2/21/97	2950	1423	5.9406	0.6645
2/21/97	2960	1433	5.9253	0.6797
2/21/97	2970	1443	5.9223	0.6828
2/21/97	2980	1453	5.9406	0.6645
2/21/97	2990	1503	5.9406	0.6645
2/21/97	3000	1513	5.9436	0.6614
2/21/97	3010	1523	5.9527	0.6523
2/21/97	3020	1533	5.9436	0.6614
2/21/97	3030	1543	5.9436	0.6614
2/21/97	3040	1553	5.9832	0.6218
2/21/97	3050	1603	5.9954	0.6096
2/21/97	3060	1613	5.9771	0.6279
2/21/97	3070	1623	6.0350	0.5700
2/21/97	3080	1633	6.3033	0.3018
2/21/97	3090	1643	6.4221	0.1829
2/21/97	3100	1653	6.4648	0.1402
2/21/97	3110	1703	6.4800	0.1250
2/21/97	3120	1713	6.4892	0.1158
2/21/97	3130	1723	6.5014	0.1036
2/21/97	3140	1733	6.5044	0.1006
2/21/97	3150	1743	6.5075	0.0975
2/21/97	3160	1753	6.5105	0.0945
2/21/97	3170	1803	6.5166	0.0884
2/21/97	3180	1813	6.5166	0.0884
2/21/97	3190	1823	6.5166	0.0884
2/21/97	3200	1833	6.5166	0.0884
2/21/97	3210	1843	6.5197	0.0853
2/21/97	3220	1853	6.5197	0.0853
2/21/97	3230	1903	6.5197	0.0853
2/21/97	3240	1913	6.5197	0.0853
2/21/97	3250	1923	6.5227	0.0823
2/21/97	3260	1933	6.5227	0.0823
2/21/97	3270	1943	6.5227	0.0823
2/21/97	3280	1953	6.5227	0.0823
2/21/97	3290	2003	6.5227	0.0823

2/21/97	3300	2013	6.5227	0.0823
2/21/97	3310	2023	6.5197	0.0853
2/21/97	3320	2033	6.5166	0.0884
2/21/97	3330	2043	6.5166	0.0884
2/21/97	3340	2053	6.5166	0.0884
2/21/97	3350	2103	6.5166	0.0884
2/21/97	3360	2113	6.5166	0.0884
2/21/97	3370	2123	6.5136	0.0914
2/21/97	3380	2133	6.5136	0.0914
2/21/97	3390	2143	6.5105	0.0945
2/21/97	3400	2153	6.5105	0.0945
2/21/97	3410	2203	6.5105	0.0945
2/21/97	3420	2213	6.5105	0.0945
2/21/97	3430	2223	6.5105	0.0945
2/21/97	3440	2233	6.5105	0.0945
2/21/97	3450	2243	6.5105	0.0945
2/21/97	3460	2253	6.5105	0.0945
2/21/97	3470	2303	6.5136	0.0914
2/21/97	3480	2313	6.5105	0.0945
2/21/97	3490	2323	6.5136	0.0914
2/21/97	3500	2333	6.5166	0.0884
2/21/97	3510	2343	6.5166	0.0884
2/21/97	3520	2353	6.5227	0.0823
2/22/97	3530	4	6.5227	0.0823
2/22/97	3540	14	6.5227	0.0823
2/22/97	3550	24	6.5227	0.0823
2/22/97	3560	34	6.5227	0.0823
2/22/97	3570	44	6.5227	0.0823
2/22/97	3580	54	6.5258	0.0792
2/22/97	3590	104	6.5227	0.0823
2/22/97	3600	114	6.5258	0.0792
2/22/97	3610	124	6.5319	0.0732
2/22/97	3620	134	6.5319	0.0732
2/22/97	3630	144	6.5349	0.0701
2/22/97	3640	154	6.5380	0.0671
2/22/97	3650	204	6.5380	0.0671
2/22/97	3660	214	6.5380	0.0671
2/22/97	3670	224	6.5380	0.0671
2/22/97	3680	234	6.5441	0.0610
2/22/97	3690	244	6.5441	0.0610
2/22/97	3700	254	6.5441	0.0610
2/22/97	3710	304	6.5502	0.0549
2/22/97	3720	314	6.5502	0.0549
2/22/97	3730	324	6.5502	0.0549
2/22/97	3740	334	6.5532	0.0518
2/22/97	3750	344	6.5562	0.0488
2/22/97	3760	354	6.5562	0.0488
2/22/97	3770	404	6.5562	0.0488
2/22/97	3780	414	6.5593	0.0457

2/22/97	3790	424	6.5623	0.0427
2/22/97	3800	434	6.5623	0.0427
2/22/97	3810	444	6.5623	0.0427
2/22/97	3820	454	6.5623	0.0427
2/22/97	3830	504	6.5623	0.0427
2/22/97	3840	514	6.5623	0.0427
2/22/97	3850	524	6.5623	0.0427
2/22/97	3860	534	6.5623	0.0427
2/22/97	3870	544	6.5623	0.0427
2/22/97	3880	554	6.5623	0.0427
2/22/97	3890	604	6.5623	0.0427
2/22/97	3900	614	6.5623	0.0427
2/22/97	3910	624	6.5623	0.0427
2/22/97	3920	634	6.5623	0.0427
2/22/97	3930	644	6.5623	0.0427
2/22/97	3940	654	6.5623	0.0427
2/22/97	3950	704	6.5623	0.0427
2/22/97	3960	714	6.5623	0.0427
2/22/97	3970	724	6.5623	0.0427
2/22/97	3980	734	6.5593	0.0457
2/22/97	3990	744	6.5593	0.0457
2/22/97	4000	754	6.5562	0.0488
2/22/97	4010	804	6.5562	0.0488

This page intentionally left blank

APPENDIX C

TIME DRAWDOWN DATA FOR HC-2

Date	Time Since Onset of Pumping (min)	Hour	Head (m)	Drawdown (m)
2/24/97	1	1707	8.0193	0.0061
2/24/97	11	1717	7.5621	0.4633
2/24/97	21	1727	7.1079	0.9174
2/24/97	31	1737	6.6446	1.3807
2/24/97	41	1747	6.1935	1.8318
2/24/97	51	1757	5.7760	2.2494
2/24/97	61	1807	5.4102	2.6152
2/24/97	71	1817	5.0566	2.9688
2/24/97	81	1827	4.6695	3.3558
2/24/97	91	1837	4.3647	3.6606
2/24/97	101	1847	4.1666	3.8588
2/24/97	111	1857	3.9837	4.0416
2/24/97	121	1907	3.7917	4.2337
2/24/97	131	1917	3.5601	4.4653
2/24/97	141	1927	3.3315	4.6939
2/24/97	151	1937	3.0084	5.0170
2/24/97	161	1947	2.7158	5.3096
2/24/97	171	1957	2.4506	5.5748
2/24/97	181	2007	2.2128	5.8125
2/24/97	191	2017	2.1397	5.8857
2/24/97	201	2027	2.0861	5.9393
2/24/97	211	2037	2.0446	5.9808
2/24/97	221	2047	1.9839	6.0414
2/24/97	231	2057	1.9273	6.0981
2/24/97	241	2107	1.8821	6.1432
2/24/97	251	2117	1.8312	6.1941
2/24/97	261	2127	1.7831	6.2423
2/24/97	271	2137	1.7547	6.2707
2/24/97	281	2147	1.7410	6.2844
2/24/97	291	2157	1.7160	6.3094
2/24/97	301	2207	1.6749	6.3505
2/24/97	311	2217	1.6398	6.3856
2/24/97	321	2227	4.7305	6.4471
2/24/97	331	2237	4.6817	6.4959
2/24/97	341	2247	4.6452	6.5325
2/24/97	351	2257	4.6025	6.5751

2/24/97	361	2307	4.5415	6.6361
2/24/97	371	2317	4.4775	6.7001
2/24/97	381	2327	4.4135	6.7641
2/24/97	391	2337	4.3525	6.8251
2/24/97	401	2347	4.2885	6.8891
2/24/97	411	2357	4.2276	6.9500
2/25/97	421	7	4.1636	7.0141
2/25/97	431	17	4.0935	7.0842
2/25/97	441	27	4.0447	7.1329
2/25/97	451	37	3.9807	7.1969
2/25/97	461	47	3.9289	7.2488
2/25/97	471	57	3.8801	7.2975
2/25/97	481	107	3.8191	7.3585
2/25/97	491	117	3.7582	7.4194
2/25/97	501	127	3.7155	7.4621
2/25/97	511	137	3.6850	7.4926
2/25/97	521	147	3.6698	7.5078
2/25/97	531	157	3.6515	7.5261
2/25/97	541	207	3.6210	7.5566
2/25/97	551	217	3.5723	7.6054
2/25/97	561	227	3.5113	7.6663
2/25/97	571	237	3.4381	7.7395
2/25/97	581	247	3.3802	7.7974
2/25/97	591	257	3.3315	7.8462
2/25/97	601	307	3.2827	7.8949
2/25/97	611	317	3.2339	7.9437
2/25/97	621	327	3.1821	7.9955
2/25/97	631	337	3.1242	8.0534
2/25/97	641	347	3.0785	8.0991
2/25/97	651	357	3.0389	8.1388
2/25/97	661	407	2.9931	8.1845
2/25/97	671	417	2.9627	8.2150
2/25/97	681	427	2.9352	8.2424
2/25/97	691	437	2.9139	8.2637
2/25/97	701	447	2.8834	8.2942
2/25/97	711	457	2.8529	8.3247
2/25/97	721	507	2.8255	8.3521
2/25/97	731	517	2.7920	8.3857
2/25/97	741	527	2.7615	8.4161
2/25/97	751	537	2.7371	8.4405
2/25/97	761	547	2.7402	8.4375
2/25/97	771	557	2.7158	8.4619
2/25/97	781	607	2.6792	8.4984
2/25/97	791	617	2.6487	8.5289
2/25/97	801	627	2.6091	8.5685
2/25/97	811	637	2.5786	8.5990
2/25/97	821	647	2.5420	8.6356
2/25/97	831	657	2.5024	8.6752
2/25/97	841	707	2.4689	8.7087

2/25/97	851	717	2.4414	8.7362
2/25/97	861	727	2.4354	8.7423
2/25/97	871	737	2.4719	8.7057
2/25/97	881	747	2.3866	8.7910
2/25/97	891	757	2.2951	8.8825
2/25/97	901	807	2.2159	8.9617
2/25/97	911	817	2.1458	9.0318
2/25/97	921	827	2.0797	9.0980
2/25/97	931	837	2.0260	9.1516
2/25/97	941	847	1.9605	9.2172
2/25/97	951	857	1.8986	9.2790
2/25/97	961	907	1.8306	9.3470
2/25/97	971	917	1.7733	9.4043
2/25/97	981	927	1.7334	9.4442
2/25/97	991	937	1.6807	9.4970
2/25/97	1001	947	1.6410	9.5366
2/25/97	1011	957	1.5935	9.5841
2/25/97	1021	1007	1.5575	9.6201
2/25/97	1031	1017	1.5149	9.6628
2/25/97	1041	1027	1.4725	9.7051
2/25/97	1051	1037	1.4344	9.7432
2/25/97	1061	1047	1.3884	9.7893
2/25/97	1071	1057	1.3618	9.8158
2/25/97	1081	1107	1.3350	9.8426
2/25/97	1091	1117	1.3103	9.8673
2/25/97	1101	1127	1.2735	9.9042
2/25/97	1111	1137	1.2424	9.9353
2/25/97	1121	1147	1.2222	9.9554
2/25/97	1131	1157	1.2030	9.9746
2/25/97	1141	1207	1.1625	10.0151
2/25/97	1151	1217	1.1403	10.0374
2/25/97	1161	1227	1.1140	10.0636
2/25/97	1171	1237	1.0958	10.0819
2/25/97	1181	1247	1.0826	10.0950
2/25/97	1191	1257	1.0674	10.1102
2/25/97	1201	1307	1.0333	10.1444
2/25/97	1211	1317	1.3591	9.8185
2/25/97	1221	1327	1.6791	9.4985
2/25/97	1231	1337	1.9867	9.1909
2/25/97	1349	1455	9.2507	7.3000
2/25/97	1399	1545	9.7323	6.8184
2/25/97	1549	1815	11.4239	5.1267
2/25/97	1699	2045	12.2987	4.2520
2/25/97	1849	2315	12.8290	3.7216
2/26/97	1999	145	13.3929	3.1577
2/26/97	2149	415	13.7861	2.7645
2/26/97	2299	645	14.0879	2.4628
2/26/97	2449	915	14.3104	2.2403
2/26/97	2599	1145	14.5725	1.9782

2/26/97	2749	1415	14.8133	1.7374
2/26/97	2899	1645	14.9200	1.6307
2/26/97	3049	1915	15.0419	1.5088
2/26/97	3199	2145	15.1729	1.3777
2/27/97	3349	15	15.3040	1.2466
2/27/97	3499	245	15.3558	1.1948
2/27/97	3649	515	15.7155	0.8352
2/27/97	3799	745	15.7764	0.7742
2/27/97	3949	1015	15.9288	0.6218
2/27/97	4099	1245	16.0965	0.4542
2/27/97	4249	1515	16.1331	0.4176
2/27/97	4399	1745	16.1727	0.3780
2/27/97	4549	2015	16.2184	0.3322
2/27/97	4699	2245	16.2428	0.3078
2/28/97	4849	115	16.2336	0.3170
2/28/97	4999	345	16.2458	0.3048
2/28/97	5149	615	16.2733	0.2774
2/28/97	5299	845	16.2824	0.2682
2/28/97	5449	1115	16.2641	0.2865
2/28/97	5599	1345	16.2580	0.2926
2/28/97	5749	1615	16.2763	0.2743
2/28/97	5899	1845	16.3098	0.2408
2/28/97	6049	2115	16.3312	0.2195
2/28/97	6199	2345	16.3220	0.2286
3/1/97	6349	215	16.3373	0.2134
3/1/97	6499	445	16.3525	0.1981
3/1/97	6649	715	16.3769	0.1737
3/1/97	6799	945	16.3647	0.1859
3/1/97	6949	1215	16.3769	0.1737
3/1/97	7099	1445	16.4165	0.1341
3/1/97	7249	1715	16.4409	0.1097
3/1/97	7399	1945	16.4805	0.0701
3/1/97	7549	2215	16.5384	0.0122
3/2/97	7699	45	16.5384	0.0122
3/2/97	7849	315	16.5354	0.0152
3/2/97	7999	545	16.5415	0.0091

APPENDIX D

TIME DRAWDOWN DATA FOR HC-4

Date	Time Since Onset of Pumping (min)	Hour	Head (m)	Drawdown (m)
2/22/97	1	1753	7.5712	0.0183
2/22/97	11	1803	7.4158	0.1737
2/22/97	21	1813	7.3457	0.2438
2/22/97	31	1823	7.2969	0.2926
2/22/97	41	1833	7.2420	0.3475
2/22/97	51	1843	7.2024	0.3871
2/22/97	61	1853	7.1658	0.4237
2/22/97	71	1903	7.1445	0.4450
2/22/97	81	1913	7.0348	0.5547
2/22/97	91	1923	6.9738	0.6157
2/22/97	101	1933	6.9220	0.6675
2/22/97	111	1943	6.9068	0.6828
2/22/97	121	1953	6.8854	0.7041
2/22/97	131	2003	6.8641	0.7254
2/22/97	141	2013	6.8428	0.7468
2/22/97	151	2023	6.8031	0.7864
2/22/97	161	2033	6.7666	0.8230
2/22/97	171	2043	6.7361	0.8534
2/22/97	181	2053	6.7026	0.8870
2/22/97	191	2103	6.6690	0.9205
2/22/97	201	2113	6.6507	0.9388
2/22/97	211	2123	6.6203	0.9693
2/22/97	221	2133	6.5959	0.9936
2/22/97	231	2143	6.5623	1.0272
2/22/97	241	2153	6.5380	1.0516
2/22/97	251	2203	6.5166	1.0729
2/22/97	261	2213	6.4892	1.1003
2/22/97	271	2223	6.4679	1.1217
2/22/97	281	2233	6.4496	1.1400
2/22/97	291	2243	6.4282	1.1613
2/22/97	301	2253	6.4099	1.1796
2/22/97	311	2303	6.3947	1.1948
2/22/97	321	2313	6.3764	1.2131
2/22/97	331	2323	6.3551	1.2344
2/22/97	341	2333	6.3337	1.2558
2/22/97	351	2343	6.3216	1.2680

2/22/97	361	2353	6.3124	1.2771
2/23/97	371	3	6.2941	1.2954
2/23/97	381	13	6.2819	1.3076
2/23/97	391	23	6.2545	1.3350
2/23/97	401	33	6.2575	1.3320
2/23/97	411	43	6.2514	1.3381
2/23/97	421	53	6.2271	1.3625
2/23/97	431	103	6.2149	1.3746
2/23/97	441	113	6.2057	1.3838
2/23/97	451	123	6.1935	1.3960
2/23/97	461	133	6.1844	1.4051
2/23/97	471	143	6.1874	1.4021
2/23/97	481	153	6.1813	1.4082
2/23/97	491	203	6.1692	1.4204
2/23/97	501	213	6.1631	1.4265
2/23/97	511	223	6.1478	1.4417
2/23/97	521	233	6.1570	1.4326
2/23/97	531	243	6.1448	1.4448
2/23/97	541	253	6.1326	1.4569
2/23/97	551	303	6.1112	1.4783
2/23/97	561	313	6.1082	1.4813
2/23/97	571	323	6.0869	1.5027
2/23/97	581	333	6.0716	1.5179
2/23/97	591	343	6.0716	1.5179
2/23/97	601	353	6.0686	1.5210
2/23/97	611	403	6.0442	1.5453
2/23/97	621	413	6.0320	1.5575
2/23/97	631	423	6.0107	1.5789
2/23/97	641	433	6.0015	1.5880
2/23/97	651	443	5.9863	1.6032
2/23/97	661	453	5.9802	1.6093
2/23/97	671	503	5.9741	1.6154
2/23/97	681	513	5.9741	1.6154
2/23/97	691	523	5.9741	1.6154
2/23/97	701	533	5.9741	1.6154
2/23/97	711	543	5.9710	1.6185
2/23/97	721	553	5.9680	1.6215
2/23/97	731	603	5.9466	1.6429
2/23/97	741	613	5.9253	1.6642
2/23/97	751	623	5.8979	1.6916
2/23/97	761	633	5.8826	1.7069
2/23/97	771	643	5.8674	1.7221
2/23/97	781	653	5.8704	1.7191
2/23/97	791	703	5.8765	1.7130
2/23/97	801	713	5.8704	1.7191
2/23/97	811	723	5.8644	1.7252
2/23/97	821	733	5.8491	1.7404
2/23/97	831	743	5.8308	1.7587
2/23/97	841	753	5.8278	1.7617

2/23/97	851	803	5.8217	1.7678
2/23/97	861	813	5.8217	1.7678
2/23/97	871	823	5.8247	1.7648
2/23/97	881	833	5.8156	1.7739
2/23/97	891	843	5.7942	1.7953
2/23/97	901	853	5.7699	1.8197
2/23/97	911	903	5.7638	1.8258
2/23/97	921	913	5.7333	1.8562
2/23/97	931	923	5.7120	1.8776
2/23/97	941	933	5.6998	1.8898
2/23/97	951	943	5.6876	1.9020
2/23/97	961	953	5.6662	1.9233
2/23/97	971	1003	5.6723	1.9172
2/23/97	981	1013	5.6571	1.9324
2/23/97	991	1023	5.6358	1.9538
2/23/97	1001	1033	5.6114	1.9782
2/23/97	1011	1043	5.6144	1.9751
2/23/97	1021	1053	5.6144	1.9751
2/23/97	1031	1103	5.6236	1.9660
2/23/97	1041	1113	5.6510	1.9385
2/23/97	1051	1123	5.6358	1.9538
2/23/97	1061	1133	5.6418	1.9477
2/23/97	1071	1143	5.6388	1.9507
2/23/97	1081	1153	5.6236	1.9660
2/23/97	1091	1203	5.6114	1.9782
2/23/97	1101	1213	5.6053	1.9842
2/23/97	1111	1223	5.5656	2.0239
2/23/97	1121	1233	5.5870	2.0025
2/23/97	1131	1243	5.5626	2.0269
2/23/97	1141	1253	5.5565	2.0330
2/23/97	1151	1303	5.5778	2.0117
2/23/97	1161	1313	5.5352	2.0544
2/23/97	1171	1323	5.5138	2.0757
2/23/97	1181	1333	5.5230	2.0665
2/23/97	1191	1343	5.5047	2.0848
2/23/97	1201	1353	5.4834	2.1062
2/23/97	1211	1403	5.4590	2.1306
2/23/97	1221	1413	5.4590	2.1306
2/23/97	1231	1423	5.4559	2.1336
2/23/97	1241	1433	5.4285	2.1610
2/23/97	1251	1443	5.4468	2.1427
2/23/97	1261	1453	5.4072	2.1824
2/23/97	1271	1503	5.4041	2.1854
2/23/97	1281	1513	5.4254	2.1641
2/23/97	1291	1523	5.4072	2.1824
2/23/97	1301	1533	5.3980	2.1915
2/23/97	1311	1543	5.3828	2.2068
2/23/97	1321	1553	5.3797	2.2098
2/23/97	1331	1603	5.3736	2.2159

2/23/97	1341	1613	5.3706	2.2189
2/23/97	1351	1623	5.3645	2.2250
2/23/97	1361	1633	5.3492	2.2403
2/23/97	1371	1643	5.3492	2.2403
2/23/97	1381	1653	5.3523	2.2372
2/23/97	1391	1703	5.3370	2.2525
2/23/97	1401	1713	5.3249	2.2647
2/23/97	1411	1723	5.3127	2.2769
2/23/97	1421	1733	5.3035	2.2860
2/23/97	1431	1743	5.2974	2.2921
2/23/97	1441	1753	5.2852	2.3043
2/23/97	1451	1803	5.2791	2.3104
2/23/97	1461	1813	5.2669	2.3226
2/23/97	1471	1823	5.2608	2.3287
2/23/97	1481	1833	5.2487	2.3409
2/23/97	1491	1843	5.2487	2.3409
2/23/97	1501	1853	5.2365	2.3531
2/23/97	1511	1903	5.2365	2.3531
2/23/97	1521	1913	5.2243	2.3652
2/23/97	1531	1923	5.2182	2.3713
2/23/97	1541	1933	5.2151	2.3744
2/23/97	1551	1943	5.2029	2.3866
2/23/97	1561	1953	5.2029	2.3866
2/23/97	1571	2003	5.1877	2.4018
2/23/97	1581	2013	5.1786	2.4110
2/23/97	1591	2023	5.1755	2.4140
2/23/97	1601	2033	5.1664	2.4232
2/23/97	1611	2043	5.1633	2.4262
2/23/97	1621	2053	5.1511	2.4384
2/23/97	1631	2103	5.1511	2.4384
2/23/97	1641	2113	5.1389	2.4506
2/23/97	1651	2123	5.1267	2.4628
2/23/97	1661	2133	5.1237	2.4658
2/23/97	1671	2143	5.1176	2.4719
2/23/97	1681	2153	5.1084	2.4811
2/23/97	1691	2203	5.1054	2.4841
2/23/97	1701	2213	5.0932	2.4963
2/23/97	1711	2223	5.0841	2.5055
2/23/97	1721	2233	5.0749	2.5146
2/23/97	1731	2243	5.0749	2.5146
2/23/97	1741	2253	5.0658	2.5237
2/23/97	1751	2303	5.0505	2.5390
2/23/97	1761	2313	5.0505	2.5390
2/23/97	1771	2323	5.0414	2.5481
2/23/97	1781	2333	5.0292	2.5603
2/23/97	1791	2343	5.0292	2.5603
2/23/97	1801	2353	5.0201	2.5695
2/24/97	1811	3	5.0079	2.5817
2/24/97	1821	13	5.0048	2.5847

2/24/97	1831	23	4.9987	2.5908
2/24/97	1841	33	4.9896	2.5999
2/24/97	1851	43	4.9774	2.6121
2/24/97	1861	53	4.9743	2.6152
2/24/97	1871	103	4.9652	2.6243
2/24/97	1881	113	4.9621	2.6274
2/24/97	1891	123	4.9591	2.6304
2/24/97	1901	133	4.9500	2.6396
2/24/97	1911	143	4.9469	2.6426
2/24/97	1921	153	4.9439	2.6457
2/24/97	1931	203	4.9378	2.6518
2/24/97	1941	213	4.9317	2.6579
2/24/97	1951	223	4.9256	2.6640
2/24/97	1961	233	4.9286	2.6609
2/24/97	1971	243	4.9164	2.6731
2/24/97	1981	253	4.9195	2.6700
2/24/97	1991	303	4.9103	2.6792
2/24/97	2001	313	4.9042	2.6853
2/24/97	2011	323	4.9042	2.6853
2/24/97	2021	333	4.9012	2.6883
2/24/97	2031	343	4.8951	2.6944
2/24/97	2041	353	4.8890	2.7005
2/24/97	2051	403	4.8829	2.7066
2/24/97	2061	413	4.8798	2.7097
2/24/97	2071	423	4.8829	2.7066
2/24/97	2081	433	4.8768	2.7127
2/24/97	2091	443	4.8798	2.7097
2/24/97	2101	453	4.8768	2.7127
2/24/97	2111	503	4.8768	2.7127
2/24/97	2121	513	4.8798	2.7097
2/24/97	2131	523	4.8859	2.7036
2/24/97	2141	533	4.8707	2.7188
2/24/97	2151	543	4.8677	2.7219
2/24/97	2161	553	4.8768	2.7127
2/24/97	2171	603	4.8585	2.7310
2/24/97	2181	613	4.8646	2.7249
2/24/97	2191	623	4.8585	2.7310
2/24/97	2201	633	4.8494	2.7402
2/24/97	2211	643	4.8524	2.7371
2/24/97	2221	653	4.8677	2.7219
2/24/97	2231	703	4.8981	2.6914
2/24/97	2241	713	4.9500	2.6396
2/24/97	2251	723	4.9957	2.5938
2/24/97	2261	733	5.0902	2.4994
2/24/97	2271	743	5.2243	2.3652
2/24/97	2281	753	5.2517	2.3378
2/24/97	2291	803	5.3553	2.2342
2/24/97	2301	813	5.4224	2.1671
2/24/97	2311	823	5.4193	2.1702

2/24/97	2321	833	5.4529	2.1366
2/24/97	2331	843	5.5047	2.0848
2/24/97	2341	853	5.5504	2.0391
2/24/97	2351	903	5.5992	1.9903
2/24/97	2361	913	5.6388	1.9507
2/24/97	2371	923	5.6723	1.9172
2/24/97	2381	933	5.6723	1.9172
2/24/97	2391	943	5.6632	1.9263
2/24/97	2401	953	5.7089	1.8806
2/24/97	2411	1003	5.7363	1.8532
2/24/97	2421	1013	5.7546	1.8349
2/24/97	2431	1023	5.7821	1.8075
2/24/97	2441	1033	5.8034	1.7861
2/24/97	2451	1043	5.8156	1.7739
2/24/97	2461	1053	5.8247	1.7648
2/24/97	2471	1103	5.7363	1.8532
2/24/97	2481	1113	5.7821	1.8075
2/24/97	2491	1123	5.8461	1.7435
2/24/97	2501	1133	5.8857	1.7038
2/24/97	2511	1143	5.9223	1.6673
2/24/97	2521	1153	5.9497	1.6398
2/24/97	2531	1203	5.9710	1.6185
2/24/97	2541	1213	5.9985	1.5911
2/24/97	2551	1223	6.0168	1.5728
2/24/97	2561	1233	5.9863	1.6032
2/24/97	2571	1243	5.9802	1.6093
2/24/97	2581	1253	5.8186	1.7709
2/24/97	2591	1303	5.7211	1.8684
2/24/97	2601	1313	5.6510	1.9385
2/24/97	2611	1323	5.5900	1.9995
2/24/97	2621	1333	5.5443	2.0452
2/24/97	2631	1343	5.5077	2.0818
2/24/97	2641	1353	5.4742	2.1153
2/24/97	2651	1403	5.4437	2.1458
2/24/97	2661	1413	5.4132	2.1763
2/24/97	2671	1423	5.3980	2.1915
2/24/97	2681	1433	5.3584	2.2311
2/24/97	2691	1443	5.3431	2.2464
2/24/97	2701	1453	5.3279	2.2616
2/24/97	2711	1503	5.4742	2.1153
2/24/97	2838	1630	14.0117	2.7523
2/24/97	2988	1900	14.3043	2.4597
2/24/97	3138	2130	14.4628	2.3012
2/25/97	3288	0	14.5999	2.1641
2/25/97	3438	230	14.7249	2.0391
2/25/97	3588	500	14.8255	1.9385
2/25/97	3738	730	14.9687	1.7953
2/25/97	3888	1000	15.8466	0.9174
2/25/97	4038	1230	16.0873	0.6767

2/25/97	4188	1500	16.1574	0.6066
2/25/97	4338	1730	16.2154	0.5486
2/25/97	4488	2000	16.2733	0.4907
2/25/97	4638	2230	16.3159	0.4481
2/26/97	4788	100	16.3464	0.4176
2/26/97	4938	330	16.3739	0.3901
2/26/97	5088	600	16.4135	0.3505
2/26/97	5238	830	16.4165	0.3475
2/26/97	5388	1100	16.4440	0.3200
2/26/97	5538	1330	16.4897	0.2743
2/26/97	5688	1600	16.5171	0.2469
2/26/97	5838	1830	16.5476	0.2164
2/26/97	5988	2100	16.5750	0.1890
2/26/97	6138	2330	16.5994	0.1646
2/27/97	6288	200	16.6177	0.1463
2/27/97	6438	430	16.6421	0.1219
2/27/97	6588	700	16.6573	0.1067
2/27/97	6738	930	16.6634	0.1006
2/27/97	6888	1200	16.6787	0.0853
2/27/97	7038	1430	16.7000	0.0640
2/27/97	7188	1700	16.7000	0.0640
2/27/97	7338	1930	16.7030	0.0610
2/27/97	7488	2200	16.6939	0.0701
2/28/97	7638	30	16.6939	0.0701
2/28/97	7788	300	16.6848	0.0792
2/28/97	7938	530	16.6817	0.0823
2/28/97	8088	800	16.6634	0.1006
2/28/97	8238	1030	16.6451	0.1189
2/28/97	8388	1300	16.6451	0.1189
2/28/97	8538	1530	16.6482	0.1158
2/28/97	8688	1800	16.6543	0.1097
2/28/97	8838	2030	16.6451	0.1189
2/28/97	8988	2300	16.6451	0.1189
3/1/97	9138	130	16.6512	0.1128
3/1/97	9288	400	16.6634	0.1006
3/1/97	9438	630	16.6665	0.0975
3/1/97	9588	900	16.6573	0.1067
3/1/97	9738	1130	16.6908	0.0732
3/1/97	9888	1400	16.7122	0.0518
3/1/97	10038	1630	16.7152	0.0488
3/1/97	10188	1900	16.7244	0.0396
3/1/97	10338	2130	16.7366	0.0274
3/1/97	10488	0	16.7488	0.0152
3/2/97	10638	230	16.7610	0.0030
3/2/97	10788	500	16.7640	0.0000

This page intentionally left blank

APPENDIX E

SHOAL WATER QUALITY AND STABLE ISOTOPE ANALYSIS

Chemical Analyses Performed by DRI on Groundwater Samples from the Shoal Site.

Well	Depth (m)	Date	T (°C)	pH[1] (S.U.)	EC[1] (μS/cm)	SiO_2 (mg/L)	Ca (mg/L)	Mg (mg/L)	Na (mg/L)	K (mg/L)	Cl (mg/L)	SO_4 (mg/L)	HCO_3 (mg/L)	NO_3 (mg/L)	Br (mg/L)
HC–1	336	2/21/97	13.6	8.00/8.01	423/467	19.8	45.7	6.01	38.7	2.79	47.7	52.2	116	11.1	0.7
HC–2	347	3/19/97	NA	NA/8.03	NA/670	20.8	58.1	7.87	64.8	3.48	80.8	108.0	118	0.44	0.59
HC–4	327	2/24/97	13.7	7.20/8.04	658/727	22.7	66.4	9.87	63.7	3.67	101.0	90.3	113	26.8	1.67

[1]First number is a measurement in the field at the time of sample collection. Second number is a laboratory measurement. If there is only one number, it is a laboratory measurement.

Isotopic Analyses Performed by DRI on Groundwater Samples from the Shoal Site.

Well	C^{14} Percent Modern Carbon	δD (‰)	$\delta^{13}C$ (‰)	$\delta^{18}O$ (‰)	Tritium (pCi/L)
HC–1	48.68 ± 0.83	–114	–10.8	–14.5	<5
HC–2	22.13 ± 0.51	–115	NA	–14.5	<5
HC–4	5408 ± 51.9	–113	–11.2	–14.2	1130±15

Preliminary Results from Analyses Performed by the U.S. Environmental Protection Agency as Part of their Long-Term Hydrologic Monitoring Program, from Samples Collected by DRI.

Well	Tritium (pCi/L)	Cs–137 (pCi/L)	Sr–89 (pCi/L)	Sr–90 (pCi/L)	Gross α (pCi/L)	Gross β (pCi/L)
HC–1	–78.43 ± 141.8 (235.9)	<6.00	<2.67	<1.37	19.19 ± 4.71 (4.75)	8.40 ± 2.81 (3.95)
HC–2	66±140 (228)	<4.9	NA	NA	59.44 ± 8.8 (8.01)	18.93 ± 3.01 (3.93)
HC–4	862.7 ± 158.2 (235.9)	<5.00	NA	NA	121.20 ± 11.27 (6.18)	40.51 ± 3.49 (3.44)

(Minimum Detectable Concentrations)

APPENDIX 5

STRESSED FLOWMETER TESTING SHOAL WELLS HC-1 AND HC-2

by Brad F. Lyles and Greg M. Pohll
July 1997

PURPOSE

In a fractured granite system, understanding the heterogeneity of the fractures is critical in the understanding of solute transport. At Shoal, a stochastic modeling approach is being used with the modeling domain described by classes of fractures. "Soft" data (geophysics, video logs, structure mapping) are the primary basis for establishing the fracture geometry because there is much greater soft data coverage as compared to hydraulic measurements. A link must be made, however, between the soft data and hard hydraulic conductivity distributions to be assigned to the various fracture classes. The stressed flowmeter testing was designed to provide that link.

The hydraulic conductivity values determined from the flowmeter tests will be used to condition the stochastic flow and transport model. Each borehole has been divided into three classes on regular vertical intervals. The classes represent varying degrees of fractures. Each fracture class will be assigned a hydraulic conductivity value based on the flowmeter testing. Ideally, multiple tests can be performed on each fracture class so that a distribution of conductivities is produced. That statistical distribution can be readily included in the stochastic modeling framework to ascertain solution uncertainty.

The vertical distribution of hydraulic conductivity can be measured in a borehole by pumping at a constant rate and measuring the vertical flow distribution. Once steady-state behavior is obtained, the discharge in a borehole is measured as a function of vertical position with the thermal flow meter (Figure 1). The data analysis is relatively simple using fully penetrating pumping test data available from earlier work (Earman and Pohll, 1997). The stressed flowmeter tests provide the relative conductivity K_i/K_{avg} for discrete vertical intervals.

DATA COLLECTION

The thermal flow meter (TFM) is a hydrologic logging tool that is designed to measure the vertical fluid flow in a borehole (Lyles, 1994; Hess, 1982). The TFM is 6.4 cm in diameter and approximately 120 cm long. The basic operation of the TFM is a measurement of the direction and speed of fluid flowing through the TFM sensor by uniformly heating a sheet of water and monitoring the thermally tagged water with two precision thermistors. The heat plume radiates upward and downward; under no-flow conditions, the heat pulse is received by the top thermistor first due to buoyancy effects (after approximately 60 seconds), then it is received by the bottom thermistor (after approximately 90 seconds). The TFM is positioned at discrete depths and a packer is inflated to divert all flow through the tool (increasing measurement resolution). The TFM directly measures

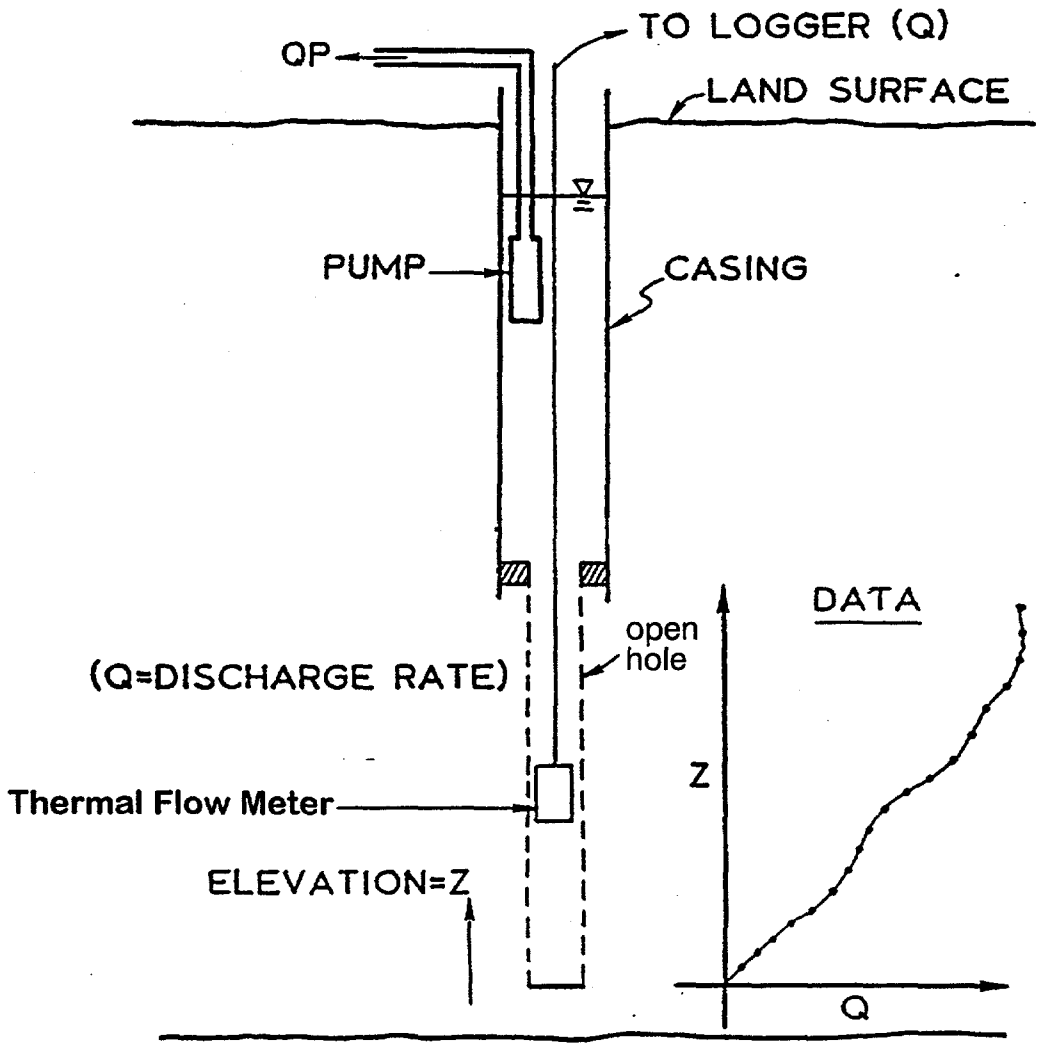

Figure 1. General operation of stressed flowmeter testing.

the rate of fluid flowing through the TFM's flow-through cell, which, when a packer seals off the rest of the cross sectional area, equals the rate in the borehole. The fluid velocity in the borehole can be calculated from the flow rate and well diameter. Repeated measurements are made at each depth to determine the mean and standard deviation. The measurement range is 0.08 to 57 L/min.

TFM surveys were conducted in wells HC-1 and HC-2 in March 1997. Wells HC-3 and HC-4 were unavailable for testing. Static measurements were performed prior to pumping to measure the natural vertical flow that may be occurring in each well; no vertical flow was measured in either well (see Tables 1 and 2). Dynamic TFM measurements were then performed while water was being pumped from each well with the Bennitt Pump. The average pumping rate in well HC-1 was 1.89 l/min (0.5 GPM) and from HC-2 was 1.14 l/min (0.3 GPM). Measurements were made at 10-meter

intervals, corresponding to discretization in the groundwater flow model. The results from the stressed measurements can be seen in Tables 3 and 4 and in Figures 2 and 3 for wells HC-1 and HC-2, respectively.

Table 1. Static Flowmeter Measurements in Well HC-1

Log Date: March 17, 1997		Operator: Brad Lyles/Greg Pohll		
Depth (m)	Bore Diameter (cm)	Response Time (sec)	Flow Rate (lpm)	Velocity (cm/min)
345.3	20.32	18.8 ± 3.120 *	0.000 ± 0.000	0.000 ± 0.000
392.9	20.32	16.8 ± 1.368	0.29 ± 0.024	0.90 ± 0.073

Table 2. Static Flowmeter Measurements in Well HC-2

Log Date: March 18, 1997		Operator: Brad Lyles		
Depth (m)	Bore Diameter (cm)	Response Time (sec)	Flow Rate (lpm)	Velocity (cm/min)
345.3	20.32	31.9 ± 2.380 *	0.000 ± 0.000	0.000 ± 0.000
359.0	20.32	999.9 ± 0.000 *	0.000 ± 0.000	0.000 ± 0.000

Table 3. Stressed Flowmeter Measurements in Well HC-1

Log Date: March 21, 1997		Operator: Brad Lyles/Sam Earman		
Depth (m)	Bore Diameter (cm)	Response Time (sec)	Flow Rate (lpm)	Velocity (cm/min)
333.1	12.70	2.58 ± 0.418	1.39 ± 0.132	10.9 ± 1.04
334.3	20.32	2.18 ± 0.184	1.80 ± 0.338	5.5 ± 1.04
345.3	20.32	2.30 ± 0.231	1.66 ± 0.314	5.1 ± 0.97
355.4	20.32	2.20 ± 0.219	1.77 ± 0.334	5.5 ± 1.02
365.4	20.32	2.20 ± 0.298	1.77 ± 0.334	5.5 ± 1.02
375.2	20.32	2.21 ± 0.199	1.76 ± 0.331	5.4 ± 1.02
385.2	20.32	2.24 ± 0.253	1.73 ± 0.325	5.3 ± 1.00
395.0	20.32	2.28 ± 0.227	1.69 ± 0.318	5.2 ± 0.97
397.0	20.32	20.0 ± 4.0 *	0.00 ± 0.00	0.0 ± 0.00

Table 4. Stressed Flowmeter Measurements in Well HC-2

Log Date: March 20, 1997		Operator: Brad Lyles/Sam Earman		
Depth (m)	Bore Diameter (cm)	Response Time (sec)	Flow Rate (lpm)	Velocity (cm/min)
355.4	20.32	7.54 ± 0.108	0.56 ± 0.054	1.7 ± 0.16
359.0	20.32	8.71 ± 0.076	0.50 ± 0.047	1.5 ± 0.15
345.3	20.32	8.81 ± 0.292	0.50 ± 0.047	1.5 ± 0.15

Negative values indicate downward flow.
Positive values indicate upward flow.
* = measurement was below calibration limits; pulse response-time was greater than 18 seconds.

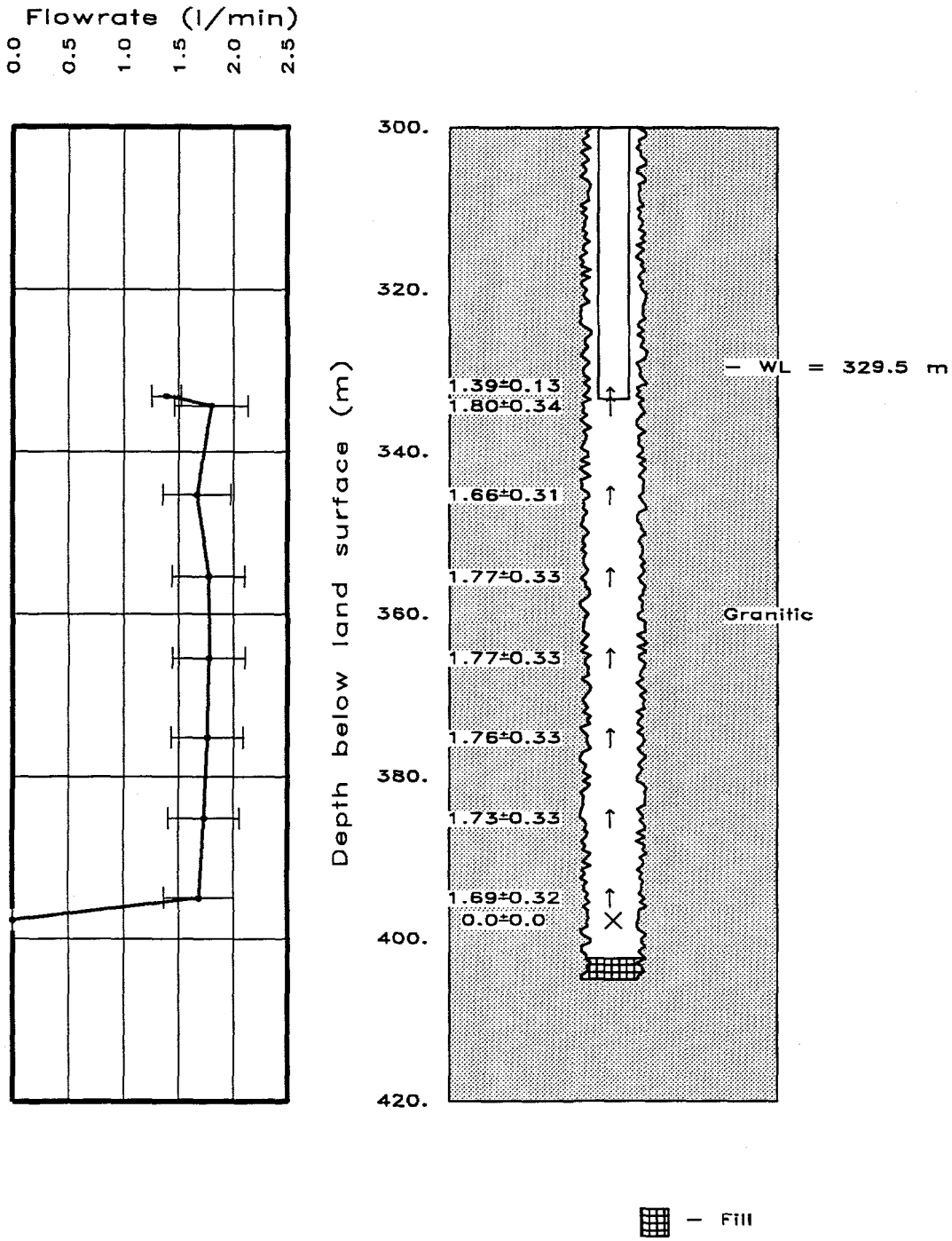

Figure 2. HC-1 well schematic and stressed thermal flow meter results.

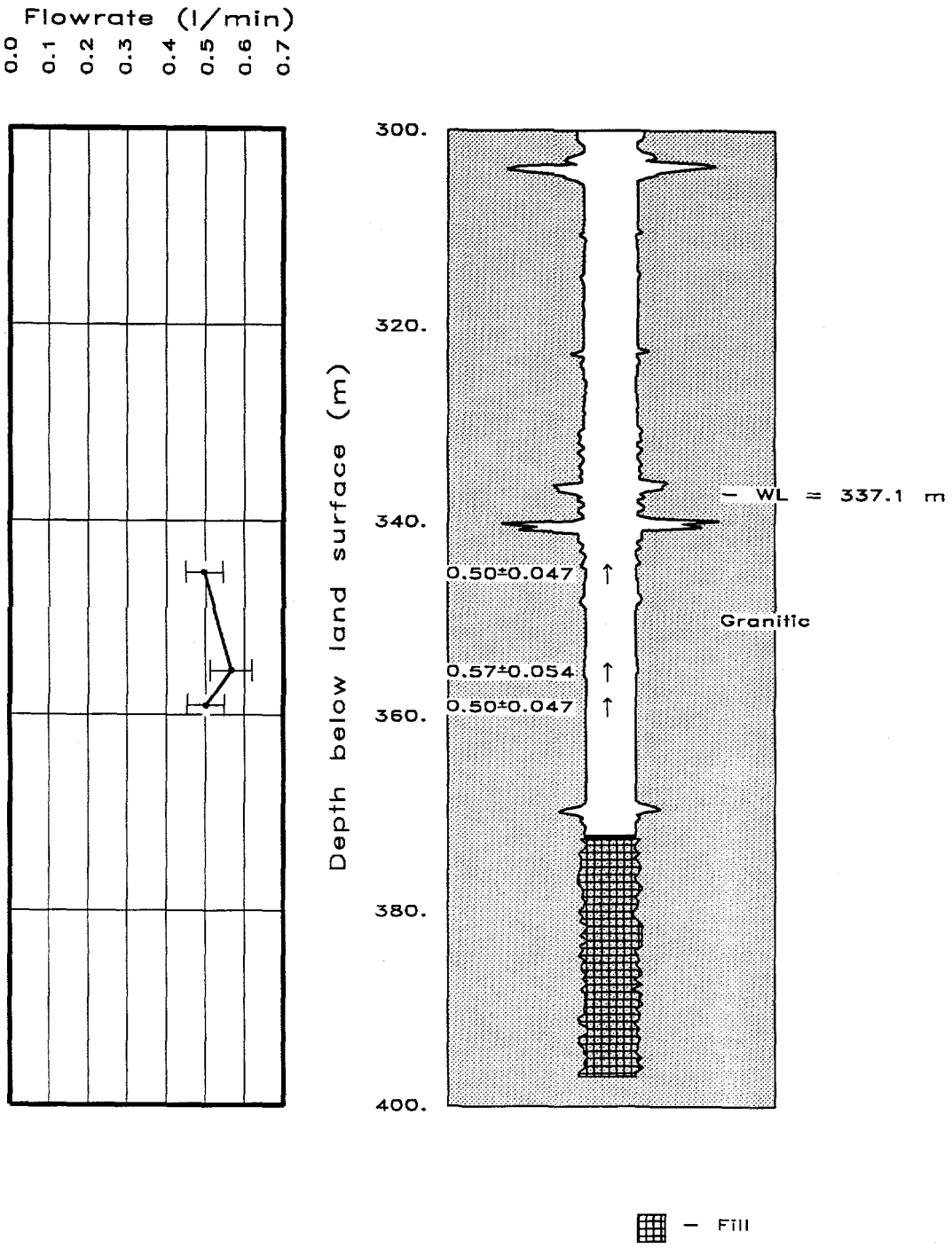

Figure 3. HC-2 well schematic and thermal flow meter results. Borehole geometry is based on caliper logs. Casing bottom is at a depth of 292 m.

HYDRAULIC CONDUCTIVITY ANALYSIS

The basic data analysis procedure assumes that the aquifer is composed of a series of n horizontal layers and the relative difference between two vertical flow readings ΔQ is proportional to the hydraulic conductivity, that is,

$$\Delta Q_i = \alpha \Delta z_i K_i$$

where α is a constant of proportionality. The average horizontal aquifer hydraulic conductivity is defined as:

$$\sum K_i \Delta z_i / B$$

where B is the aquifer thickness. To solve for the constant of proportionality one sums the ΔQ over the entire aquifer thickness Q_t to obtain:

$$Q_i = \alpha \sum_{i=1}^{n} \Delta z_i K_i$$

solving for K_i we have (Molz et al., 1989):

$$\frac{K_i}{\overline{K}} = \frac{\Delta Q_i / \Delta z_i}{Q_t / B}$$

Table 5 shows the hydraulic conductivities calculated from the stressed thermal flow analysis. In low conductivity zones the differences in flow rates between successive test intervals can be less than the resolution of the thermal flow meter. In these cases the hydraulic conductivity was not calculated.

Table 5. Hydraulic Conductivity as Determined by Thermal Flow Meter Stressed Test.

Well	Top Depth (m)	Bottom Depth (m)	K (cm/sec)
HC–1	335.28	345.34	3.97E–5
HC–1	365.46	375.51	3.4E–6
HC–1	375.51	385.27	1.0E–5
HC–1	385.27	395.33	1.4E–5
HC–1	395.33	402.34	7.7E–4
HC–2	355.4	359.0	1.5E–6

DISCUSSION AND CONCLUSIONS

TFM results from HC-1 suggest that most of the flow contributed to the well during pumping is coming from one fracture near the bottom of the well (between 395 and 397 m bls). Proportionally

little water is yielded from the remainder of the borehole, but the flow rate is gradually increasing up the borehole. Although the flow measurement at 345 m does not plot exactly on this trend-line, its measured deviation is consistent with this trend. The flow measurement within the casing (331 m) should equal the measured discharge from the Bennitt Pump, and should be greater than or equal to the flow rate measured in the lower portion of the borehole; the apparent reduced flow measured at this point is thought to be related to turbulent flow that may be occurring near the Bennitt Pump intake, and therefore this reading should be ignored.

TFM results from HC-2 suggest that most of the water pumped from the well is being yielded from the water table (*i.e.*, wellbore storage). The highest flow rate was measured at the first measurement location (355 m), the second highest rate was measured at the deepest station (359 m), and the lowest flow rate was measured at the shallowest depth (345 m); the measured flow rates were decreasing as a function of time, further suggesting that the well had not come to dynamic equilibrium prior to our TFM survey. This is supported by the measurements of hydraulic head in the well during pumping, which show that the water levels continued to decline throughout the test. Therefore; the TFM data collected at HC-2 are inconclusive.

REFERENCES

Hess, A.E., 1982. A heat-pulse flow meter for measuring low flow velocities in boreholes: U.S. Geological Survey Open-File Report 82–699, 44p.

Lyles, B.F., 1994. Increased thermal-pulse flowmeter resolution by adding a packer and computer: Ground Water Monitoring and Remediation, 14(4):191–199.

Earman, S. and G. Pohll, 1997. Shoal Field Operations: Letter Report submitted to the U.S. Department of Energy. Desert Research Institute, Water Resources Center.

Molz, F.J., R.H. Morin, A.E. Hess, J.G. Melville and O. Güven, 1989. The impeller meter for measuring aquifer permeability variations: Evaluation and comparison with other tests. *Water Resources Research,* 25(7):1677–1683.

This page intentionally left blank

APPENDIX 6

Stressed Flowmeter Testing
Shoal Wells HC-1 and HC-4

by Brad F. Lyles and Greg M. Pohll
August 1997

PURPOSE

In a fractured granite system, understanding the heterogeneity of the fractures is critical in the understanding of solute transport. At Shoal, a stochastic modeling approach is being used with the modeling domain described by classes of fractures. "Soft" data (geophysics, video logs, structure mapping) are the primary basis for establishing the fracture geometry because there is much greater soft data coverage as compared to hydraulic measurements. A link must be made, however, between the soft data and hard hydraulic conductivity distributions to be assigned to the various fracture classes. The stressed flowmeter testing was designed to provide that link.

The hydraulic conductivity values determined from the flowmeter tests will be used to condition the stochastic flow and transport model. Each borehole has been divided into three classes on regular vertical intervals. The classes represent varying degrees of fractures. Each fracture class will be assigned a hydraulic conductivity value based on the flowmeter testing. Ideally, multiple tests can be performed on each fracture class so that a distribution of conductivities is produced. That statistical distribution can be readily included in the stochastic modeling framework to ascertain solution uncertainty.

The vertical distribution of hydraulic conductivity can be measured in a borehole by injecting water at a constant rate and measuring the vertical flow distribution. Once steady-state behavior is obtained, the injection in a borehole is measured as a function of vertical position with the thermal flow meter (Figure 1). The data analysis is relatively simple using fully penetrating pumping test data available from earlier work (Earman and Pohll, 1997). The stressed flowmeter tests provide the relative conductivity K_i/K_{avg} for discrete vertical intervals.

DATA COLLECTION

The thermal flow meter (TFM) is a hydrologic logging tool that is designed to measure the vertical fluid flow in a borehole (Lyles, 1994; Hess, 1982). The TFM is 6.4 cm in diameter and approximately 120 cm long. The basic operation of the TFM is a measurement of the direction and speed of fluid flowing through the TFM sensor by uniformly heating a sheet of water and monitoring the thermally tagged water with two precision thermistors. The heat plume radiates upward and downward; under no-flow conditions, the heat pulse is received by the top thermistor first due to buoyancy effects (after approximately 60 seconds), then it is received by the bottom thermistor (after approximately 90 seconds). The TFM is positioned at discrete depths and a packer is inflated to

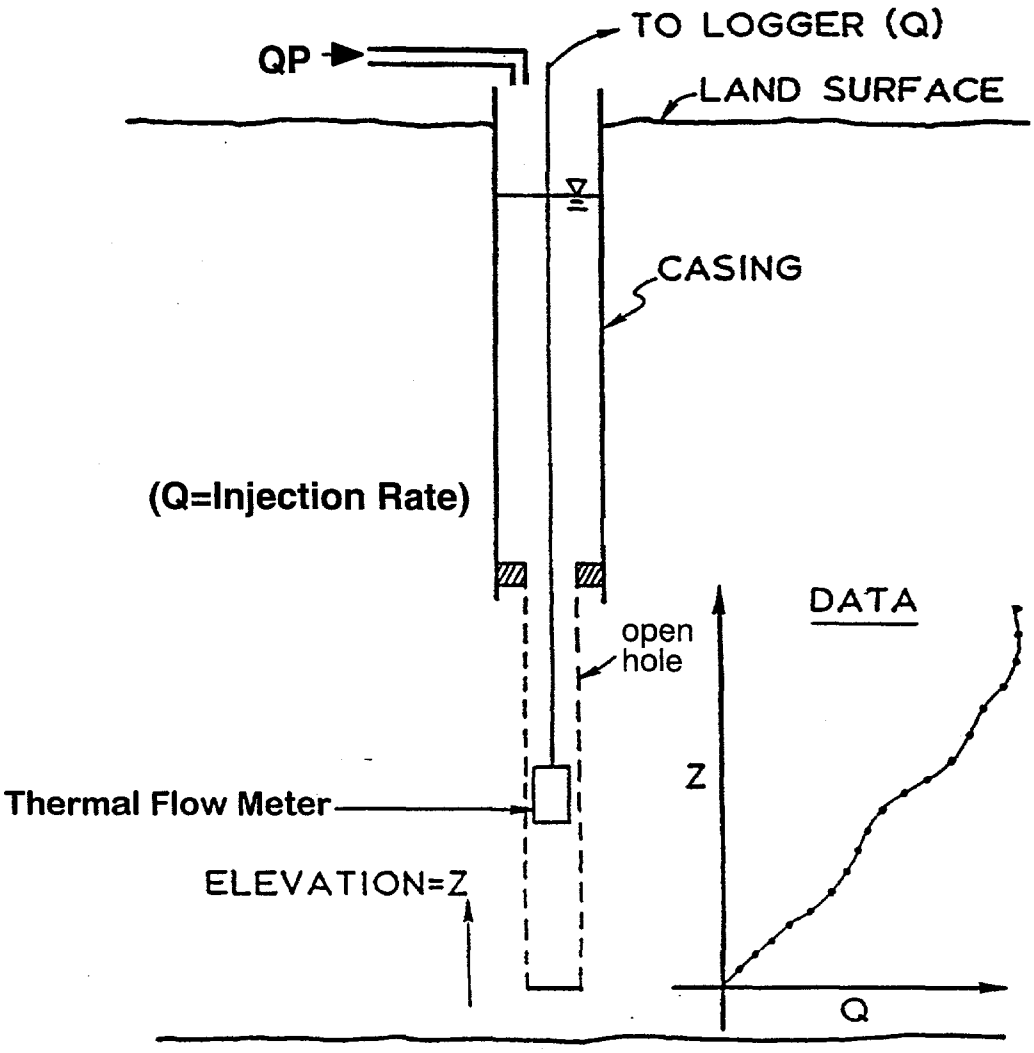

Figure 1. General operation of stressed flowmeter testing.

divert all flow through the tool (increasing measurement resolution). The TFM directly measures the rate of fluid flowing through the TFM's flow-through cell, which, when a packer seals off the rest of the cross sectional area, equals the rate in the borehole. The fluid velocity in the borehole can be calculated from the flow rate and well diameter. Repeated measurements are made at each depth to determine the mean and standard deviation. The measurement range is 0.03 to 57 L/min.

TFM surveys were conducted in wells HC-1 and HC-4 in July and August, 1997, respectively. Well HC-3 was unavailable for testing. The water level in the well HC-2 did not come to equilibrium within 48-hours of injection; therefore, no flow measurements were performed in the well. Static measurements were performed prior to pumping to measure the natural vertical flow that may be occurring in each well; no vertical flow was measured in the wells. Dynamic TFM measurements were then performed while water was being injected into each well. Injection water was trucked

from the Kennecott/Rawhide mine and was tagged with LiBr prior to injection. The average injection rate in well HC-1 was 4.0 l/min (1.1 GPM) and for HC-4 was 1.0 l/min (0.3 GPM). Measurements were made at 10-meter intervals, corresponding to discretization in the groundwater flow model (additional measurements were made at irregular intervals to measure inflow to specific fracture zones). The results from the stressed measurements can be seen in Tables 1 and 2 and in Figures 2 and 3 for wells HC-1 and HC-4, respectively.

Table 1. Stressed Flowmeter Measurements in Well HC-1

Log Date: July 9, 1997		Operator: Brad Lyles/Todd Mihevc		
Depth (m)	Bore Diameter (cm)	Response Time (sec)	Flow Rate (lpm)	Velocity (cm/min)
334.3	20.32	-1.49 ± 0.100	-3.50 ± 0.96	-10.8 ± 2.9
345.3	20.32	-1.45 ± 0.160	-3.61 ± 0.99	-11.1 ± 3.1
355.4	20.32	-1.47 ± 0.096	-3.56 ± 0.98	-11.0 ± 3.0
365.4	20.32	-1.41 ± 0.060	-3.73 ± 1.02	-10.6 ± 3.2
375.2	20.32	-1.51 ± 0.062	-3.45 ± 0.95	-10.6 ± 2.9
385.2	20.32	-1.50 ± 0.000	-3.47 ± 0.96	-10.7 ± 2.9
395.0	20.32	-1.64 ± 0.100	-3.15 ± 0.86	-9.67 ± 2.7
397.0	20.32	-40.0 ± 4.0 *	0.00 ± 0.00	0.0 ± 0.00

Table 2. Stressed Flowmeter Measurements in Well HC-4

Log Date: August 7, 1997		Operator: Brad Lyles/Greg Pohll		
Depth (m)	Bore Diameter (cm)	Response Time (sec)	Flow Rate (lpm)	Velocity (cm/min)
317.0	20.32	-2.20 ± 0.260	-0.63 ± 0.105	-1.94 ± 0.32
328.9	20.32	-3.12 ± 0.080	-0.39 ± 0.065	-1.20 ± 0.20
336.5	20.32	-4.20 ± 0.832	-0.26 ± 0.044	-0.80 ± 0.14
347.8	20.32	-7.61 ± 1.512	-0.15 ± 0.006	-0.46 ± 0.02
356.6	20.32	-8.65 ± 2.076	-0.13 ± 0.006	-0.41 ± 0.02
367.3	20.32	-11.80 ± 1.000	-0.10 ± 0.004	-0.31 ± 0.01
374.9	20.32	-16.30 ± 0.760	-0.08 ± 0.003	-0.24 ± 0.01

Negative values indicate downward flow.
Positive values indicate upward flow.
* = measurement was below calibration limits; pulse response-time was less than -24 seconds.

HYDRAULIC CONDUCTIVITY ANALYSIS

The basic data analysis procedure assumes that the aquifer is composed of a series of n horizontal layers and the relative difference between two vertical flow readings ΔQ is proportional to the hydraulic conductivity, that is,

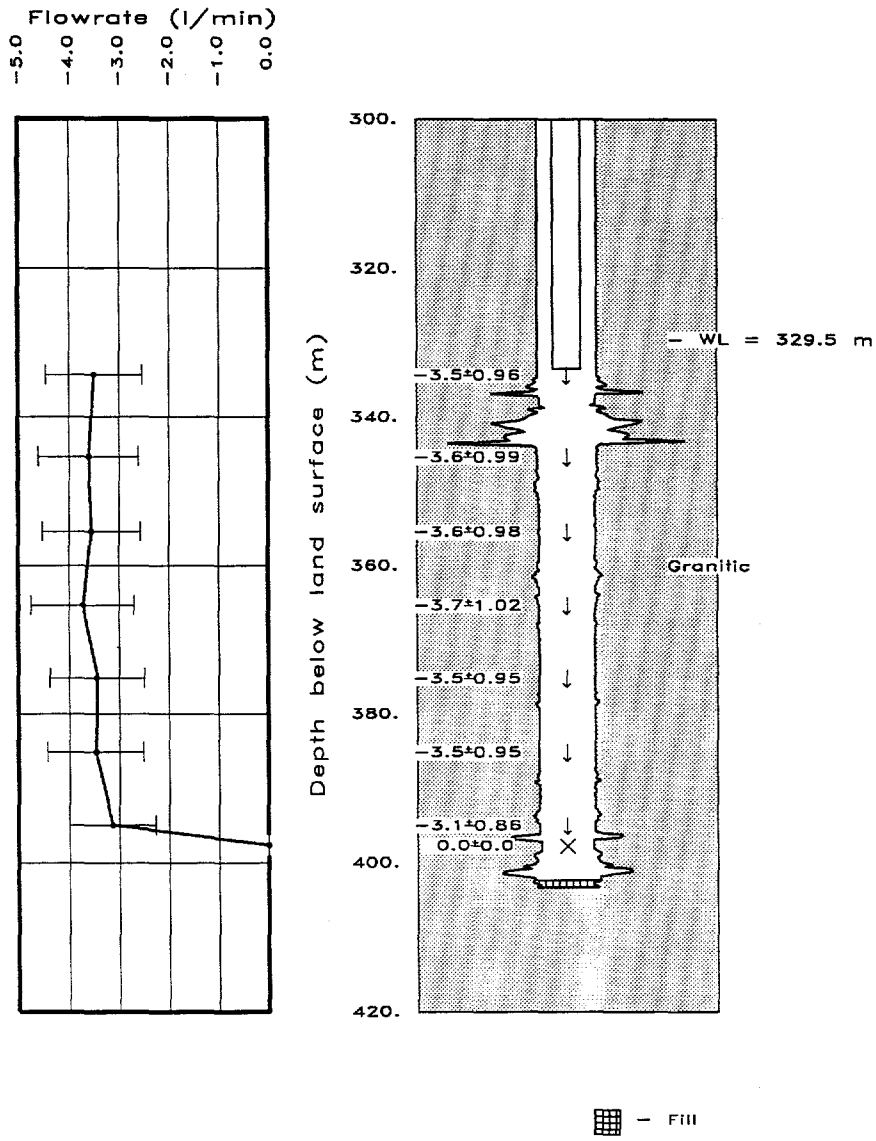

Figure 2. HC-1 well schematic and stressed thermal flow meter results.

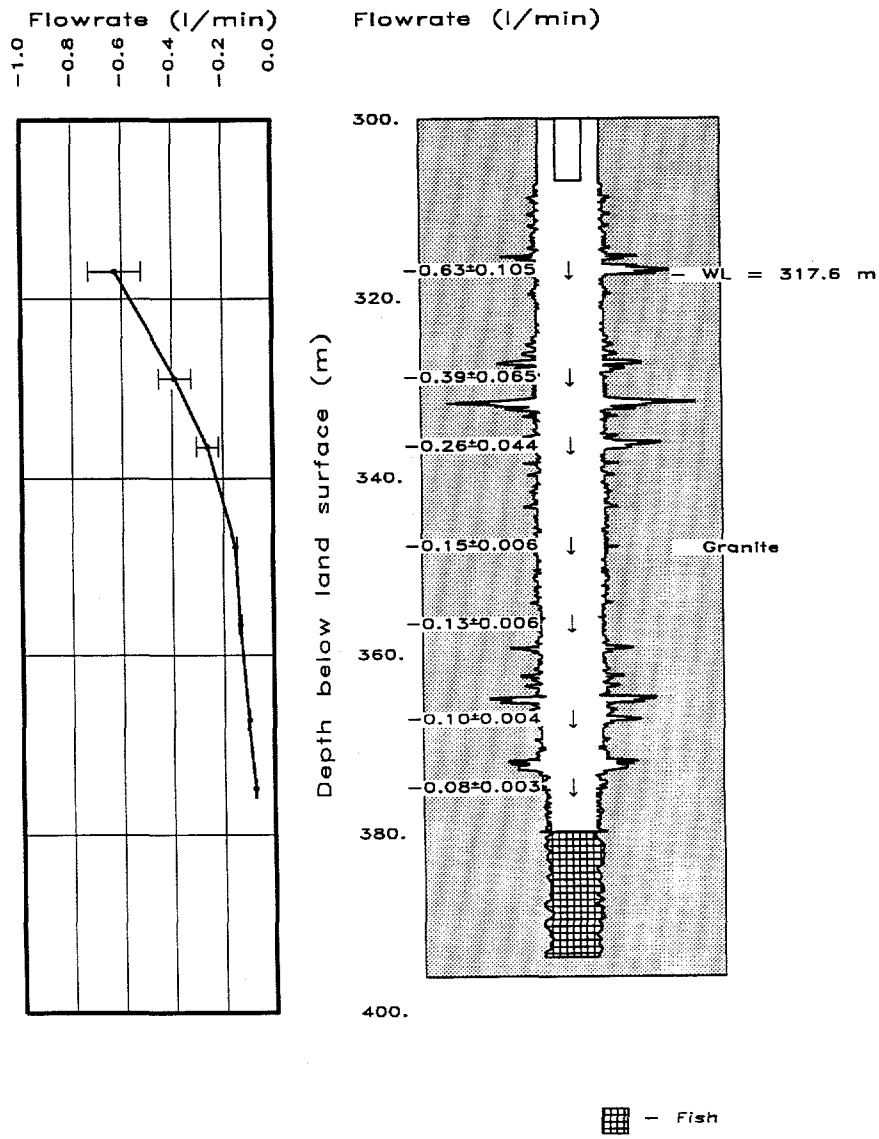

Figure 3. HC-4 well schematic and stressed thermal flow meter results.

$$\Delta Q_i = \alpha \Delta z_i K_i$$

where α is a constant of proportionality. The average horizontal aquifer hydraulic conductivity is defined as:

$$\sum K_i \Delta z_i / B$$

where B is the aquifer thickness. To solve for the constant of proportionality one sums the ΔQ over the entire aquifer thickness Q_t to obtain:

$$Q_i = \alpha \sum_{i=1}^{n} \Delta z_i K_i$$

solving for K_i we have (Molz et al., 1989):

$$\frac{K_i}{\overline{K}} = \frac{\Delta Q_i / \Delta z_i}{Q_t / B}$$

Table 5 shows the hydraulic conductivities calculated from the stressed thermal flow analysis. In low conductivity zones, the differences in flow rates between successive test intervals can be less than the resolution of the thermal flow meter. In these cases, the hydraulic conductivity was not calculated.

Table 5. Hydraulic Conductivity as Determined by Thermal Flow Meter Stressed Test.

Well	Top Depth (m)	Bottom Depth (m)	K (cm/sec)
HC-1	385.	395.	5.3E-5
HC-1	395.	402.	7.1E-4
HC-4	311.	317.	1.0E-5
HC-4	317.	329.	3.4E-6
HC-4	329.	336.	2.3E-6
HC-4	336.	348.	1.5E-6
HC-4	348.	357.	3.6E-6
HC-4	357.	367.	1.0E-6
HC-4	367.	375.	4.4E-6

In well HC-4, the flow could not be measured near the top of the section due to the turbulent action of the injected water. As such, the flow at 311 m below ground surface was assumed to be equal to the injection rate of 1 L/min. This assumption allowed for the calculation of hydraulic conductivity in the 311-317 section of the borehole.

DISCUSSION AND CONCLUSIONS

TFM results from HC-1 suggest that the most transmissive section of the well is associated with one fracture near the bottom of the well (between 395 and 397 m bls). Proportionally little water is yielded from the remainder of the borehole, but the flow rate is gradually increasing up the borehole. The hydraulic conductivity values near the bottom of the well were similar to those values computed from the pumped stressed TFM test performed previously (5.3E-5 compared to 1.4E-5 and 7.1E-4 compared to 7.7E-4, see Lyles and Pohll, 1997).

TFM measurements were not performed in well HC-2. The well did not come to equilibrium after 48-hours of injection, due the low hydraulic conductivity of the well.

TFM results from HC-4 suggest that the most transmissive section is near the top of the well and that there is progressively decreased flow as a function of depth.

REFERENCES

Hess, A.E., 1982. A heat-pulse flow meter for measuring low flow velocities in boreholes: U.S. Geological Survey Open-File Report 82-699, 44p.

Lyles, B.F. and G. Pohll, 1997. Stressed Flowmeter Testing Shoal Wells HC-1 and HC-2: Letter Report submitted to the U.S. Department of Energy. Desert Research Institute, Water Resources Center.

Lyles, B.F., 1994. Increased thermal-pulse flowmeter resolution by adding a packer and computer: Ground Water Monitoring and Remediation, 14(4):191-199.

Earman, S. and G. Pohll, 1997. Shoal Field Operations: Letter Report submitted to the U.S. Department of Energy. Desert Research Institute, Water Resources Center.

Molz, F.J., R.H. Morin, A.E. Hess, J.G. Melville and O. Güven, 1989. The impeller meter for measuring aquifer permeability variations: Evaluation and comparison with other tests. *Water Resources Research,* 25(7):1677-1683.

This page intentionally left blank

APPENDIX 7

EQUILIBRIUM STUDIES OF LEAD, CESIUM, STRONTIUM, CHROMATE, AND SELENITE SORPTION ON GRANITE FROM THE PROJECT SHOAL TEST SITE, FALLON, NEVADA

prepared by

Charalambos Papelis and Derek A. Sloop

Water Resources Center
Desert Research Institute
University and Community College System of Nevada

prepared for

Nevada Operations Office
U.S. Department of Energy
Las Vegas, Nevada

July 1997

This page intentionally left blank

ACKNOWLEDGMENTS

It is our pleasure to acknowledge the individuals who contributed to the timely completion of this project component. Greg Pohll for his assistance with sample collection, for providing the groundwater analysis, and for useful discussions throughout the project; Bill Albright for coordinating the granite processing; Steve Manning for his careful experimental work and for data reduction; and Clay Crow for the XRD of the granite. The continued support of Robert Bangerter is greatly appreciated.

EXECUTIVE SUMMARY

During the period of nuclear weapon production and testing, the U.S. conducted a series of tests at several test sites. These tests resulted in contamination from radionuclides as well as from other toxic metals and organic compounds. These contaminants are considered health hazards either because of their toxicity or because they are suspected or proven carcinogens. The fate and transport of dissolved contaminants are largely determined by the degree of contaminant interaction with the soil matrix. Radionuclides and metals with high sorption affinity for the mineral phases present, are expected to be severely retarded compared to groundwater flow. Inorganic contaminants with little affinity for the mineral phases present are expected to be retarded significantly less. To reduce the uncertainty in modeling the transport of contaminants of concern in the subsurface, parameters quantifying the extent and rate of partitioning of these contaminants at the mineral-water interface are required. The scope of this project component was to estimate the affinity of a strongly and a weakly binding cation (lead and strontium, respectively) and a strongly and a weakly binding anion (selenite and chromate, respectively) for aquifer material from the Project Shoal Underground Test Area, Fallon, Nevada. The Project Shoal Test Area is the site of an underground test conducted on October 26, 1963.

The granite from the Project Shoal Test Site was ground, characterized by a number of physicochemical methods, and subsequently used for equilibrium sorption experiments in simple electrolyte matrices and synthetic groundwaters from the test area. Lead displayed a typical cation sorption behavior with fractional uptake increasing with increasing pH. In addition, lead sorption was essentially ionic strength independent, suggesting strong binding and substantial retardation on these mineral surfaces. Sorption experiments with strontium and the granite sample from the Project Shoal site proved impossible to perform, because of the high strontium content of the rock and the dissolution of significant quantities of strontium during the experiments. It is therefore expected that under these conditions strontium would be highly mobile. Additional sorption experiments were, therefore, performed with the Cs cation, which is assumed to have a binding affinity between that of Pb and Sr. Sorption of cesium by the granite was weakly influenced, if at all, by pH indicating that cesium sorption may not be controlled by sorption on amphoteric surface sites.

Both chromate and selenite displayed a typical behavior for anions sorbed on amphoteric oxide surfaces. For both anions it appeared as if increased ionic strength resulted in increased fractional uptake. The effects of ionic strength, however, at least in most cases, were not dramatic.

Based on the experimental sorption data, parameters describing both linear and Freundlich isotherms were estimated for a variety of conditions. The results indicate that equilibrium partitioning at the granite-water is strongly pH dependent for all ions studied except cesium. As a consequence, modeling of the transport of these contaminants requires knowledge of or assumptions about the groundwater pH. Under certain conditions, the isotherms were approximately linear, thereby allowing the use of a linear isotherm to model the data. In most other cases, however, deviations from linearity were so severe, that the use of the Freundlich isotherm would be required. In general, cation isotherms were more linear than anion isotherms.

The isotherm parameters determined in this study can be used to reduce the uncertainty in radionuclide transport modeling by accounting for retardation of radionuclides and other contaminants of concern because of sorption on aquifer materials. It should be emphasized, however, that the parameters determined in this project only describe the equilibrium partitioning of contaminants at the mineral-water interface and do not provide any information on the rate of these reactions. Although the aquifer materials at the Project Shoal Test Site do not appear to be porous and, therefore, kinetic limitations are not expected to play a major role in contaminant sorption, this possibility should be investigated. Finally, it cannot be overemphasized that the results reported here are specific to the conditions used and that, given the non-linearity of some of these systems, use of these parameters outside their range of applicability might result in significant errors.

CONTENTS

ACKNOWLEDGMENTS i

EXECUTIVE SUMMARY ii

CONTENTS iv

FIGURES v

TABLES vi

INTRODUCTION 1

MATERIALS AND METHODS 4

ADSORBENT CHARACTERIZATION 4

EXPERIMENTAL PROCEDURES 7

RESULTS AND DISCUSSION 10

CATION SORPTION ON PROJECT SHOAL GRANITE 10

ANION SORPTION ON PROJECT SHOAL GRANITE 15

SUMMARY, CONCLUSIONS, AND RECOMMENDATIONS 20

REFERENCES 23

FIGURES

FIGURE 1. GENERAL MAP OF THE LOCATION OF THE PROJECT SHOAL UNDERGROUND NUCLEAR TEST.

FIGURE 2. SCANNING ELECTRON MICROGRAPH OF THE ADSORBENT (150X MAGNIFIED).

FIGURE 3. SCANNING ELECTRON MICROGRAPH OF ILMENITE PRESENT IN THE GRANITE.

FIGURE 4. SCANNING ELECTRON MICROGRAPH OF BIOTITE PRESENT IN THE GRANITE.

FIGURE 5. SCANNING ELECTRON MICROGRAPH OF QUARTZ PRESENT IN THE GRANITE.

FIGURE 6. SCANNING ELECTRON MICROGRAPH OF PLAGIOCLASE PRESENT IN THE GRANITE.

FIGURE 7. SCANNING ELECTRON MICROGRAPH OF A Zr MINERAL PRESENT IN THE GRANITE.

FIGURE 8. PARTICLE SIZE DISTRIBUTION OF THE ADSORBENT.

FIGURE 9. SORPTION OF Pb ON 10 g/L GRANITE AS A FUNCTION OF CONCENTRATION (I=0.01 M).

FIGURE 10. SORPTION OF Pb ON GRANITE AS A FUNCTION OF IONIC STRENGTH.

FIGURE 11. SORPTION OF Pb ON GRANITE IN THREE DIFFERENT SYNTHETIC GROUNDWATERS.

FIGURE 12. SORPTION OF Pb IN 0.01 M IONIC STRENGTH AND SYNTHETIC HS-1 GROUNDWATER.

FIGURE 13. DISSOLVED Sr AS A FUNCTION OF pH AND IONIC STRENGTH (SHOAL GRANITE 10 g/L).

FIGURE 14. SORPTION OF Cs IN HC-4 GROUNDWATER ON GRANITE AS A FUNCTION OF METAL CONCENTRATION.

FIGURE 15. SORPTION OF CHROMATE ON 10 g/L GRANITE AS A FUNCTION OF CHROMATE CONCENTRATION (I=0.01 M).

FIGURE 16. SORPTION OF Cr ON GRANITE IN THREE SYNTHETIC GROUNDWATERS.

FIGURE 17. SORPTION OF Cr ON 10 g/L GRANITE AS A FUNCTION OF IONIC STRENGTH.

FIGURE 18. SORPTION OF SELENITE ON 10 g/L GRANITE AS A FUNCTION OF SELENITE CONCENTRATION (I=0.01 M).

FIGURE 19. SORPTION OF SELENITE ON 10 g/L GRANITE AS A FUNCTION OF SELENITE CONCENTRATION (I=1.0 M).

FIGURE 20. SORPTION OF SELENITE ON 10 g/L GRANITE AS A FUNCTION OF IONIC STRENGTH.

TABLES

TABLE 1. MAJOR AND TRACE ELEMENT COMPOSITION OF GRANITE, BY WEIGHT, IN TERMS OF OXIDE PERCENTAGES.

TABLE 2. COMPOSITION OF GROUNDWATERS USED IN SORPTION STUDIES.

TABLE 3. LINEAR AND FREUNDLICH ISOTHERM PARAMETERS FOR LEAD SORPTION.

TABLE 4. LINEAR AND FREUNDLICH ISOTHERM PARAMETERS FOR CESIUM SORPTION.

TABLE 5. LINEAR AND FREUNDLICH ISOTHERM PARAMETERS FOR CHROMATE SORPTION.

TABLE 6. LINEAR AND FREUNDLICH ISOTHERM PARAMETERS FOR SELENITE SORPTION.

INTRODUCTION

During the period of nuclear weapon production and testing, the U.S. conducted a series of tests at several test sites. These tests resulted in contamination from radionuclides as well as from other toxic metals and organic compounds. Common radionuclides found in contaminated areas include both uranium and heavy transuranic elements (man-made radionuclides heavier than uranium), mainly neptunium, plutonium, and americium, as well as lighter radionuclides, frequently fission products of the heavier radioisotopes.

In addition to radionuclides, the nuclear tests resulted in substantial contamination by other inorganic and organic hazardous substances. These contaminants include the metals lead, copper, and cadmium, anions of arsenic and chromium, and organic contaminants such as polyvinyl chloride (PVC), polystyrene, and phenols (Bryant and Fabryka-Martin, 1991). Substantial quantities of these contaminants were incorporated in the nuclear devices and were released in the environment by the detonation of the device. The above contaminants are considered health hazards either because of their toxicity or because they are suspected or proven carcinogens (Francis, 1994; Sax, 1981).

The potential adverse health effects of radionuclides and other inorganic contaminants released during detonation of nuclear devices have long been recognized. The health hazard potential of these contaminants depends on the migration potential away from the source of contamination and into the accessible environment. Once in the accessible environment, contaminants can adversely affect the health of humans and animals. The fate and transport of dissolved contaminants are largely determined by the degree of contaminant interaction with the soil matrix. Radionuclides and metals with high sorption affinity for the mineral phases present, are expected to be severely retarded compared to groundwater flow. Inorganic contaminants with little affinity for the mineral phases present are expected to be retarded significantly less and, in the limiting case of truly conservative ions, solutes are expected to travel essentially with the velocity of the groundwater.

Any attempt for a realistic estimate of the time required for any contaminant to travel from the source of contamination to the accessible environment, therefore, requires experimental studies to evaluate the affinity of the contaminants of concern for the mineral phases likely to be encountered in the flowpath of the groundwater. Estimates

for the movement of contaminants away from sources of contamination are obtained from hydrologic and geochemical transport codes (Anderson and Woessner, 1992; Hemond and Fechner, 1994). These codes require hydrologic and geochemical parameters as input which must be either estimated or experimentally determined. The reliability of predictions based on these codes depends directly on the quality of the input parameters. Uncertainties in parameter estimation can lead to significant uncertainties in radionuclide transport simulations because of the frequently long time allowed for contaminant migration in model simulations (up to 10 000 years).

The scope of this project was to provide parameters used by transport codes to describe the equilibrium partitioning of contaminants between the aqueous and mineral interface. Specifically, the scope of this project component was to estimate the affinity of two cations (lead and strontium) and two anions (chromate and selenite) for aquifer material from the Project Shoal Underground Test Area, Fallon, Nevada. The Project Shoal Test Area is the site of an underground test conducted on October 26, 1963, where a device was detonated approximately 366 m below ground in granitic rocks.

The adsorbates used in this study are likely to be found in sites contaminated by nuclear testing. Lead (Pb) is very commonly found in nuclear test sites because large quantities of Pb, tens of tons typically, were used for the shielding of nuclear devices. Environmental concerns associated with Pb stem from its high toxicity (Francis, 1994; Laws, 1993). Lead is expected to be retarded strongly in many geological settings, because of its high affinity for oxides, hydroxides, clays, zeolites, and other aluminosilicate minerals and its potential for precipitation, even at low concentrations. To assess the migration potential of a cation with lower affinity for these types of mineral surfaces, experiments were conducted with strontium (Sr) and cesium (Cs) as well. Strontium is a radionuclide commonly found in nuclear test sites, known to sorb primarily by ion-exchange reactions. Health-hazard-related concerns are not based on the toxicity of Sr, but rather on the biogeochemical similarity of this element to calcium, a fact which can potentially result in accumulation of this radioisotope in bones (Laws, 1993). Cesium is also commonly found in nuclear test sites, and is believed to sorb, primarily, by cation-exchange reactions. Because of its smaller hydrated radius compared to Sr, however, it is expected to bind stronger than Sr, although by the same mechanisms. These cations, therefore, cover a broad range of affinity for the mineral surfaces present at the Shoal site.

In addition to the cations, two anions, chromate and selenite, were used as models for a relatively weakly and a strongly binding anion, respectively. Chromate was selected because it is fairly toxic, it is a known carcinogen, and is commonly found among the contaminants associated with nuclear testing. For oxides and hydroxides, chromate displays intermediate binding affinity. Selenite, however, has been shown to bind strongly on oxides and hydroxides (Hayes and Leckie, 1987; Hayes et al., 1987). Although selenium is a trace nutrient, it is fairly toxic at higher concentrations and a suspected carcinogen.

The remainder of this report is organized as follows. The adsorbent characterization and the general experimental procedures are presented next. The results and discussion are presented subsequently, organized by adsorbate type, followed by a section summarizing the results and presenting conclusions and recommendations for further study.

MATERIALS AND METHODS

ADSORBENT CHARACTERIZATION

The adsorbent was granite obtained from the Project Shoal site. The location of the Project Shoal site is shown in Figure 1. A fairly extensive characterization of the adsorbent was conducted which included solid structure as determined by x-ray diffraction (XRD), soil pH measurement, total carbon and total organic carbon content, particle size distribution, surface area determination, and density determination. In addition, the morphology and composition of the granite was examined by scanning electron microscopy (SEM) combined with energy dispersive x-ray spectroscopy (EDX). These parameters provided important information for the experimental design and are also required for the estimation of geochemical transport parameters obtained from the experimental data.

The adsorbent was first reduced in size. Size reduction was necessary for performance of batch equilibrium experiments to allow use of small quantities of solids in aqueous solutions, as sorption capacity is proportional to the total surface area available and the total surface area of non-porous particles is inversely proportional to the particle diameter. The size reduction and subsequent sieving resulted in eight size fractions from 3/8 in. (9 510 μm) to less than 200 mesh (smaller than 75 μm). This smaller size fraction was used for all subsequent experimental work, because of the surface area considerations mentioned above. The actual particle size distribution of the selected size fraction was determined by Micromeritics Corporation and will be discussed later.

The crystal structure of the granite was determined by XRD after particle size reduction. Spectra were collected in the 5 to 60° 2θ-range using 0.03° 2θ steps and Cu Kα radiation (λ = 1.54060 Å). Inspection of the spectrum and an automated search of the peaks obtained is consistent with the presence of the following minerals: quartz, plagioclase feldspars, chlorite, and biotite. This composition is not unusual for granitic rocks (Klein and Hurlbut, 1993). To further quantify the mineralogical composition of the granite sample, the XRD analysis was complemented by estimation of bulk elemental composition, as determined by x-ray fluorescence (XRF) and energy dispersive x-ray spectrometry (EDX). The XRF results, presented as percentage composition of the sample in terms of oxides, are shown in Table 1 and will be discussed first.

It appears by inspection of Table 1, that SiO_2 represents the majority of the sample by weight. This almost expected because SiO_2 would be present either as quartz, or as a component of any aluminosilicate. The second largest component is Al_2O_3, a result which is also not surprising, although the concentration of aluminol sites appears to be substantially lower than the concentration of silanol sites. This result has significant implications for the sorption studies and will be discussed later. In addition to the major silica and alumina components, smaller concentrations of Ti, Fe, Ca, K, Na, and Mg were also present. Finally, in terms of trace elements, the granite sample had considerable concentrations of strontium (Sr) and zirconium (Zr), 721 and 418 ppm, respectively. The concentration of chromium, which was used in its anionic form for these experiments, was relatively minor (32.7 ppm).

In order to obtain a better picture of the morphology and particle size of the adsorbents, the sample was examined by scanning electron microscopy (SEM). In addition, an average composition of individual particles imaged with the SEM was determined, using an energy dispersive x-ray (EDX) attachment to the SEM. A JEOL JSMñ840A SEM/EDX was used to examine several areas of the sample under different magnifications. A general view of the sample is shown in Figure 2. It appears that the particles had dimensions on the order of 100 μm or smaller. These results are consistent with the expected particle size, based on the sieve sizes used.

An attempt was made to identify individual minerals in the sample by SEM/EDX. Analyses can be performed with a spatial and depth resolution of about 1-2 μm and an accuracy of 5-10%. This allows, at least semi-quantitative, identification of individual mineral crystals. Identification is based on the relative abundance of common components (oxides) in minerals. It should be mentioned, however, that because several different minerals may have similar composition in terms of oxides, independent information on the types of minerals present, for example from XRD, may be required for unambiguous mineral identification. Several minerals were identified based on morphology and elemental composition and they are shown in the following figures. A Ti and Fe bearing mineral, most likely ilmenite ($FeTiO_3$), is at the center of Figure 3. Ilmenite is often found in granite, albeit in small concentrations, approximately 1% by volume (Klein and Hurlbut, 1993). A biotite crystal is shown at the center of Figure 4. The presence of biotite is consistent with the results of the XRD analysis. As expected, quartz is a very common constituent of the granitic rock and its presence could be verified by XRD and the combination SEM/EDX. A characteristic example of a quartz crystal is shown in Figure 5. Feldspars and quartz make up essentially all of granite. An

example of a plagioclase feldspar crystal is shown in Figure 6. Finally, a Zr mineral is shown in Figure 7. The presence of Zr is consistent with the relatively high concentration of this element determined by XRF (Table 1).

The particle size distribution was determined by Micromeritics using a SediGraph 5100 by x-ray scattering and sedimentation in a 60% glycerin, 0.3% Daxad23 solution. The mass fraction (percent of total mass) vs. particle diameter is shown in Figure 8. The results are consistent with the expected particle size distribution for particles passing through a 200-mesh screen (i.e., particles smaller than 75 μm).

The true and bulk densities of the adsorbent were measured and reported by the Micromeritics Materials Analysis Laboratory (Norcross, GA). The bulk density was determined by mercury porosimetry and the true density was determined by nitrogen adsorption. The bulk density measured was 1.21 g/cm^3 and the true density was 2.67 g/cm^3. The value for the true density is consistent with the theoretical and measured densities of quartz and plagioclase, the two major components of the granite (Nickel and Nichols, 1991).

The surface area of the adsorbent was determined based on nitrogen adsorption measurements, using a Micromeritics ASAP 2400 Analyzer, and appropriate models, specifically the BET method (Brunauer et al., 1938). This method can be used to obtain an estimate of the total surface area of adsorbents having surface areas from a fraction of a square meter per gram to several hundred square meters per gram. Although the method has several shortcomings, it continues to be the most widely used and general method for particle surface area estimation (Gregg and Sing, 1982). The measured surface area was 0.79 m^2/g. The small specific surface area suggests absence of porosity, a result expected for granite.

The soil solution pH was measured by suspending an amount of the sorbent in NANOpure™ water (high purity water with at least 18 MΩ cm resistivity). The pH value obtained was approximately 8 for solid concentration 10 g/L. This value was somewhat higher than expected. Soil solution pH values are frequently correlated to a mineralís PZC, or point of zero charge, defined as the pH value at which a mineral with amphoteric surface functional groups has no surface charge. On such minerals (common examples are hydrous oxides and hydroxides), the PZC is frequently estimated by potentiometric titrations of the mineral surface at different ionic strengths. The pH value at which these

curves intersect is an estimate of the PZC (strictly speaking, the point of zero salt effect, PZSE (Sposito, 1984)).

Minerals with silanol sites tend to have low PZCs (e.g., quartz has a PZC of approximately 2-3) whereas minerals with aluminol sites have higher PZCs (gibbsite has a PZC of approximately 8-9). Minerals with a combination of aluminol and silanol sites tend to have intermediate PZCs (the PZC of kaolinite, for example, is approximately 4-5) (Sposito, 1989). PZC values for feldspars are not easily available, but since they are composed of both silica tetrahedra and alumina octahedra, they are also expected to have an intermediate PZC between quartz and aluminum (hydr)oxides. Granite, therefore, composed mainly of quartz and feldspars, is likely to have a PZC below 7. The pH measured in the laboratory, however, (around 8) is in good agreement with the groundwater pH measured in wells in the field (see the results of groundwater analysis below). A possible explanation for the higher than expected pH is the presence of carbonates.

To evaluate this scenario, the total carbon and total organic carbon (TOC) of a granite sample was measured at the Water Analysis Laboratory of the Water Resources Center at the Desert Research Institute, using an Astro 2001 Total Organic Carbon Analyzer. The TOC was 30 μg/g and the total carbon was 575 μg/g, so by difference the total inorganic carbon was 545 μg/g. Using calcite as a model carbonate, with a carbon content of approximately 12%, the estimated carbonate content (as calcite) would therefore probably be around 0.5% by weight. Similarly, assuming that all Sr is in the form of carbonates (strontianite) the resulting Sr carbonate concentration would be approximately 0.12% by weight. It seems therefore likely that carbonates do not comprise more than 1% of the sample. It seems rather unlikely that such a small concentration would have a substantial effect on solution pH.

EXPERIMENTAL PROCEDURES

Sorption experiments were performed in individual 12-mL polypropylene centrifuge tubes. A specific amount of solid was added to the centrifuge tube. The amount of solid varied depending on the final solid concentration desired. Almost all experiments were conducted with 10 g/L granite. A specific amount of 1.0 or 0.1 M $NaNO_3$ (sodium nitrate) was added to achieve the desired final ionic strength of the

experiment. A variable amount of either 1.0 M HNO_3 (nitric acid) or 0.1 M NaOH (sodium hydroxide) was added to adjust the pH to the approximate final pH value desired. The amounts of acid and base required for pH adjustment were determined by trial and error. After the initial acid or base addition, the solution was allowed to equilibrate without further pH adjustments.

Typically a set of eight individual centrifuge tube-reactors was set up at a time with varying target pH values. Approximately 30 µL of either 1.7×10^{-4} or 1.7×10^{-2} M metal ion were added to the centrifuge tube to achieve the desired final total metal concentration in the samples, ranging from 10^{-7} to 10^{-4} M. The adsorbate added was either $Pb(NO_3)_2$ (lead nitrate), $Sr(NO_3)_2$ (strontium nitrate), $CsNO_3$ (cesium nitrate), K_2CrO_4 (potassium chromate), or Na_2SeO_3 (sodium selenite) depending on the experiment being performed. The necessary quantity of high quality, NANOpure™ water was added to result in a final solution volume of 10 mL. All reagents used were of ACS reagent grade quality or better. NANOpure™ water was used exclusively for all solutions prepared.

The individual centrifuge tubes were equilibrated for at least 24 h by end-over-end rotation at 8 rpm. Given the non-porous structure of the adsorbent, and the fast intrinsic rate of sorption reactions (Hayes and Leckie, 1986), 24 h equilibration time was considered adequate. An equilibration time of 24 h was therefore adopted for all subsequent experiments. Although true equilibrium, in a strict thermodynamic sense, was most likely not reached within the 24 h equilibration period, the conclusions presented here are still valid, based on the much shorter time scale for the sorption processes described here, compared to processes such as solid solution formation and phase transformations, which would tend to shift the position of equilibrium.

Following equilibration, the pH of the suspension was measured using an Orion model 720 pH meter with an Orion Ross glass combination electrode. The pH meter was calibrated daily using pH 4.00, 7.00, and 10.00 buffers. Solid-solution separation was achieved by centrifugation at 9,000 rpm for 20 min using a Marathon K/R 21 centrifuge and a 2ñmL aliquot of the supernatant was removed for metal analysis. The supernatant was acidified with 24 µL of concentrated HNO_3 (Fisher Optima™ quality) before analysis.

The samples were analyzed using a Perkin Elmer 4110 ZL atomic absorption spectrometer with graphite furnace and Zeeman background correction. Duplicates were run for each sample and the results were averaged. In all cases a peak area mode was

used for analysis using appropriate metal standards. The fractional uptake (percent adsorbed) for each sample was calculated as:

$$\%Adsorbed = \frac{C_o - C_s}{C_o} \times 100 \qquad (1)$$

where C_o is the total metal concentration added to the sample and C_s is the Co concentration remaining in the supernatant.

Most experiments were conducted in a 0.01 M $NaNO_3$ matrix. This choice was made in order to keep the matrix as simple as possible, thereby allowing a more fundamental understanding of the sorption reactions involved, while at the same time approximating as much as possible the ionic strength of the groundwater of interest at the Project Shoal Site. It is well documented that ionic strength can have significant effects on the sorption behavior of cations and anions onto different types of mineral surfaces (Hayes and Leckie, 1987; Hayes et al., 1988; Papelis and Hayes, 1996). Experiments were therefore also conducted at higher ionic strengths, up to 1.0 M.

In addition to the experiments conducted in simple electrolytes, experiments were also conducted with synthetic groundwaters reflecting the composition of groundwater in three wells near the site: well HS-1, representing groundwater with the lowest ionic strength (0.0058), well H-2, representing groundwater with the highest ionic strength (0.6292), and well HC-4, representing the groundwater most likely to flow through the test site. The composition of all three groundwaters, including major cation and anion concentration, cation/anion imbalance, ionic strength, electrical conductivity, and pH is given in Table 2. The location of the wells is shown in Figure 1.

RESULTS AND DISCUSSION

CATION SORPTION ON PROJECT SHOAL GRANITE

Cation sorption, including sorption of Pb, Sr, and Cs on the Project Shoal granite will be discussed first, followed by estimation of the isotherm parameters describing the partitioning of these cations at the mineral-water interface at equilibrium.

Lead Sorption

Sorption of Pb on 10 g/L granite at concentrations ranging from 10^{-4} to 10^{-7} M and at 0.01 M ionic strength is shown in Figure 9. It can be seen from Figure 9 that, as expected, the fractional uptake is a function of Pb concentration, decreasing with increasing metal concentration. This behavior is well documented. It should be kept in mind that although the fractional uptake decreases with increasing concentration (as a *fraction* of total metal concentration sorbed) the total metal sorbed is actually increasing. The behavior of Pb in these graphs is typical for a cation, i.e., sorption increases with increasing pH. At low pH fractional uptake is very low but at higher pH values quantitative removal of the metal is observed. This type of cation sorption behavior on mineral surfaces with sites which can be protonated or deprotonated (amphoteric sites), such as oxide mineral surfaces, has been known for many years (Leckie et al., 1980).

It should be emphasized, however, that, based on these macroscopic observations alone, one cannot determine the mechanism responsible for the observed partitioning behavior. Additional spectroscopic experiments would be required to clarify the type of sorption complexes formed on these mineral surfaces (Sposito, 1986). The type of surface complex formed may be important for the stability of the complex under different geochemical conditions and therefore the fate and transport of the contaminant of concern. Several mechanisms are typically understood under the general term sorption, including adsorption, absorption, and surface precipitation (Davis and Hayes, 1986). Distinguishing between these mechanisms would require additional spectroscopic investigations. It is entirely possible that under the low Pb concentration conditions, adsorption is responsible for the observed sorption behavior, while at the higher Pb concentrations surface precipitation may be occurring. This scenario is entirely possible, given the high tendency of Pb to hydrolyze (Baes and Mesmer, 1986).

Sorption of 10^{-7} M Pb on 10 g/L granite as a function of ionic strength is shown in Figure 10. Although the ionic strength varies over two orders of magnitude (0.01 - 1.0 M), fractional uptake is essentially identical. The independence of metal ion uptake on ionic strength has been interpreted as an indication of strong binding and the presence of strong, inner-sphere coordination complexes on mineral surfaces (Hayes and Leckie, 1987). This type of sorption behavior has been repeatedly observed for Pb (Chisholm-Brause et al., 1990; Chisholm-Brause et al., 1989).

The sorption of 10^{-4} M Pb on granite, in the presence of the three different synthetic groundwaters (HS-1, H-2, and HC-4) is shown in Figure 11. As almost expected, there was essentially no difference in the sorption behavior of Pb as a function of ionic medium. This can be easily interpreted based on the previously discussed independence of fractional uptake on ionic strength. The ionic strengths of the three synthetic groundwaters were very similar to the set of ionic strengths used in the experiments with the simple background electrolyte (Table 2).

As a confirmation of the similarity of sorption results under conditions of similar ionic strength, regardless of the specific chemical composition of the medium, sorption results in the presence of 0.01 M sodium nitrate and a synthetic HS-1 groundwater are compared in Figure 12. The data are consistent with sorption independent on the specific composition of the aqueous solution. These results have significant implications for the modeling of Pb fate and transport. Based on these results, isotherm parameters obtained in the laboratory in simple, clean systems could be used to predict the behavior of contaminants of concern in more complex groundwater systems.

Strontium Sorption

As stated in the previous section, Pb is considered to bind very strongly on oxide surfaces and to form inner-sphere surface coordination complexes which are stable even in high-ionic-strength media. In addition, its high tendency to hydrolyze and to precipitate may also contribute to significant retardation of this contaminant. For these reasons, despite its toxicity, Pb is not always considered a serious problem with respect to contaminant migration to the accessible environment. To evaluate the migration potential of a more mobile, more conservative cation, sorption experiments with Sr were also conducted.

Strontium, a divalent alkaline earth metal, has a very different aqueous chemistry compared to Pb. It has a much lower tendency to hydrolyze and to form surface and bulk precipitates (Baes and Mesmer, 1986). In addition, and as a consequence of the described behavior, all macroscopic and microscopic sorption studies performed to date, to this authorís knowledge, are consistent with formation of weak, ion-pair, outer-sphere complexes on amphoteric oxide surfaces (Chen et al., in press). For this reason, and because it is essentially always found among radionuclides produced by nuclear tests, it was chosen as an analog for weakly binding cations.

Unfortunately, sorption experiments with Sr and the granite sample from the Project Shoal site proved to be impossible to perform, because of the high Sr content of the rock. As pointed out in the adsorbent characterization section, the bulk concentration of Sr in the sample was 721 ppm (Table 1). This is a relatively high concentration which resulted in significant release of Sr under all experimental conditions. Experiments were attempted with different metal and solid concentrations, at different pH values and at different ionic strengths. The significant amount of Sr released in solution, shown as a function of pH and ionic strength in Figure 13, prevented any meaningful interpretation of the data.

Several experiments resulted in negative fractional uptakes, as the equilibrium Sr concentration was higher than the concentration of Sr added to the sample. This result is not unreasonable considering that the Sr concentration in solution, in excess of 200 μg/L at the higher ionic strength (2.5×10^{-6} M), would be in the same order of magnitude as the Sr concentrations added under most experimental conditions. Although no quantitative interpretation of the data is possible under these conditions, the experiments performed have significant implications for the mobility of Sr. Under the conditions tested, Sr must be treated as a conservative contaminant.

Cesium Sorption

To evaluate the migration potential of a cation more mobile than Pb, and because the experiments with Sr were unsuccessful, sorption experiments with Cs were also conducted. It was assumed that the affinity of Cs for the granite would be between that of the strongly binding Pb cation and the weakly binding Sr cation. Sorption of Cs on 10 g/L granite at concentrations ranging from 10^{-4} to 10^{-6} M in the HC-4 groundwater is shown in Figure 14. It can be seen from Figure 14 that, like the Pb cation, the fractional uptake is a function of Cs concentration, decreasing with increasing metal concentration.

It can also be seen that there is some scatter associated with the data points at pH values above 7, but the overall trend is that fractional uptake decreases with increasing cation concentration. Unlike the Pb cation, however, Cs sorption was weakly influenced, if at all, by pH. This behavior suggests that the sorption of Cs by the granite is primarily controlled by sorption on cation-exchange sites. Specifically, the observed Cs uptake may indicate partial sorption on ion-exchange sites of clay minerals present in the granite, which have a permanent charge, independent of pH.

Estimation of Equilibrium Partitioning of Cations at the Granite-Water-Interface

Most transport codes which attempt to incorporate chemical reactions to model the migration of contaminants in the subsurface environment require parameters describing the partitioning of the contaminants of concern between the aqueous and mineral interfaces. Although sorption modeling based on the surface-complexation paradigm has been extensively used during the last two decades, most transport codes still use parameters derived from isotherms to incorporate surface chemical reactions into numerical models.

Several sorption isotherms have been developed and used during the years. Among the most commonly used are the linear, Langmuir, and Freundlich isotherms (Davis and Hayes, 1986). Plotting of sorption data as a linear isotherm results in estimation of a conditional distribution coefficient, K_d, a ratio of the mass of sorbate sorbed per mass of sorbent, q_e (g/g) to the concentration of sorbate in equilibrium with the sorbed contaminant, C_e (g/m^3), as shown in Eq (2).

$$K_d = \frac{q_e}{C_e} \tag{2}$$

Distribution coefficients have been used extensively to model organic contaminant sorption on aquifer materials. For inorganic contaminants, however, K_d is frequently a strong function of pH, temperature, and other geochemical conditions (e.g., speciation and redox potential) (Stumm, 1992).

Use of distribution coefficients to model contaminant partitioning at the mineral-water interface assumes that the isotherm is linear and that sorption is controlled by equilibrium, as opposed to kinetics (usually referred to as the local equilibrium approach). Sorption of inorganic contaminants on mineral surfaces is frequently non-linear. In addition, distribution coefficients can result in severe errors when used without reference

to the specific experimental conditions under which they were determined. Unfortunately, neglecting the above guidelines is still fairly common in radionuclide transport models (Nakamura et al., 1988; Ohnuki et al., 1989; Ooi et al., 1987).

In this project, distribution coefficients were estimated, based on the experimental data, as a function of the parameters controlling cation sorption. The parametric study discussed earlier, was conducted exactly to identify these parameters. In addition, to test the linearity of these isotherms and therefore whether a K_d approach would be applicable, the data were linearized, a process which results in the estimation of parameters for the non-linear Freundlich isotherm, shown in Eq (3).

$$q_e = K_F \, C_e^{\,1/n} \tag{3}$$

These parameters, K_F, $(g/g)/(g/m^3)^{1/n}$, and $1/n$ (-), represent the equivalent of K_d and the exponent of the equilibrium concentration, respectively ($1/n$ is assumed to be 1, by definition, for linear isotherms). The linear and Freundlich isotherm parameters for Pb sorption on Project Shoal granite are given in Table 3. Parameters were calculated and reported for experiments in the simple electrolyte at the ionic strength relevant to this project (0.01 M) and for two different types of groundwaters, HS-1 and HC-4. The data set corresponding to 0.01 M ionic strength is the most complete and covers concentrations ranging from 10^{-7} to 10^{-4} M.

Several conclusions can be drawn by inspection of Table 3. First, as mentioned earlier, the isotherm parameters can vary by orders of magnitude for pH-dependent sorption and this is, obviously, the case for Pb. Second, the isotherms are not, strictly speaking, linear, as can be concluded by the fact that the Freundlich exponents are not one, although the lowest Freundlich exponent is 0.75, suggesting a reasonably low deviation from linearity. Third, because the Freundlich exponents are reasonably close to one, the linear and Freundlich isotherm parameters are also reasonably similar (at least same order of magnitude).

The linear and Freundlich isotherm parameters for Cs sorption on Project Shoal granite are given in Table 4. Data are presented for the synthetic HC-4 groundwater only. Several conclusions can be drawn by inspection of the data. First, unlike the parameters obtained for the Pb cation, the sorption parameters for Cs are not highly dependent on pH. This behavior can be attributed to the fact that the fractional uptake of Cs was not highly dependent on pH. Second, the isotherms are not linear as can be concluded by the fact that the Freundlich exponents are not one, although they are closer to one than the

exponents of the Pb isotherms. Third, because the Freundlich exponents are reasonably close to one, the linear and Freundlich isotherm parameters are also reasonably similar (at least same order of magnitude).

Strictly speaking, obviously, the Freundlich isotherm would be more appropriate to describe Pb and Cs sorption on granite. Because the non-linearity of the isotherms, however, is not too severe, linear isotherms could be used instead, if there were a significant computational advantage to using the simpler isotherm. At any rate, recognition of the limits of applicability of this approach (concentration range and other conditions requirements) would be necessary before using the simpler linear isotherm. In conclusion, it is worth repeating how pH dependent the interactions between inorganic contaminants and amphoteric surfaces, such as the granite surface, can be and that therefore no transport simulations can be performed realistically without previously assuming a groundwater pH value. In addition, one must be aware that any changes in groundwater pH could have a dramatic impact on cation mobility, although the role of pH could depend on the particular cation of concern.

ANION SORPTION ON PROJECT SHOAL GRANITE

Chromate Sorption

Chromate sorption on Project Shoal granite will be discussed first, followed by discussion of selenite sorption. Sorption of the chromate ion on 10 g/L granite as a function of pH and chromate concentration is shown in Figure 14. Sorption of Cs in HC-4 groundwater on granite as a function of metal concentrations.

Figure 15. In the rest of the document, the chromate anion will be abbreviated as Cr, with the understanding that we refer to Cr in the +6 oxidation state, in the anionic form, as opposed to Cr metal in the +3 oxidation state. Similarly, the chromate ion (not dichromate) was used in these experiments. In the following Figures the chromate ion is abbreviated as Cr(VI), to include the oxidation state of the anion.

The experimental results shown in Figure 14. Sorption of Cs in HC-4 groundwater on granite as a function of metal concentrations.

Figure 15 are consistent with anion sorption at amphoteric mineral surfaces. Anion sorption is a mirror image of cation sorption, generally increasing with decreasing pH. In addition, fractional uptake decreases as the ion concentration increases. At the

lowest concentration, 10^{-7} M, Cr is removed from solution regardless of pH. Only under acidic conditions is Cr slightly dissolved in solution. This behavior has been observed frequently and is related to the relative charges of the adsorbate and adsorbent. Decreasing pH results in increased positive charge on amphoteric oxide surfaces, making them more attractive to the negatively charged anions. At low pH values, however, the anions tend to be (fully) protonated, thereby loosing part of their affinity for the (positively charged) surface. Thus, anion fractional uptake frequently goes through a maximum around neutral or slightly negative pH, decreasing in either direction away from this maximum.

This type of sorption behavior can be observed in Figure 14. Sorption of Cs in HC-4 groundwater on granite as a function of metal concentrations.

Figure 15. At the lowest concentration, sorption is essentially complete, regardless of pH, except for the low pH region. As the concentration increases, Cr sorption becomes more "anion-like" and fractional uptake decreases. At the highest concentration (10^{-4} M) limited sorption is possible only at the lowest pH values.

Sorption of Cr in the three different groundwaters is shown in Figure 16. For comparison purposes, sorption in the simple system (0.01 M) is also included. Except for the H-2 groundwater, the composition of the other two groundwaters is fairly similar to the simple electrolyte solution and the sorption results reflect this fact. It will be remembered that H-2 was the groundwater at the highest ionic strength (Table 2). It is somewhat surprising that increased ionic strength would result in increased anion sorption. The sorption of weakly binding anions (selenate) on iron and aluminum (hydr)oxides has been shown to decrease with increasing ionic strength (Hayes et al., 1988).

One possible explanation for the observed behavior is related to the surface charge characteristics of the granite surface and, specifically, the quartz component of the rock. It is known that quartz has a very low PZC (reported as 2-3), a fact that results in a negatively charged surface, essentially throughout the pH range of interest. This negative charge would tend to reduce anion fractional uptake. At the higher ionic strength, more counterions (positively charged ions) would be attracted to the surface, thereby screening the negative surface charge more effectively and allowing more negatively charged ions (anions) to sorb.

To test this hypothesis, sorption experiments with 10^{-5} M Cr on 10 g/L granite were conducted, and the results are shown in Figure 17. Although not very pronounced, one might argue that sorption is increasing with increasing ionic strength, at least in the higher pH region. This can be explained based on the above hypothesis. It is reasonable to assume that the effect would be more pronounced in the high pH region, where the negative charge of the mineral surface is substantially higher.

Selenite Sorption

Selenite (selenium anion in the +4 oxidation state), was the last sorbate used in the sorption study. As with Pb and Cr, experiments were conducted in the simple electrolyte, as well as with synthetic groundwater from wells HS-1, H-2, and HC-4, although not all experiments are shown here. In the following, the selenite anion will be abbreviated as Se; in the Figures, the symbol Se(IV) is used to indicate the oxidation state of the anion.

Sorption of Se on granite as a function of Se concentration (10^{-6} and 10^{-5} M), in the simple electrolyte, is shown in Figure 18. As observed for Cr, the fractional uptake is characteristic for an anion, reaching a maximum at or near neutral pH. As expected, fractional uptake increases with decreasing Se concentration, especially at higher pH values. The differences in fractional uptake as a function of total Se concentration were more pronounced at higher ionic strength, 1.0 M, and are shown in Figure 19. Both curves have the typical shape of an anion sorption curve, with maximum uptake around pH 5-6, showing higher fractional uptake at the lower Se concentration.

Sorption of Se on 10 g/L granite as a function of ionic strength is shown in Figure 20. Although differences between experiments at different ionic strengths can be observed, these differences are not very significant and could be partly due to uncertainties in the experimental data. Selenite sorption on iron and aluminum oxides has been generally considered as ionic-strength independent, suggesting the formation of strong, inner-sphere, surface coordination complexes (Hayes et al., 1988; Papelis et al., 1995). The formation of such complexes is consistent with x-ray absorption spectroscopic evidence (Hayes et al., 1987). It is, therefore, not very surprising that there are no dramatic ionic strength effects on Se sorption. If Figure 20 shows any trend in Se fractional uptake as a function of ionic strength, this trend would be towards increased sorption with increasing ionic strength. This type of behavior was also observed with Cr and was attributed to a more favorable (more positive) surface charge of quartz and feldspar minerals for anion sorption with increasing ionic strength.

Sorption of 10^{-5} M Se in synthetic HC-4 groundwater is also shown in Figure 20 for comparison. The results are within the range of fractional uptake curves obtained at the different ionic strengths. These results are not surprising, and are consistent with the hypothesis that the behavior of individual ions is a function of the ionic strength of the medium, rather than the specific matrix. Similar results were obtained with the Pb and Se (see discussion above).

Estimation of Equilibrium Partitioning of Anions at the Granite-Water Interface

As for the cations, Pb and Cs, parameters describing equilibrium partitioning of the anions, Cr and Se, at the granite-water interface were determined for both the linear and Freundlich isotherms and the results are presented in Table 5 for Cr and Table 6 for Se. It should be noted that the parameters reported for both isotherms were calculated in terms of the respective elements, not the corresponding anions (e.g., for Se isotherm calculations, the molecular weight of selenium was used, not the molecular weight of the selenite anion).

The results of Cr isotherm calculations are summarized in Table 5 for experiments in the simple electrolyte (0.01 M) and the synthetic groundwaters H-2 and HC-4. As can be seen from Table 5, the isotherm parameters are a strong function of pH, although not as strong as for Pb. Inspection of the Freundlich isotherm parameter $1/n$, however, the exponent of the Freundlich isotherm which is a measure of the linearity of the isotherm, reveals that the isotherms are highly non-linear under all conditions studied. The non-linearity appears to be solution independent but appears to be increasing with increasing pH. Exponents as low as 0.20 are obtained at the higher pH values.

Because the linear isotherm assumes an exponent of one, whereas the best fit of the data is obtained with exponents substantially lower, it should be expected that K_d and K_F would be substantially different, more so than in the case of Pb. Comparison of Tables 3 and 4 is consistent with this expectation. Comparison of the available data for the three different matrices indicates that sorption is comparable under these conditions. Again, based on the similarity of Cr fractional uptake under these conditions discussed earlier, this should have been expected. Finally, because the results are similar for the different aqueous matrices and because a more complete set of data was available with the clean, simple system (0.01 M), these isotherm parameters should be used for modeling purposes. In addition, because of the strong non-linearity of the system, use of the Freundlich isotherm is strongly recommended.

The linear and Freundlich isotherm parameters for Se sorption on Project Shoal granite are shown in Table 6. Data are presented for two different ionic strengths and synthetic HC-4 groundwater. By inspection of the Table we can come up with several conclusions. First, sorption parameters, similar to results for the other ions, are highly pH dependent and vary by as much as three orders of magnitude in some cases. Second, although under certain conditions the isotherms appear to be fairly linear, primarily under conditions of high fractional uptake, under conditions of lower fractional uptake the isotherms become strongly non-linear. This is reflected in the corresponding differences between K_d and K_F. Under specific conditions, therefore, a linear isotherm could be used to describe Se sorption in this system; in general, however, a Freundlich isotherm would be required to describe the system more accurately.

Finally, a comparison of Tables 5 and 6 for similar conditions of ionic strength (0.01M) suggests substantially stronger sorption of Se compared to Cr, in most cases, even after accounting for differences in atomic weight between the two elements. The observed selectivity between the two anions has been observed on a number of mineral surfaces and it was one of the reasons why the two anions were selected for experimental work.

SUMMARY, CONCLUSIONS, AND RECOMMENDATIONS

During the period of nuclear weapon production and testing, the U.S. conducted a series of tests at several test sites. These tests resulted in contamination from radionuclides as well as from other toxic metals and organic compounds. These contaminants are considered health hazards either because of their toxicity or because they are suspected or proven carcinogens. The fate and transport of dissolved contaminants are largely determined by the degree of contaminant interaction with the soil matrix. Radionuclides and metals with high sorption affinity for the mineral phases present, are expected to be severely retarded compared to groundwater flow. Inorganic contaminants with little affinity for the mineral phases present are expected to be retarded significantly less.

The scope of this project component was to estimate the affinity of two cations (lead and strontium) and two anions (chromate and selenite) for aquifer material from the Project Shoal Underground Test Area, Fallon, Nevada. The Project Shoal Test Area is the site of an underground test conducted on October 26, 1963.

The adsorbent was granite obtained from the Project Shoal site. It was reduced in size and it was characterized by x-ray diffraction (XRD), soil pH measurement, total carbon and total organic carbon content, particle size distribution, surface area determination, and density determination. In addition, the morphology and composition of the granite was examined by scanning electron microscopy (SEM) combined with energy dispersive x-ray spectroscopy (EDX). Based on a combination of these techniques, it was determined that the granitic rock consisted of quartz, plagioclase feldspars, chlorite, and biotite.

Most sorption experiments were conducted in a 0.01 M $NaNO_3$ matrix. In addition to the experiments conducted in simple electrolytes, experiments were also conducted with synthetic groundwaters reflecting the composition of groundwater in three wells near the site: well HS-1, well H-2, and well HC-4.

Lead displayed a typical cation sorption behavior with fractional uptake increasing with increasing pH. In addition, Pb sorption was essentially ionic strength independent, indicating strong binding and the formation of strong, inner-sphere coordination complexes on these mineral surfaces. There was essentially no difference in

the sorption behavior of Pb as a function of ionic medium. Sorption experiments with Sr and the granite sample from the Project Shoal site proved impossible to perform, because of the high Sr content of the rock and the dissolution of significant quantities of Sr, in excess of 200 μg/L at the higher ionic strength, during the experiments. It is therefore expected that under these conditions Sr would be highly mobile. Cesium sorption was essentially independent of pH, unlike Pb, suggesting that sorption of Cs by the granite is primarily influenced by sorption on cation-exchange sites.

Both chromate and selenite displayed a typical behavior for anions sorbed on amphoteric oxide surfaces. A maximum in the fractional uptake was typically observed at neutral or slightly below neutral pH. For both anions it appeared as if increased ionic strength resulted in increased fractional uptake. This behavior was attributed to increased screening of the negative oxide surface charge by an increased concentration of positively charged counterions. The effects of ionic strength, however, at least in most cases, were not dramatic.

Based on the experimental data, parameters describing both linear and Freundlich isotherms were estimated for a variety of conditions. The results indicate that equilibrium partitioning at the granite-water interface is strongly pH dependent for all ions studied except cesium. As a consequence, realistic modeling of the transport of these contaminants would require knowledge of or assumptions about the groundwater pH. In some cases the variation in these parameters reached several orders of magnitude, as a function of pH.

The linearity of the isotherms was also a function of specific conditions, most notably pH. Under specific conditions, the isotherms were approximately linear, allowing the use of a linear isotherm to model the equilibrium data. In many other cases, however, deviations from linearity were so severe, that the corresponding parameters describing the isotherms differed by orders of magnitude. Under such conditions, use of the Freundlich isotherm is required. In general, Pb and Cs isotherms were more linear than Cr and Se isotherms.

Generally, sorption results in the presence of synthetic groundwater matrices were very similar to results obtained with simple background electrolytes, provided that the ionic strength was the same in the two systems. Determination of appropriate sorption isotherm parameters, therefore, could be accomplished in the simpler systems. Finally,

these results were consistent with the frequently made assumption that the selenite anion binds stronger than the chromate anion on oxide-like surfaces.

The isotherm parameters determined in this study can be used to reduce the uncertainty in radionuclide transport modeling by accounting for retardation of radionuclides and other contaminants of concern because of sorption on aquifer materials. It should be emphasized, however, that the parameters determined in this project only describe the equilibrium partitioning of contaminants at the mineral-water interface and do not provide any information on the rate of these reactions. Although the aquifer materials at the Project Shoal Test Site do not appear to be porous and, therefore, kinetic limitations are not expected to play a major role in contaminant sorption, this possibility should be investigated.

In addition, a correlation between particle size and concentration with partitioning coefficients has frequently been reported. During this project, sorption experiments with only one size fraction could be performed because of time and resource limitations. Additional experiments with at least one coarser size fraction would allow the evaluation of particle size effects. Finally, it cannot be overemphasized that the results reported here are specific to the conditions used and that, given the non-linearity of some of these systems, use of these parameters outside their range of applicability might result in significant errors.

REFERENCES

Anderson, M.P. and W.W. Woessner (1992). *Applied Groundwater Modeling: Simulation of Flow and Advective Transport.* Academic Press, San Diego, 381 pp.

Baes, C.F., Jr. and R.E. Mesmer (1986). *The Hydrolysis of Cations.* Robert E. Krieger, Malabar, FL, 489 pp.

Brunauer, S., P.H. Emmett, and E. Teller (1938). "Adsorption of gases in multimolecular layers," *J. Am. Chem. Soc.* **60,** 309-319.

Bryant, E.A. and J. Fabryka-Martin (1991). "Survey of hazardous materials used in nuclear testing," Report No. LA-12014-MS, Los Alamos National Laboratory, Los Alamos, NM.

Chen, C.-C., C. Papelis, and K.F. Hayes (in press). ìExtended x-ray absorption fine structure (EXAFS) analysis of aqueous Sr^{II} ion sorption at clay-water interfaces.î In *Sorption of Metals by Earth Materials*, (Edited by E.A. Jenne), Academic Press, San Diego,

Chisholm-Brause, C.J., K.F. Hayes, A.L. Roe, G.E. Brown, Jr., G.A. Parks, and J.O. Leckie (1990). ìSpectroscopic investigation of Pb(II) complexes at the γ-Al_2O_3/water interface,î *Geochim. Cosmochim. Acta.* **54,** 1897-1909.

Chisholm-Brause, C.J., A.L. Roe, K.F. Hayes, G.E. Brown, Jr., G.A. Parks, and J.O. Leckie (1989). ìXANES and EXAFS study of aqueous Pb(II) adsorbed on oxide surfaces,î *Physica B.* **158,** 674-675.

Davis, J.A. and K.F. Hayes (1986). ìGeochemical processes at mineral surfaces: an overview.î In *Geochemical Processes at Mineral Surfaces*, (Edited by J.A. Davis and K.F. Hayes), ACS Symposium Series, No. 323. American Chemical Society, Washington, D.C., 2-18.

Francis, B.M. (1994). *Toxic Substances in the Environment.* Environmental Science and Technology. John Wiley & Sons, New York, 360 pp.

Gregg, S.J. and K.S.W. Sing (1982). *Adsorption, Surface Area and Porosity.* Academic Press, London, 303 pp.

Hayes, K.F. and J.O. Leckie (1986). ìMechanism of lead ion adsorption at the goethite-water interface.î In *Geochemical Processes at Mineral Surfaces*, (Edited by J.A. Davis and K.F. Hayes), ACS Symposium Series, No. 323. American Chemical Society, Washington, D.C., 114-141.

Hayes, K.F. and J.O. Leckie (1987). ìModeling ionic strength effects on cation adsorption at hydrous oxide/solution interfaces,î *J. Colloid Interface Sci.* **115,** 564.

Hayes, K.F., C. Papelis, and J.O. Leckie (1988). ìModeling ionic strength effects on anion adsorption at hydrous oxide/solution interfaces,î *J. Colloid Interface Sci.* **125,** 717-726.

Hayes, K.F., A.L. Roe, G.E. Brown, Jr., K.O. Hodgson, J.O. Leckie, and G.A. Parks (1987). ìIn situ X-ray absorption study of surface complexes: selenium oxyanions on α-FeOOH,î *Science.* **238,** 783.

Hemond, H.F. and E.J. Fechner (1994). *Chemical Fate and Transport in the Environment.* Academic Press, San Diego, 338 pp.

Klein, C. and C.S. Hurlbut, Jr. (1993). *Manual of Mineralogy (after J.D. Dana).* John Wiley & Sons, New York, 681 pp.

Laws, E.A. (1993). *Aquatic Pollution: An Introductory Text.* Environmental Science and Technology. John Wiley & Sons, New York, 611 pp.

Leckie, J.O., M.M. Benjamin, K. Hayes, G. Kaufman, and S. Altmann (1980). ìAdsorption/Coprecipitation of Trace Elements from Water with Iron Oxyhydroxide,î Electric Power Research Institute Report No. CS-1513, Palo Alto, CA.

Nakamura, S., S. Mori, H. Yoshimuta, Y. Ito, and M. Kanno (1988). ìUranium adsorption properties of hydrous titanium oxide granulated with polyacrylonitrile,î *Separ. Sci. Technol.* **23,** 731-743.

Nickel, E.H. and M.C. Nichols (1991). *Mineral Reference Manual.* Van Nostrand Reinhold, New York, 250 pp.

Ohnuki, T., S. Takebe, and T. Yamamoto (1989). ìDevelopment of a migration prediction system (MIGSTEM) for cationic species of radionuclides through soil layers,î *J. Nucl. Sci. Technol.* **28,** 795-804.

Ooi, K., K. Ashida, S. Katoh, and K. Sugasaka (1987). ìRate of uranium adsorption on hydrous titanium (IV) oxide granulated with poly acrylic hydrazide,î *J. Nucl. Sci. Technol.* **24,** 315-322.

Papelis, C., G.E. Brown, Jr., G.A. Parks, and J.O. Leckie (1995). ìX-ray absorption spectroscopic studies of cadmium and selenite adsorption on aluminum oxides,î *Langmuir.* **11,** 2041-2048.

Papelis, C. and K.F. Hayes (1996). ìDistinguishing between interlayer and external sorption sites of clay minerals using x-ray absorption spectroscopy,î *Colloids & Surfaces, A.* **107,** 89-96.

Sax, N.I. (1981). *Cancer Causing Chemicals.* Van Nostrand Reinhold, New York, 466 pp.

Sposito, G. (1984). *The Surface Chemistry of Soils.* Oxford University Press, Oxford, 234 pp.

Sposito, G. (1986). ìDistinguishing adsorption from surface precipitation.î In *Geochemical Processes at Mineral Surfaces,* (Edited by J.A. Davis and K.F. Hayes), ACS Symposium Series, No. 323. American Chemical Society, Washington, D.C., 217-228.

Sposito, G. (1989). *The Chemistry of Soils.* Oxford University Press, New York, 277 pp.

Stumm, W. (1992). *Chemistry of the Solid-Water Interface*. John Wiley & Sons, New York, 428 pp.

Table 1. Major and Trace Element Composition of Granite, by Weight, in Terms of Oxide Percentages.

Major Elements	(wt. %)	Trace Elements	(ppm)
SiO_2	67.70	Rb	78.2
Al_2O_3	17.00	Sr	721.0
TiO_2	0.85	Y	19.2
Fe_2O_3	1.91	Zr	418.0
CaO	3.84	Nb	9.2
K_2O	3.15	Cr	32.7
MnO	0.04	Ni	177.0
P_2O_5	0.31		
Na_2O	4.77		
MgO	0.43		

Table 2. Composition of groundwaters used in sorption studies.

	HS-1			H-2, 219.5 m, 15-Jun-93			HC-4		
CATIONS	Conc. (mg/L)	Conc. (M)	Conc. (meq/L)	Conc. (mg/L)	Conc. (M)	Conc. (meq/L)	Conc. (mg/L)	Conc. (M)	Conc. (meq/L)
Ca	31.5	7.86E-04	1.57E+00	5.51	1.37E-04	2.75E-01	66.4	1.66E-03	3.31E+00
Mg	5.37	2.21E-04	4.42E-01	218	8.97E-03	1.79E+01	9.87	4.06E-04	8.12E-01
Na	47.2	2.05E-03	2.05E+00	12500	5.44E-01	5.44E+02	63.7	2.77E-03	2.77E+00
K	7.11	1.82E-04	1.82E-01	73.4	1.88E-03	1.88E+00	3.67	9.39E-05	9.39E-02
Totals			4.25E+00			5.64E+02			6.99E+00
ANIONS									
Cl	29.3	8.26E-04	8.26E-01	17700	4.99E-01	4.99E+02	101	2.85E-03	2.85E+00
SO4	51.5	5.36E-04	1.07E+00	3610	3.76E-02	7.52E+01	90.3	9.40E-04	1.88E+00
HCO3	140	2.29E-03	2.29E+00	605	9.91E-03	9.91E+00	113	1.85E-03	1.85E+00
CO3		0.00E+00	0.00E+00	253	4.22E-03	8.43E+00		0.00E+00	0.00E+00
NO3	3.99	6.44E-05	6.44E-02	0.04	6.45E-07	6.45E-04	26.8	4.32E-04	4.32E-01
Br	0.1	1.25E-06	1.25E-03		0.00E+00	0.00E+00		0.00E+00	0.00E+00
Totals			4.26E+00			5.93E+02			7.01E+00
Cation/Anion Imbalance (%)			0.24			-5.14			-0.33
Ionic Strength			0.0058			0.6292			0.0100
EC (µS/cm)			438			48300			727
pH			8.14			9.06			8.04

Table 3. Linear and Freundlich Isotherm Parameters for Lead Sorption.

Ionic Strength (M) or Groundwater Type	pH	K_d (m^3/g)	K_F $(g/g)/(g/m^3)^{1/n}$	$1/n$ (–)
I=0.01M	4.0	1.78×10^{-5}	1.85×10^{-5}	0.94
	5.0	4.53×10^{-5}	2.05×10^{-5}	0.74
	6.0	3.56×10^{-4}	1.42×10^{-4}	0.81
	7.0	2.40×10^{-3}	5.44×10^{-4}	0.82
	8.0	9.99×10^{-2}	9.99×10^{-2}	1.00
	9.0	9.99×10^{-2}	9.99×10^{-2}	1.00
HS-1	4.0	4.08×10^{-5}	2.32×10^{-5}	0.87
	5.0	4.49×10^{-5}	1.10×10^{-5}	0.67
	6.0	1.33×10^{-3}	4.67×10^{-4}	0.84
	7.0	9.99×10^{-2}	9.99×10^{-2}	1.00
	8.0	9.99×10^{-2}	9.99×10^{-2}	1.00
	9.0	9.99×10^{-2}	9.99×10^{-2}	1.00
HC-4	6.0	7.33×10^{-4}	2.11×10^{-4}	0.79
	7.0	1.90×10^{-3}	9.3×10^{-4}	0.90
	8.0	4.90×10^{-3}	4.90×10^{-3}	1.00

Table 4. Linear and Freundlich Isotherm Parameters for Cesium Sorption

Groundwater Type	pH	K_d (m^3/g)	K_f $(g/g)/(g/m3)^{1/n}$	1/n (-)
HC-4	5	3.07×10^{-5}	4.56×10^{-5}	0.85
	6	2.75×10^{-5}	3.88×10^{-5}	0.88
	7	3.11×10^{-5}	3.62×10^{-5}	0.98
	8	4.29×10^{-5}	3.88×10^{-5}	1.07
	9	5.45×10^{-5}	4.14×10^{-5}	1.13

Table 5. Linear and Freundlich Isotherm Parameters for Chromate Sorption.

Ionic Strength (M) or Groundwater Type	pH	K_d (m^3/g)	K_F $(g/g)/(g/m^3)^{1/n}$	$1/n$ (-)
I=0.01M	4.0	1.00×10^{-4}	2.16×10^{-6}	0.46
	5.0	1.00×10^{-4}	3.96×10^{-6}	0.48
	6.0	9.96×10^{-6}	6.12×10^{-7}	0.35
	7.0	8.89×10^{-6}	4.38×10^{-7}	0.34
	8.0	6.65×10^{-6}	2.53×10^{-7}	0.32
	9.0	5.44×10^{-6}	1.25×10^{-7}	0.28
H-2	5.0	4.00×10^{-4}	9.53×10^{-6}	0.46
	7.0	1.23×10^{-4}	4.60×10^{-6}	0.46
	8.0	1.79×10^{-5}	2.06×10^{-7}	0.18
	9.0	1.65×10^{-5}	2.15×10^{-7}	0.20
HC-4	9.0	4.25×10^{-6}	2.49×10^{-7}	0.47

Table 6. Linear and Freundlich Isotherm Parameters for Selenite Sorption.

Ionic Strength (M) or Groundwater Type	pH	K_d (m^3/g)	K_F $(g/g)/(g/m^3)^{1/n}$	$1/n$ (-)
I=0.01M	4.0	2.20×10^{-5}	1.46×10^{-5}	0.94
	5.0	3.91×10^{-5}	7.69×10^{-6}	0.78
	6.0	8.20×10^{-5}	4.28×10^{-5}	0.92
	7.0	5.41×10^{-5}	7.06×10^{-6}	0.73
	8.0	2.53×10^{-5}	5.85×10^{-8}	0.25
	9.0	1.39×10^{-5}	1.86×10^{-7}	0.41
I=1.0M	4.0	2.07×10^{-5}	7.10×10^{-8}	0.23
	5.0	5.38×10^{-5}	8.15×10^{-8}	0.14
	6.0	1.64×10^{-4}	2.31×10^{-6}	0.47
	7.0	1.00×10^{-4}	1.52×10^{-6}	0.46
	8.0	5.66×10^{-5}	5.05×10^{-6}	0.68
	9.0	2.07×10^{-5}	1.27×10^{-6}	0.62
HC-4	4.0	1.51×10^{-5}	6.32×10^{-7}	0.57
	5.0	4.12×10^{-5}	6.17×10^{-7}	0.44
	6.0	2.13×10^{-4}	1.80×10^{-4}	0.98
	7.0	1.00×10^{-4}	2.84×10^{-5}	0.84
	8.0	4.32×10^{-5}	1.89×10^{-6}	0.58
	9.0	2.08×10^{-5}	1.66×10^{-7}	0.34

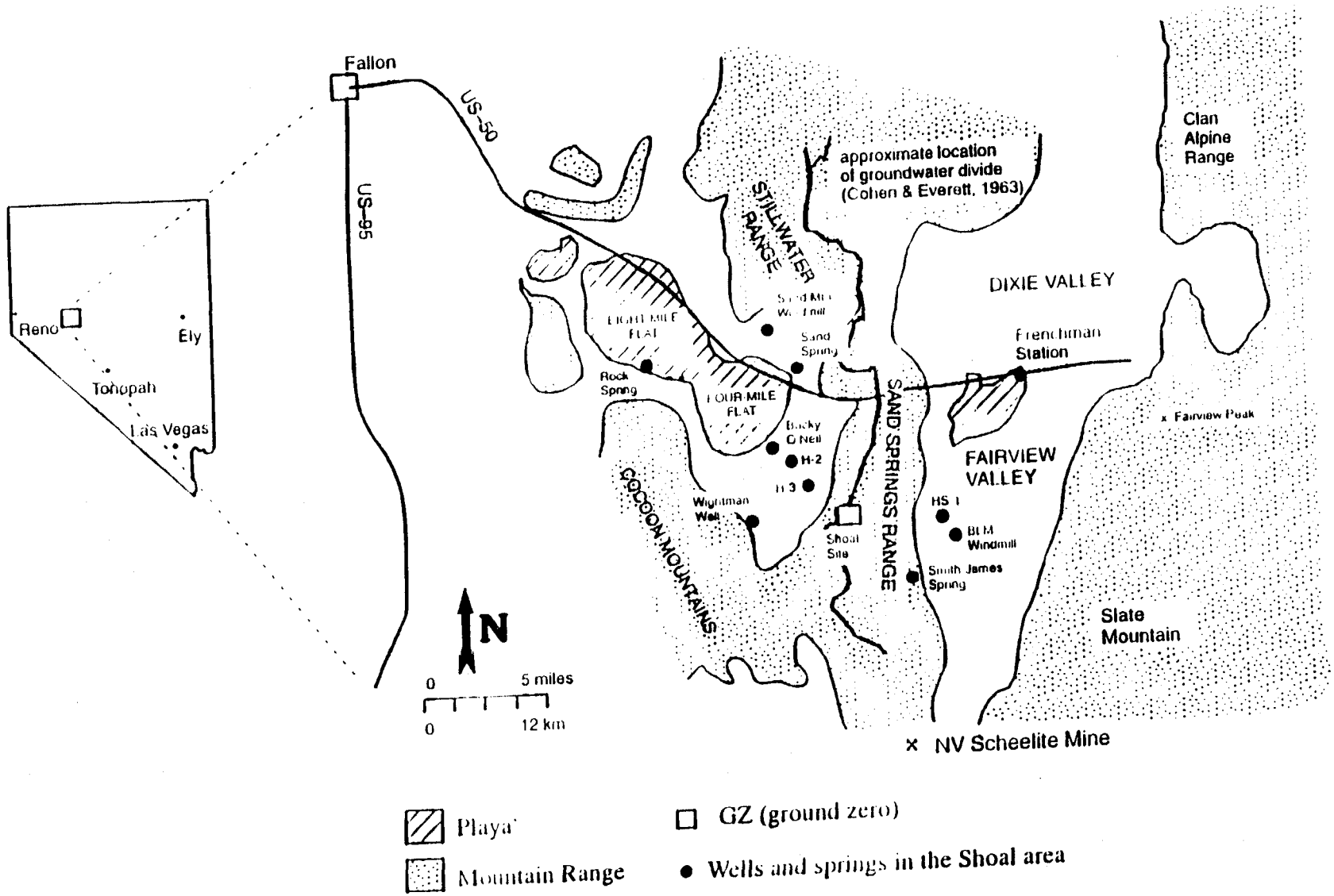
Fallon
US-50
US-95
Reno
Ely
Tonopah
Las Vegas
approximate location
of groundwater divide
(Cohen & Everett, 1963)
STILLWATER RANGE
Clan
Alpine
Range
DIXIE VALLEY
Frenchman
Station
Sand
Spring
Rock
Spring
FOUR-MILE
FLAT
Bucky
O'Neil
H-2
H-3
Wightman
Well
COCOON MOUNTAINS
Shoal
Site
SAND SPRINGS RANGE
FAIRVIEW
VALLEY
HS 1
BLM
Windmill
Smith James
Spring
Fairview Peak
Slate
Mountain
NV Scheelite Mine
N
0
5 miles
0
12 km
Playa
Mountain Range
GZ (ground zero)
Wells and springs in the Shoal area

Figure 1

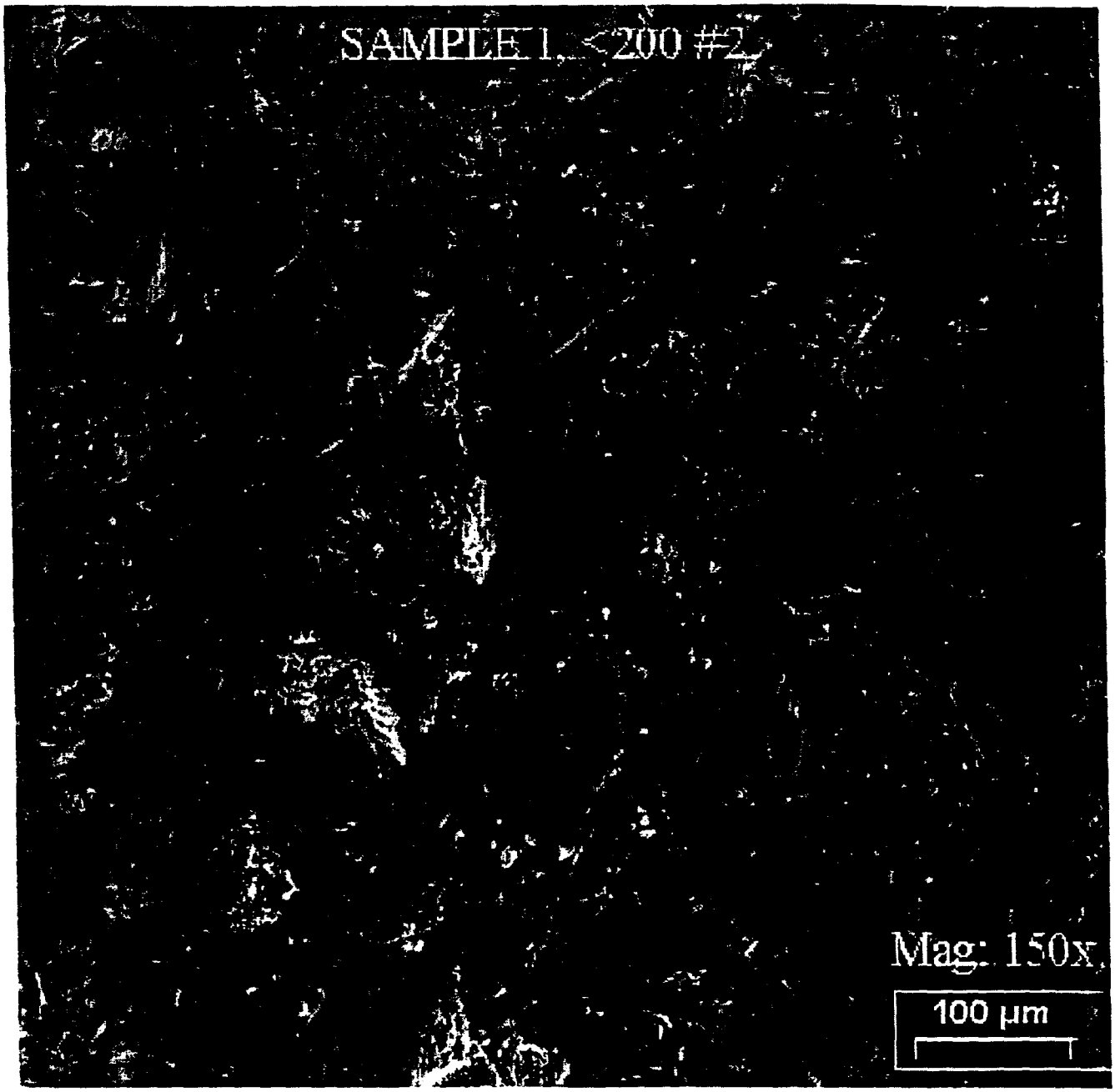

Figure 2

Figure 3

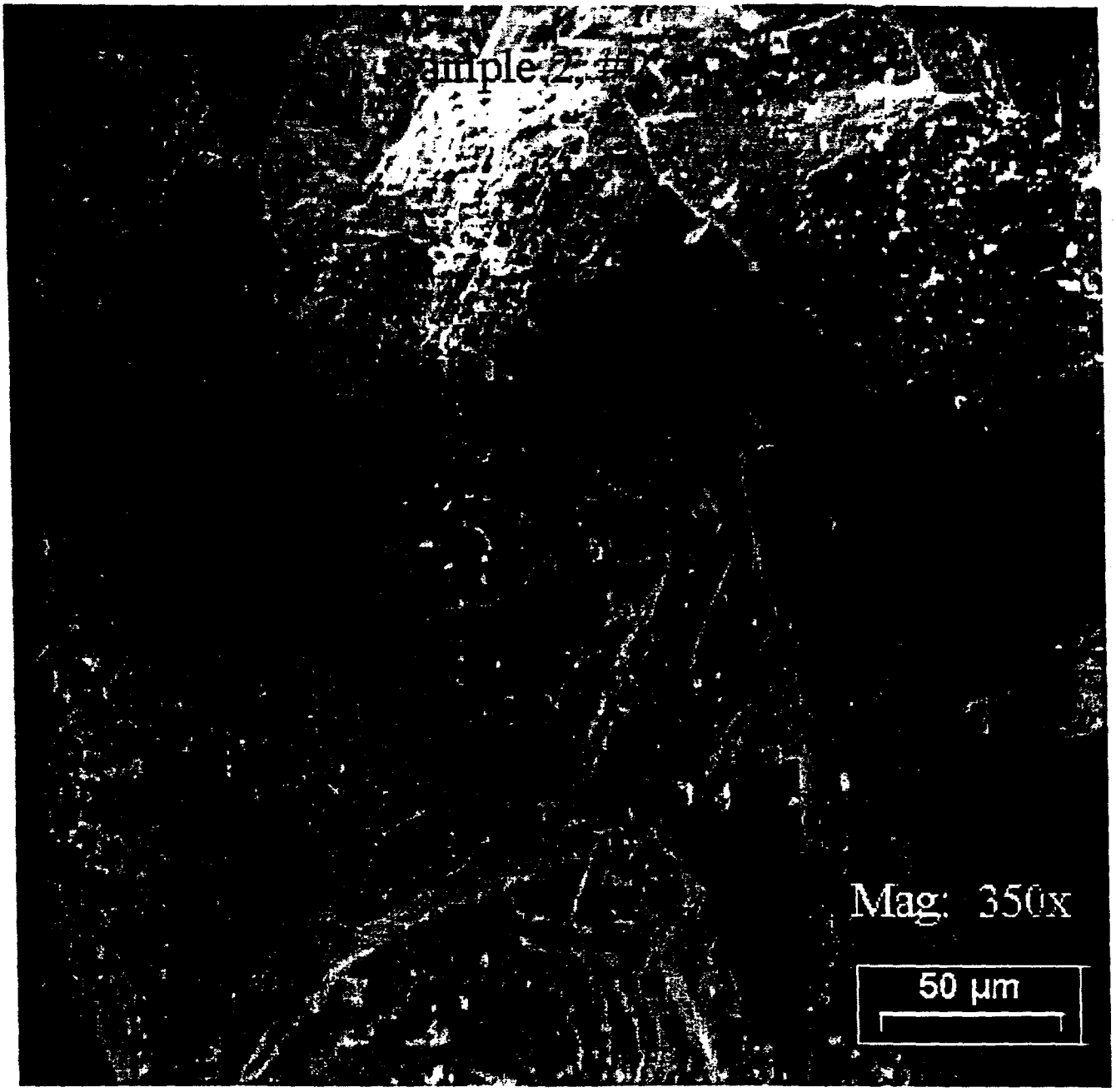

Figure 4

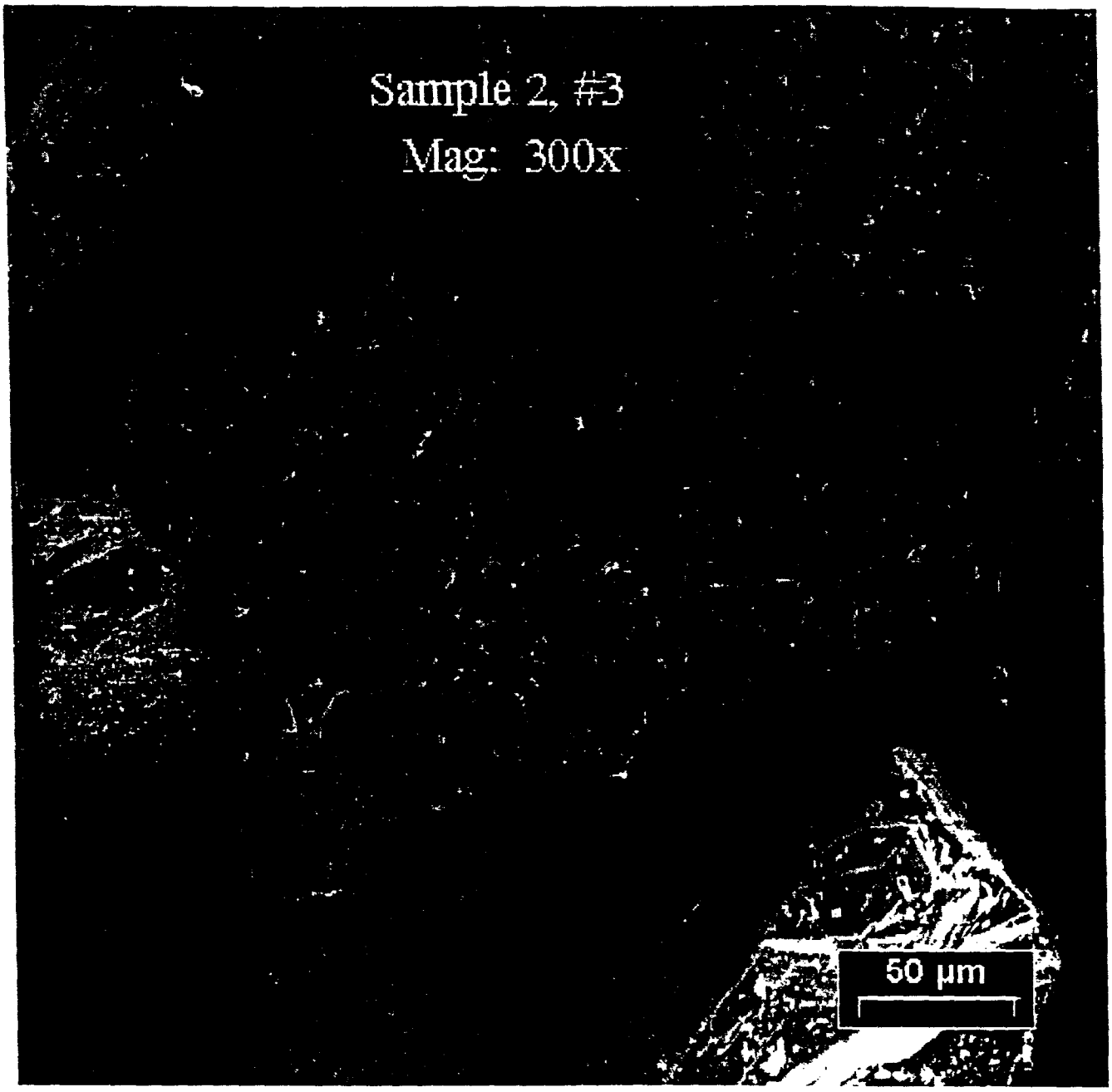

Figure 5

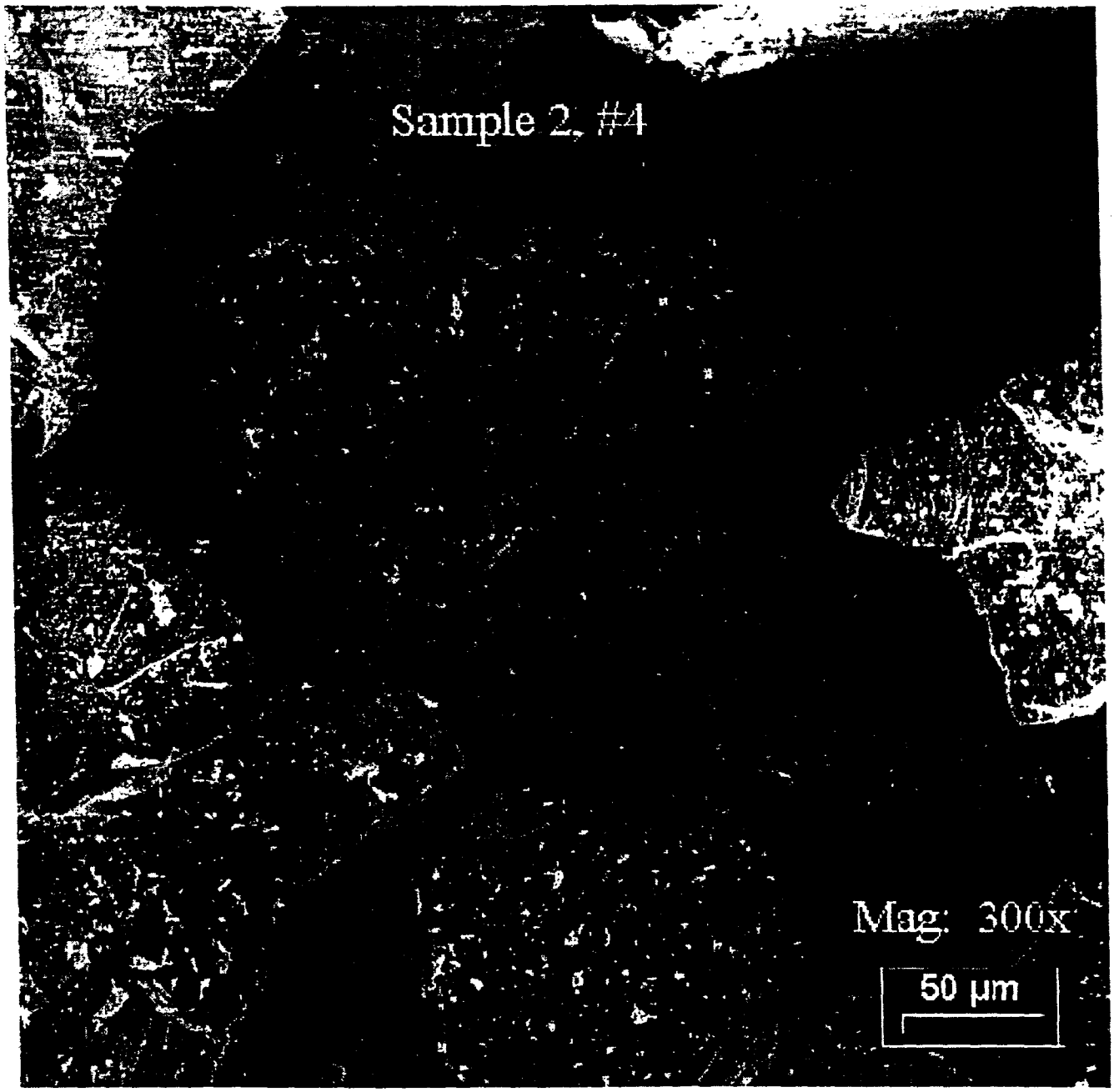

Figure 6

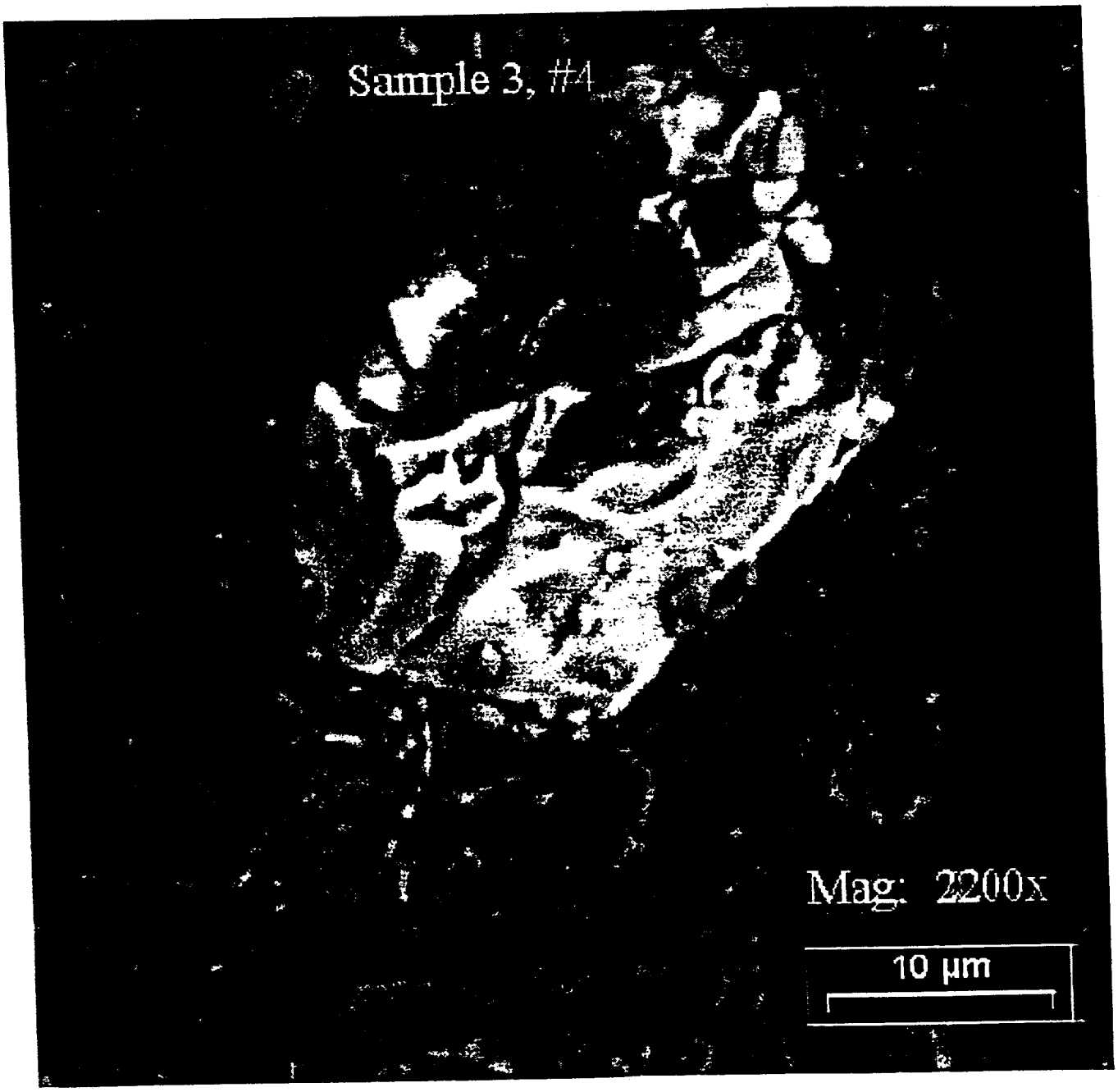

Figure 7

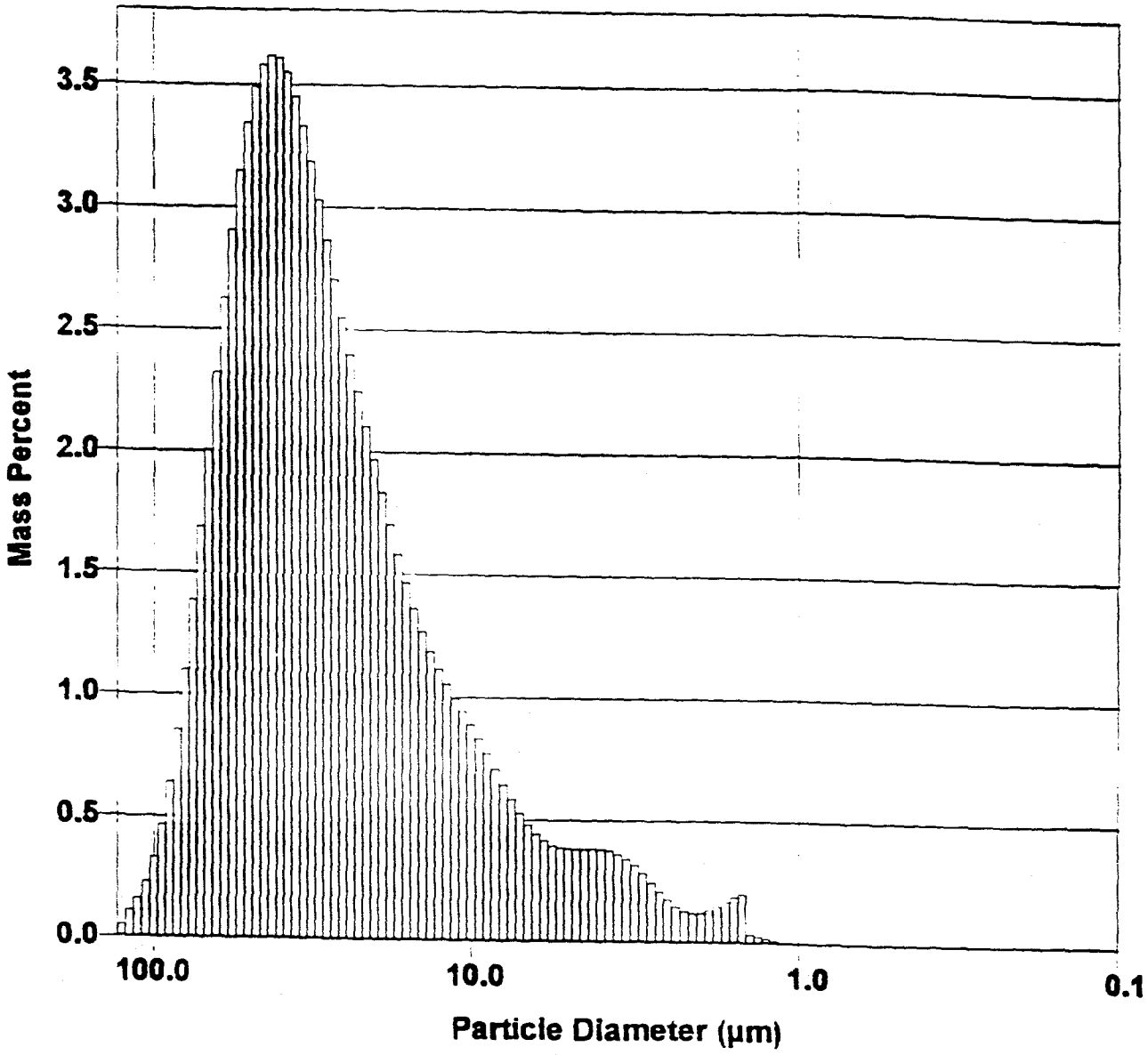
3.5
3.0
2.5
2.0
1.5
1.0
0.5
0.0
Mass Percent
100.0
10.0
1.0
0.1
Particle Diameter (µm)

Figure 8

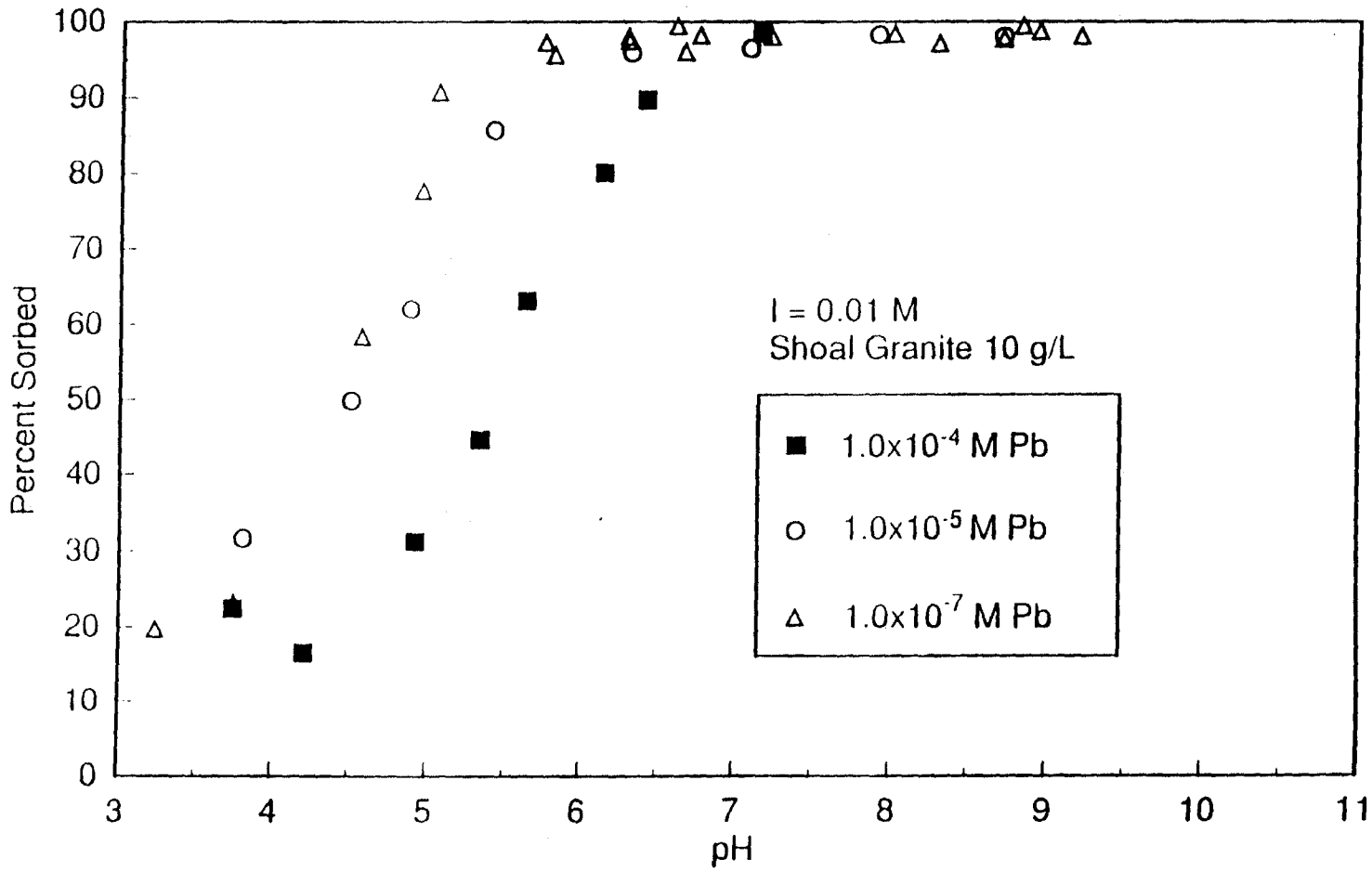
100
90
80
70
60
50
40
30
20
10
0
Percent Sorbed
3
4
5
6
7
8
9
10
11
pH
I = 0.01 M
Shoal Granite 10 g/L
1.0x10-4 M Pb
1.0x10-5 M Pb
1.0x10-7 M Pb

Figure 9

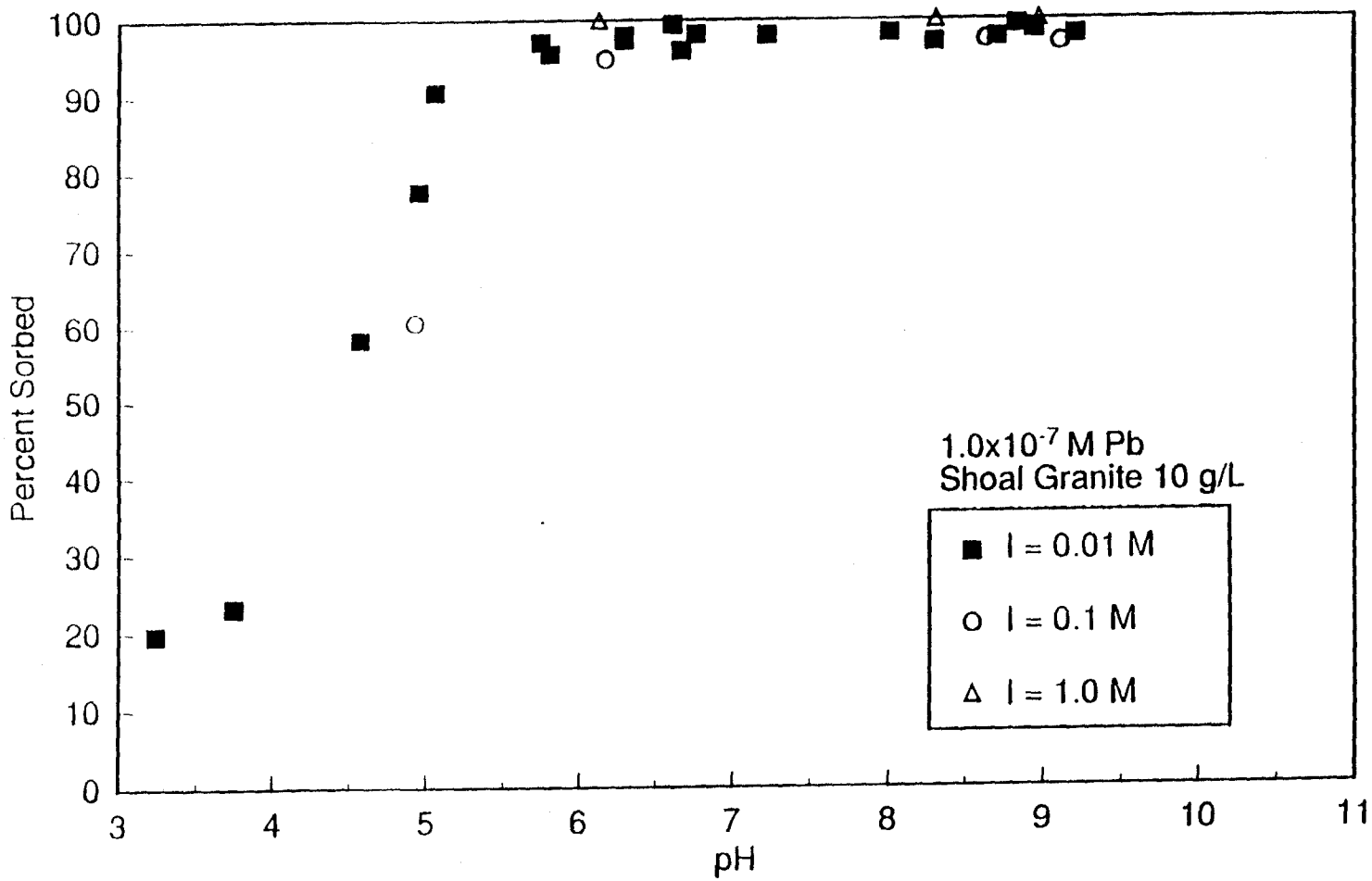
100
90
80
70
60
50
40
30
20
10
0
Percent Sorbed
3
4
5
6
7
8
9
10
11
pH
1.0x10-7 M Pb
Shoal Granite 10 g/L
I = 0.01 M
I = 0.1 M
I = 1.0 M

Figure 10

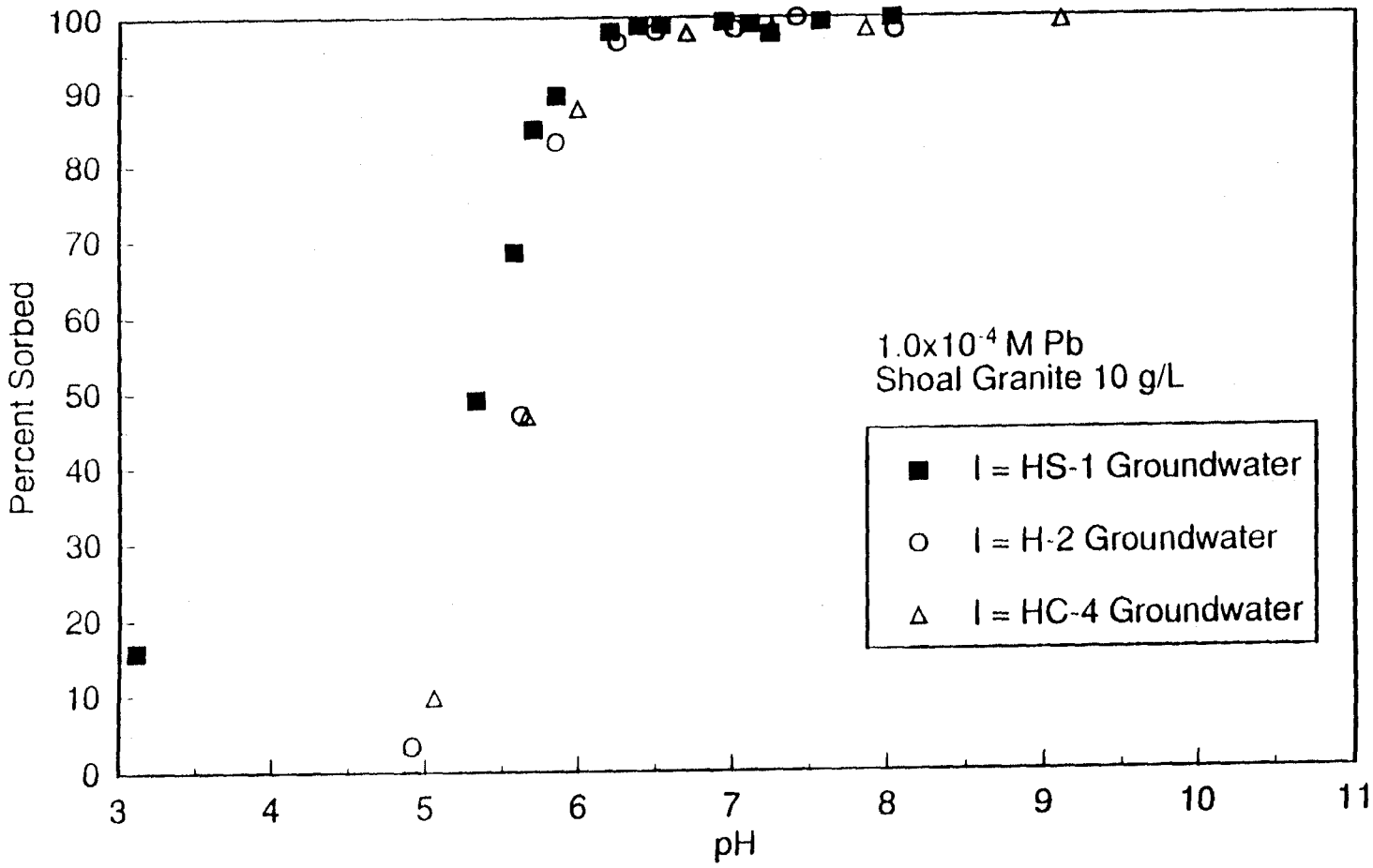
100
90
80
70
60
50
40
30
20
10
0
Percent Sorbed
3
4
5
6
7
8
9
10
11
pH
1.0x10-4 M Pb
Shoal Granite 10 g/L
I = HS-1 Groundwater
I = H-2 Groundwater
I = HC-4 Groundwater

Figure 11

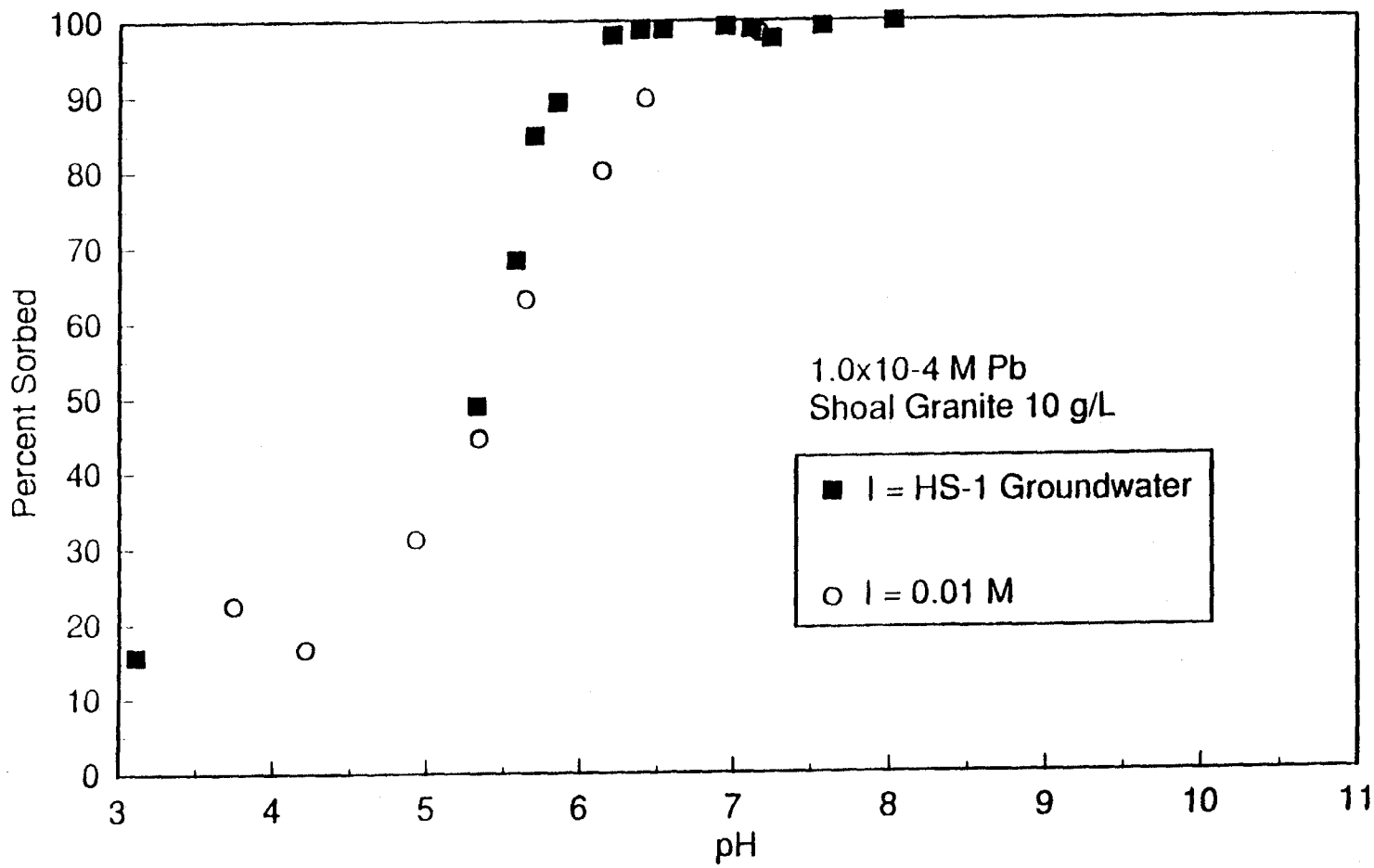
100
90
80
70
60
50
40
30
20
10
0
Percent Sorbed
3
4
5
6
7
8
9
10
11
pH
1.0x10-4 M Pb
Shoal Granite 10 g/L
I = HS-1 Groundwater
I = 0.01 M

Figure 12

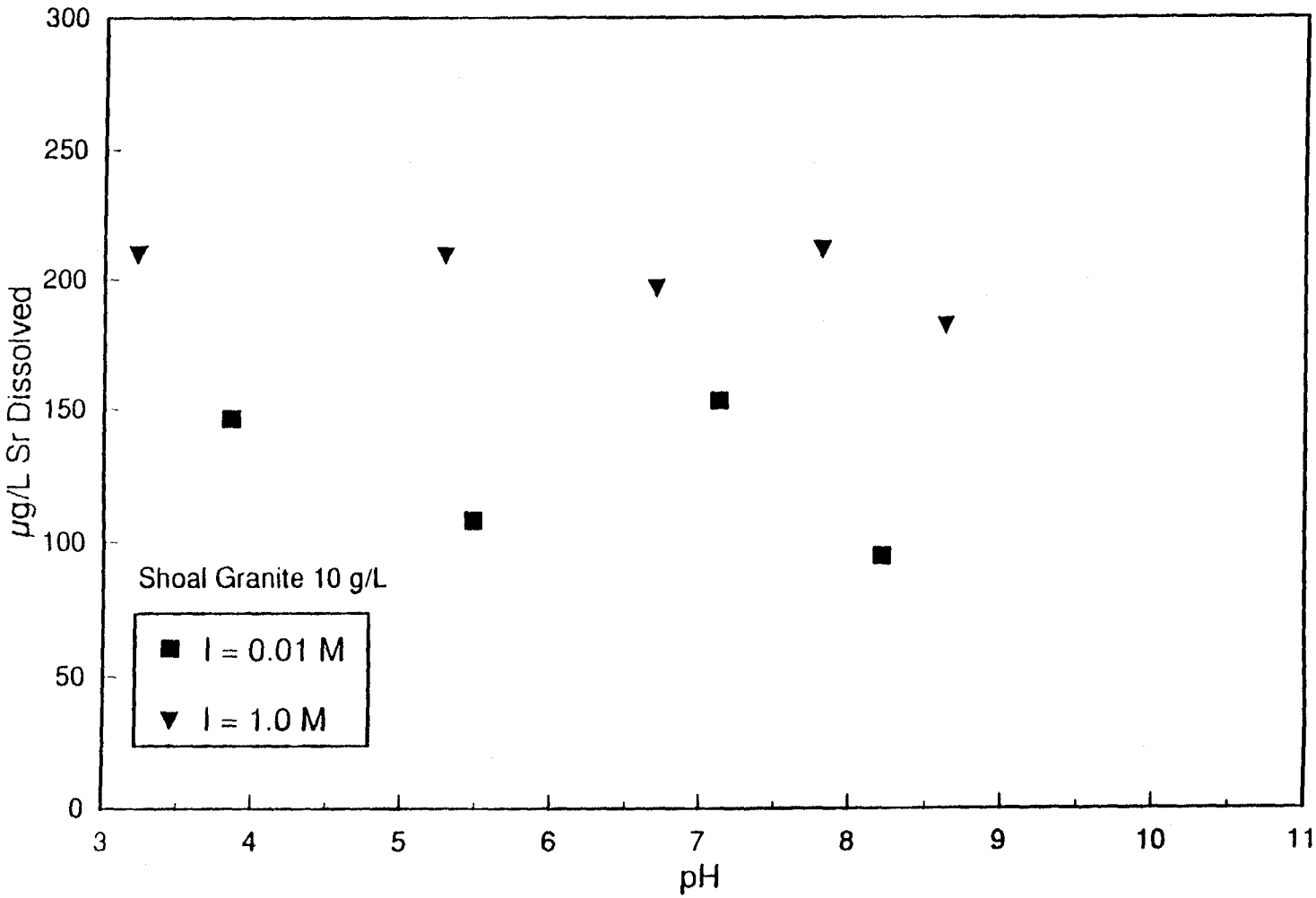
300
250
200
150
100
50
0
μg/L Sr Dissolved
Shoal Granite 10 g/L
I = 0.01 M
I = 1.0 M
3
4
5
6
7
8
9
10
11
pH

Figure 13

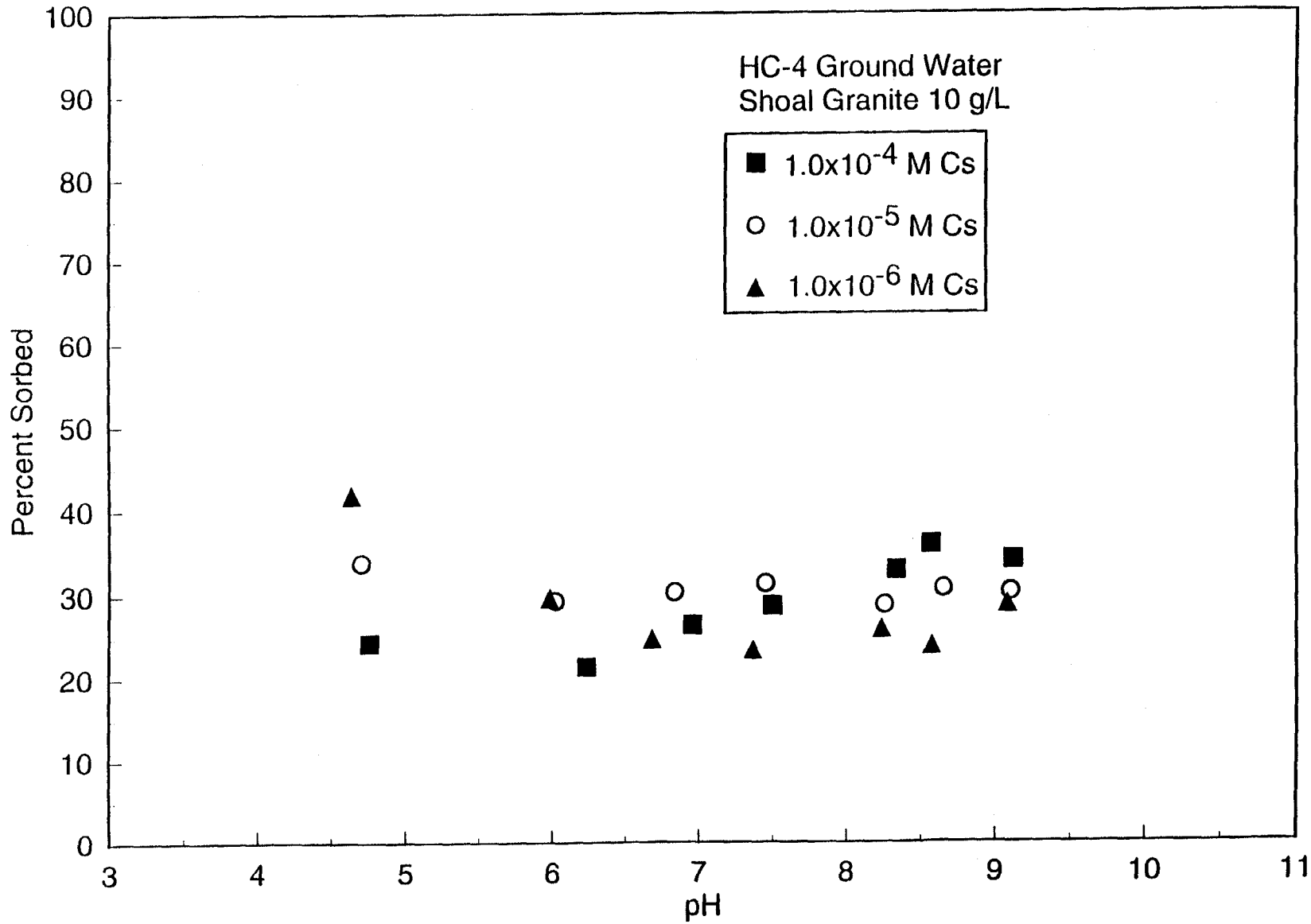
HC-4 Ground Water
Shoal Granite 10 g/L
1.0x10-4 M Cs
1.0x10-5 M Cs
1.0x10-6 M Cs
Percent Sorbed
pH
0
10
20
30
40
50
60
70
80
90
100
3
4
5
6
7
8
9
10
11

Figure 14

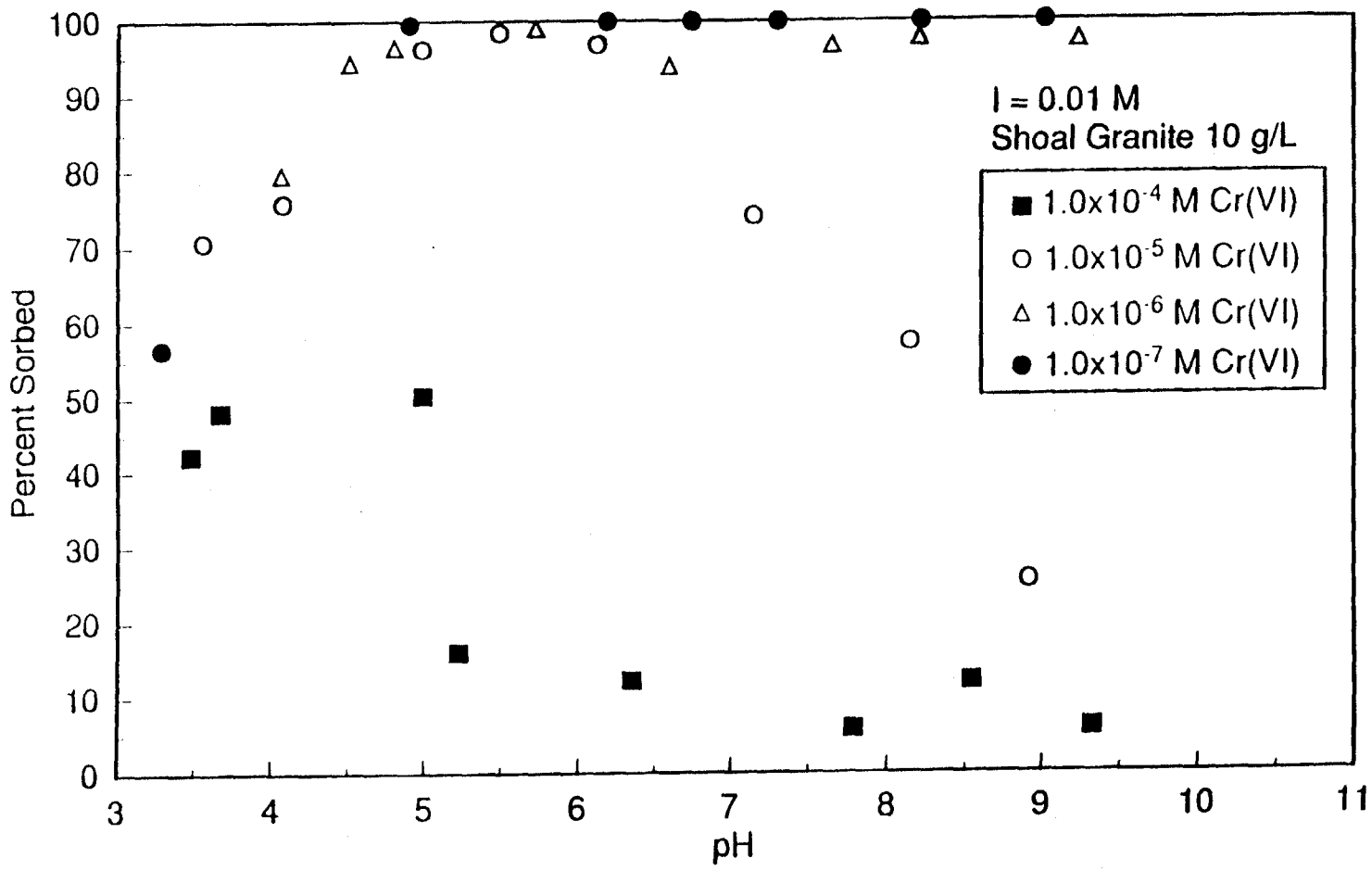
I = 0.01 M
Shoal Granite 10 g/L
1.0x10-4 M Cr(VI)
1.0x10-5 M Cr(VI)
1.0x10-6 M Cr(VI)
1.0x10-7 M Cr(VI)
Percent Sorbed
pH
0
10
20
30
40
50
60
70
80
90
100
3
4
5
6
7
8
9
10
11

Figure 15

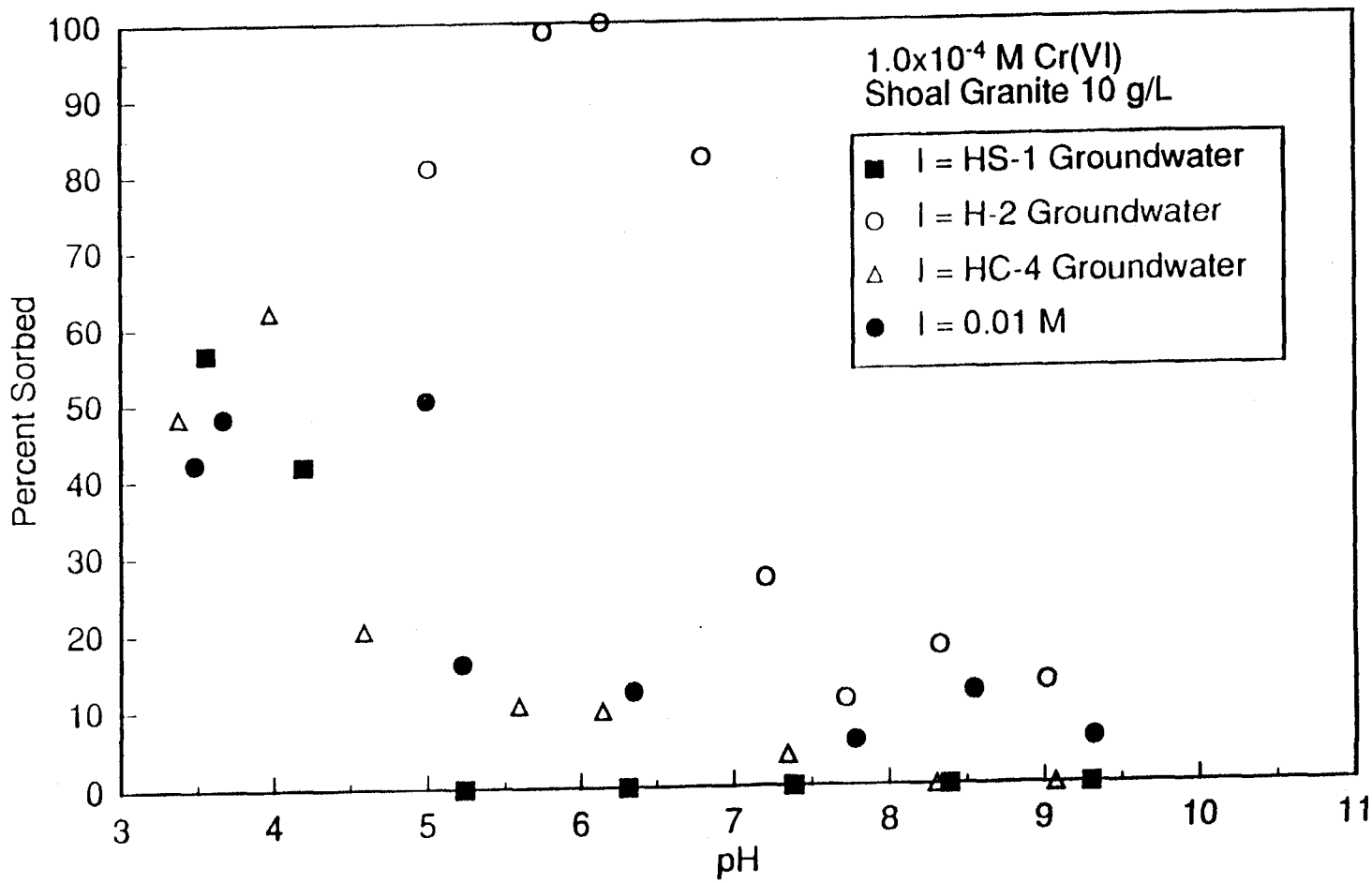
1.0x10-4 M Cr(VI)
Shoal Granite 10 g/L
I = HS-1 Groundwater
I = H-2 Groundwater
I = HC-4 Groundwater
I = 0.01 M
Percent Sorbed
pH
100
90
80
70
60
50
40
30
20
10
0
3
4
5
6
7
8
9
10
11

Figure 16

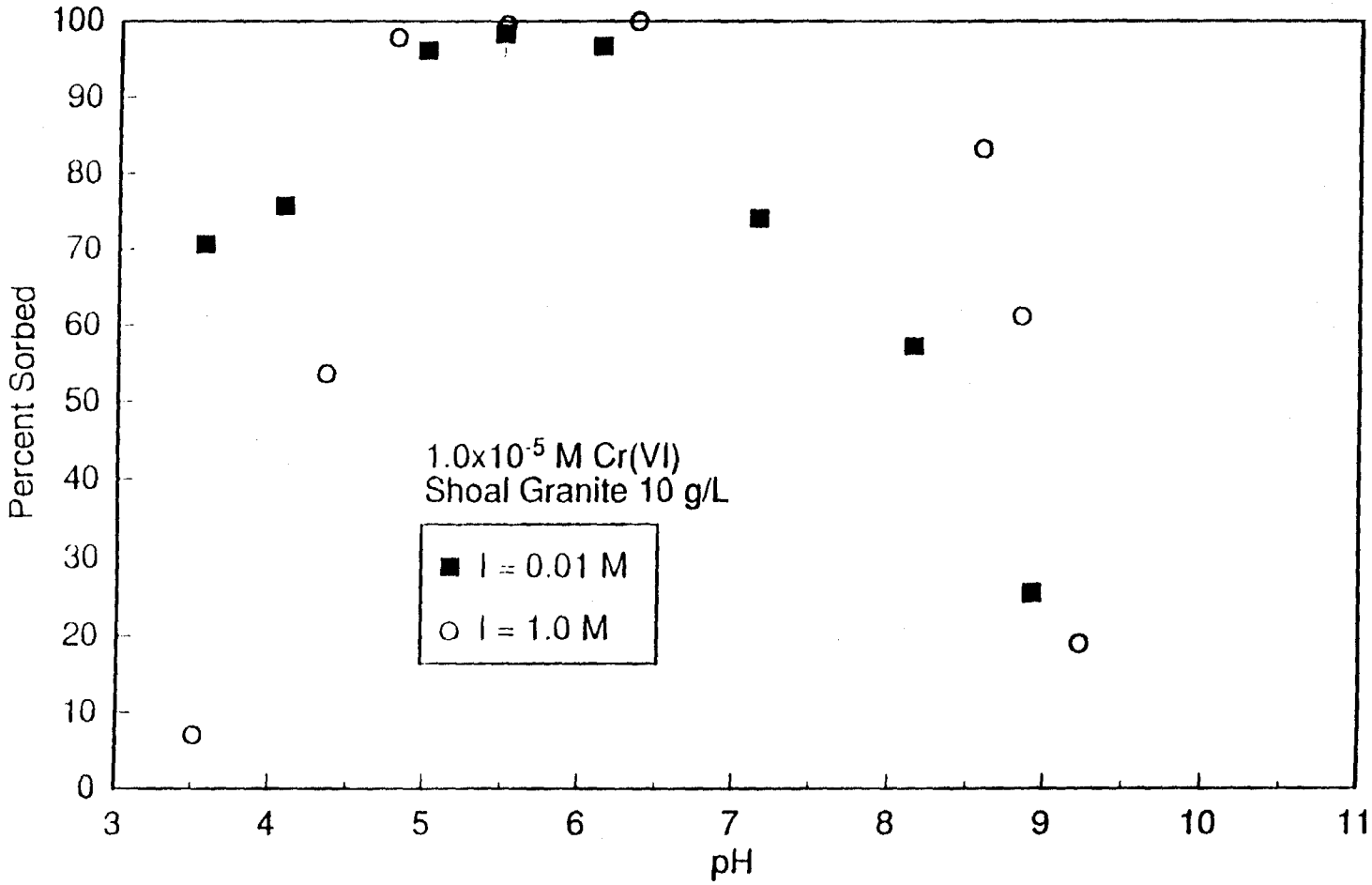
100
90
80
70
60
50
40
30
20
10
0
Percent Sorbed
3
4
5
6
7
8
9
10
11
pH
1.0x10-5 M Cr(VI)
Shoal Granite 10 g/L
I = 0.01 M
I = 1.0 M

Figure 17

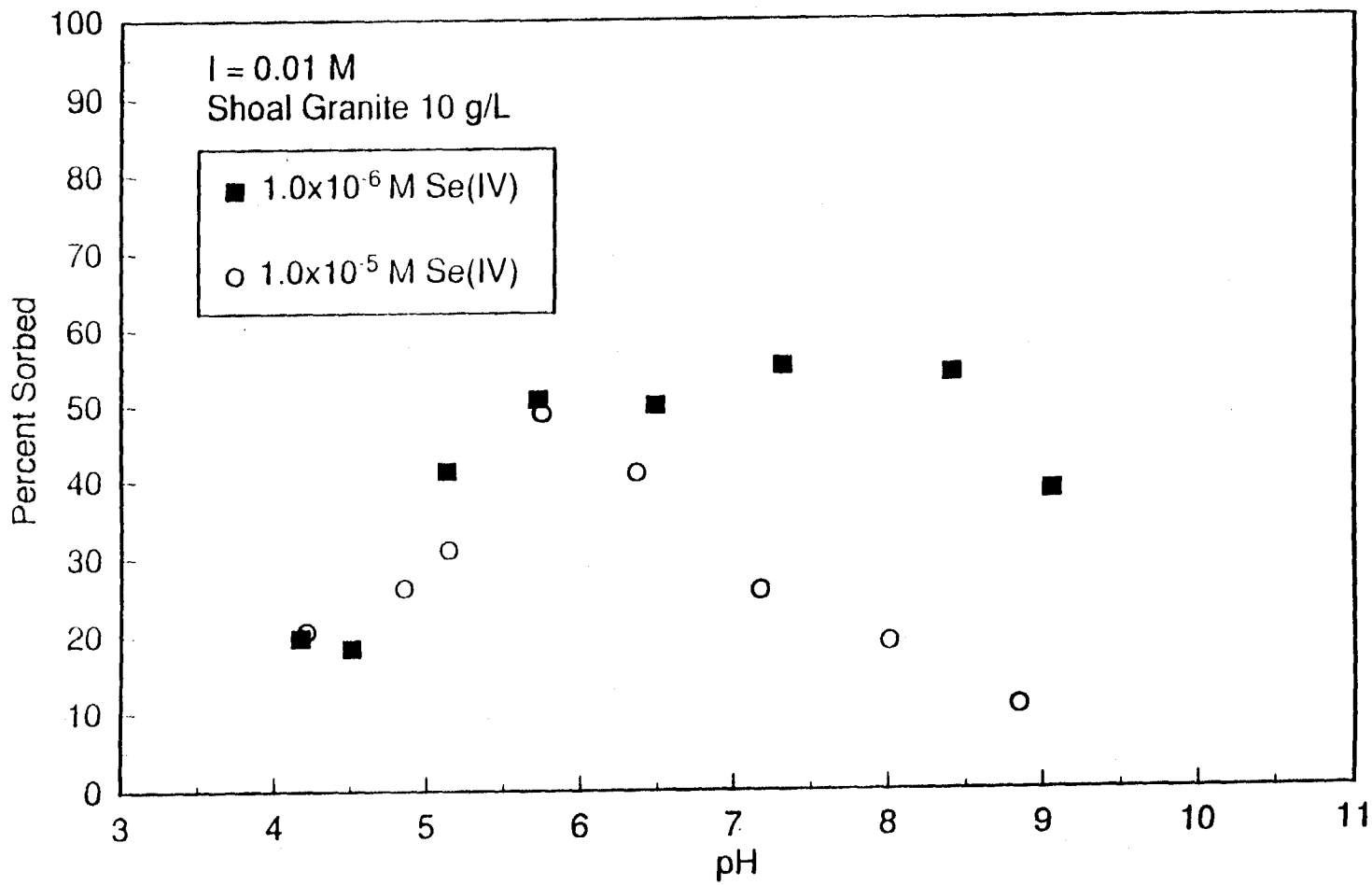
I = 0.01 M
Shoal Granite 10 g/L
1.0x10-6 M Se(IV)
1.0x10-5 M Se(IV)
Percent Sorbed
pH
0
10
20
30
40
50
60
70
80
90
100
3
4
5
6
7
8
9
10
11

Figure 18

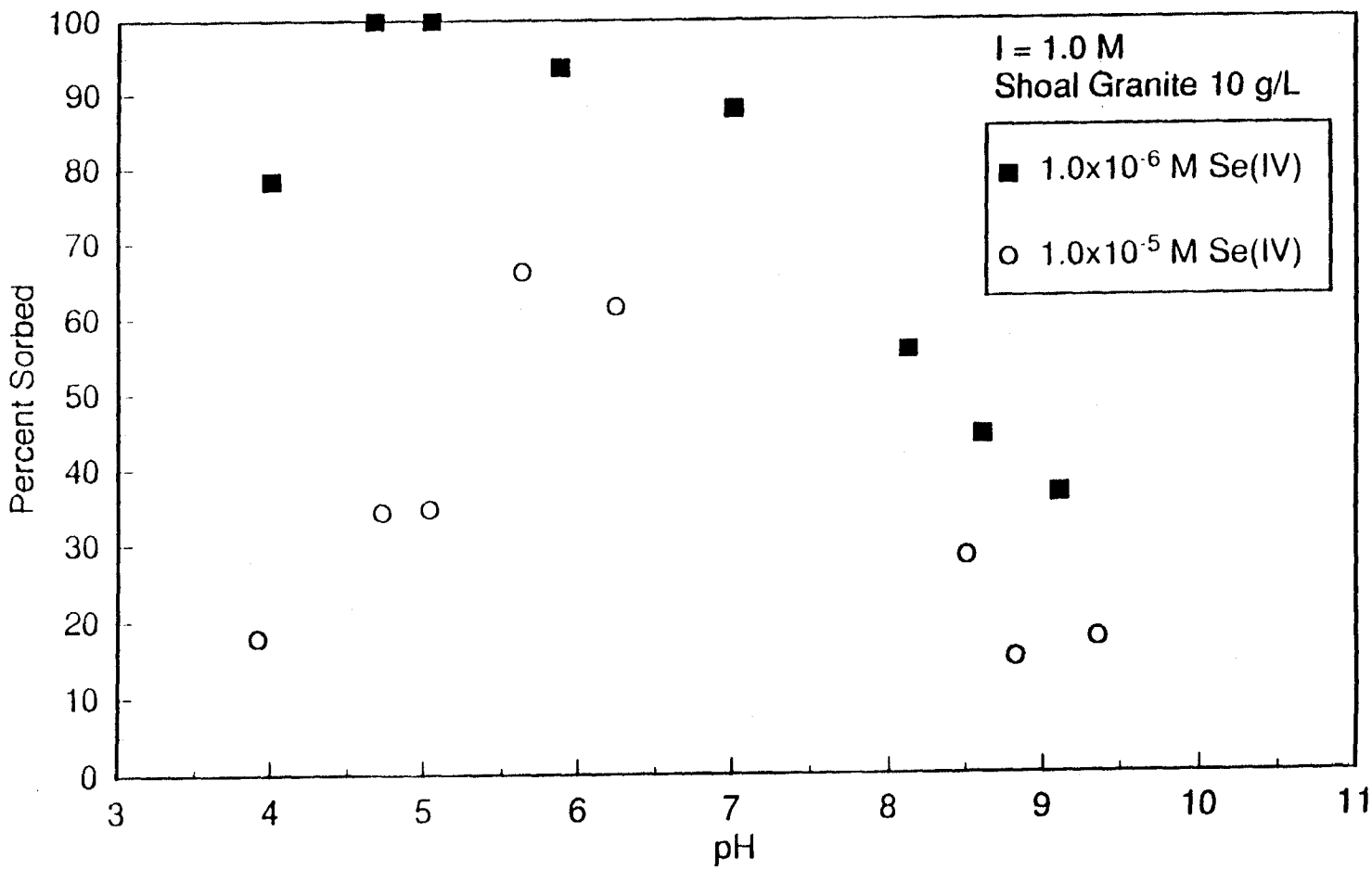
I = 1.0 M
Shoal Granite 10 g/L
1.0x10-6 M Se(IV)
1.0x10-5 M Se(IV)
Percent Sorbed
pH
0
10
20
30
40
50
60
70
80
90
100
3
4
5
6
7
8
9
10
11

Figure 19

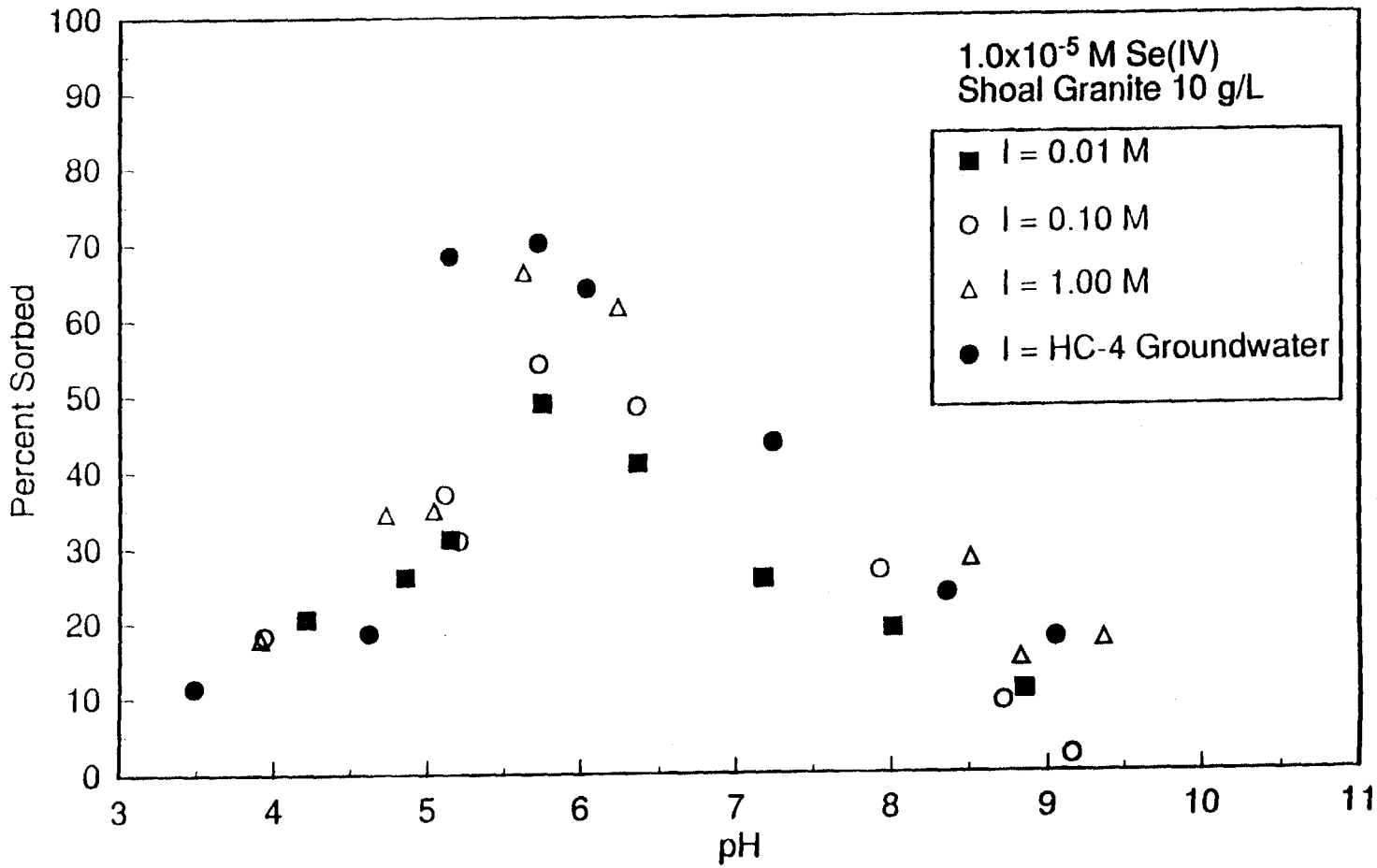
1.0x10-5 M Se(IV)
Shoal Granite 10 g/L
I = 0.01 M
I = 0.10 M
I = 1.00 M
I = HC-4 Groundwater
Percent Sorbed
pH
0
10
20
30
40
50
60
70
80
90
100
3
4
5
6
7
8
9
10
11

Figure 20

APPENDIX 8

RADIONUCLIDES PERTINENT TO EVALUATING TRANSPORT FROM UNDERGROUND NUCLEAR TESTS, AND THEIR DECAY CHAINS

$^{3}H \xrightarrow{12.3y\ \beta^-} {}^{3}He$ stable gas

$^{14}C \xrightarrow{5730\ y\ \beta^-} {}^{14}N$ stable gas

$^{26}Al \xrightarrow{7.4 \times 10^5\ y\ \beta^+, EC} {}^{26}Mg$ stable

$^{36}Cl \xrightarrow{3.0 \times 10^5\ y\ \beta^-} {}^{36}Ar$ stable gas

$^{39}Ar \xrightarrow{269\ y\ \beta^-} {}^{39}K$ stable

$^{40}K \xrightarrow{1.28 \times 10^9\ y\ \beta^-} {}^{40}Ca$ stable

$^{41}Ca \xrightarrow{1.03 \times 10^5\ y\ EC} {}^{40}K$ stable

$^{59}Ni \xrightarrow{7.6 \times 10^4\ y\ EC} {}^{59}Co$ stable

$^{63}Ni \xrightarrow{92\ y\ \beta^-} {}^{63}Cu$ stable

$^{81}Kr \xrightarrow{2.1 \times 10^5\ y\ EC} {}^{81}Br$ stable

$^{85}Kr \xrightarrow{10.7\ y\ \beta^-} {}^{85}Rb$ stable

$^{90}Sr \xrightarrow{29.1\ y\ \beta^-} {}^{90}Y \xrightarrow{64\ hrs\ \beta^-} {}^{90}Zr$ stable

$^{93}Zr \xrightarrow{1.5 \times 10^6 y\ \beta^-} {}^{93}Nb$ stable

$^{92g}Nb \xrightarrow{3.6 \times 10^7 y}$

$^{93m}Nb \xrightarrow{16.1\ y\ IT} {}^{93}Nb$ stable

$^{94}Nb \xrightarrow{2.0 \times 10^4 y\ \beta^-} {}^{94}Mo$ stable

$^{98}Tc \xrightarrow{4.2 \times 10^6\ y\ \beta^-} {}^{98}Ru$ stable

$^{99g}Tc \xrightarrow{2.13 \times 10^5 y\ \beta^-} {}^{99}Ru$ stable

$^{107}Pd \xrightarrow{6.5 \times 10^{6}\ y\ \beta^-} {}^{107}Ag$ stable

$^{113m}Cd \xrightarrow{14.1\ y\ \beta^-} {}^{113}In$ stable

$^{121m}Sn \xrightarrow{55\ y\ \beta^-} {}^{121}Sb$ stable

$^{126}Sn \xrightarrow{1 \times 10^{5}\ y\ \beta^-} {}^{126}Sb \xrightarrow{12.5\ d\ \beta^-} {}^{126}Te$ stable

$^{129}I \xrightarrow{1.57 \times 10^{7}\ y\ \beta^-} {}^{129}Xe$ stable gas

$^{134}Cs \xrightarrow{2.065\ y\ \beta^-} {}^{134}Ba$ stable

$^{135}Cs \xrightarrow{2.3 \times 10^{6}\ y\ \beta^-} {}^{135}Ba$ stable

$^{137}Cs \xrightarrow{30.2\ y\ \beta^-} {}^{137}Ba$ stable

$^{146}Sm \xrightarrow{1.03 \times 10^{8}\ y\ \alpha} {}^{142}Nd$ stable

$^{151}Sm \xrightarrow{90\ y\ \beta^-} {}^{151}Eu$ stable

$^{150}Eu \xrightarrow{36\ y\ EC} {}^{150}Sm$ stable

$^{152}Eu \xrightarrow{13.5\ y\ \beta^-} {}^{152}Gd \xrightarrow{1 \times 10^{14}\ y\ \alpha} {}^{148}Sm \xrightarrow{1.2 \times 10^{13}\ \alpha} {}^{144}Nd \xrightarrow{5 \times 10^{15}\ y\ \alpha} {}^{140}Ce$ stable

$^{154}Eu \xrightarrow{8.6\ y\ \beta^-} {}^{154}Gd$ stable

$^{166m}Ho \xrightarrow{1.2 \times 10^{3}\ y\ \beta^-} {}^{166}Er$ stable

$^{232}Th \xrightarrow{1.4 \times 10^{10}\ y\ \alpha} {}^{228}Ra \xrightarrow{5.7\ y\ \beta^-} {}^{228}Ac \xrightarrow{6\ hours\ \beta^-} {}^{228}Th \xrightarrow{1.9\ y\ \alpha} {}^{224}Ra \xrightarrow{3.6\ days\ \alpha}$

$^{220}Rn \xrightarrow{55\ s\ \alpha} {}^{216}Po \xrightarrow{0.15\ s\ \alpha} {}^{212}Pb \xrightarrow{10.6\ hr\ \beta^-} {}^{212}Bi \xrightarrow{60\ m\ \beta^-} {}^{212}Po \xrightarrow{0.3\ s\ \alpha} {}^{208}Pb$ stable

$\xrightarrow[\alpha]{} {}^{208}Tl \xrightarrow{3\ m\ \beta^-} {}^{208}Pb$ stable

$^{232}U \xrightarrow{70\ y\ \alpha} {}^{228}Th \rightarrow$ see above (ultimately ^{208}Pb)

$^{233}U \xrightarrow{1.6 \times 10^{5}\ y\ \alpha} {}^{229}Th \xrightarrow{7340\ y\ \alpha} {}^{225}Ra \xrightarrow{15\ days\ \beta^-} {}^{225}Ac \xrightarrow{10\ days\ \alpha}$

$^{221}Fr \xrightarrow{4.8\ min.\ \alpha} {}^{217}At \xrightarrow{0.03\ sec\ \alpha} {}^{213}Bi \xrightarrow{47\ min.\ \beta^-} {}^{213}Po \xrightarrow{4 \times 10^{-6}\ sec.\alpha}$

$\xrightarrow[\alpha]{} {}^{209}Tl \xrightarrow{2\ min.\ \beta^-}$

$^{209}Pb \xrightarrow{3\ hr.\ \beta^-} {}^{209}Bi$ stable

$^{234}U \xrightarrow{2.46\times10^5\ y\ \alpha} {}^{230}Th \xrightarrow{8\times10^4\ y\ \alpha} {}^{226}Ra \xrightarrow{1600\ yr\ \alpha} {}^{222}Rn \xrightarrow{3.8\ days\ \alpha}$

$^{218}Po \xrightarrow{3\ min\ \alpha} {}^{214}Pb \xrightarrow{26\ min\ \beta^-} {}^{214}Bi \xrightarrow{20\ min\ \beta^-} {}^{214}At \xrightarrow{short\ \alpha}$

$^{210}Bi \xrightarrow{5\ days\ \beta^-} {}^{210}Po \xrightarrow{138\ days\ \alpha} {}^{206}Pb$ stable

$^{235}U \xrightarrow{7.04\times10^8 y\ \alpha,\ SF} {}^{231}Th \xrightarrow{25\ hr\ \beta^-} {}^{231}Pa \xrightarrow{3\times10^4\ yr\ \alpha} {}^{227}Ac \xrightarrow{21\ yr\ \beta^-}$

$^{227}Th \xrightarrow{18\ days\ \alpha} {}^{223}Ra \xrightarrow{11\ days\ \alpha} {}^{219}Rn \xrightarrow{4\ sec\ \alpha} {}^{215}Po \xrightarrow{1.7\times10^{-3} sec\ \alpha}$

$^{211}Pb \xrightarrow{36\ min.\ \beta^-} {}^{211}Bi \xrightarrow{2\ min.\ \alpha} {}^{207}Tl \xrightarrow{4\ min.\ \beta^-} {}^{207}Pb$ stable

$^{236}U \xrightarrow{2.3\times10^7\ y\ \alpha,\ SF} {}^{232}Th$ (see previous page, ultimately ^{208}Pb)

$^{238}U \xrightarrow{4.5\times10^9 y\ \alpha,\ SF} {}^{234}Th \xrightarrow{24\ days\ \beta^-} {}^{234}Pa \xrightarrow{6.7\ hrs\ \beta^-} {}^{234}U$ (see above, ult. ^{206}Pb)

$^{237}Np \xrightarrow{2.14\times10^6 y\ \alpha} {}^{233}Pa \xrightarrow{27\ days\ \beta^-} {}^{233}U$ (see above, ult. ^{209}Bi)

$^{238}Pu \xrightarrow{87.7\ y\ \alpha,\ SF} {}^{234}U$ (see above, ult. ^{206}Pb)

$^{239}Pu \xrightarrow{2.4\times10^4 y\ \alpha} {}^{235}U$ (see above, ult. ^{207}Pb)

$^{240}Pu \xrightarrow{6.56\times10^3\ y\ \alpha,\ SF} {}^{236}U$ (see above, ult. ^{208}Pb)

$^{241}Pu \xrightarrow{14\ y\ \beta^-} {}^{241}Am \xrightarrow{433\ y\ \alpha} {}^{237}Np$ (see above, ult. ^{209}Bi)

$^{242}Pu \xrightarrow{3.7\times10^5\ y\ \alpha,\ SF} {}^{238}U$ (see above, ult. ^{206}Pb)

$^{241}Am \xrightarrow{433\ y\ \alpha} {}^{237}Np$ (see above, ult. ^{209}Bi)

$^{243}Am \xrightarrow{7.3\times10^3\ y\ \alpha} {}^{239}Np \xrightarrow{2\ days\ \beta^-} {}^{239}Pu$ (see above, ult. ^{207}Pb)

DISTRIBUTION

Raymon D. Cox, Acting, Director
Contract Management Division
Nevada Operations Office
U.S. Department of Energy
P.O. Box 98518
Las Vegas, NV 89193-8518

Beverly Colbert
Contract Management Division
Nevada Operations Office
U.S. Department of Energy
P.O. Box 98518
Las Vegas, NV 89193-8518

Doug Duncan
Hydrology Program Manager
Environmental Protection Division
Nevada Operations Office
U.S. Department of Energy
P.O. Box 98518
Las Vegas, NV 89193-8518

Kenneth A. Hoar, Director
Environment, Safety & Health Division
Nevada Operations Office
U.S. Department of Energy
P.O. Box 98518
Las Vegas, NV 89193-8518

Roger Jacobson
Desert Research Institute
Water Resources Center
P.O. Box 19040
Las Vegas, NV 89132-0040

Marjory Jones
Desert Research Institute
Water Resources Center
P.O. Box 60220
Reno, NV 89506-0220

Randy Laczniak
U.S. Geological Survey
Water Resources Division
6770 S. Paradise Rd.
Las Vegas, NV 89119

Runore C. Wycoff, Director
Environmental Restoration Division
Nevada Operations Office
U.S. Department of Energy
P.O. Box 98518
Las Vegas, NV 89193-8518

Leslie A. Monroe
Environment, Safety & Health Division
Nevada Operations Office
U.S. Department of Energy
P.O. Box 98518
Las Vegas, NV 89193–8518

Mike Sabbe
Bechtel Nevada
P.O. Box 98521
Las Vegas, NV 89193-8521

Peter Sanders
Environmental Restoration Division
Nevada Operations Office
U.S. Department of Energy
P.O. Box 98518
Las Vegas, NV 89193-8518

David K. Smith
Isotopes Sciences Division
Lawrence Livermore National Laboratory
P.O. Box 808, M/S L231
Livermore, CA 94550

Doug Trudeau
U.S. Geological Survey
Water Resources Division
6770 S. Paradise Rd.
Las Vegas, NV 89119

Tim White
International Technology Corporation
P.O. Box 93838, M/S 439
Las Vegas, NV 89193–3838

Nevada State Library and Archives
State Publications
100 North Stewart Street
Carson City, NV 89710-4285

Archives
Getchell Library
University of Nevada, Reno

Beverly Carter
MacKay School of Mines Library
University of Nevada, Reno

Document Section, Library
University of Nevada, Las Vegas
4505 Maryland Parkway
Las Vegas, NV 89154

Library
Desert Research Institute
P.O. Box 60220
Reno, Nevada 89506–0220

Library
IT Corporation
Bldg. B–1
P.O. Box 93838, M/S 439
Las Vegas, NV 89193–3838
ATTN: Toni Miller, M/S 439

Library
Southern Nevada Science Center
Desert Research Institute
P.O. Box 19040
Las Vegas, NV 89132-0040

Technical Information Resource Center
Nevada Operations Office
U.S. Department of Energy
P.O. Box 98518
Las Vegas, NV 89193–8518

Public Reading Facility
Bechtel Nevada
P.O. Box 98521
Las Vegas, NV 89193-8521

Office of Scientific and Technical Information
U.S. Department of Energy
P.O. Box 62
Oak Ridge, TN 37831–9939